Swansea University
Prifysgol Abertawe

College of Engineering

Engineering Doctorate Research Project

2016-2021

Project Title:

Aesthetic and performance enhancements of ZMA coated steels

Name:	**Amar Dhoj Malla**
Supervisor:	**Professor James Sullivan**
Research Centre:	**Materials Engineering**
Discipline:	**Materials**
Submission date:	**16/04/2021**

Aesthetic and performance enchancements of ZMA coated steels

By

Amar Dhoj Malla

A Thesis

Presented to Swansea University

In fulfilment of the

requirements for the degree of

Engineering Doctorate (EngD)

In

Materials Engineering

College of Engineering, Swansea University, 2021

Author's Declaration:

This work has not previously been accepted in substance for any degree and is not being concurrently submitted in candidature for any degree.

Signed: Amar Malla

Date: 16/04/2021

STATEMENT 1

This thesis is the result of my investigations, except where otherwise stated. Other sources are acknowledged by footnotes giving explicit references.

Signed: Amar Malla

Date: 16/04/2021

STATEMENT 2

I hereby give consent for my thesis, if accepted, to be available for photocopying and inter-library loan, and for the title and summary to be made available to outside organisations.

Signed: Amar Malla

Date: 16/04/2021

Abstract:

The motivation for the investigations performed in this thesis is the aspiration to develop a metallic coating and an environmentally friendly duplex coating system with superior corrosion & mechanical properties. This in turn will reduce the raw material usage, prolong the structural integrity and save money to the manufacturers and customers. To this end, a quaternary metallic coating alloy system and a duplex coating system with a synergy between the metallic and organic layers with enhanced corrosion properties are developed. A combination of novel techniques such as; Scanning vibrating electrode technique (SVET) and Time-lapse microscopy (TLM) are used to understand and establish the corrosion mechanism of a quaternary metallic alloy and duplex coating system. Miniature testing techniques such as Nanoindentation, Vicker hardness and Small punch tensile test are used to understand the mechanical properties of the quaternary metallic alloy. The original contributions to knowledge are the establishment and validation that a magnesium source such as Mg_2Ge and Mg_2Si could perform as a corrosion inhibitor and provide a transient level of protection when embedded in the metallic coating systems.

A varying amount of germanium (Ge) was introduced into the ternary Zinc Magnesium Aluminium system (ZMA- 0 Ge). The introduction of Ge had a significant impact leading to the formation of Mg_2Ge. The area fraction of the eutectic phase diminished with increasing Ge addition, accompanied by a corresponding increase in area fraction of primary zinc and Mg_2Ge. These microstructural changes have significantly enhanced the corrosion performance and altered the corrosion mechanism, particularly on the highest Ge addition (ZMA-1.8 Ge). Both SVET and TLM showed a significant delay in visible anode formation however SEM-EDS analysis and TLM using indicator revealed the phenomenon of Mg^{2+} ions discharge from Mg_2Ge during this delayed period, which is associated with the enhanced corrosion protection. Nanoindentation revealed a significant difference in hardness between the zinc phase and the eutectic phase of ZMA-0 Ge. All Ge containing alloys demonstrated a significant decline in plastic deformation however the magnitude of declination was similar.

Mg_2Si particulates embedded as a source of magnesium in a zinc-rich powder-based galvanising system (Zn) perform as corrosion inhibitors and reduce the SVET

measured aqueous corrosion metal loss exponentially. Similar to Mg_2Ge, Mg_2Si particles preferentially anodically dissolved discharging Mg^{2+} ions galvanically protecting the zinc surface consequently reducing the initial Zn corrosion. In addition, the presence of Mg_2Si delayed the initiation and diminished the cathodic delamination rate of Zn. In both cases (Mg_2Ge and Mg_2Si), once exposed to the corrosive electrolyte the initial discharge of Mg^{2+} ions enabled the pH to rise above 8 as Mg^{2+} ions will not hydrolyse. This rise in pH will encourage the precipitation of $Mg(OH)_2$ and also stabilise pre-existing Zinc oxide/hydroxides on the sample surface.

The addition of 1 wt.% of calcium (Ca) to Zn led to the formation of intermetallic $CaZn_{13}$. SVET and LPR measurements demonstrated a significant enhancement in corrosion resistance. TLM demonstrated that corrosion initiated and preferentially grew via $CaZn_{13}$. The addition of Na_3PO_4 enhanced the corrosion resistance significantly of both systems with the effect being much higher in presence of Ca. TLM revealed a significant variation in the corrosion mechanism of Zn and Zn-1Ca in presence of Na_3PO_4. For Zn, the growth of the anode was restricted by the precipitation of insoluble corrosion product in the vicinity of the anode whereas for Zn-1Ca it leads to a formation of a protective film that covers the whole of the exposed surface. It is postulated that the superior corrosion resistance offered by Zn-1Ca in the presence of Na_3PO_4 could be due to the formation of $Ca_3(PO4)_2$ and $Zn_2Ca(PO_4)_2.2H_2O$ with a more compact structure and better preventive ability.

Acknowledgements:

Firstly, I would like to express my gratitude to the Doctorate Training in Functional Coatings scheme (COATED) at Swansea University, industrial partner TATA Steel and the funding bodies Engineering and Physical Sciences Research Council (EPSRC) and European Social Fund (ESF).

I would especially like to thank my supervisor and mentor, Professor James Sullivan. Thank you for all the guidance and patience over the years, I couldn't have asked for a better supervisor and mentor. Hopefully, this relationship will continue for years to come. I also appreciate the help provided by Dr Nathan Cooze, Dr Natalie Wint and Professor David Penney. I would also like to thank the administrative team at M2A.

Finally, I would like to thank my family for their belief and encouragement. It would not have been possible without your support. Lastly, thank you to each individual who has helped me through my EngD journey. I will remember my time very fondly.

Contents

List of Figures:

List of Tables:

List of Videos:

Video V1: ZMA-0 Ge in 0.17 mol.dm^{-3} NaCl pH 7 electrolyte

Video V2: ZMA-1.8 Ge in 0.17 mol.dm^{-3} NaCl pH 7 electrolyte

Video V3: ZMA-0 Ge in 0.17 mol.dm^{-3} NaCl pH 7 electrolyte with phenolphthalein indicator

Video V4: ZMA-1.8 Ge in 0.17 mol.dm^{-3} NaCl pH 7 electrolyte with phenolphthalein indicator

Video V5: Zn (Zinga) in 0.17 mol.dm^{-3} NaCl pH 7 electrolyte

Video V6: Zn + Mg_2Si Ge in 0.17 mol.dm^{-3} NaCl pH 7 electrolyte

Video V7: Zn (Zinga) in 0.17 mol.dm^{-3} NaCl pH 7 electrolyte with phenolphthalein indicator

Video V8: Zn + Mg_2Si Ge in 0.17 mol.dm^{-3} NaCl pH 7 electrolyte with phenolphthalein indicator

Video V9: Zn in 0.17 mol.dm^{-3} NaCl pH 7 electrolyte

Video V10: Zn-1Ca in 0.17 mol.dm^{-3} NaCl pH 7 electrolyte

Video V11: Zn in 0.17 mol.dm^{-3} NaCl pH 7 electrolyte with phenolphthalein indicator

Video V12: Zn-1Ca in 0.17 mol.dm^{-3} NaCl pH 7 electrolyte with phenolphthalein indicator

Definitions/ List of Symbols:

ZMA	Zinc-Magnesium-Aluminium
$Mol.dm^{-3}$	Moles per $decimetre^3$
Wt. (%)	Weight percentage
μm	Microns
E	Electrode potential
E_{corr}	Free corrosion potential
i_{corr}	Corrosion current
i	Current
i_a	Anodic current density
i_c	Cathodic current density
F	Faradays constant (96487 $C.mol^{-1}$)
R	universal gas constant (8.31 J mol^{-1} K^{-1})
$A.m^2$	Amps per $metre^2$
Q	Charge (C)
n	No. of electrons
j_z	Normal current density
HDG	Hot-dip galvanisation
SVET	Scanning vibrating electrode technique
TLM	Time-lapse microscopy
SEM	Scanning electron microscopy
EDS	Energy-dispersive X-ray spectroscopy
OCP	Open circuit potential
SCE	Saturated calomel electrode
K_{sp}	Solubility product

Chapter 1 Background

1.1 Introduction

Steel and its products are used extensively in various construction and manufacturing industries. Steel has been the foundation of the last 100 years of development and progress and will continue to be fundamental in overcoming new challenges in the coming years. World crude steel production reached 1867 million tonnes for the year 2019 [1]. Steel is relatively inexpensive, found in abundance, offers high strength to weight ratio and has good formability. However, steel comes with a nemesis, it is prone to corrosion which can cause a substantial problem with its structural integrity. This steel corrosion is typically seen as; an oxide layer (Fe_2O_3) on the steel surface. The cost of corrosion is astronomical. It is estimated to be US$2.5 trillion, which is 3.4% of the global Gross Domestic Product (GDP) of 2013 [2].

Several approaches have been used to prevent corrosion in the steel industry among which galvanisation has been the most widely used. Hot-dip galvanised (HDG) steel utilises the electrochemical properties of the zinc (Zn) to preferentially corrode to protect the steel, as it has more negative electrode potential under the galvanic series. In addition to Zn sacrificially protecting the steel it also acts as a protective barrier between the steel and the environment [3]–[6]. Zinc alloyed with varying amounts of aluminium such as Galfan (Zn-5Al) and Galvalume (Zn-55Al) offers greater corrosion protection than conventional HDG Zn coated steel. In comparison to Zn only coating, Galfan and Galvalume offer 1.5-2 and 2-4 times improved protection respectively [7]–[9]. In recent years ternary systems such as zinc magnesium aluminium (ZMA) have been found to offer even greater corrosion protection compared to a binary system (Galfan) and Zn only metallic coating [10]–[12]. Hence, ZMA is a subject of significant interest to numerous industries such as automotive and construction.

Although ZMA offers better protection compared to Zn and Zn-Al coatings, significant effort has been put to further improve the corrosion resistance of ZMA. Several approaches have been applied, i) though modification of its microstructure via alteration in processing parameters [13], [14] ii) by changing the concentration of Mg and Al [15], [16] and iii) by adding quaternary alloy additions [17][18]. Here, we implement the 3rd approach i.e addition of a quaternary element to ZMA.

1.2 Fundamentals of corrosion

The corrosion process is typically associated with processed metals. This is due to the energy needed to remove the metals from their ore and process them into alloys that have the desired properties. This processing makes alloys, such as steel, in a metastable state and is thermodynamically unstable. Corrosion is the natural process in which these processed metastable metals will return to their oxidised form when exposed to atmospheric conditions [19]–[21].

1.2.1 Gibbs Free Energy

The tendency of a metal to corrode in terms of thermodynamics is given by Gibbs free energy (ΔG). It is the driving force for the corrosion to occur. Therefore, the value of ΔG is used to predict whether the corrosion will occur or not. If $\Delta G < 0$, the corrosion reaction will occur spontaneously however if $\Delta G > 0$ it will not occur. The Gibbs free energy is given by equation 1.1.

$$\Delta G = -nFE \qquad [1.1]$$

Where, *n* is the number of moles of electrons, F is Faraday's constant (96485 $Cmol^{-1}$), and *E* is the cell potential (in volts).

Figure 1.1 represents the Gibbs free energy of metal. ΔG^* in Figure 1.1 is the activation energy. For corrosion to occur ΔG^* must be overcome and the lower the value of ΔG^* greater is the tendency of a metal to corrode [20]. In the presence of an electrolyte (water, salt solution, moisture) the activation energy of metal reduces and the corrosion rate of metal increases. The corrosion products possess the same energy level (state) as that of ore.

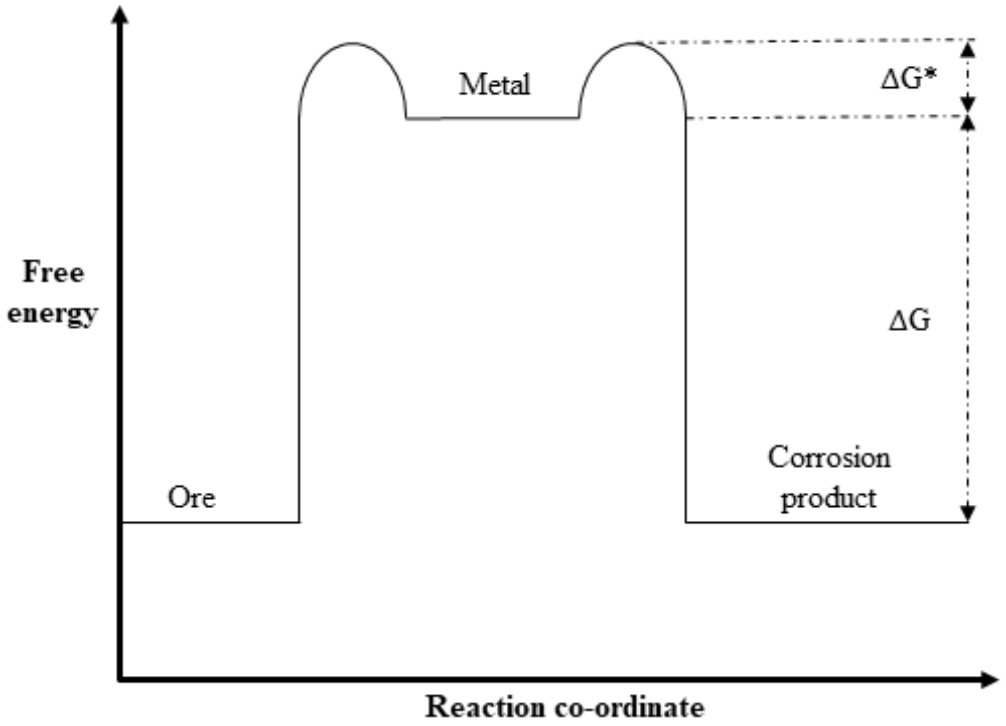

Figure 1.1: Gibbs Free Energy diagram of a metal

1.2.2 Electrochemistry of Corrosion

Corrosion is an electrochemical process in which transfer of electron occurs and is also known as Redox reaction where two different reactions, oxidation and reduction reactions occur simultaneously. For example in the case of iron (Fe) in aerated water (H_2O) at neutral pH:

Oxidation reaction which occurs at the anodic site:

$$2Fe \rightarrow 2Fe^{2+} + 4e^{-} \qquad [1.2]$$

Reduction reaction which occurs at the cathodic site:

$$O_2 + 2H_2O + 4e^{-} \rightarrow 4OH^{-} \qquad [1.3]$$

Full reaction

$$2Fe + 2H_2O + O_2 \rightarrow 2Fe^{2+} + 4OH^{-} \rightarrow 2Fe(OH)_2 \qquad [1.4]$$

An electrochemical cell is established during corrosion. The cell comprises four primary components; an anode, a cathode, an electrolyte and an electrical connection between anode and cathode. The distance between anodic and cathodic sites determine the type of corrosion. In situations where anodes and cathode are small,

relatively close and are numerous, it is termed ‘general corrosion’ whereas if they are large and discrete, it is termed as ‘localized corrosion’.

Oxidation reaction occurring at the anodic site leads to the formation of metal cations and the production of free electrons, as presented in equation 1.5.

$$M \rightarrow M^{n+} + ne^{-} \qquad [1.5]$$

Where ‘M’ is a metal atom. The produced metal cations (M^{n+}) are dissolved into the electrolyte and the excess electrons are transferred and consumed at the cathodic sites for the reduction reaction. A schematic of the corrosion cell established on a metal surface is presented in Figure 1.2. The anodic reaction remains unchanged however the cathodic reactions are influenced by the pH ($-\log[H^{+}]$) of the electrolyte and are presented in equations 1.6 - 1.9.

Hydrogen

$$2H^{+} + 2e^{-} \rightarrow H_2 \text{ (acidic conditions)} \qquad [1.6]$$

Oxygen

$$O_2 + 4H^{+} + 4e^{-} \rightarrow 2H_2O \text{ (acidic conditions)} \qquad [1.7]$$

$$O_2 + 2H_2O + 4e^{-} \rightarrow 4OH^{-} \text{ (neutral/basic conditions)} \qquad [1.8]$$

Water

$$2H_2O + 2e^{-} \rightarrow H_2 + OH^{-} \text{ (neutral/basic conditions)} \qquad [1.9]$$

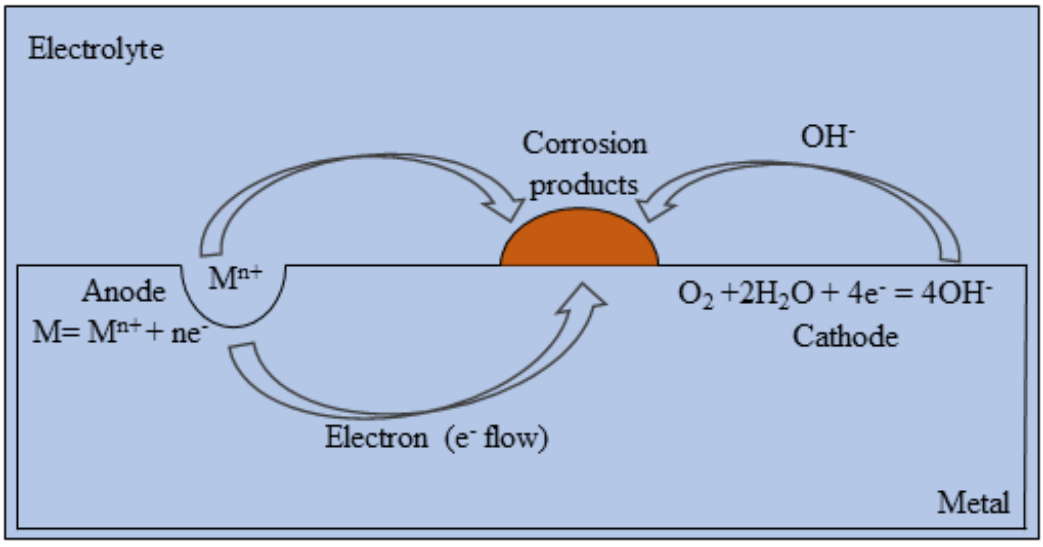

Figure 1.2: Corrosion cell established on a metal surface.

1.2.3 Electrode potential

When two metals are in electrochemical contact the relative potentials of the reactants will allow us to predict the direction and the magnitude of the driving force for the electrochemical reactions. A scale of relative potentials exists for typical redox reactions (equation 1.10) when measured against a standard hydrogen electrode in comparable conditions and all of the species in their standard states. This is typically termed at the standard cell potential (E_{cell}).

The standard electrode potential (E^o) is the measurement of relative strength as an oxidising or reducing agent of a material. Thus, E^o gives us the measure of the thermodynamic possibility of corrosion occurrence. Whilst E^o provides useful information regarding the likelihood of corrosion occurrence, it has a limitation as it does not provide information regarding the corrosion rate.

When two different metals form an electrochemical cell, metal with higher E^o acts as a cathode and the other an anode. The potential difference (ΔE) between two metals (electrodes) is called the electromotive force (e.m.f) and is presented in equation 1.10.

$$\Delta E\ (E_{cell}) = E_1\ (E_{cathode}) - E_2\ (E_{anode}) \qquad [1.10]$$

The larger the ΔE, the greater is the driving force for the reaction [22]. To determine the electrode potential two-electrode setup consisting of a working electrode and reference electrode are used. Where :

working electrode = electrode of interest

reference electrode = electrode delivers stable and well-known potential.

Different types of reference electrodes are available but here we will only discuss standard hydrogen electrodes and calomel electrodes.

Standard Hydrogen Electrode (SHE):

The standard hydrogen electrode consists of a platinised platinum electrode submerged in a 1 mol dm^{-3} acid (HCl) and 1 atmospheric pressure hydrogen gas at 298 ^oK. In this half cell, the hydrogen ions are reduced to produce hydrogen gas as presented in equation 1.11.

$$2H^+ + 2e = H_2 \qquad E=0.00V \qquad [1.11]$$

It is arbitrarily assumed to have zero potential hence providing a zero reference point for electrode potential [23].

Calomel electrode :

In this system, the potential is dependent on the chloride ion concentration. The potential determining equilibrium is presented in equation 1.12.

$$Hg_2Cl + 2e = 2Hg + 2Cl^- \qquad [1.12]$$

Any measurements made using the calomel electrode could be converted to the SHE scale by adding 0.242V.

1.2.3.1 Electrochemical series

Metals are arranged in electrochemical series per their electrode potential (E^o) measured against a standard reference electrode. Metals with high positive E^o are recognised to have good corrosion resistance conversely, metals with high negative E^o exhibit a tendency to corrode easily [23]. E^o of different elements measured against the standard hydrogen electrode at room temperature (25^oC) are shown in Table 1.1. [22]

Table 1.1: The electrochemical series

Electrode Reaction	Potential E^o (V vs SHE)
$Au^+ + e^- = Au$	+ 1.498
$Pt^{2+} + 2e^- = Pt$	+ 1.200
$Ag^+ + e^- = Ag$	+ 0.799
$Hg^{2+} + 2e^- = Hg$	+ 0.788
$Cu^{2+} + 2e^- = Cu$	+ 0.337
$2H^+ + 2e^- = H_2$	0.000
$Pb^{2+} + 2e^- = Pb$	- 0.126
$Sn^{2+} + 2e^- = Sn$	- 0.136
$Ni^{2+} + 2e^- = Ni$	- 0.250
$Cd^{2+} + 2e^- = Cd$	- 0.403
$Fe^{2+} + 2e^- = Fe$	- 0.440
$Cr^{3+} + 3e^- = Cr$	- 0.744
$Zn^{2+} + 2e^- = Zn$	- 0.763
$Al^{3+} + 3e^- = Al$	- 1.662
$Mg^{2+} + 2e^- = Mg$	- 2.363
$Na^+ + e^- = Na$	- 2.714
$Ca^{2+} + 2e^- = Ca$	- 2.870
$K^+ + e^- = K$	- 2.925

1.2.4 Corrosion kinetics

Electrode potential indicates the thermodynamics possibility of corrosion reaction to occur, whereas kinetics addresses the rates at which they occur. In general, metals are exposed to non-standard conditions and the variables such as temperature, concentrations have a significant influence on the undergoing oxidation and reduction reactions. The electrode potential when the temperature and concentration are not standard is given by the Nernst equation, as given in equation 1.13.

$$E = E^o + \frac{RT}{nF}\ In\frac{[Products]}{[Reactants]} \qquad [1.13]$$

Where,

E = non-standard condition electrode potential

E^o = standard electrode potential

R = universal gas constant (8.31 J mol^{-1} K^{-1})

T = absolute temperature (^oK)

n = number of electrons

F = Faraday constant (96500 C mol^{-1})

[Products] = concentration of aqueous products from oxidation reaction

[Reactants] = concentration of aqueous reactants from reduction reaction

As in Figure 1.2, when a corrosion cell initiates on a metallic surface, the anodic and cathodic reactions are established. The rate of corrosion on those reactions are determined by the current (rate of ions/electron) flow with respect to time. The rate of corrosion is used to determine the current densities (current per unit area) at anode and cathode. If the currents rate at anodic and cathodic are given by I_a and I_c respectively. At equilibrium, the anodic and cathodic current densities are equal, therefore, the net exchange current density of the cell is equal to zero as given in equation 1.14.

$$I_a = -I_c = I_o \qquad [1.14]$$

Where,

I_a = anodic current rate (oxidation rate)

I_c = cathodic current rate (reduction rate)

I_o = net exchange current density

However, during the corrosion phenomenon, this equilibrium is lost and the potential of the system is different than that predicted by the Nernst equation. This deviation of potential from the equilibrium is called the over potential (η) and is given by equation 1.15.

$$\eta = E - E_e \qquad [1.15]$$

Where E is electrode potential and E_e is the Nernst electrode potential.

1.2.4.1 Evans diagram

A graphical representation of potential, E, against the logarithm to the base of 10 of the current, I, is known as the Evans diagram. A plot of E vs $\log_{10}$ I produces a straight line known as a Tafel plot. A combination of Tafel plots of individual anodic and cathodic processes produces Evans diagram. Evans diagram for a metal immersed in an aerated solution is presented in Figure 1.3.

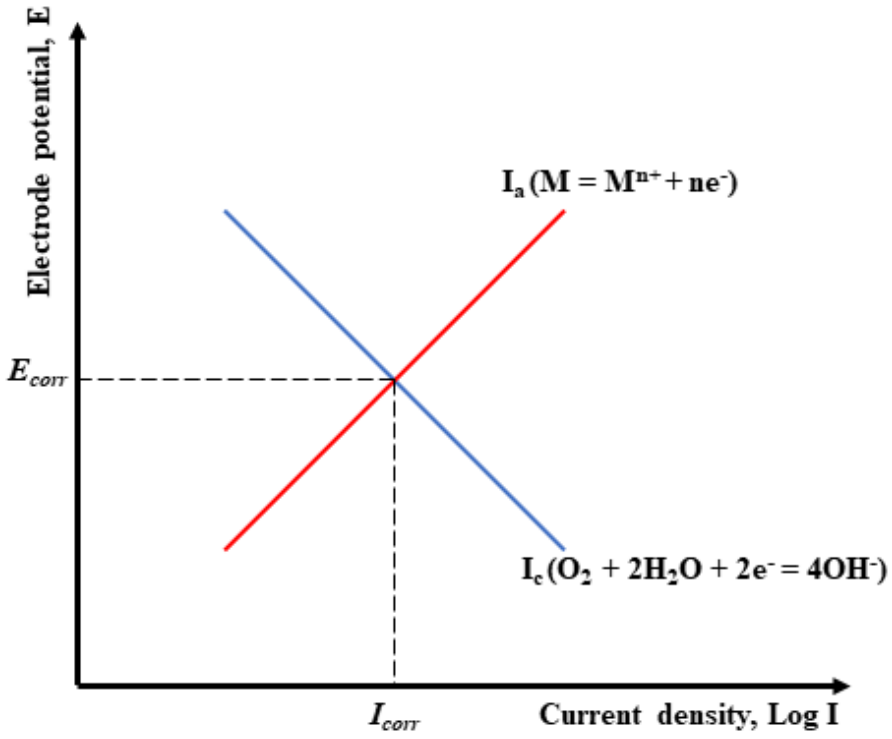

Figure 1.3: Evans diagram / Tafel plots for a metal immersed in an aerated solution.

Evans diagram demonstrates a potential that a freely corroding system adopts which is denoted as E_{corr} . The corresponding corrosion rate in the form of current density is denoted as I_{corr}. The Evans diagram represents the effect of over potential (η) on each half-reaction (anodic and cathodic) taking place on the electrode. The diagram provides valuable information regarding the rate of reaction for overall corrosion events in a system. At the point where two individual slopes (anodic and cathodic) intersect, the sum of anodic and cathodic current densities is equal to zero and the corresponding potential is known as open circuit potential.

1.2.5 Mechanics of corrosion

The corrosion rate of metal in an electrochemical cell is affected by several factors such as the electrode potential of the metal in the electrolyte, the pH of the electrolyte and the temperature of the cell. However, during corrosion two different types of electrochemical cells could form; galvanic corrosion cell and differential aeration cell.

1.2.5.1 Galvanic corrosion cell

In a galvanic corrosion cell, the anode and cathode are two different materials with different electrode potentials. Typically the materials with more negative potential act as anode and material with relative more positive potential acts as the cathode. The galvanic corrosion cell is driven by the potential difference between the anode and the cathode. The representation of a galvanic corrosion cell is presented in Figure 1.4.

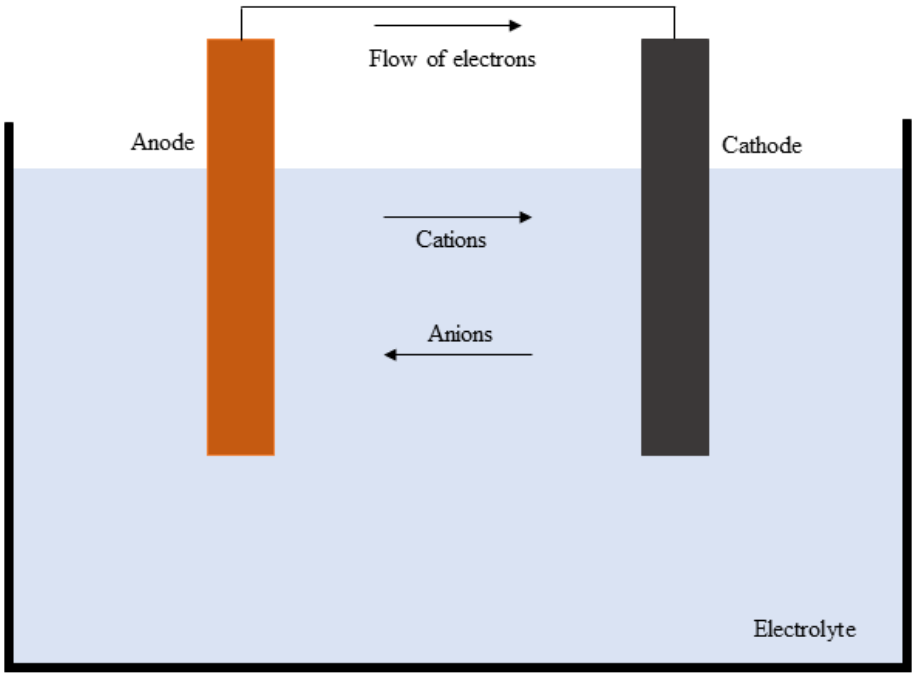

Figure 1.4: Galvanic corrosion cell

1.2.5.2 Differential aeration cell

When a metal surface is exposed to an electrolyte, the oxygen concentration acts as the driving force for anodic and cathodic activities. The region with higher oxygen concentration will predominantly form a cathodic site, where the region with lower oxygen concentration acts as an anodic site. This differential aeration cell is well

visualised by a drop of water on the surface of iron also known as Evans Water Drop. The schematic of Evans Water Drop is presented in Figures 1.5 (a) & 1.5 (b).

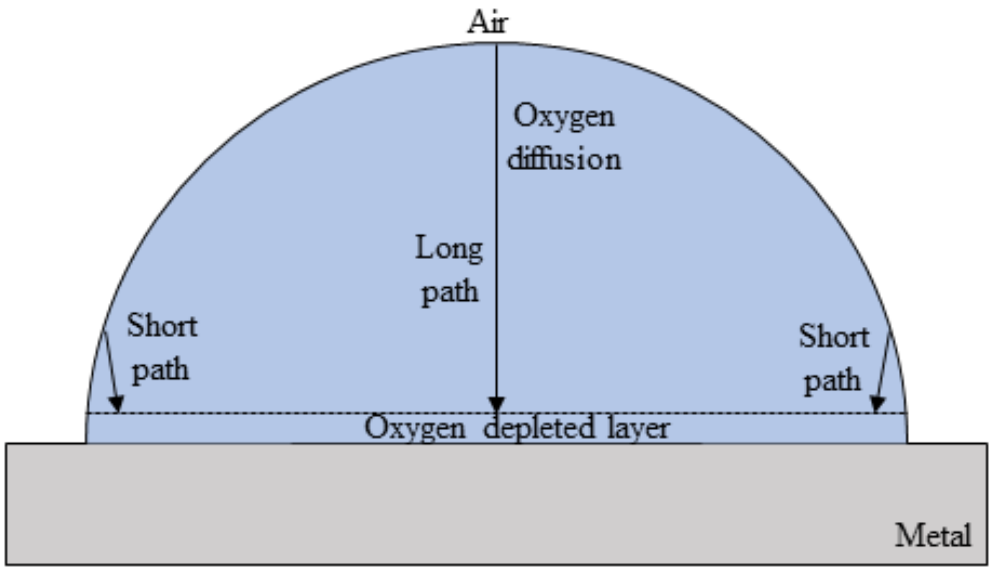

Figure 1.5(a): Evans water drop on the metal surface

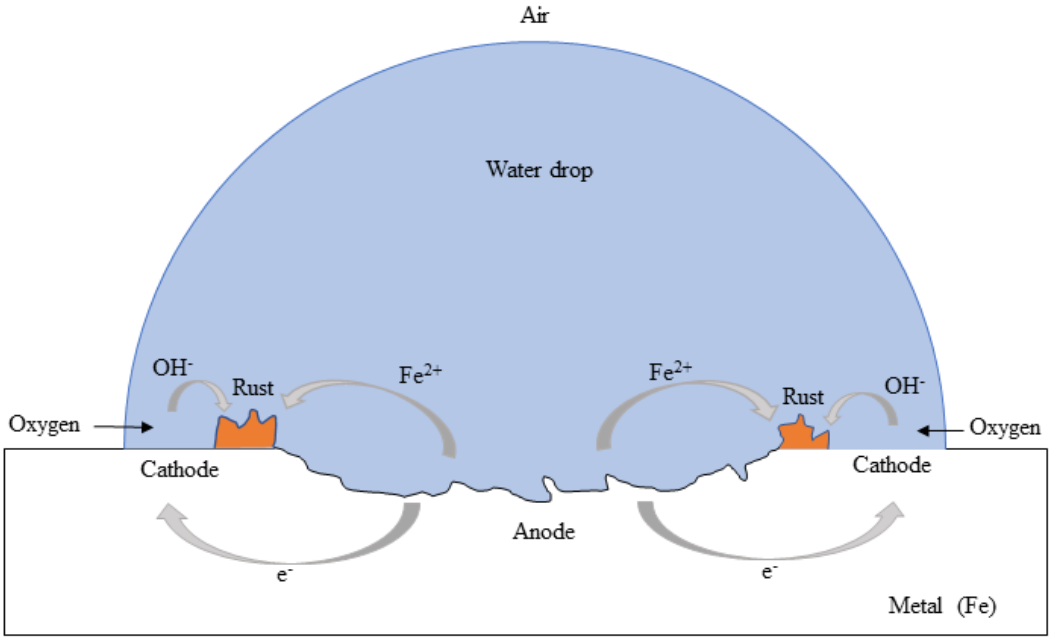

Figure 1.5(b): Differential aeration cell (Evans Water Drop mechanism)

The oxygen concentration at the interface between the waterdrop and metal surface dictates the site of preferential cathodic and anodic reactions. The oxygen diffusion path varies along with the water droplet hemispherical profile as shown in Figure 1.5(a). The diffusion path for oxygen along the water drop edge is shorter whereas

the centre of the water drop has the longest diffusion path. The longer diffusion path restricts the oxygen availability at the centre of the water droplet, thus forming a preferential anodic site. Meanwhile, at the edges of the water droplet oxygen replenish more easily, therefore, forming a preferential cathodic site. The metal ions dissolved in the solution encounter the hydroxide ions moving inward forming corrosion product at the interaction point. This process can be envisaged in Figure 1.5(b).

1.2.6 Selective attack

Corrosion which occurs at particular sites on a surface is referred to as selective attack corrosion. The selective attack occurs due to the difference in physical or compositional variation. Metals and alloys at a microscopic level are rarely uniforms due to the presence of grain boundaries and imperfections such as dislocations, voids and cracks. These imperfections possess higher thermodynamic energy levels as a result are prone to corrosion. In addition, the presence of intermetallics and metallic compounds within the microstructure also leads to selective corrosion attack. The selective attack can be categorised into grain boundary corrosion, intergranular corrosion and selective leaching.

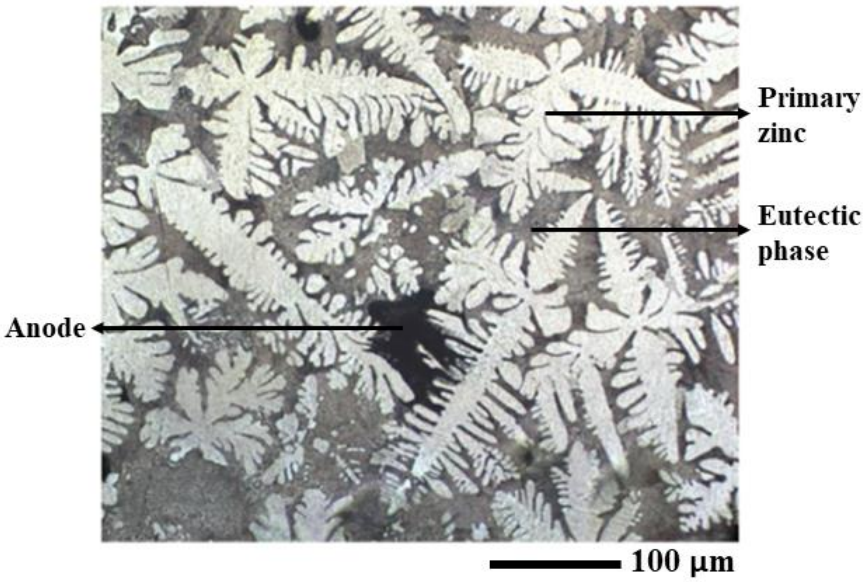

Figure 1.6: ZMA immersed in 1wt.% NaCl showing the anodic initiation site located in the inter-dendritic arm spacing of the primary zinc dendrites and growing preferentially through the eutectic phase.

Zinc magnesium aluminium (ZMA) metallic coating alloys are also subject to selective attack corrosion. During corrosion, anodes are initiated at the eutectic phase and grow preferentially through the eutectic phase leaving behind islands of zinc phases. This selective attack phenomenon on ZMA is presented in Figure 1.6.

1.2.7 Pourbaix diagrams

Potential – pH diagrams are known as Pourbaix diagrams and represent the stability of a metal as a function of potential and pH. These diagrams are based on the Nernst equation and solubility of metal and its species such as Zn, Zn^{2+}, $Zn(OH)_2$ etc for Zn metal. Pourbaix diagram exhibits whether the metal is in three different states i) immunity, when metal ions are $< 10^{-6}$ mol dm^{-3} ii) actively corroding when metal ions are $\geq 10^{-6}$ mol dm^{-3} and ii) passive when the metal surface is covered by insoluble layer [23]. The Pourbaix diagrams for zinc, aluminium and magnesium are shown in Figure 1.7.

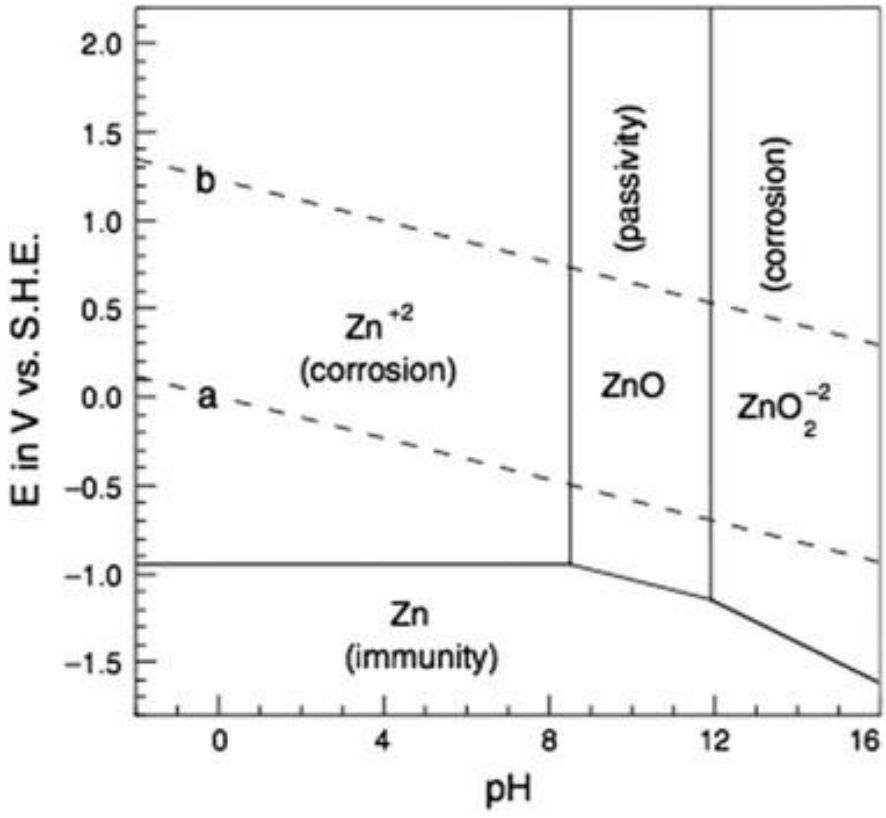

Figure 1.7(a): Pourbaix diagram for zinc in water [24]

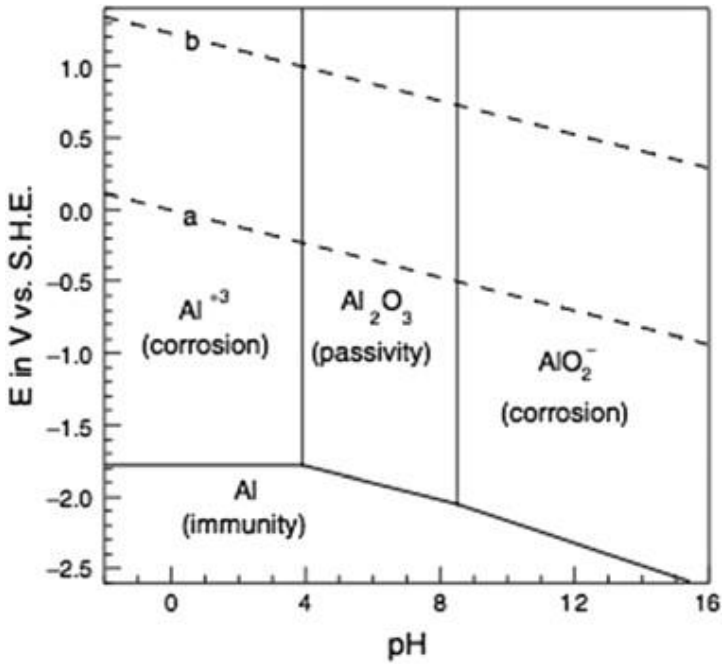

Figure 1.7(b): Pourbaix diagram for aluminium in water [24]

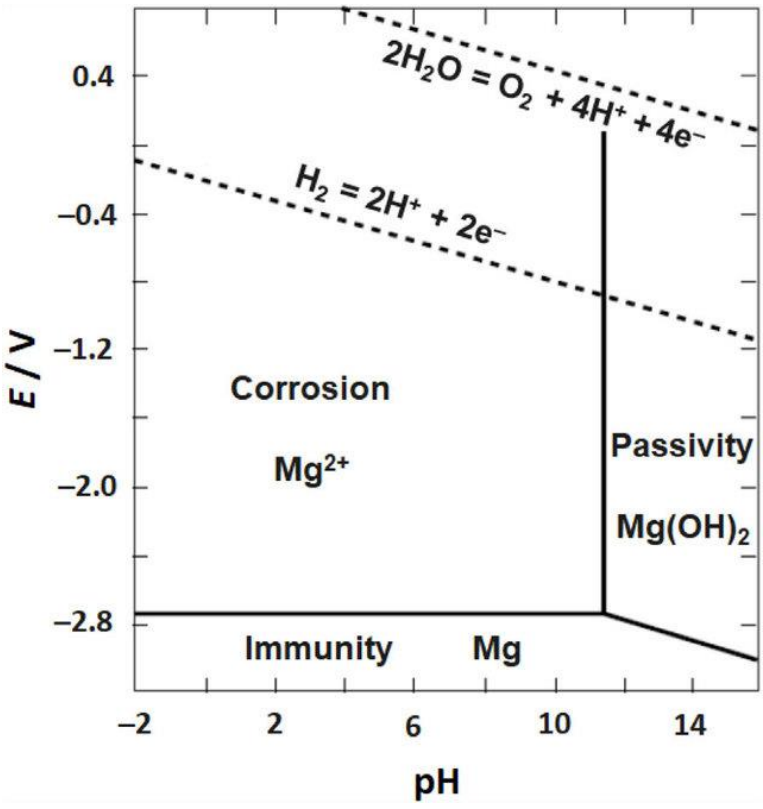

Figure 1.7(c): Pourbaix diagram for magnesium in water [25]

Pourbaix diagrams are based on thermodynamic equilibrium and omit the kinetic effects and provide no information on corrosion rate [23] however, it enables interpretation of otherwise complex systems more easily with respect to the potential

and pH environment. For example, for a ZMA system at high pH -13, both Zn and Al phases actively corrode whereas the Mg phase remains passive. Similarly, for Zn only system Zn is immune in certain conditions of pH and potential (Figure 1.7(a)) whereas in others it is passive or corrodes. Therefore, the Pourbaix diagram allows immediate assessment of your metal is safe or not.

1.3 Corrosion protection and control

Corrosion in metals and their alloys will occur sooner or later, therefore, it is inevitable. There are measures developed to delay the initiation of corrosion and reduce the rate at which corrosion occurs. Corrosion could be prevented if one of the four elements of an electrochemical cell; anode, cathode, electrolyte or the electrical contact between both anode and cathode is eliminated.

1.3.1 Protective coatings

Protective coatings are divided into a barrier and a sacrificial coating.

1.3.1.1 Barrier coatings

The barrier coating is the simplest approach to corrosion prevention via the physical separation of the metal from its environment. It prevents metal from direct contact with the electrolyte and air/moisture, therefore, inhibit the formation of the electrochemical cell. Organic coatings (enamels and paints), metallic coatings (tin, chromium and aluminium) and sol-gels (SiO_2) are used as barrier coatings. The presence of defects such as scratches initiates the corrosion of underlying metal typically via the delamination of the coating.

1.3.1.2 Sacrificial coatings

The sacrificial coating is also known as the anodic coating. The principle is based on dissimilar metals corrosion whereby metal is coated with more negative electrode potential metal. The more negative electrode potential metal acts as anode and corrodes preferentially protecting the underlying metal. The most common example is the use of zinc (E^o_{zn} = -0.763 V) to protect the steel substrate (E^o_{Fe} =-0.44V).

1.3.2 Corrosion inhibitor

The method of corrosion prevention by adding substances that can substantially impede corrosion is known as inhibition. In an organic coated steel system corrosion inhibitors are embedded into the primer and pre-treatment layers. Usually, inhibitors

are integrated into the system as pigments which are based on sparingly soluble salts such as strontium chromate or zinc phosphate. When the incorporation of inhibitor into the coating system is unviable, it could be dissolved into the electrolyte or suitable solvent and introduced into the system. Inhibitors affect the rate of either anodic oxidation or cathodic reduction or both, therefore, restricting the overall corrosion progress. A schematic of a multi-layered organically coated steel system is shown in Figure 1.8.

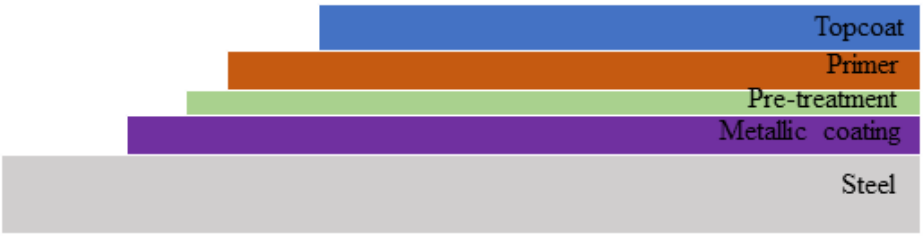

Figure 1.8: Schematic of organically coated steel.

They are classified into anodic and cathodic inhibitors.

1.3.2.1 Anodic inhibitors

Anodic inhibitors are further divided into two types. The first type affects the oxidation reaction. These inhibitors react with the metal ions to precipitate low-solubility compounds. These compounds are deposited at the anodic site forming a protective film impermeable to metal ions [26]. This impermeable film diminishes the anodic reaction lowering the corrosion current. The second type of anodic inhibitor is known as cathodic depolarisers or oxidising inhibitors. These species utilise the free electrons which are otherwise involved in oxygen reduction at the cathode. This increases the cathodic rate and shifts the E_{corr} value higher within the passive region for certain systems.

Some of the examples of anodic inhibitors are phosphate (PO_4^{3-}), molybdates (MoO_4^{2-}), silicates (SiO_4^{4-}), borate (BO_3^{2-}). The effect of anodic inhibitors on the corrosion rate is pictured on an Evans diagram, as presented in Figure 1.9(a). The addition of anodic inhibitor shifts the anodic metal dissolution curve, which results in an increase in system potential from E_{corr} to $E_{corr\ anodic}$ and reduction in corrosion current from I_{corr} to $I_{corr\ anodic}$. As anodic inhibitors increase the system's potential, an inadequate inhibitor presence will lead to pitting corrosion (aggressive metal dissolution).

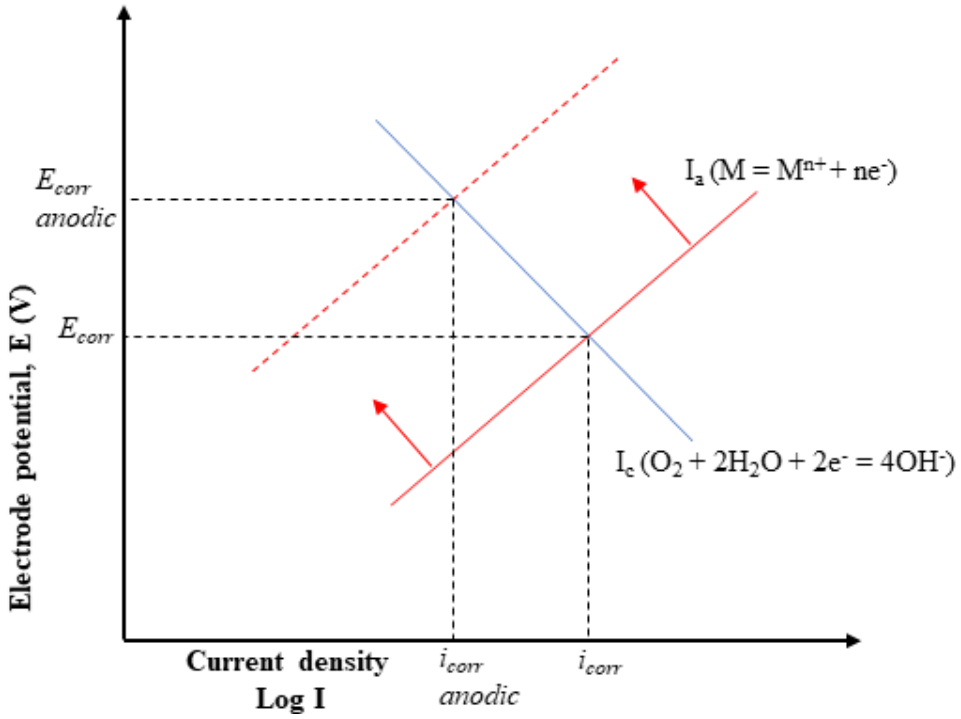

Figure 1.9(a): Evans diagram demonstration the effects of anodic inhibitor.

1.3.2.2 Cathodic inhibitors

Cathodic inhibitors perform in the same way as anodic inhibitors, but at the reduction reaction. Cathodic inhibitors react with the hydroxide ions and precipitate insoluble compounds at the cathodic sites [26]. These precipitated compounds limit the availability of oxygen for reduction reaction reaching the metal surface thus slowing the corrosion rate. Some examples of cathodic inhibitors are Ca^{2+}, Sr^{3+}, Ce^{3+}, Mg^{2+} and Zn^{2+}. The effect of cathodic inhibitors on the corrosion rate is pictured on an Evans diagram, as presented in Figure 1.9(b).

The addition of cathodic inhibitor shifts the cathodic oxygen reduction curve, which results in a decrease in both system potential from E_{corr} to $E_{corr\ cathodic}$ and corrosion current from I_{corr} to $I_{corr\ cathodic}$. However, they are often less effective than anodic inhibitors as they do not intercept the aggressive half of the reaction.

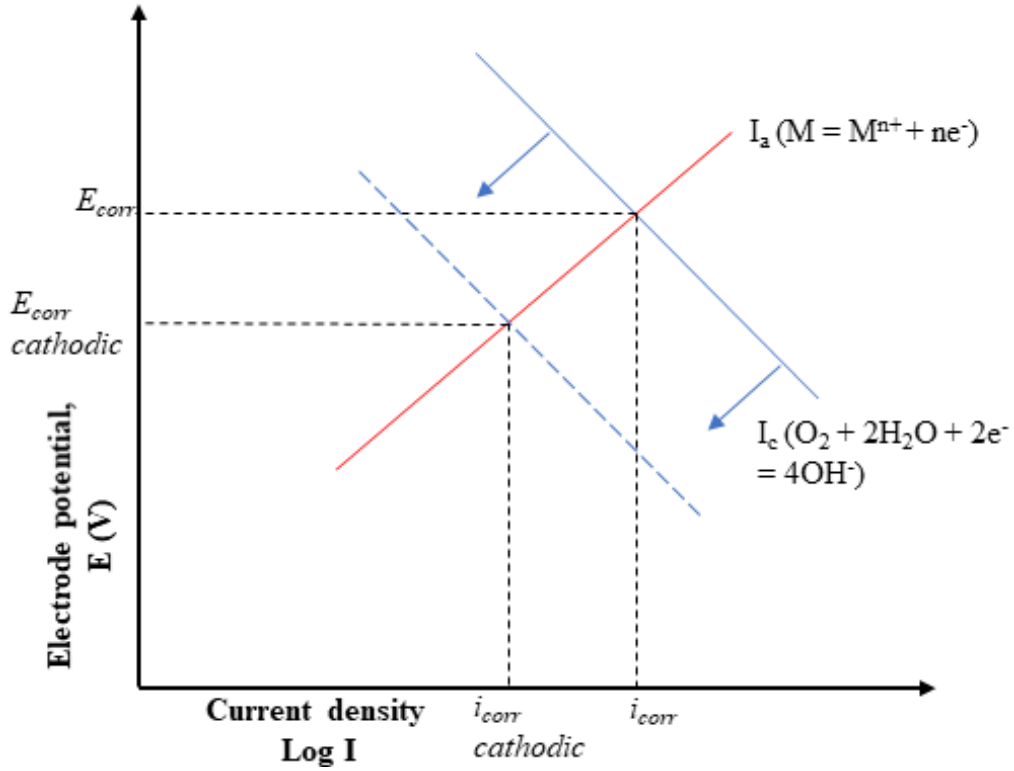

Figure 1.9(b): Evans diagram demonstration the effects of cathodic inhibitor.

1.3.3 Chromate and phosphate inhibitors

Hexavalent chromium provides incredible corrosion protection over a wide range of pH and electrolyte concentrations. Until now, it is considered the benchmark corrosion preventative compound and has been successfully implemented into corrosion protection coatings and primers [27]. When morphological failure occurs in coating or primer containing hexavalent chromium (CrO_4^{2-}) ions, CrO_4^{2-} seeps into the electrolyte and undergoes a reduction reaction to form chromium oxide (Cr_2O_3) film which is very insoluble and insulating [27]–[29]. Regardless of its effectiveness due to its environmental threats and carcinogenic (nasal and lung) nature, hexavalent chromium usage has been restricted in Europe as of January 2019. This has propelled an intensive research effort to find a suitable alternative that provides a comparable level of protection.

Phosphates have appeared as viable replacements for chromate inhibitors however the mechanism by which it provides the inhibition is not well understood [30]. Phosphates act as an anodic inhibitor in the presence of oxygen by precipitating metal phosphate local to the anodic features [31], [32]. Under certain conditions such presence of divalent cations (Ca^{2+}, Zn^{2+}) they also act as a cathodic inhibitor by

restricting the access of dissolved oxygen to the metal surface by forming an insulating layer by precipitating metal phosphate local to the cathodic features [30], [33].

Among the non-toxic and environmentally friendly corrosion inhibitors, phosphate is the most widely accepted and has been incorporated in paint formulations. Due to the widespread industrial usage of phosphate as a corrosion inhibitor especially in hot-dip galvanised steel, sodium phosphate has been nominated as a corrosion inhibitor under study within this body of work.

1.4 Galvanisation

Zinc coatings are widely used for the protection of steel. Zn coating protects the steel in two different ways i) acts as a barrier between the steel and the environment ii) corroding preferentially to the steel thus preventing the steel from undergoing anodic corrosion reaction. Zn is applied to the steel via various methods: hot-dip galvanisation, metalizing (zinc spraying), electroplating, zinc-rich paints and mechanical plating [34]. Among them, hot-dip galvanisation (HDG) is the most prevalent method of application as it offers superior properties such as formability, low cost, lightweight and recyclability. This technique has been proven feasible since the 18^{th} century and has been used extensively since then.

The process of creating a Zn alloy coating on steel by immersing the steel into a molten Zn bath at a temperature around $450^{o}C$ is known as HDG. HDG comprises a complex series of diffusion processes, thermodynamic transformations and metallurgical reactions [35]. HDG can be sub-divided into the continuous and batch process. The continuous process is used for steel strip where the first coil is processed, another is welded to the trailing end of the first and so on to provide the continual supply of the steel. The batch process is not continuous and is used for more complex shapes such as pipes and forgings.

In summary, the HDG process involves surface preparation, hot-dipping and cooling. The steel surface has to be chemically cleaned for the proper adhesion between the Zn and steel. Therefore, acidic or alkali solution is used to remove the organic impurities such as grease and then rinsed in water. The steel is then immersed in an acid solution (Sulphuric or hydrochloric acid) to remove surface oxide and scale. The steel surface is then activated to obtain the proper wetting by passing it through the

reduction atmosphere of nitrogen and hydrogen. The steel is then immersed into the molten Zn bath. The immersion times are generally less than 5 seconds. As the steel emerges out of the bath “air knives” are used to wipe excess zinc and also to control the thickness of the Zn layer followed by cooling.

1.4.1 Hot-dip galvanisation coatings

Initially, coatings were based on the Zn systems however research has led to the development of more corrosion-resistant coatings. Modern coatings are based on binary or ternary alloys systems. Quaternary systems are the subject of interest and importance of the current industry. The increased corrosion resistance offered by modern coatings has led to the reduction of coating thickness, weight and cost providing the industry with financial gain. Corrosion occurs either on the cut edge or on the surface. The microstructure of the coating is affected by various factors such as cooling rate, annealing time and nucleation temperature. The corrosion is influenced by the microstructure of coating, constituents such as CO_2, SO_x and Cl^- and the time of wetness etc [36]. Different composition metallic coatings are commercially available and the most common examples are Zn, binary Zn-aluminium and ternary zinc-magnesium-aluminium.

1.4.1.1 Zinc coatings

A conventional HDG coating predominately consists of Zn and 0.15-0.5 wt.% Al. HDG coating consists of a heterogeneous assembly of different phases which are formed due to the diffusion-reaction between the atoms of Zn and steel [34]. In the HDG Zn bath, the presence of Al diminishes iron loss into the bath and suppresses the formation of Fe-Zn intermetallic layers. This is achieved by the formation of intermetallic Fe_2Al_5 and $FeAl_3$ between steel and Zn layer interface [34], [37]. A cross-section of hot-dip galvanised steel without Al addition is presented in Figure 1.10(a).

The coated Zn layer without Al consists of four different phases; gamma (γ) (75% Zn-25% Fe), delta (δ) (90% Zn- 10% Fe), zeta (ζ) (94% Zn-6% Fe) and eta (η) (100% Zn) [38], [39]. The content of iron (Fe) on the Zn layer decreases as we move away from the Fe-Zn interface. This Fe-Zn intermetallic formation is suppressed by Al addition by the formation of Fe_2Al_5 as presented in Figure 1.10(b).

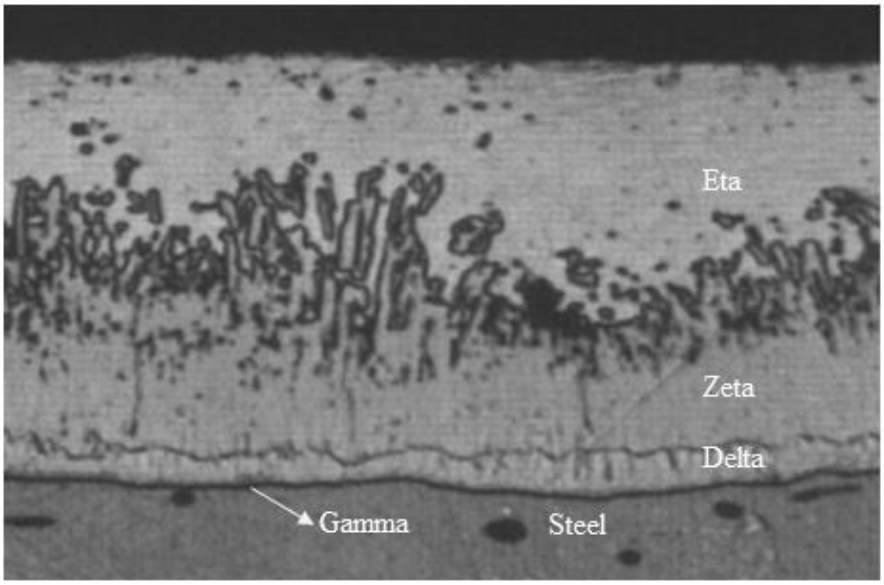

Figure 1.10(a): Cross-section of hot-dip galvanised zinc coating without 0.15-0.5 wt.% Al addition [4].

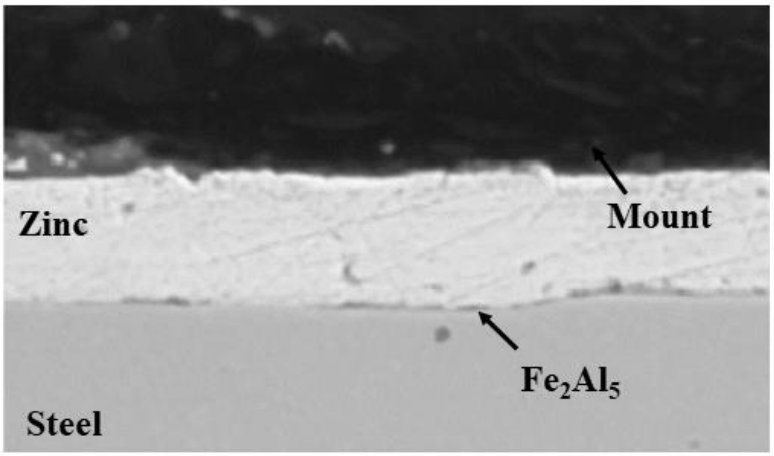

Figure 1.10(b): Cross-section of hot-dip galvanised zinc coating with 0.15-0.5 wt.% Al addition [40].

1.4.1.1.1 Corrosion mechanism of zinc coatings

The investigation on corrosion of zinc coatings under different environmental (atmospheric and immersion) conditions have suggested that the corrosion behaviour and the morphology of the corrosion products formed are influenced by the exposure conditions such as dissolved species, concentration, pH and temperature [36], [41]–[49]. The formation of corrosion products is a complex process, sensitive to environmental conditions and changes continuously with time. Techniques such as Electrochemical Impedance Spectroscopy (EIS) [50], Scanning Vibrating Electrode

Technique (SVET) [45], [49], [51] and Scanning Kelvin Probe (SKP) [52]–[54]are used to obtain invaluable mechanistic information on corrosion of both organically coated and uncoated HDG Zn.

During atmospheric corrosion, when Zn reacts with oxygen, a thin layer of Zincite (ZnO) is formed however it has a minimal protective effect because they are promptly transformed into hydroxide in the presence of water [42]. Whereas, in a humid atmosphere thin layer of hydroxycarbonate ($Zn_5(OH)_6CO_3$) (hydrozincite) is formed [55] instead of ZnO. Under immersion conditions, the exact mechanism of zinc passivation is unclear however $Zn(OH)_2$ and/or ZnO have been proposed to be the passivating species in an alkaline environment [47], [56]. It has also been reported that the presence of sodium and chlorine leads to the formation of Simonkolleite ($Zn_5(OH)_8Cl_2.H_2O$) (zinc hydroxychloride) which eventually evolves into sodium zinc hydroxychlorosulfate (Gordaite, $Na_4Zn_4SO_4(OH)_6Cl_{2}.6H_2O$) [55].

The anodic dissolution and passivation of Zn have been investigated utilising various electrochemical techniques in conjunction with surface analysis techniques in a variety of corrosive environments however, they have been focused on near-neutral or alkaline media, as Zn is observed to be passive in pH range 10-13 [45], [46] [56]. The literature suggests that Zn corrodes via pitting in both aggressive (presence of chloride anions) as well as dilute environments (distilled water) [44], [45]. It has also been suggested that pitting in Zn initiates due to local acidification of the metal surface and pitting potential is close to the equilibrium potential for equation 1.16 [57].

$$Zn = Zn^{2+} + 2e^{-} \qquad [1.16]$$

1.4.1.2 Zinc-Aluminium coatings

Galfan/Galvalloy is a binary system with 95 wt.% Zn and 5 wt.% Al. Further increase in the aluminium (Al) from ≤ 0.5 wt.% in Zn only coating to 5 wt.% has enhanced corrosion resistance and ductility [16]. In addition to the suppression of formation of Fe-Zn intermetallic at Fe-Zn interface, the presence of higher Al leads to the formation of Al_2O_3 oxide film protecting the metallic coating itself [58]–[60]. Galfan (ZA) consists of primary Zn rich dendrites surrounded by Zn/Al lamellar eutectic matrix [55]. A cross-section and surface image of the galfan is presented in Figure 1.11.

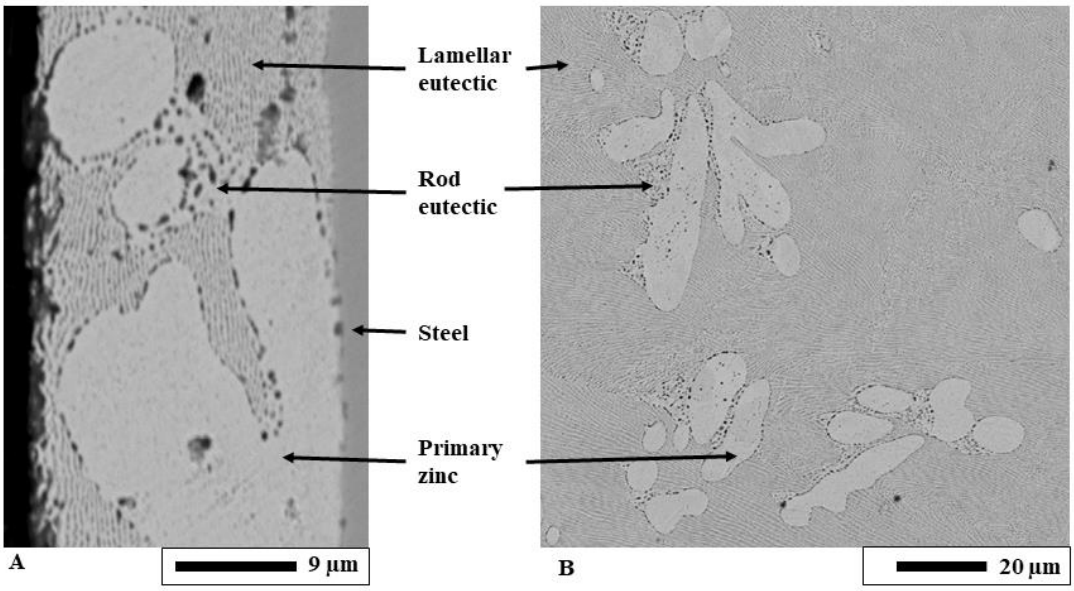

Figure 1.11: SEM images showing A) cross-section B) surface of HDG Galfan coated steel.

One alloy coating with considerably higher Al content is Galvalume (AZ) with 55 wt.% Al, 43.4 wt.% Zn and 1.6wt.% Si. However, 55 wt.% Al is considered to be the upper limit to retain the sacrificial property of Zn to protect the underlying steel.

1.4.1.2.1 Corrosion mechanism of Zn-Al coatings

Galfan (95 wt.% Zn and 5 wt.% Al) offers 2-3 times greater protection compared to Zn only coating in marine and industrial environments [61]. This improvement in corrosion resistance of Galfan is due to the change in microstructure. The presence of aluminium rich eutectic phase which covers about 40-50% of the total volume improves the corrosion resistance through the formation of aluminium oxide that is very adherent and insulating [62]. The presence of a two-phase microstructure (Primary zinc and Zn/Al eutectic) also encourages the preferential corrosion of the least noble phase [63]. In marine conditions, Al^{3+} ions help in the precipitation of double-layered hydroxide (DLH) ($Zn_6Al_2(OH)_{16}CO_3{\cdot}4H_2O$) earlier than when Zn^{2+} ions are present and this DLH is a strong barrier for oxygen diffusion [55], [64]. Thus offering better corrosion resistance compared to HDG Zn coating.

Research using SVET has shown that processing parameters such as cooling rate [63], coating thickness [65], substrate thickness [49] and application of ultrasound during the solidification process [59] have significant effects on the microstructure of Galfan and its subsequent corrosion performance. The increase in cooling rate has

improved the cut-edge corrosion performance whilst reducing the surface corrosion performance. Similarly increase in the coating thickness also improved the cut-edge corrosion performance whereas in contrast increasing the substrate thickness led to a decline in corrosion performance. The change in corrosion performance due to cooling rate and coating thickness altercation was attributed to the change in size and volume fraction of primary zinc and Zn/Al eutectic phase. Whereas, the cut-edge investigation on substrate thickness revealed the decline in corrosion performance with an increase in thickness, as the corrosion rate is predominantly determined by the cathodic reaction. Attempts have also been made to further improve the corrosion resistance of Zn/Al alloy via the addition of a small amount of Mg up to 0.05 wt.% but resulted in a negative effect on the cut-edge corrosion resistance [16].

1.4.1.3 Zinc magnesium aluminium (ZMA) coatings

Zinc magnesium aluminium (ZMA) is a ternary HDG system that utilizes the electrochemical properties of magnesium and aluminium in combination with zinc to cathodically protect the steel substrate. Because of their improved corrosion resistance compared to Zn and Zn-Al systems, ZMA is of great interest to industries from automotive to construction. The addition of magnesium (Mg) into the Zn bath enhances the wettability of the steel substrate and reduces the surface tension of the bath [62]. ZMA provides a 4-20 fold improvement in corrosion resistance compared to HDG Zn in neutral salt spray test in terms of red rust time appearance [12]. The change in their ability to resist corrosion has been attributed to the vast change in the microstructure which occurs with the additions of up to 3 wt. % of Al and 3 wt. % of Mg [16]. A cross-section and surface image of ZMA (MagiZinc)(Zn-(1-2) wt.% Al-(1-2) wt.%Mg) is presented in Figure 1.12. HDG ZMA microstructure consists of Zn phase, coarser lamellar structural binary eutectic (Zn and $MgZn_2$) and fine ternary eutectic (Zn, $MgZn_2$ and Al nodules) [32]. ZMA coatings have been available for the last two decades and some of the compositions are ZAM (91 wt.% Zn-6 wt.% Al-3 wt.% Mg), Super Dyma (85.8 wt.% Zn-11 wt.% Al-3 wt.% Mg-0.2 wt.% Si) [66] and Magizinc (96.8 wt.% Zn-(1-2) wt.% Al (1-2) wt.% Mg). The composition of ZMA changes depending upon where it is used. European ZMA systems contents (0.4-3) wt.% Al and (1-2) wt.% Mg compared to (0.2-11) wt.% Al and Mg (0.1-3) wt.% in East Asia countries e.g Japan [67].

Equilibrium phase diagrams offer a prediction of solidification sequence and resultant microstructure under equilibrium conditions. However, the rapid solidification during the galvanisation process results in a deviation in the chemical composition of phases formed compared to the equilibrium values. Furthermore, the fast cooling rate leads to a fine and complex microstructure. The phase diagram of the ZMA alloys system presented in Figure 1.12 suggests that the final microstructure of ZMA (Zn –(1-2) wt.% Mg – (1-2) wt.% Al) would be composed of Zn-rich phase, an Zn/Al phase and Mg_2Zn_{11} phase upon equilibrium solidification conditions. However, due to the high cooling rate associated with the HDG process the formation of Mg_2Zn_{11} is inhibited leading to the formation of $MgZn_2$ instead. HDG ZMA microstructure consists of Zn phase, coarser lamellar structural binary eutectic (Zn and $MgZn_2$) and fine ternary eutectic (Zn, $MgZn_2$ and Al nodules) [32]. A cross-section and surface image of HDG ZMA (MagiZinc)(Zn-(1-2) wt.% Al-(1-2) wt.%Mg) is presented in Figure 1.13.

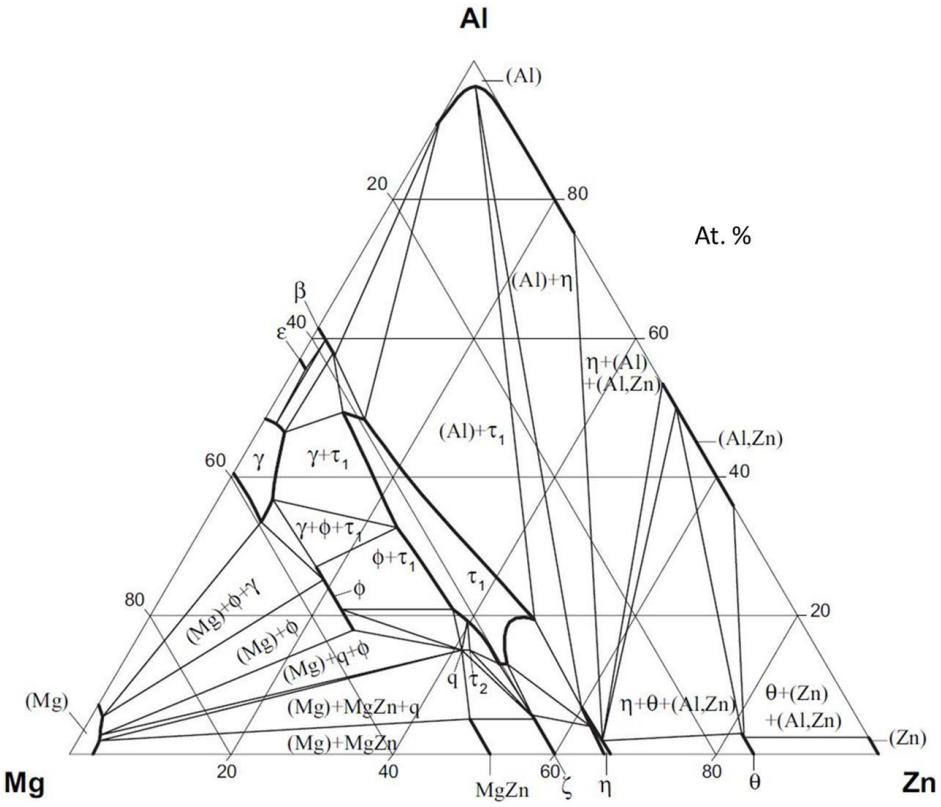

Figure 1.12: Ternary phase diagram for Zn-Al-Mg system [68]

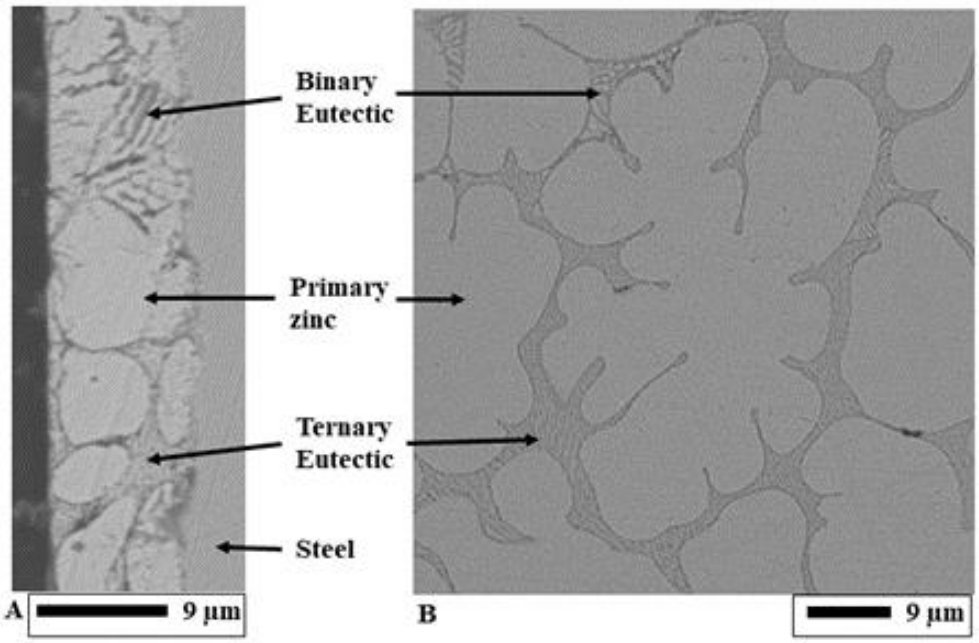

Figure 1.13: SEM images showing A) cross-section B) surface of HDG ZMA coated steel.

1.4.1.3.1 Solidification of ZMA alloy coatings

The investigation [69] on the solidification process of HDG ZMA (Zn – (1-2) wt.% Mg – (1-2) wt.% Al) coating revealed that the zinc phase is the first phase to solidify which nucleates off the steel surface. The solidification process of ZMA (Zn – (1-2) wt.% Mg – (1-2) wt.% Al) coating is presented in Figure 1.14.

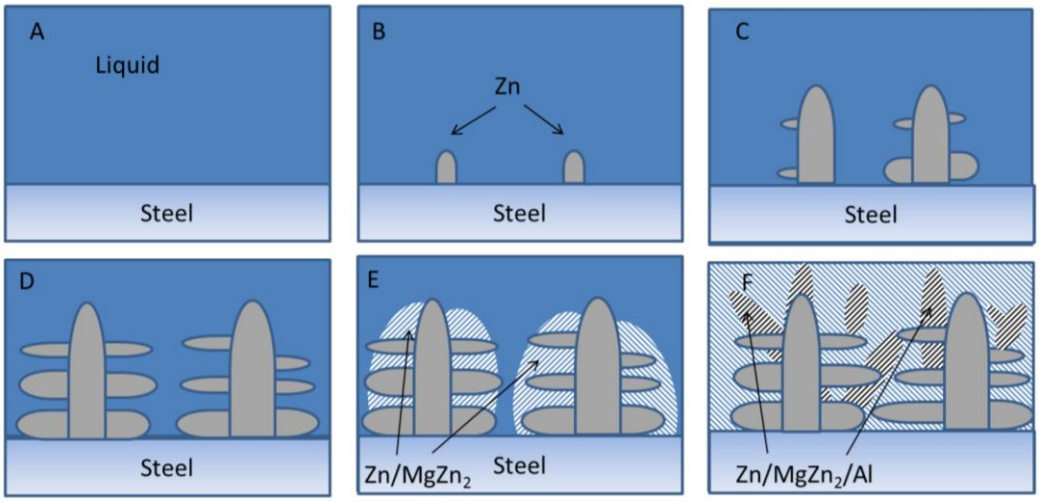

Figure 1.14: Solidification sequence of the ZMA (Zn –(1-2) wt.% Mg – (1-2) wt.% Al) coating [69].

The solidification of ZMA (Zn – (1-2) wt.% Mg – (1-2) wt.% Al) coating is divided into three steps [69]:

i. The Zn dendrites nucleate and grow off the steel surface (Figure 1.14 (A-D)). It contains around 1 wt.% of Al and < 0.1 wt.% Mg in solid solution.
ii. Formation of binary eutectic which comprises Zn and $MgZn_2$ (Figure 1.14 E)
iii. Formation of ternary eutectic which comprises Zn, $MgZn_2$ and Al nodules (Figure 1.14 F)

1.4.1.3.1 Corrosion mechanism of ZMA coatings

The corrosion performance of ZMA in chloride-rich environments [12] and in conditions of varying carbon dioxide (CO_2) [70] has been studied by several authors. Several mechanisms have been proposed to explain the enhanced corrosion performance of ZMA alloy coatings;

- Buffering of pH at cathodic sites resulting from Mg dissolution (9,49)
- The stabilisation of a compact zinc hydroxy-chloride / simonkolleite ($Zn_5(OH)_8Cl_2 \cdot H_2O$) on the surface layer due to the presence of Mg^{2+} ions [71]
- The production of magnesium-rich oxide limits the overall corrosion rate through cathodic deactivation [72]
- Formation of layered double hydroxide (LDH) of type $Zn_2Al(OH)_6(CO_3)_{1/2}.xH_2O$ or/and $Mg_6Al_2(OH)_{16}CO$ resulting from Al dissolution (9,50,52)

It should also be considered that several of these above mention mechanisms could act together and also the environmental conditions have an influence upon the corrosion reaction and rate. Most of the investigations are conducted in extreme aggressive and accelerated corrosion conditions such as in concentrated NaCl electrolyte, salt spray test or automotive cyclic corrosion test. The results gathered via these experiments are vital and lead to several theories on the role of magnesium and aluminium during its corrosion process. However, the limitation is that it might not be the actual representation of the corrosion process. The corrosion product formed in a very harsh environment could be the corrosion product formed at the end of the coating life [12].

In ZMA due to the presence of Al and Mg, new oxide layers and complex corrosion products are produced which are not found on HDG [67], [71], [73], [74]. The corrosion initiates as the eutectic phase (contains Mg) in ZMA [32], Mg ions diffuse and migrate to the cathodic sites and form magnesium hydroxide and magnesium carbonate [75]. These Mg ions also buffer the pH at the cathodic site restricting ZnO formation [75]. It is also suggested that Mg ions enhance the insulation property of Zn compounds formed [76] and Mg limits the charge transfer via grain boundaries [77]. The Al present at the eutectic phase (ternary) remain insoluble at the early stage of corrosion and when it participates at the later stage, it leads to the formation of simonkolleite instead of Zn oxide [64]. The effect of magnesium and aluminium ion (Mg^{2+} & Al^{3+}) on the formation of zinc products in the different electrolytes is shown below in Figure 1.13.

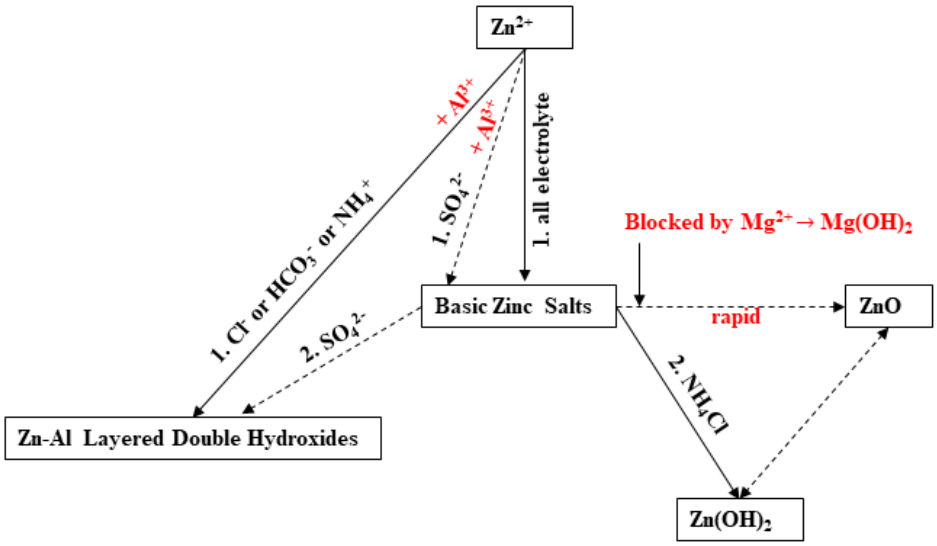

Figure 1.13: Schematic illustration of the formation and conversion of corrosion products in the existence of different species in the electrolyte [64].

Studies using the Time-lapse microscopy technique have shown that in Zn-(1-2) wt.% Al-(1-2) wt.% Mg, corrosion is highly localised and initiates at the eutectic phase by de-alloying of intermetallic $MgZn_2$, after eutectic dissolution anodic attack proceeds on the primary zinc phase [32], [78]. This mechanism of anodic attack is presented in Figure 1.16. Both investigations demonstrate that corrosion products ring precipitate radially around the anodic site and the ring becomes more defined with time. The pH gradient across the corrosion cell was also highlighted by using a phenolphthalein indicator in 0.1 % NaCl electrolyte [78].

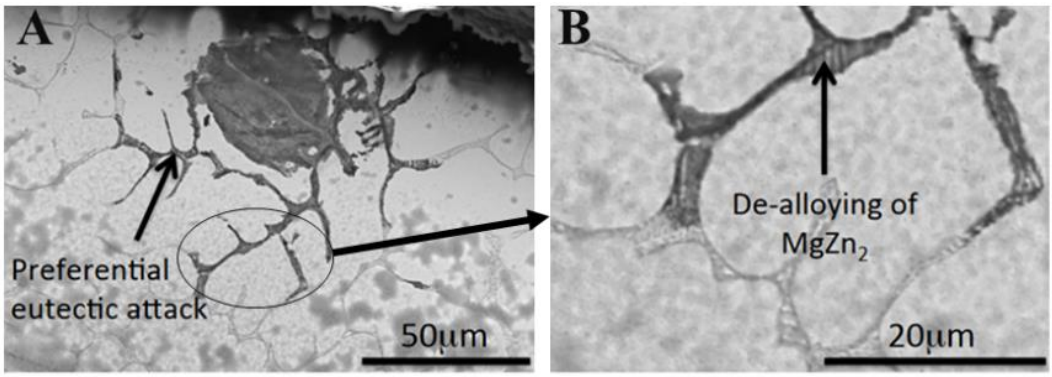

Figure 1.16: SEM image of ZMA (Zn-(1-2) wt.% Al-(1-2) wt.% Mg) coating after 4 hours immersion in 0.17 M NaCl solution showing A) the preferential eutectic attack B) de-alloying of $MgZn_2$ from the eutectic phase [32].

Several investigations are conducted using SVET to understand the kinetics, mechanism of corrosion and evaluate the corrosion performance of ZMA coating systems with various compositions and cooling rates [13], [32], [79]. SVET investigation on ZMA with varying amounts (up to 3 wt.%) of Mg and Al revealed an increase in corrosion resistance with an increase in Mg and Al content. In addition, SVET investigations also revealed that the lateral spreading of the focal anode was much greater in finer microstructure compared to coarse microstructure. The large primary Zn phase present in the coarse microstructure deflected and constrained the lateral spreading of the anode.

1.4.1.3 Zinc magnesium aluminium-X (Quaternary additions)

The ideal of a quaternary metallic coating system has also been a subject of interest and research. The effect of the addition of a variety of elements such as Silicon (Si), Manganese (Mn), Titanium (Ti), Calcium (Ca), Chromium (Cr), Cerium (Ce) [17] and Zirconium (Zr) [80] has shown further improvement in corrosion resistance in cyclic accelerate corrosion test. These quaternary additions (Zn-Al-Mg-X) outperformed Zn-X, Zn-Al-X and Zn-Mg-X alloys.

Investigations have shown that conversion coatings applied to Zn surfaces containing Zr and Ti inhibit corrosion due to the formation of dielectric oxide films with high insulating properties [81], [82]. Ce has a low work function similar to Mg, hence, the low reversible potential for the formation of corrosion products [83]. Therefore, cerium oxide and hydroxide can reduce the surface film potential, electron-emitting properties and efficiency of cathodic oxygen reduction [17]. Cr is incorporated in Zn

inhibitors and conversion coatings due to its self-passivation properties. Ca also possesses a low electron work function and CaO have one of the highest band gaps of 6.9 eV [84]. The addition of germanium (Ge) into ZMA alloy [18] has also been studied in relation to its effect on microstructure and corrosion performance. Investigations on quaternary additions of all the above elements have shown improvement in the corrosion resistance of the ZMA but the mechanism by which it inhibits has not been well understood [18] and requires further investigations.

1.5 Thesis aims

This body of work has been conducted with the aims to i) enhance the corrosion and mechanical properties of ZMA coating alloy ii) develop a duplex coating system with synergy between metallic and organic coating layers. The main objectives are, therefore :

- Investigate the effect of the addition of 0.19 -1.8 wt.% of Ge to the microstructure of ZMA alloy and its subsequent effect on corrosion and mechanical properties of ZMA alloys. Preliminary studies showed the formation of a new phase within microstructure, improvement in corrosion resistance and reduction in hardness of the ZMA alloy.

- Investigate the use of Mg_2Si particulates as a corrosion inhibitor. Mg_2Si particles are embedded into a zinc-rich powder-based galvanising system (ZINGA Zinc / Zn) as a source of Mg which corrode preferentially to Zn. Studies have shown that alloying Zn with Mg has significantly enhanced the corrosion resistance of Zn.

- Investigate the effect of 1 wt.% of Calcium addition on the microstructure & corrosion property of zinc and the effect of sodium phosphate inhibitor on the corrosion behaviour of Zn and Zn-Ca alloy. Calcium being more electronegative than Zn, phase containing Ca should preferentially corrode releasing Ca^{2+} ions, which react with phosphate to provide more complete inhibition of corrosion.

Time-lapse Microscopy (TLM) and Scanning Vibrating Electrode Technique (SVET) are two major techniques utilized to conduct the investigations. TLM enables to take images under immersion conditions and provide mechanistic information on a micron scale. SVET enables us to study the kinetics of anodic and cathodic propagation with time on a millimetre scale.

Chapter 2 Experimental

2.1. Sample preparation

Samples were pressure mounted in a non-conductive phenolic resin and finished with 1µm diamond polish to produce a flat surface free from scratches. Samples that undergo any form of imaging were then etched with 3 % nital acid, rinsed with deionised water and then dried to reveal the grain structure. 1 wt.% NaCl (0.17 $mol.dm^{-3}$ NaCl) pH 7 solution was used for all the corrosion experiments.

2.1.1 Chemicals and materials

Table 2.1: List of items used throughout the body of work for experimental purposes.

Chemicals, Materials	Supplier	Purity, Grade
De-ionised water, H_20	In-situ	18MΩ-cm
Hydrochloric acid, HCL	Sigma-Aldrich	≥ 99%
Sodium chloride, NaCl	Sigma-Aldrich	≥ 99%
Sodium phosphate, Na_3PO_4	Sigma-Aldrich	≥ 99%
Sodium hydroxide, NaOH	Sigma-Aldrich	≥ 99%
PTFE Tape	3M	-
Germanium, Ge	Goodfellow	≥ 99%
Magnesium silicide	Sigma-Aldrich	≥ 99%
Calcium	Sigma-Aldrich	≥ 99%
Zinc-magnesium-aluminium, ZMA	TATA Steel	Zn-1.6 wt.% Mg-1.6 wt.% Al
Zinga cold galvanising system	Frost Auto Restoration Technique Ltd	96 % zinc
Zinc	TATA Steel, UK	Zn-(0.15-0.5) wt.% Al
Low carbon steel substrate	TATA Steel, UK	-
Polyvinyl butyral	Sigma-Aldrich	≥ 99%
Collidal silica	Sigma-Aldrich	≥ 99%

2.2 Microstructural analysis

A Hitachi TM3000 Scanning Electron Microscope (SEM) with a Bruker Energy Dispersive X-ray Spectroscopy (EDS) module was used to investigate the microstructure of the alloys. The SEM beam accelerating voltage used was 15 kV. A Bruker D8 Discover X-ray Diffractometer (XRD) with a Copper source (40 kV and 40 mA) was used to identify the crystal phases. As the samples were mounted in non-conductive resin, a strip of conductive tape was used to provide the electron flow between the sample and the SEM stage. The volume fraction of different microstructural phases was determined by image analysis of several SEM images taken across the sample at 200 X magnification using Adobe Photoshop software.

2.3 Time-lapse microscopy technique

Time-lapse microscopy (TLM) is a novel technique developed at Swansea University, which allows microstructural imaging of corroding surfaces under immersion conditions [32], [78]. TLM consists of Meiji Techno 7100 optical microscope with a polyethene waterproof shroud for the microscope objective lens and an Infinity 2-5C microscope mounted digital camera with Infinity Imaging Software. The base of the polyethene waterproof shroud encases a glass window that allows imaging of the sample area whilst submerged in the electrolyte. The TLM schematic setup is presented below in Figure 2.1.

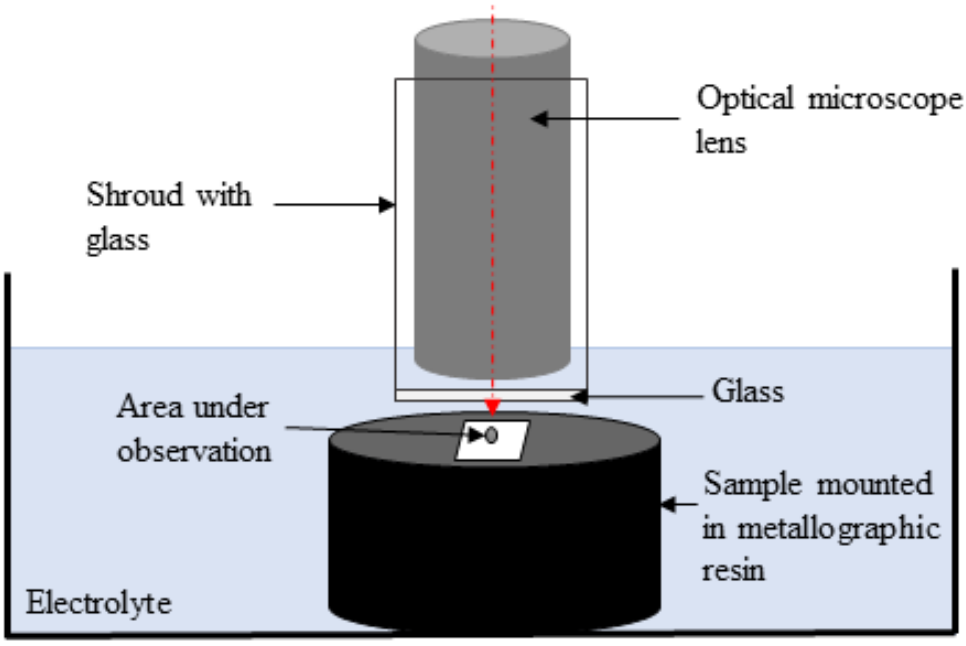

Figure 2.1 Schematic of in-situ time-lapse microscopy configuration.

The glass window used at the bottom of the protective shroud is 0.16 mm thick, sealed with inert resin. The system is such that to take an image the light has to travel through the air and the electrolyte. The objective lens of the microscope is designed to image through the air which has the refractive index (n) of 1. However, the refractive index of the electrolyte is different from the air. The refractive index of water (n_1) at room temperature is 1.33 [85]. Due to the difference in refractive index between the air and the electrolyte, the image becomes more distorted the more the light travels through the electrolyte. Hence the shroud is manoeuvred into place so that it is as closest to the sample's surface as possible whilst also leaving a thin layer of electrolyte over the sample.

A pipette was used to remove any air trapped during the introduction of electrolyte between the bottom of the shroud and the exposed sample surface. The imaging software was programmed to capture an image every 2 minutes at 100 X magnification for 24 hours. A time-lapse video was created using Windows Movie Maker where each image has a frame time of 0.05 seconds.

2.3.1 Sample preparation for time-lapse microscopy

The sample was prepared as explained in section 2.1. A sample surface was covered using 3M non-conductive PTFE tape with of 0.78 mm^2 area masked off using a 1 mm diameter biopsy pen. The prepared sample was secured to the base of the petri dish using double-sided tape and 3M non-conductive PTFE tape.

2.3.2 Anodic area growth rate

The anodic area was highlighted for an image in the data set using imaging software Adobe Photoshop CS6, see Figure 2.2. The software was first calibrated using a known length from an image taken using the same TLM setup as used for experiments. This permits the anodic area to be presented in μm^2, which was exported to Microsoft Excel to be represented graphically.

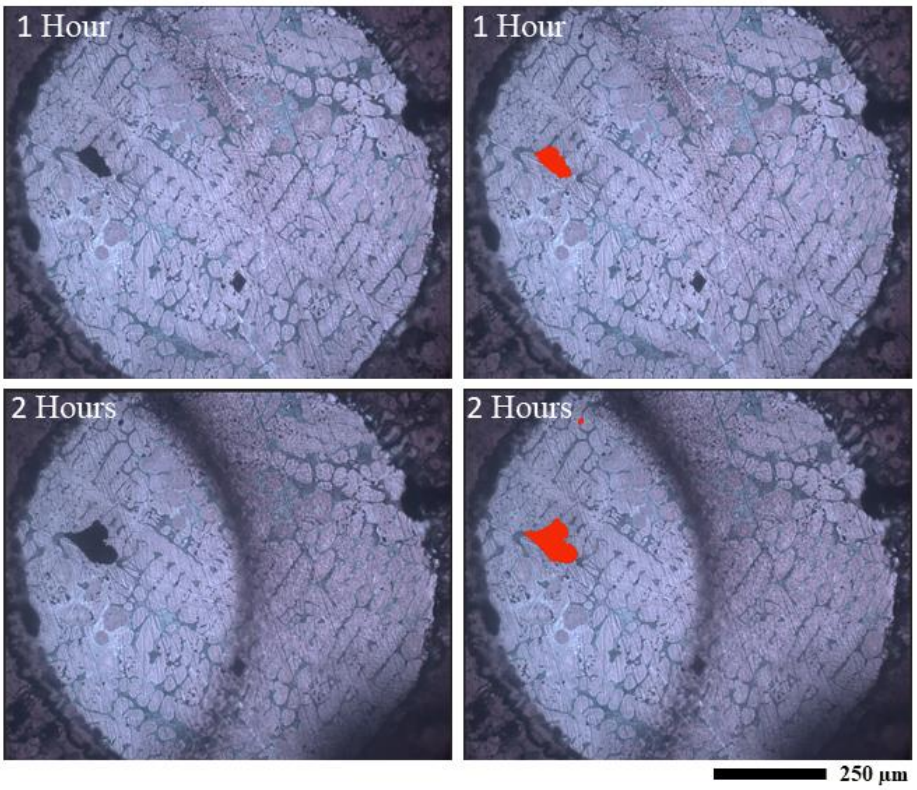

Figure 2.2: Anodic area growth measurement on ZMA-Ge using Adobe Photoshop showing the highlighted area (red) increasing in size over time.

2.4 Scanning Vibrating Electrode Technique (SVET)

The scanning vibrating electrode technique (SVET) was developed in the 1980s and has been employed in corrosion research since then [86]. It is considered an iteration of the scanning reference electrode technique (SRET). It allows to monitor corrosion behaviour and generate mechanistic understandings in an aqueous environment. SVET has been used comprehensively to understand the surface and cut-edge corrosion of metallic coatings [13], [16], [32], [51], [63], [65]. In this body of work, SVET has been used as a three-dimensional technique to compliment the two-dimensional TLM technique. SVET is a semi-quantitative technique as it provides anodic current density, which in turn could be used to calculate mass loss value. A strong relationship has been observed between SVET derived corrosion inhibition efficiency values and those of gravimetric mass loss, polarization data and calculated using EIS [87]. The SVET derived mass loss were also comparable with those obtained from external Zn runoff tests [51].

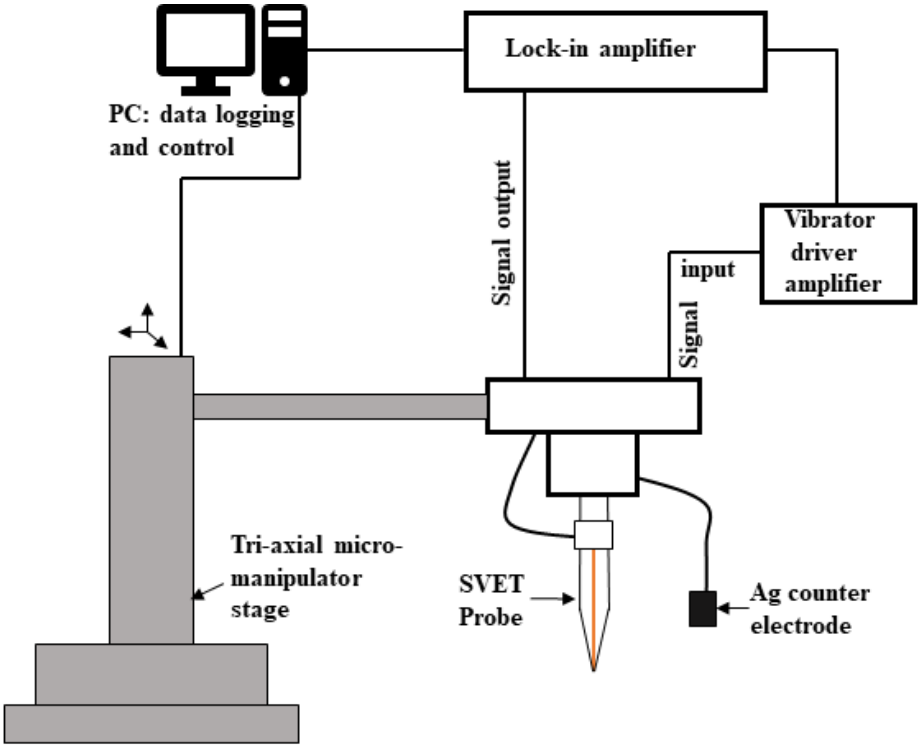

Figure 2.3: Schematic representation of SVET step-up.

A schematic of SVET is presented in Figure 2.3 and the instrumental design, operating procedure and calibration process have been described in detail elsewhere [86], [88]–[90]. SVET probe consists of a 125 µm diameter platinum wire micro-tip encased in an insulating glass tube, which vibrates at a constant frequency, amplitude and height above the sample surface whilst submerged in an electrolyte. The vibration of 140 Hz with an amplitude of 25 µm (z-direction) to the probe is provided by the lock-in amplifier (EG&G Instruments 7265) via an external amplifier. The probe scans in a set-wise manner at 100 µm above the sample surface in x and y-direction. The movement of the probe is provided by the tri-axial micro-manipulator stage, in conjunction with PC.

During corrosion, ionic current flux originates and an iso-potential field is established around the anode through the electrolyte as presented in Figure 2.4. The SVET probe registers the alternating potential by crossing the lines of current flux. The registered alternating potential is directly proportional to the potential gradient at z-direction established by the ionic current flux and can be represented graphically in the form of colour contour maps. The potential data is used to calculate the current densities via the use of a calibration factor.

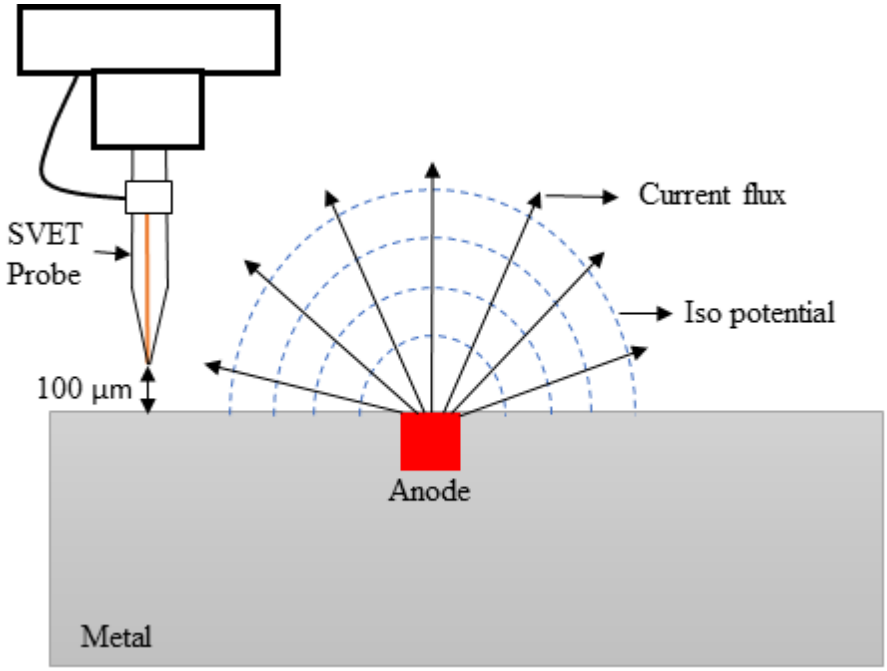

Figure 2.4: A schematic representation of current flux and iso-potential lines above anode.

The electric field strength (F) or potential gradient due to point source measured by the SVET probe in the direction of probe vibration (z-direction/normal to sample surface) is given by equation 2.1.

$$F = \frac{dE}{dZ} = \frac{-iz}{2\pi k(x^2+y^2+z^2)^{1.5}} \qquad [2.1]$$

k = electrolyte conductivity

x,y,z = coordinate plane value

i = current source

The maximum field strength (F_{max}) exists at height z exactly above the origin (x = 0, y = 0) of the source and is given by equation 2.2.

$$F_{max} = \frac{-1}{2\pi k z^2} \qquad [2.2]$$

The inverse-square relationship between SVET probe height and F_{max} make SVET scanning height critical.

2.4.1 SVET calibration

The potential gradients are measured in nano-volts (nV) by SVET. These nV values are converted into current density values in Am^{-2} via the means of calibration. Calibration could be achieved by the use of a point current source.

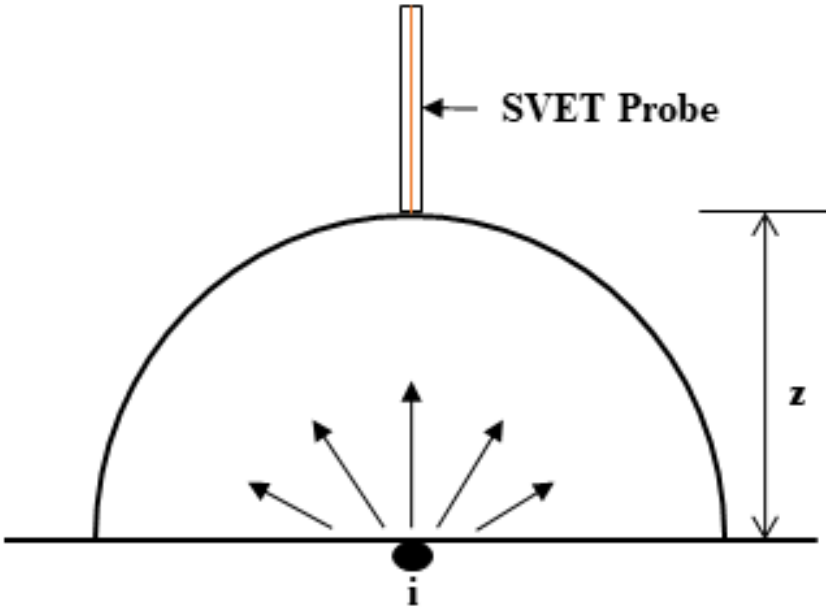

Figure 2.5: Current emerging from a point current source

At a point of a current source, current fluxes emerge from its centre and are distributed evenly with a hemispherical profile as shown in figure 2.5. Hence, the current density (j_z) in the direction of SVET probe vibration (z-direction) is given by dividing the applied current by surface area of the hemisphere ($2\pi z^2$), as set out in equation 2.3.

$$j_z = \frac{i}{2\pi z^2} \qquad [2.3]$$

i = applied current

z = height of hemisphere and also the height of SVET probe from the current source

The plot of peak-to-peak SVET voltage signal (V_{pp}) vs j_z provides a means of converting SVET registered voltage signal to current density in the direction of probe vibration.

Calibration of the SVET was accomplished using a two-compartment cell, a schematic is presented in Figure 2.6.

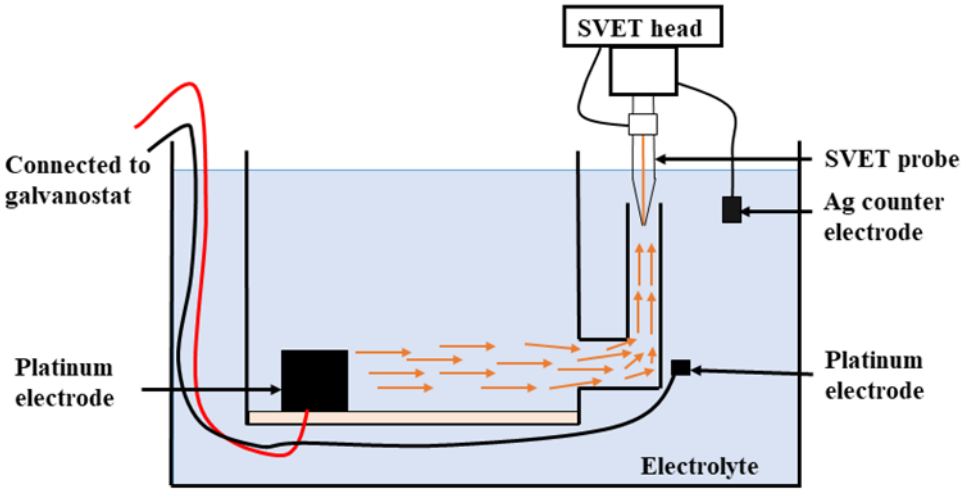

Figure 2.6: Schematic of SVET calibration setup using two-compartment cell

Each compartment contains a 1 cm^2 platinum (Pt) electrode, both filled with electrolyte under investigation and connected by a vertically oriented glass tube of 4.8 mm internal diameter. The SVET probe was lowered into the vertical opening and a range of currents were applied with the help of a battery-powered nano-galvanostat. The current densities were calculated for each applied current, for the area of the glass tube (radius = 2.4 x 10^{-3} m). The tube allows current flux to ally vertically, parallel to the tube axis creating uniform current density in the direction of SVET probe vibration. The gradient of a plot of current densities vs measured SVET voltage provides a calibration factor for the instrument and electrolyte under investigation. This method of calibration is prompt, independent of probe height and an efficient means of converting SVET measured potential (voltage) into current density.

2.4.2 Manipulation of SVET data

The SVET measured data (potential (nV)) are subjected to calibration as outlined in 2.4.1. The recorded data are converted in normal current density (j_z) by applying the conversion factor. A surface modelling package, Golden Software's Surfer 10 was used to produce spatially resolved maps of normal current density as presented in Figure 2.7. The anodic and cathodic activities are identified by the change in colour. Red represents the anodic activity and blue represents the cathodic activities.

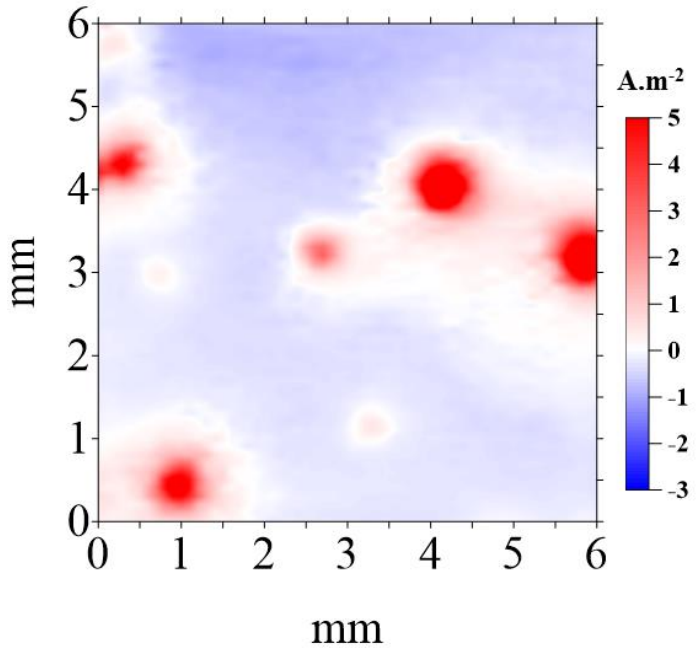

Figure 2.7: Current density resolved colour map created from SVET scan using Golden Software's Surfer 10.

The current density could also be used to calculate the total mass loss due to anodic activity. Numerically integrating all the positive anodic current density (j_z) gives the total anodic current for the scan, as presented in equation 2.4.

$$I_{at} = \int_0^x \int_0^y [j_{z(x,y)}]\, dx\, dy \qquad [2.4]$$

I_{at} = anodic current

j_z = normal current density

x,y = length and width of SVET scan

Dividing the total anodic current I_{at} by scan area (A) gives an area average anodic current density (j_{at}) as shown in equation 2.5.

$$j_{at} = \frac{I_{at}}{A} \qquad [2.5]$$

Assuming that the corrosion activity remains constant between the scans i.e for 3600 seconds, time (t), hourly charge (Q) can be calculated using equation 2.6

$$Q = j_{at}\, x\, t \qquad [2.6]$$

Then using the Faraday equation given in equation 2.7 along with other information concerning the material corroding, the mass loss could be calculated.

$$Mass\ loss = \frac{Q}{nF} A_r \qquad [2.7]$$

Q = charge (C)

F = Faraday's constant (96487 C mol^{-1})

n = no. of electrons involved

A_r = atomic weight of corroding material

A total mass loss for the experiment could be calculated using equation 2.7 and summing all the hourly mass losses.

2.4.3 Limitations of SVET

SVET only detects the normal component of the current flux. It is only able to resolve localised corrosion features that are separated by a distance greater than 1.5 times scan height of 100 μm i.e 150 μm [32]. It will also not detect the current loops that terminate under the plane of the scan of 100 μm. In this body of work SVET also conducted scan every hour and assumed a constant corrosion rate over that hour whereas, in reality, the corrosion rate could vary. Regardless of these limitations, the SVET has proven a useful technique in comparing the performance of similar metals and alloys.

2.4.2 Sample preparation

The samples were prepared as explained in section 2.1. The samples were not etched and an area of 36 mm^2 was exposed to the electrolyte. Tests were conducted at room temperature and the dissolved oxygen concentration in bulk solution was assumed to be constant at 2.8 x10-4 mol dm^{-3} [91]. 60 measurements along the x and y-direction were made, generating 3600 data points for each scan for experiments in Chapter 3. 29 measurements along the x and y-direction were made, generating 841 data points for each scan for experiments in Chapter 5 and 6. One scan was taken every hour for 24 hours and three repeat tests were carried out for each sample.

2.5 Electrochemical measurements

2.5.1 Open circuit potential

Open circuit potential (OCP) is also referred to as mixed corrosion potential as it represents it consists of both cathodes and anodes. At the OCP the corroding metal is neutral as the net measurable current is zero. This is because all the electrons generated by anodic processes are consumed by cathodic processes. The more positive the OCP value, the nobler is the metal.

To measure OCP, a two-electrode cell was set up where the metal of investigation was the working electrode and the potential was measured against saturated calomel electrode (SCE). A schematic of the two-electrode cell set-up is presented in Figure 2.8. Samples were ground to a European P grade P1200 finish using abrasive silicon carbide (SiC) paper, rinsed with deionised water and ethanol. An area of 0.78 cm^2 was exposed to 250 ml of electrolyte. The measurements were carried out using a Solatron 1280 potentiostat for 24 hours.

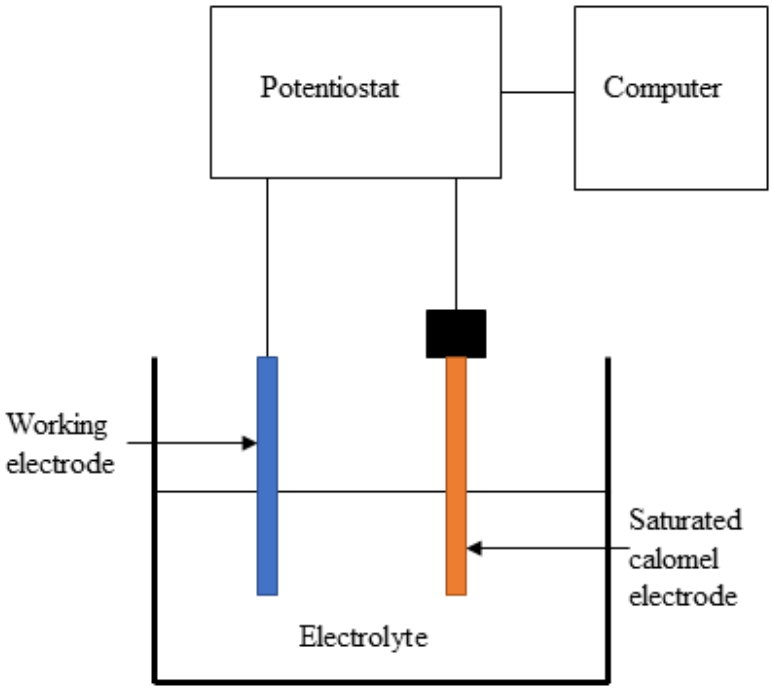

Figure 2.8: A schematic of the two-electrode set-up used to measure OCP.

2.5.2 Potentiodynamic Measurements

Polarisation involves applying an external potential on the working electrode and measuring the resulting current. The applied potential is increased or decreased at a constant rate from OCP and the resultant current is constantly monitored. For the

anodic polarization, the applied potential is increased whereas for cathodic polarization the applied potential is decreased.

Polarization utilizes a three-electrode cell, a working electrode (sample under investigation), a reference electrode (SCE) and a counter electrode (platinum gauze sheet). An external potential of ± 1.5 V was applied to the working electrode at a pre-determined rate of 1 mVs^{-1} from OCP and the corresponding current was measured. The schematic setup of polarization is shown in Figure 2.9.

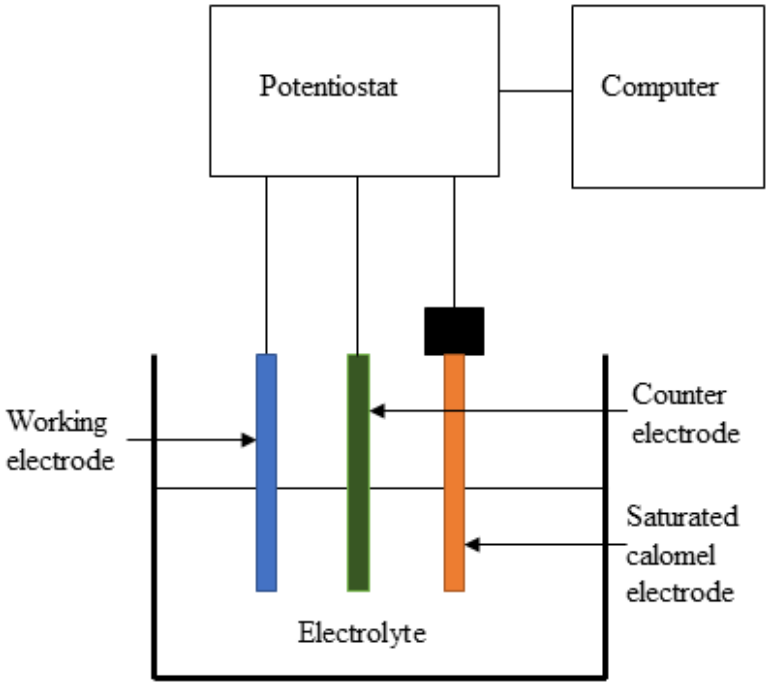

Figure 2.9: Three-electrode cell set-up for polarization experiment

Samples were ground to a European P grade P1200 finish using abrasive silicon carbide (SiC) paper, rinsed with deionised water and ethanol. An area of 0.78 cm^2 was exposed to 250 ml of electrolyte. The measurements were carried out using a Solatron 1280 potentiostat.

2.6 Scanning Kelvin Probe

The scanning Kelvin Probe (SKP) technique is well-established means of measuring metallic work function. Stratmann established the application of SKP to the investigation of atmospheric corrosion affecting the metallic surface. The electrochemical potential of metallic surfaces under a thin layer of electrolyte and also a thin film of an organic coating could be measured using SKP. A schematic of the SKP is presented in Figure 2.10 (a). The sample and probe are enclosed in a

chamber that permits the alterations of experimental parameters such as temperature, humidity and atmosphere.

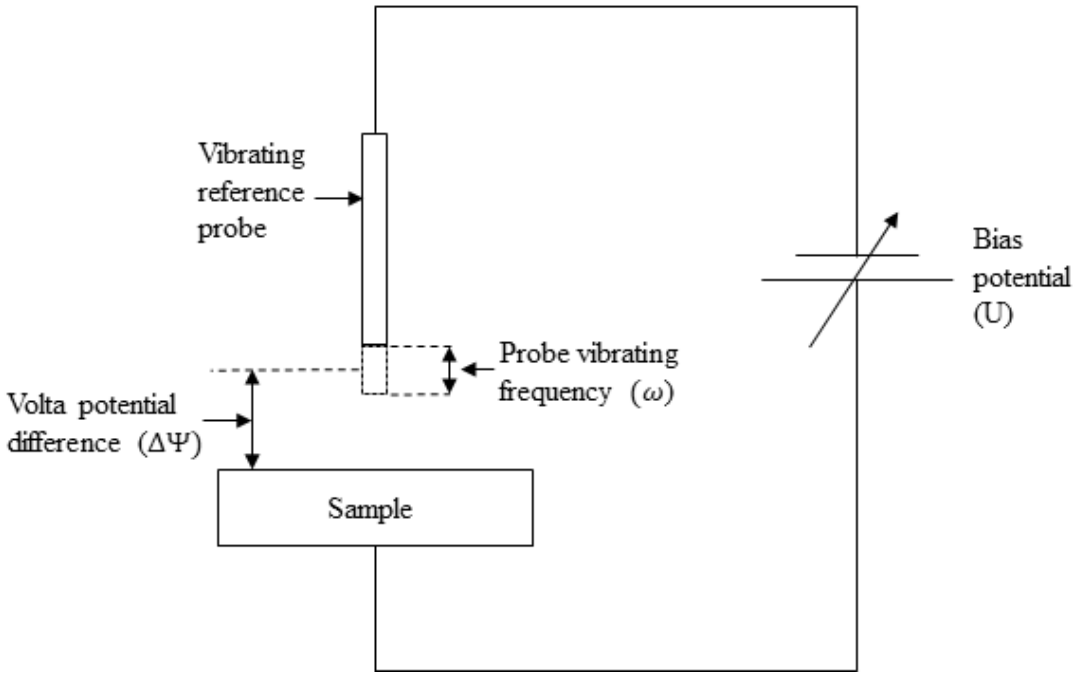

Figure 2.10 (a): Schematic representation of SKP

SKP apparatus consists of a vibrating gold reference probe/electrode connected to a sample of interest via an external circuit. The gold probe and the sample form the parallel plate capacitor and when electrically connected, electrons flow from the capacitor with lower work function to the capacitor with higher work function. The capacitance (C) of the parallel plate capacitor is given by equation 2.8.

$$C = \frac{\varepsilon \varepsilon_0 A}{d} \qquad [2.8]$$

ε_0 = permittivity of dielectric (free space)

ε = dielectric constant of the capacitor dielectric

A = area of the capacitor plate

d = distance between plates

The reference electrode probe is vibrated at a frequency (ω) in a sinusoidal fashion relative to the sample surface. Thus, the distance (d) between the reference probe and the sample surface varies with time (t) during probe vibration at a frequency (ω), which is given by equation 2.9.

$d = d_o + \Delta d sin(\omega t)$ *[2.9]*

d_0 = mean plate separation.

The capacitance (C) during the probe vibration is given by equation 2.10.

$$C = \frac{\varepsilon \varepsilon_0 A}{d_0 + \Delta d sin(\omega t)} \quad [2.10]$$

If volta potential difference ($\Delta\Psi_{Sample}^{Ref}$) exists between the reference probe and sample surface, an alternating current (I_{ac}) will be induced between them and is given by equation 2.11.

$$I_{ac} = \Delta\Psi_{Sample}^{Ref} \frac{dC}{dt} \quad [2.11]$$

The Kelvin probe signal current (I_{ac}) in equation 2.11 is not used to measure the open circuit value of $\Delta\Psi_{Sample}^{Ref}$ but instead $\Delta\Psi_{Sample}^{Ref}$ is achieved indirectly by applying external DC bias voltage (U). The applied U is adjusted such that the null current condition is achieved i.e $I_{ac} = 0$. Under null current condition the potential across the dielectric must be equal to zero so that:

$$-U_{null} = \Delta\Psi_{Sample}^{Ref} \quad [2.12]$$

Hence, applied voltage $-U_{null}$ is measured and recorded as $\Delta\Psi_{Sample}^{Ref}$.

Therefore, the kelvin probe potential (E_{kp}) is expressed as;

$$E_{kp} = -U_{null} = \Delta\Psi_{Sample}^{Ref} \quad [2.13]$$

2.6.1 SKP Calibration

The calibration of the SKP apparatus is conducted using a calibration cell. The calibration cell consists of a circular hole with 1 mm depth and 15 mm diameter in a disc made of relevant metal. This well is filled with 1 mol.dm^{-3} aqueous solution of the respective metal chloride salt as shown in Figure 2.10 (a). $\Delta\Psi$ is obtained by positioning the vibrating reference probe 100 μm above the electrolyte meniscus at the centre of the well. The electrode potential of the metal is also measured simultaneously using voltameter or potentiostat against SCE. For a system with polymer coating, a thin self-supporting polymer film (about 30 μm in thickness) is

placed over the electrolyte meniscus present in the well. The polymer film is then permitted to equilibrate for about 6 hours and $\Delta\Psi$ value is measured. The plot for E_{corr} vs standard hydrogen electrode (SHE) against $\Delta\Psi_{El}^{Ref}$ and $\Delta\Psi_{Pol}^{Ref}$ for Zn/Zn^{2+}, Fe/Fe^{2+}, Cu/Cu^{2+} and Ag/Ag^{+} couple with (i) and without PVB film (ii) is presented in Figure 2.10 (c).

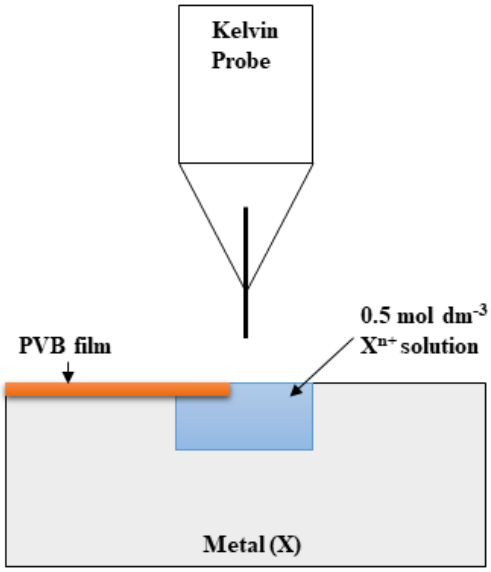

Figure 2.10 (b): Scanning kelvin probe calibration cell

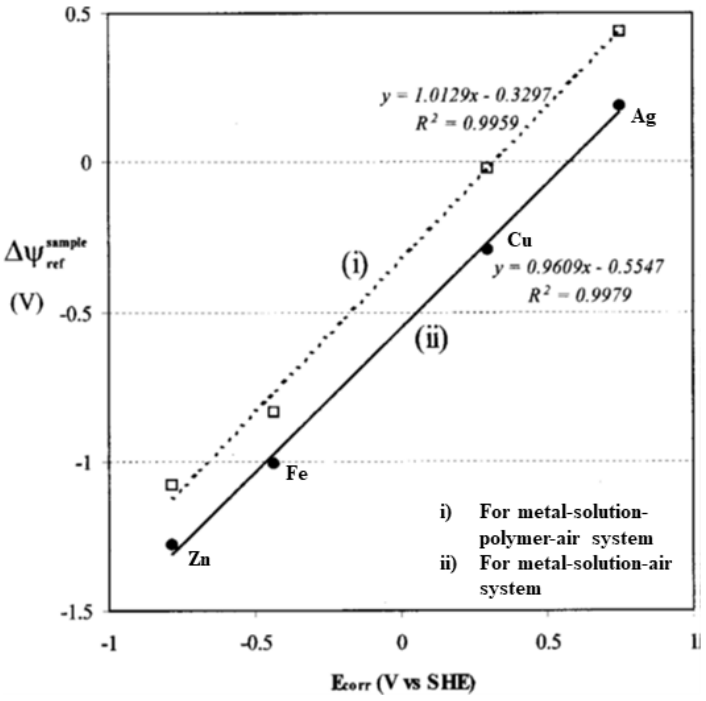

Figure 2.10 (c): Scanning kelvin probe calibration curves for coated (PVB) and bare system [92]

2.6.2 SKP in cathodic disbondment experiment

The corrosion driven cathodic delamination of organic coating applied to zinc or steel substrates has been proven to proceed by the establishment of a "delamination cell" [92]. In this process, a thin layer of electrolyte ingresses between the coating layer and the substrate where the anodic activities occur at the penetrative defect and the cathodic activities occur near the site of coating-substrate disbondment [92]. Stratmann developed the SKP technique to measure the rate of cathodic delamination of polymer coating adherent to metal substrates [53], [93], [94]. A schematic representation of corrosion-driven cathodic delamination cell showing correspondence with various regions of time-dependent E_{corr} (x) profile is presented in Figure 2.11.

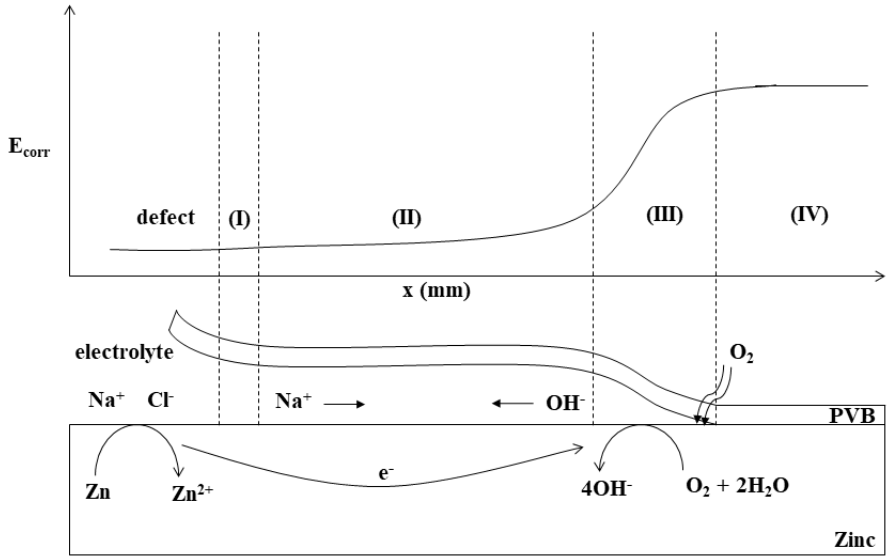

Figure 2.11: Schematic representation of corrosion-driven cathodic delamination cell showing correspondence with various regions of the time-dependent E_{corr} (x) profile.

In Figure 2.11 four regions of the delaminating cell are presented relative to the E_{corr} of zinc substrate, where:

Region I :

The region is next to the defect and E_{corr} value is very low similar to the free corroding Zn. Anodic metal dissolution of the underlying Zn also occurs.

Region II:

The E_{corr} gradually increases from the region I. It is under film delamination region and ionic current flux Na^+ from the defect site (region I) and OH^- from region III meet.

Region III:

There is a sharp rise in E_{corr} . This region is the delamination front where polymer disbondment occurs and electrolyte ingresses.

Region IV:

The E_{corr} is higher than the other three regions and is also referred to as E_{intact}. The polymer coating remains attached to the substrate.

2.6.3 Cathodic delamination preparation

The sample preparation used in this body of work is based on the methods presented in work first demonstrated by Stratmann et. al [53], [54], [95], [96]. The samples were cut into 5 cm x 5 cm coupons. A 15 mm x 50 mm area from the edge and perpendicular to the rolling direction of the sample was covered using adhesive tape. PVB layer was produced by bar casting PVB solution (15.5 % w/w) onto the substrate using 145 µm thick electrical tape as height guide that was placed 4.5 cm in from both sides of the sample cell and normal to the defect. The coated sample is then air-cooled at room temperature, producing a thin dry film of 16 µm thickness as measured by a micrometre. A penetrative defect of 10 mm length was created by cutting adhesive tape using a scalpel blade. Non-corrosive silicone sealant was used to create a wall around the defect thus creating a well for the electrolyte. All the experiments were conducted at room temperature, 95 % relative humidity using a 5 % NaCl pH 7 solution. A schematic of Stratmann cell preparation and the resulting experimental sample is presented in Figure 2.12.

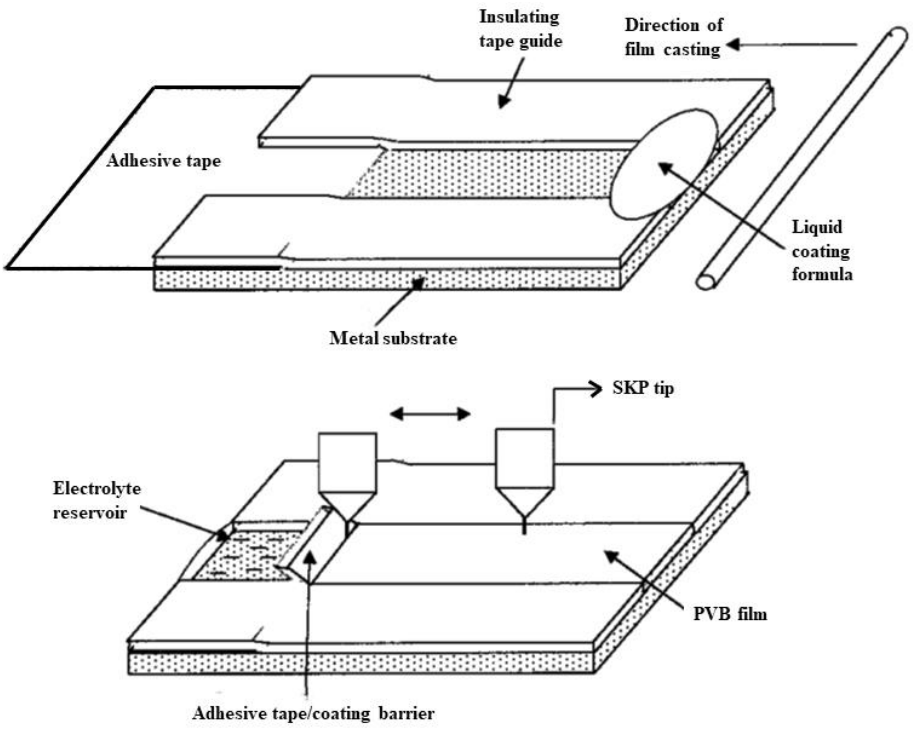

Figure 2.12: Schematic illustration of the Stratmann cell preparation and the resulting sample

2.7 Hardness test

The hardness test is the most common technique used for evaluating the mechanical properties of metal and alloys. The resistance of the material to permanent deformation under load is known as hardness. Generally, an indenter is pressed into the sample surface under a particular load for a fixed time interval and a measurement of the size or depth of the residual indent is made. The hardness test is popular because it is simple, easy and relatively non-destructive. Brinell hardness test was the first hardness test developed followed by a Vickers test or the Knoop test, the difference being the indenter geometry [97]. The two hardness measurement techniques used in this body of work are the Vickers hardness test and the nanoindentation technique.

2.7.1 Vicker hardness test

In the Vickers hardness (VH) test, a pointed diamond pyramid indenter with a square base is used. The opposite faces of the pyramid have an included angle of 136^{o}. A schematic of a VH pyramid indenter is presented in Figure 2.13. [98]

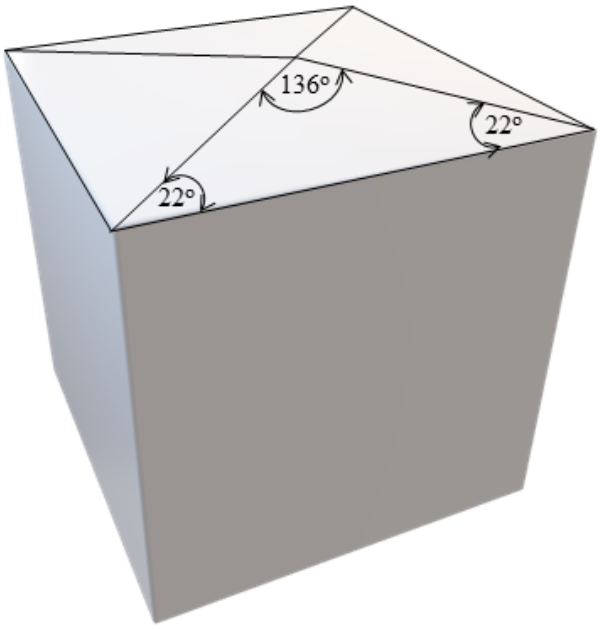

Figure 2.13: Standard Vickers diamond pyramid indenter

The pyramid's base opposite has an included angle of 136° whereas the base angles are 22° each. The indenter is pressed against the test sample surface at a selected force (P) and the area of the resultant indent is measured. The Vickers hardness number (H_V) is determined by equation 2.14.

$$H_V = \frac{P}{A} \qquad [2.14]$$

P = applied force

A = surface area of the indentation.

The surface area of the indent is calculated by equation 2.15.

$$A = \frac{d^2}{2Sin(\frac{136^O}{2})} \qquad [2.15]$$

$$A = \frac{d^2}{1.8544}$$

d = the average diagonal length of the indent

Therefore, the Vicker hardness value could be obtained using equation 2.16.

$$H_V = \frac{P}{A} = \frac{1.8544P}{d^2} \qquad [2.16]$$

2.7.1.1 Sample preparation

The samples were prepared as explained in section 2.1. Mitutoyo AVK-CL Vickers hardness tester was used to conduct the experiments. The test parameters were; the objective lens was set at 10 X for the measurement of the indent length, test force was set to 4.9 N and the dwelling time was 10 seconds.

2.7.2 Nanoindentation technique

In the last two decades, nanoindentation has been very popular in investigating the mechanical properties of materials because of its use of small test samples and small loading forces. Nanoindentations has been employed to measure the hardness and Young's modulus of thin films [99]–[101], microstructural phases [102], [103] and bulk materials [104]. Although nanoindentation has been primarily implemented in the study of engineering materials, several investigations have explored its application in the study of biomaterials like bones and DNA as well [105], [106].

Previously during the Vickers hardness test, an indenter with known force was applied into the specimen surface and hardness was estimated using the resultant indent. Whereas, nanoindentation technique is the depth-sensing technique where the indenter's displacement and the applied load are continuously recorded as the indenter is pressed into and removed from the sample surface. Oliver and Pharr developed an analysis method to calculate hardness and Young's modulus from the obtained load vs displacement data or (P-h) curve [107], [108]. During the loading process, elastic deformation occurs on the surface of the material at the beginning of the loading process with the gradual increase in load, plastic deformation occurs up until maximum load. After the maximum load, the elastic deformation of the material will gradually disappear with unloading and the plastic deformation remains as the residual indent on the surface as shown in Figure 2.16(a). Data (P-h curve) could be obtained from one complete cycle of loading, holding and unloading.

A generic schematic of a nanoindenter testing instrument is presented in Figure 2.14. An indenter tip is attached to a shaft. The applied force and the resultant displacement are measured and recorded using the transducers attached to the shaft.

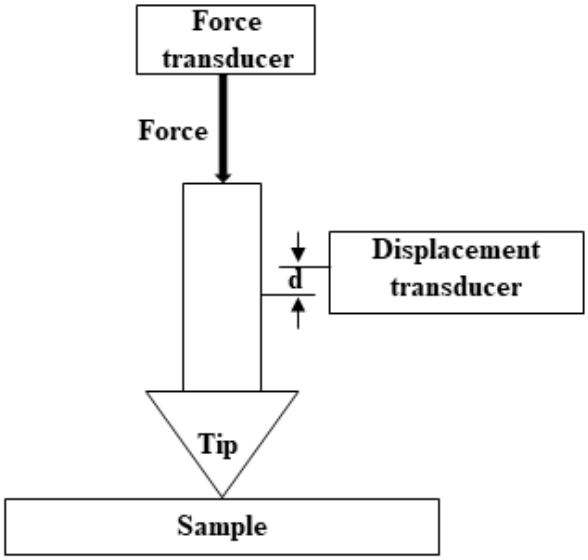

Figure 2.14: Schematic of a nanoindenter testing instrument.

In this body of work, indentations were conducted with a three-sided pyramid Berkovich indentor with a tip radius of 200 nm. A schematic of the Berkovich indentor is presented in Figure 2.15. The contact area (A_c) of Berkovich indenter during loading and unloading is calculated as a function of h_c and is given by equation 2.17 [109].

$A_c = 3\sqrt{3}\ h_c^2 \tan^2 65.3$

$$A_c = 24.5\ h_c^2 \qquad [2.17]$$

h_c = depth of the indent at the contact.

A schematic representation of the data set obtained with a Berkovich indenter is presented in Figure 2.16(b). Some of the important parameters measured from the P-h curves are the maximum load (P_{max}), the maximum displacement (h_{max}), final displacement or permanent displacement (h_f) and the elastic unloading stiffness (S =dP/dh). The S is also known as contact stiffness, the slope of the upper portion of the unloading curve as shown in Figure 2.16(b).

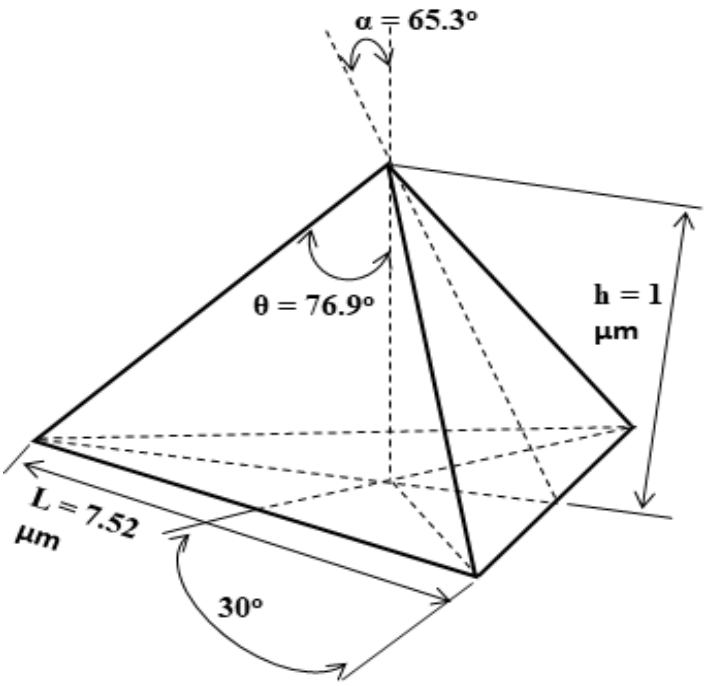

Figure 2.15: A schematic of the Berkovich indentor [110]

Once the contact area (A_c) is determined using equation 2.17, the hardness (H) is estimated from:

$$H = \frac{P_{max}}{A_c} \qquad [2.18]$$

P_{max} = maximum load displacement

If the sample under investigation has a significant elastic recovery during unloading, the nanoindentation hardness may deviate from Vickers hardness because nanoindentation hardness is based on contact area under load whereas Vickers hardness is based on residual indent area.

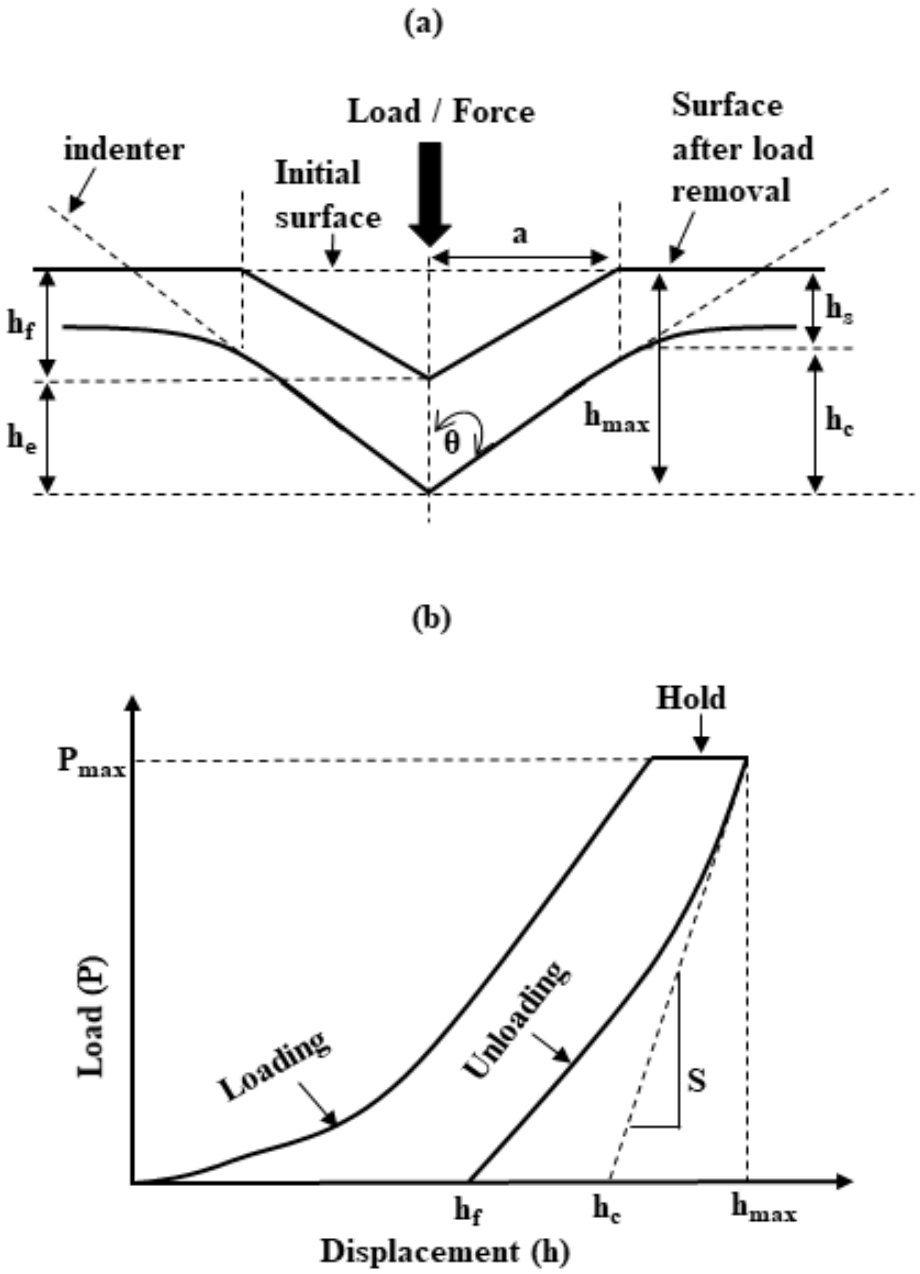

Figure 2.16:(a) A schematic representation of the unloading process displaying parameters illustrating the contact geometry (b) A schematic representation of the load vs displacement curve.

The stiffness, S, of the elastic region of the unloading curve is given as:

$$S = \frac{2\beta\sqrt{A_c}}{\sqrt{\pi}} E_r \qquad [2.19]$$

A_c = contact area

E_r = reduced Young's modulus

β = is constant, (β = 1.034 for Berkovich indenter)[109]

E_r accounts for the elastic deformation occurring in both the indenter and the sample. The relationship between E_r and Young's modulus of indenter and samples is given by equation 2.20.

$$\frac{1}{E_r} = \left(\frac{1-v^2}{E}\right) + \left(\frac{1-v_i^2}{E_i}\right) \qquad [2.20]$$

E = Young's modulus of the sample

v = Poisson's ratio of sample

E_i = Young's modulus of the indenter

v_i = Poisson's ratio of indenter

2.7.2.1 Sample preparation

The samples were prepared as explained in section 2.1 and finished with colloidal silica to give a 0.2 µm finish. Bruker's Ti 950 Tribolndenter nanoindenter was used to conduct the experiments at room temperature. The maximum indentation load was 500 µN and the indents were separated by 3 µm.

2.8 Small punch test

Small punch (SP) testing was first introduced in the 1980s and is being used to determine mechanical properties since then. During the industrial components lifetime, its degradation over time must be taken into account for its structural integrity. Orthodox techniques of mechanical testing utilize the large specimen leading to high structural material consumption, whose availability and volume is often limited. Therefore determining mechanical properties using orthodox techniques may lead to affecting the structural integrity or even lead to the destruction of the component due to access of the large test specimen from it. In contrast to orthodox techniques, SP allows the direct measurement of mechanical properties using miniature specimens. Due to its semi-destructive in nature, it has huge potential in fields where only a small volume of material is available such as the nuclear industry, aerospace industry and new alloys development. Given that the availability of ZMA-Ge materials is limited, the SP test technique is a promising option to rank their mechanical properties.

During the early years of the SP test, it was used in the power generation and nuclear industry to assess the remnant life of structural materials due to thermal ageing, neutron irradiation etc [111], [112]. Now its application has extended to other industries such as aerospace [113], [114], automotive [115], off-shore [116] and also non-metallic materials like bones and polymer [117], [118]. Mechanical properties such as tensile properties (yield strength, ultimate tensile strength, tensile elongation)[119], [120], fracture toughness [121], creep deformation rate and rupture time [122], [123] could be obtained using the SP test.

Even though SP has been used for over 3 decades, the technique is unfortunately not supported by globally accepted fully-fledged normative document [124]. In 2007, the first initiative towards full standardisation was established, when the pre-normative document "CWA1562" was designed by collaboration within the Europen community of testing laboratories and is under continual development [125]. The "CWA1562" is also known as the European Code of Practice (EUCoP) 2007 for Small Punch Testing.

2.8.1 SP testing rig

The small punch technique uses small-sized specimens measuring 8 mm in diameter and 0.5mm in thickness. The miniature disc specimens are clamped in between upper and lower dies with a receiving hole of 4 mm diameter. Biaxially deformed by static (creep test) and variable load (tensile test) using a hemispherical indenter punch with 2.5 mm in diameter. As the load is applied through the indenter, the indenter and fracture surface are driven through the receiving hole. A schematic of the SP testing setup is presented in Figure 2.17.

The test set-up and relevant geometries are as per the European Code of Practice (EUCoP) 2007 for Small Punch Testing. Disc displacement is measured using a standard single linear variable displacement transducer (LVDT), which is placed below the specimen disc via a quartz rod.

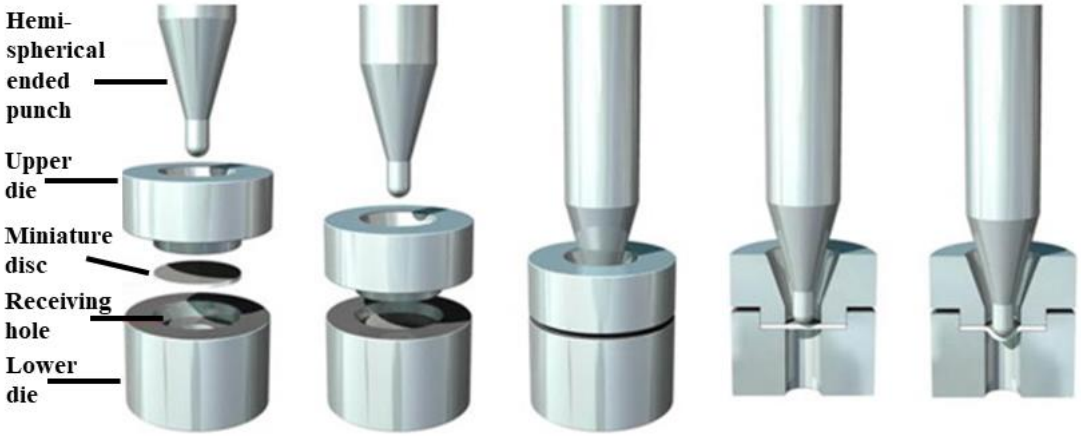

Figure 2.17: Schematic representation of SP apparatus, disc retention and punch application [113].

2.8.2 Characteristics of the force-displacement curve

The small punch tensile test is a displacement controlled technique where the punch is driven through the specimen at a constant velocity. The load applied to move the punch through the specimen is recorded as a function of punch displacement v (at the punch tip) or specimen deflection u (opposite to the contact point between punch and specimen, on the lower side of the specimen). A typical force-displacement (P-u) curve for the ductile material is presented in Figure 2.18.

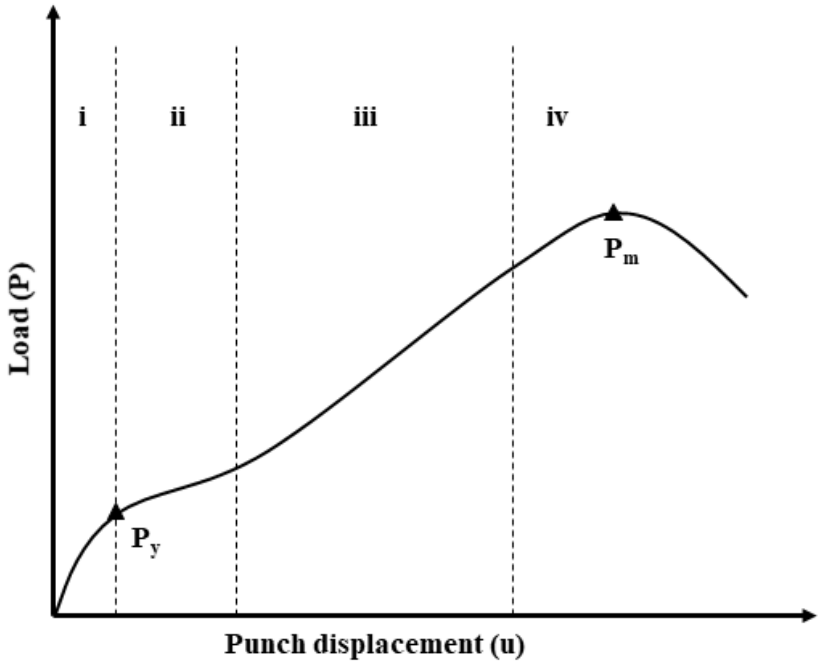

Figure 2.18: Load vs displacement (P- u) curve for ductile material obtained from the SP test.

The P-u curve is generally divided into four zones [126]. Zone (i) represents the indenting of the specimen surface due to the punch head and the elastic deformation, zone (ii) represents the plastic deformation, zone (iii) represent the membrane stretching which predominates the curve and zone (iv) plastic instabilities such as necking and crack occurs leading to the failure of the material.

2.8.2.1 Correlating SP properties with the uniaxial tensile test

Different characteristic data are extracted from the P-u curve such as:

- P_y, yield load or elastic-plastic transition load
- P_m, maximum load
- u_m, displacement at maximum load
- u_o, displacement at yield load
- $slope_{ini}$, the initial slope of zone I

Due to the biaxiality nature of the SP test and the test specimen, the traditional method of translating load to stress cannot be applied [127]. Therefore, the characteristic data obtained from (P-u) curve are empirically correlated to determine effective yield stress, ultimate tensile stress (UTS) and Young's modulus (E) using the following equations [126], [128], [129]:

$$\textit{yield stress } (\sigma_y) = \alpha_1 \frac{P_y}{h_0^2} + \alpha_2 \qquad [2.21]$$

$$\textit{ultimate tensile strength } (\sigma_{UTS}) = \beta_1 \frac{P_m}{h_0 u_m} + \beta_2 \qquad [2.22]$$

$$\textit{ultimate tensile strength } (\sigma_{UTS}) = \beta_1' \frac{P_m}{h_0^2} + \beta_2' \qquad [2.23]$$

P_y= elastic-plastic transition load

P_m= maximum load

h_o= sample thickness

u_m= deflection at maximum force

The parameters α_1, α_2, $\beta_1, \beta_2, \beta_1'$, β_2', are test constants or correlation factors that are obtained by directly equating known uniaxial stress data against corresponding loads for a series of materials and temperature [127]. Two different equations 2.22 and 2.23

are found in the literature for UTS, however, the normalization of P_m with $h_o u_m$, equation 2.22, is the preferred formulation because at P_m the specimen is in a state of membrane stretching/necking occurring state, therefore, the force can be expected to depend proportionally on specimen thickness [126].

2.8.3 Sample preparation

The samples were cut into discs of 8 mm in diameter and 0.8 mm in thickness. The individual discs were grounded down to a thickness of 0.5 mm (500 µm ± 5 µm) using incrementally finer silicon carbide abrasive papers, finally finishing with grit paper of 1200 grade, in accordance to EUCoP. The experiments were carried out at a constant displacement rate of 0.5 $mm.min^{-1}$ at room temperature. To study the post corrosion mechanical properties, SP test ready discs were immersed in 0.17 M NaCl pH 7 solution for 24 hours with one side covered with PTFE tape.

Chapter 3 Corrosion mechanism of ZMA-Ge alloys

3.1 Introduction

Hot-dip galvanised (HDG) pre-finished steels are used extensively in a wide variety of industries such as automotive and construction. Galvanising alloys are recognised to be a major element of these steels. Galvanising alloys (zinc and zinc-based alloys) provide sacrificial protection to the underlying steel substrates. Despite the enhanced corrosion protection offered by zinc-based coatings, there is a rising challenge to both further improve coating performance and lower coating weights. Enhancement of corrosion resistance of HDG steel coatings has been undergoing for the last two decades through binary and ternary additions such as aluminium and magnesium. The corrosion mechanism by which these additions offer greater corrosion protections is discussed in section 1.4.1. Among the commercially available HDG zinc-based coating systems; zinc (Zn), zinc-aluminium (ZA) and zinc-magnesium-aluminium (ZMA), ZMA provides superior protection. Recently the approach of introducing a fourth alloying element into the ternary ZMA alloy systems has also been explored and initial research has shown to have a positive influence.

Previously a variety of different alloy additions were made to ZMA alloy [69], [130]. Among the various additions, germanium (Ge) has displayed the lowest Vickers hardness value and initial corrosion experiments also displayed the improvement of corrosion performance. Ge additions of 0.01 wt. %, 0.78 wt.% and 1.7 wt.% were investigated. Corrosion investigation using SVET showed a decrease in corrosion performance with small Ge additions (up to 0.05 wt. %) whereas 0.78 wt. % Ge increased the corrosion resistance by more than 50 % [18]. This improvement in corrosion enhancement was attributed to the change in the microstructure i.e volume fraction of the eutectic phase. However, an in-depth investigation of the corrosion mechanism of ZMA-Ge alloys was not conducted.

Here in this chapter, we explore the effects of Ge additions (0 - 1.8 wt.%) in terms of the alloy's microstructure and corrosion resistance using a combination of techniques. A combination of in-situ Scanning Vibrating Electrode Technique (SVET) and Time Lapse Microscopy (TLM) is used to study the effect of Ge additions on the corrosion resistance of ZMA alloys freely corroding in 0.17 M sodium chloride (NaCl) pH 7 electrolyte. SVET derived mass loss is used to assess

the corrosion performance of ZMA-Ge alloys and TLM is used to provide information regarding the corrosion mechanism at a microstructural level. Complimentary electrochemical (open circuit measurements (OCP)) measurements are also conducted. [1] Therefore, we aim to gain insight into how the changes in microstructure due to Ge additions affect the corrosion rate and mechanism of ZMA alloy.

3.2 Sample production

The production of the ZMA-Ge samples was completed in a closed controlled environment in the presence of argon gas. ZMA (96.80 % Zn, 1.6 % Mg and 1.6 % of Al) pieces, provided by TATA Steels were heated to 650^{o}C in a crucible. Varying amounts of Ge were added to the mixture to produce a range of four alloy compositions and was further heated to 1000^{o}C. Samples were then air-cooled within the crucible. A pyrometer was used to measure the temperature on the alloy surface.

3.3 Microstructural structural analysis of ZMA-Ge alloys

The target compositions of the produced samples under investigation are presented in Table 3.1. The ZMA-0 Ge sample is composed of 96.80 wt.% of Zn, 1.60 wt.% of Mg, 1.60 wt. % of Al and 0.00 wt.% of Ge. The wt. percentage of Zn, Mg and Al decrease slightly with an increase in Ge content. Therefore, the highest Ge content sample ZMA-1.8 Ge consists of 95.08 wt. % of Zn, 1.57 wt. % of Mg & Al and 1.8 wt. % of Ge.

Table 3.1:Compositions in wt. % of the Zn-Mg-Al-Ge (ZMA-Ge) alloys

Sample	Zn (wt. %)	Mg (wt. %)	Al (wt. %)	Ge (wt. %)
ZMA-0 Ge	96.80	1.60	1.60	0.00
ZMA-0.19 Ge	96.61	1.59	1.59	0.19
ZMA-0.87 Ge	95.96	1.58	1.58	0.87
ZMA-1.8 Ge	95.08	1.57	1.57	1.80

[1] The work presented in this chapter has been published elsewhere.

N. Wint, A.D. Malla, N. Cooze, T. Savill, S. Mehraban, T. Dunlop, J.H. Sullivan, D. Penney, G. Williams, H.N. McMurray, The ability of Mg_2Ge crystals to behave as 'smart release' inhibitors of the aqueous corrosion of Zn-Al-Mg alloys, Corrosion Science, Volume 179, 2021. https://doi.org/10.1016/j.corsci.2020.109091

The SEM image of the ZMA-0 Ge alloy is presented in Figure 3.1. ZMA-0 Ge alloy is composed of three different phases; primary zinc, binary eutectic and ternary eutectic. Primary zinc phases are surrounded by binary and ternary eutectic phases. Binary eutectic is a lamellar structure made up of primary zinc and $MgZn_2$ whereas the ternary eutectic is made up of primary zinc, $MgZn_2$ and aluminium nodules [78]. The SEM images of the microstructures of different ZMA-Ge samples are shown in Figure 3.2.

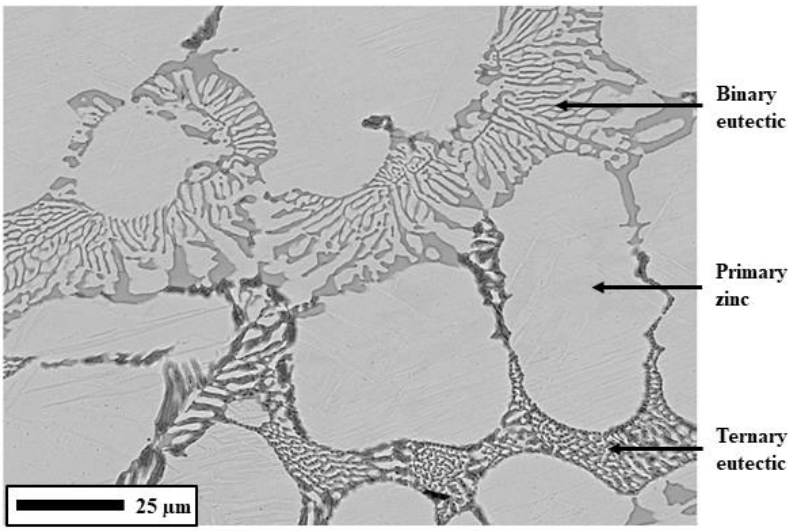

Figure 3.1: SEM image showing the ZMA-0Ge alloy

The addition of Ge into the ZMA alloy system results in the formation of a new phase within the microstructure (Figure 3.2D). EDS and XRD analysis (Figure 3.3 and 3.4) confirms that the phase formed is magnesium germanide (Mg_2Ge) which has been shown to form previously in ZMA alloys [18] and magnesium [131] which contain Ge additions. These Mg_2Ge exist in two different forms; Mg_2Ge plate-like structure (present in Ge containing samples) and faceted Mg_2Ge crystals (present in high Ge containing samples). In ZMA-1.8 Ge (Figure 3.2D) (highest Ge concentration) large Mg_2Ge crystals are observed in the microstructure that demonstrate a 'Hopper' crystal morphology. The "Hopper" crystals have fully developed edges with hollow interior spaces. The microstructural morphology suggests that the Mg_2Ge crystals and plates are encased within the primary Zn phase suggesting that Mg_2Ge solidifies first during freezing and provide subsequent nucleation sites for the primary Zn.

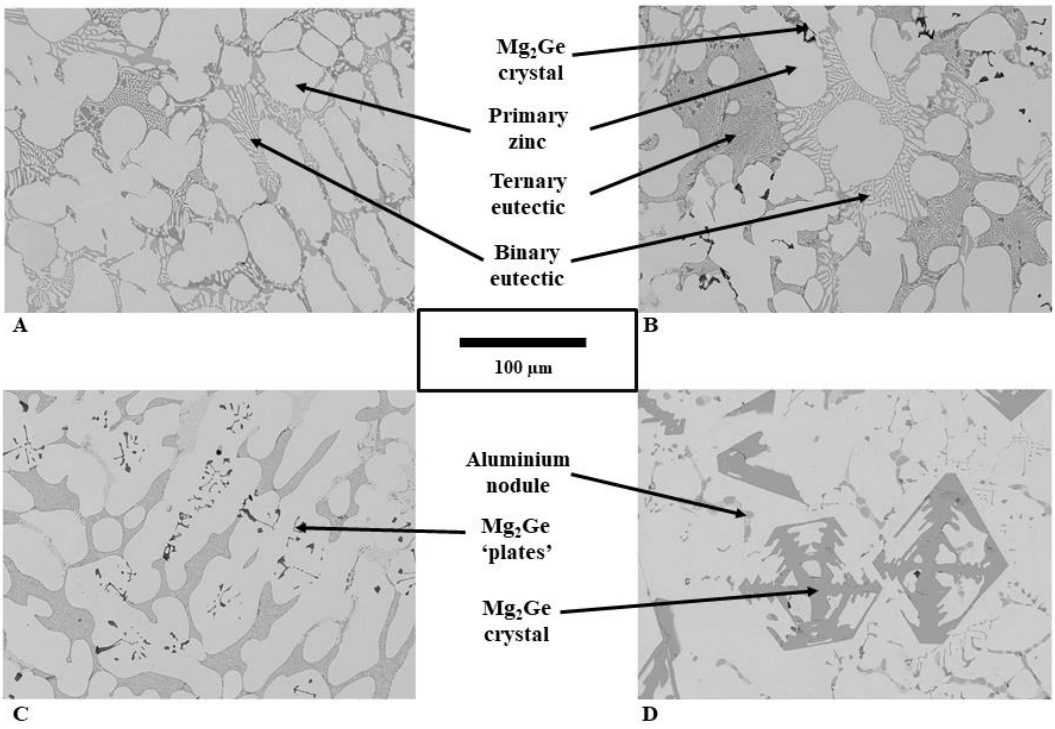

Figure 3.2: SEM images showing. A) ZMA-0 Ge, B) ZMA-0.19 Ge, C) ZMA-0.87 Ge and D) ZMA-1.8 Ge.

Table 3.2: Area fraction of phases of ZMA-Ge samples with different Ge additions

Sample	Area % of Primary Zn	Area % of Eutectic	Area of Mg_2Ge
ZMA-0 Ge	67.52 ± 2.18	32.34 ± 1.92	0.00 ± 0.00
ZMA-0.19 Ge	69.89 ± 6.21	28.54 ± 6.27	1.57 ± 0.07
ZMA-0.87 Ge	75.17 ± 0.45	22.23 ± 0.64	2.60 ± 0.22
ZMA-1.8 Ge	78.31 ± 5.67	7.41 ± 1.27	14.28 ± 6.84

The average area fraction of different phases taken from 3 different areas for each sample are shown in Table 3.2. The percentage of the surface area covered by Mg_2Ge increases from 1.57 % in the ZMA-0.19 Ge sample to 14.28 % in the ZMA-1.8 Ge sample. Correspondingly the Mg containing the eutectic phase decreases from

32.34 % to 7.41 %. Also, the surface area fraction of primary Zn increases from 67.52% for ZMA-0 Ge to 78.31 % for ZMA-1.8 Ge.

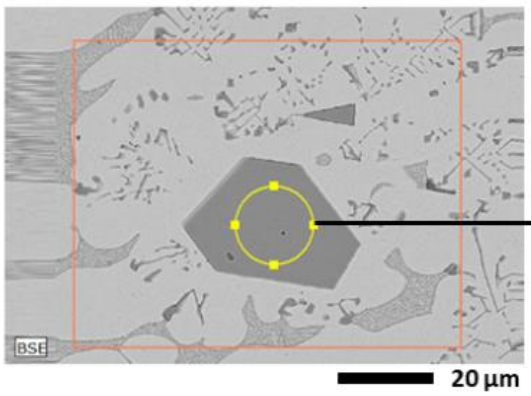

Element	Atomic. C [at. %]
Germanium	31.65
Magnesium	62.62
Zinc	5.32
Aluminium	0.41

Figure 3.3: EDS analysis of Mg_2Ge crystal

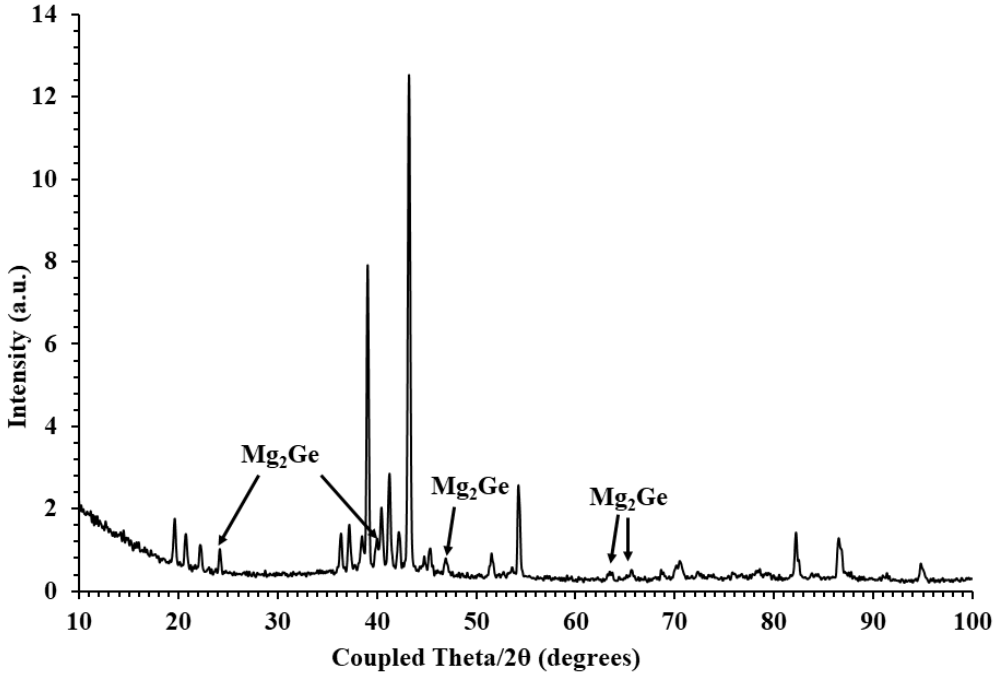

Figure 3.4: XRD analysis of ZMA-0.87 Ge alloy

3.4 Electrochemical Measurements

Figure 3.5 (a) presents the OCP of the ZMA-Ge samples over 24 hours immersed in pH 7 0.17 mol.dm^{-3} NaCl. The initial potential of ~ -1.02 V vs. SCE is measured for all samples after which a shift to more negative potential is observed for the first hour of the experiment. This shift in potential is dependent upon Ge content. For ZMA-0 Ge there is a small shift in OCP to ~ -1.03 V vs SCE. The OCP values then fluctuate between -1.02 V and -1.04 V vs SCE over the 24-hour experiment. For

ZMA-0.19 Ge and ZMA-0.87 Ge, the potential shifts to ~ -1.04 V vs. SCE and ~ -1.06 V vs. SCE respectively. However, in the case of ZMA-1.8 Ge after the initial shift to more negative potential (~ -1.14 V vs. SCE), the potential steadily shifts back to a more positive potential and reaches ~ -1.05 V vs. SCE after 6 hours. The potentials for all the alloys converge towards ~ -1.04V ± 0.01V vs SCE after 24 hours.

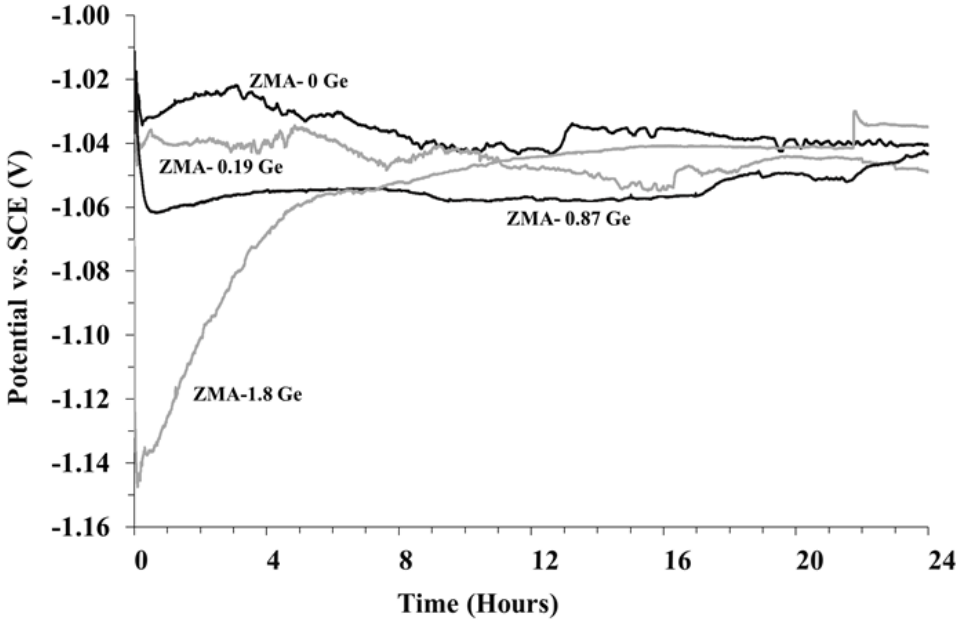

Figure 3.5 (a): The time-dependent OCP for various ZMA-Ge immersed in 0.17 M NaCl at pH 7.

To further examine the change in corrosion behaviour during the initial hours of the experiment observed during OCP measurement, the ZMA-0 Ge and ZMA-1.8 Ge were subjected to linear polarisation measurements. The measurements were performed for 5 hours with the first measurement taken after 10 min and subsequently after each hour. The polarisation resistance (R_p) values are presented in Figure 3.5 (b). The samples were polarised by ±15 mV from OCP at a scan rate of 0.166 mVs^{-1} in 0.17 $mol.dm^{-3}$ pH 7 NaCl solution.

Throughout the 5 hours, R_p values of ZMA-1.8 Ge are around one order of magnitude larger than those of ZMA-0 Ge. As $i_{corr} \alpha 1 / R_p$, it indicates consistently lower corrosion current on ZMA- 1.8 Ge. Thus, suggesting an enhanced corrosion resistance for ZMA-1.8 Ge.

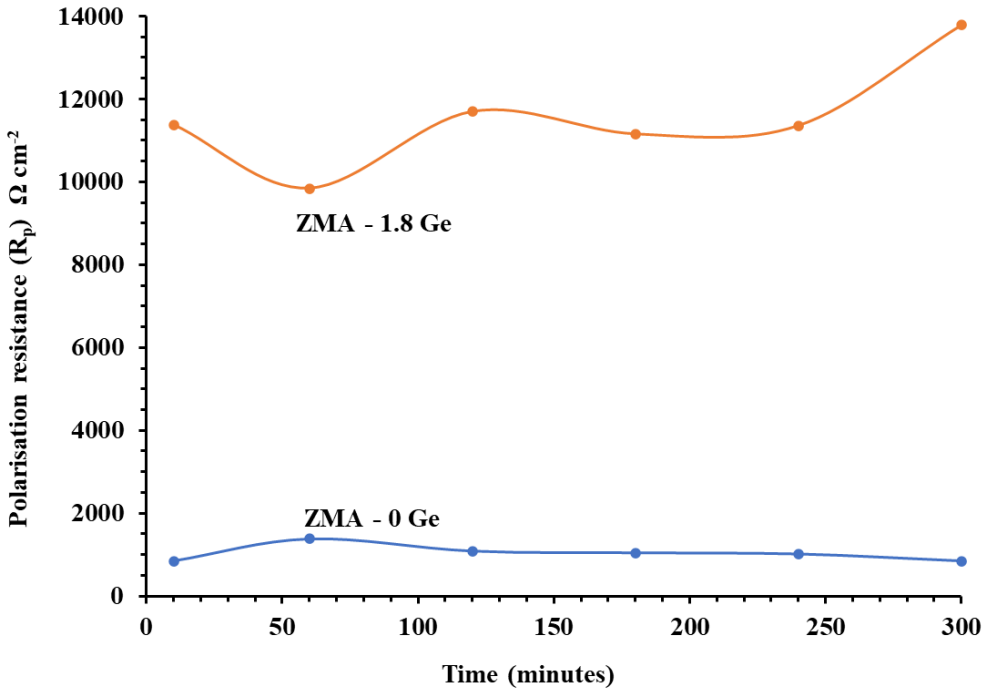

Figure 3.5 (b): Linear polarization resistance measurements obtained for ZMA-0 Ge and ZMA-1.8 Ge.

3.5 Scanning Vibrating Electrode Technique (SVET)

Figure 3.6 (a) shows the normal current density measured above the surface of the ZMA-Ge alloys freely corroding in pH 7 0.17 mol.dm^{-3} NaCl solution. For ZMA-0 Ge, ZMA-0.19 Ge and ZMA-0.87 Ge corrosion is highly localized from the onset and the anodic positions remain rather fixed with time once initiated. Approximately 5 A.m^{-2} peak anodic current densities are recorded. As the content of Ge increases the number of individual anodic features decreases. The initiation of anodic attack is delayed for several hours for ZMA-1.8 Ge and, once established it is more generalised in nature. Lower values of peak anodic current densities are observed for ZMA-1.8 Ge.

The SVET derived hourly metal loss (average of three measurements) as a function of time for both ZMA – 0 Ge and Zn – 1.8 Ge during immersion on pH 7 0.17 M NaCl for 24 hours are presented in Figure 3.6 (b). The figure shows that the corrosion rate of ZMA – 0 Ge is higher compared to ZMA – 1.8 Ge throughout the experimental time but remains reasonably constant ~ 0.25 g.m^{-2}. However, for ZMA – 1.8 Ge the corrosion rate is considerably lower ~ 0.02 g.m^{-2} at the beginning of the experiment and increase with time.

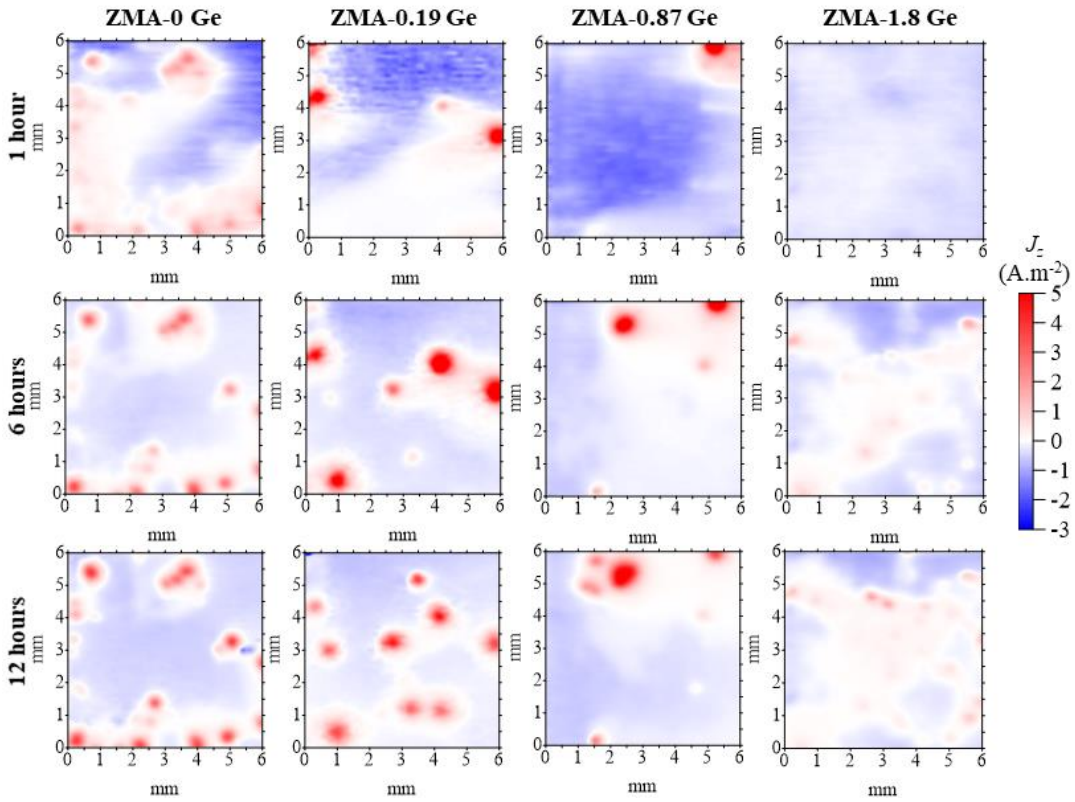

Figure 3.6 (a): SVET false colour maps showing normal current density measured above ZMA-Ge alloys immersed in pH 7 0.17 M NaCl solution.

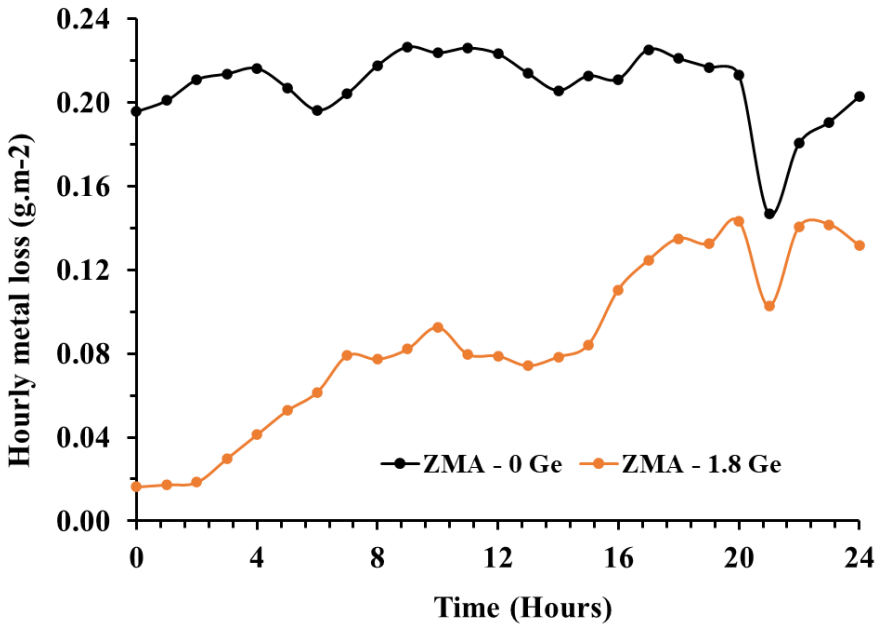

Figure 3.6 (b): SVET derived hourly metal loss as a function of time for ZMA – 0 Ge and ZMA – 1.8 Ge after immersion in pH 7 0.17 M NaCl solution for 24 hours.

Table 3.4: SVET derived metal loss for ZMA-Ge samples immersed in pH 7 1 wt. % NaCl solution after 24 hours.

Sample	Mass Loss ($g.m^{-2}$)
ZMA-0 Ge	5.01 ± 0.49
ZMA-0.19 Ge	8.53 ± 2.16
ZMA-0.87 Ge	4.41 ± 0.51
ZMA-1.80 Ge	2.11 ± 0.84

The measured current density (also represented in form of colour maps in Figure 3.6 (a)) could also be used to calculate the total mass/metal loss. The current density measured could be converted into charge then convert to total metal loss by the application of the Faraday law. The SVET derived metal loss for ZMA-Ge samples after 24 hours of immersion in 0.17 $mol.dm^{-3}$ NaCl is presented in Table 3.4. The errors shown are based on the standard deviation of three measurements. The metal loss for ZMA-0.19 Ge is 8.53 $g.m^{-2}$ compared to 5.01 $g.m^{-2}$ for ZMA-0 Ge. The values for ZMA-0.87 Ge and ZMA-1.8 Ge were 4.41 $g.m^{-2}$ and 2.11 $g.m^{-2}$ respectively. It, thus, seems that the Ge additions can substantially diminish the metal loss in these alloys when alloyed at levels above a threshold amount.

3.6 Time-Lapse Microscopy (TLM)

The variation in corrosion mechanism observed in ZMA-1.8 Ge during SVET experiments and electrochemical measurement is further investigated using TLM. TLM enables the acquisition of mechanistic knowledge of corrosion at a microstructural level with respect to time. Figure 3.7 shows optical microscopy images of the surface of ZMA-Ge alloys after 1 hour, 6 hours and 12 hours of immersion in pH 7 0.17 $mol.dm^{-3}$ NaCl. Two anodic features (Figure 3.7a) are observed on the surface of ZMA-0 Ge after 1 hour of immersion, after which they expand in size (see also Video V1). A corrosion product ring is also observed at a distance from the anodes which becomes thicker with time. Corrosion product rings have previously been claimed to form at boundaries where metal ions generated at the anodic site and hydroxide ions generated at the cathodic site encounter [32].

In the case of ZMA-1.8 Ge (Figure 3.8b) similar corrosion features are not observed on the surface (primary zinc and eutectic phase) at 1 hour of immersion. However, blackening of the Mg_2Ge crystals was observed during this initial period (see Video V2). After the initial delay, corrosion (attack on the Zn phase) is initiated at the boundary between primary zinc and Mg_2Ge crystals. The anodic features and development of the corrosion phenomenon are similar to those observed in the ZMA-0 Ge alloy however it is somewhat constrained. The anode-cathode spacing as determined by the distance from the anode to the corrosion product ring is considerably smaller (typically ~ 75 µm) than that observed on ZMA-0 Ge (typically ~ 250 µm). This delay in initiation is explicit in the TLM video shown (V2) and is further analysed by measuring the anodic area.

From the time-lapse images, it is possible to measure the anodic area with respect to time. However, it should be considered that this measurement assumes that the anode growth is laterally progressive and the growth with respect to the depth of attack is not considered. Plots of the average anode area of three experiments versus time for ZMA-0 Ge and ZMA-1.8 Ge are shown in Figure 3.8.

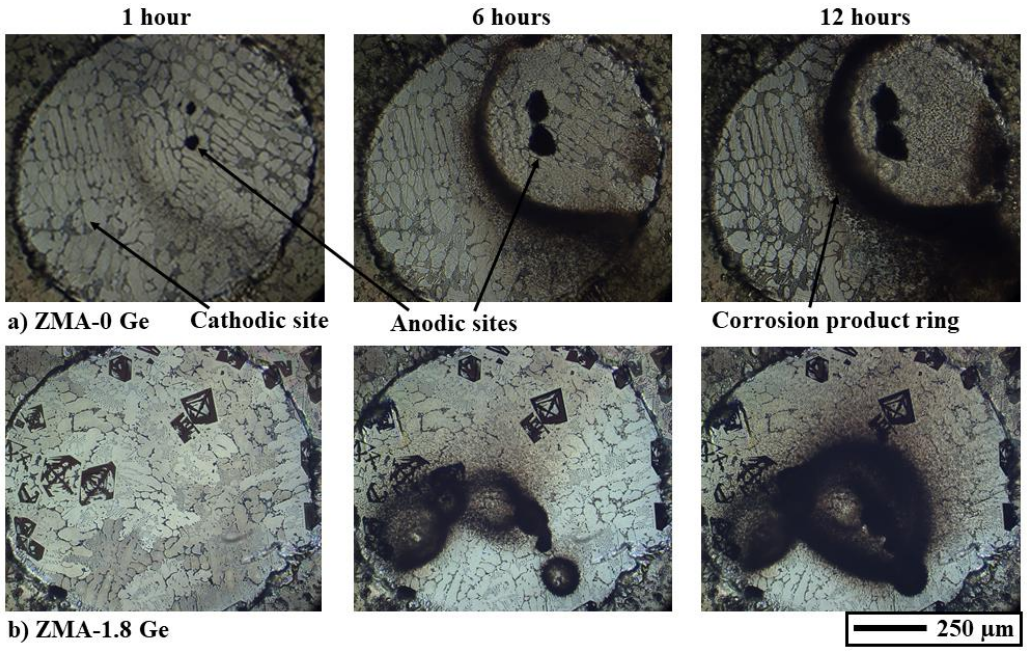

Figure 3.7: Optical microscope image of the a) ZMA-0 Ge and b) ZMA-1.8 Ge surface taken in-situ under immersion conditions in 0.17M NaCl pH 7 solution.

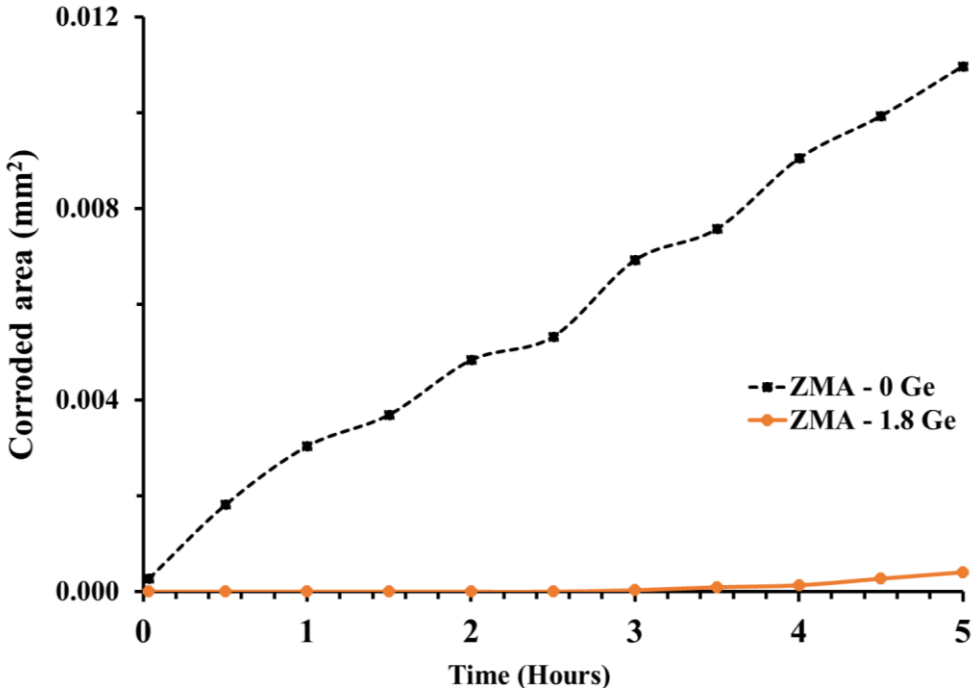

Figure 3.8: Corroded area versus time for ZMA-0 Ge and ZMA-1.8 Ge for immersed in 0.17M NaCl pH 7 solution for 5 hours.

In Figure 3.8, a linear increase in the corroded area can be observed for ZMA-0 Ge. However, in contrast, for ZMA-1.8 Ge, a delay of ~ 4 hours is observed before any significant anodic area in primary zinc and eutectic is observed. This delay in initiation is dependent on the surface area covered by the Mg_2Ge crystal of the overall exposed surface. The instantaneous formation of an anode for ZMA-0 Ge and significantly delayed anodic features formation for ZMA-1.8 Ge can be observed in Video V1 and Video V2 respectively.

It would seem rational that the enhanced protection and change in corrosion mechanism afforded by the ZMA-1.8 Ge are due to the change in microstructure and the presence of Mg_2Ge crystals. Therefore, corrosion of Mg_2Ge crystals was investigated by completing EDS analysis prior to and following immersion in 0.17 $mol.dm^{-3}$ pH 7 NaCl solution for 2 hours. Figure 3.9 (a & b) presents SEM images of Mg_2Ge crystals prior to immersion in NaCl solution. The weight percentage of Mg, calculated using EDS, is 40.92 wt. % and 40.36 wt. % respectively. Figure 3.9 (c & d) presents that the Mg content of those same crystals has dropped to 20.91 wt. % and 17.63 wt. % after 2 hours of immersion.

ZMA-0 Ge and ZMA-1.8 Ge were subject to further TLM investigation in the presence of the phenolphthalein indicator. Phenolphthalein is an indicator that is colourless at pH values below pH 8 and turns pink at pH above 8. The NaCl electrolyte was dosed with 1 wt. % phenolphthalein. Figure 3.10 shows a TLM image of the ZMA-0 Ge surface after 4 minutes of immersion in 0.17 mol.dm^{-3} pH 7 NaCl solution dosed with 1 wt.% phenolphthalein. Figure 3.10 and video V3 shows the establishment of a pH gradient with respect to anodic and cathodic sites. The pH > 8 is observed surrounding the cathodic sites and pH < 8 is observed surrounding the anodic sites. A similar pH gradient has been observed previously during the study of ZMA coatings [78].

The change in electrolyte pH for ZMA-1.8 Ge after immersion for 2 minutes, 4 minutes, 1 hour and 14 hours in pH 7 0.17 mol.dm^{-3} NaCl containing 1 wt. % phenolphthalein is presented in Figure 3.11. Figure 3.11 and Video V4 show the pH value of the electrolyte across the entire surface to be below 8 at the beginning of the experiment. After 1 hour, the colour throughout the surface transforms into pink showing a pH value greater than 8. Finally, after 14 hours a potential gradient is set up across the electrolyte (Figure 3.11(d)) similar to that observed in ZMA-0 Ge (Figure 3.10).

To further examine the nature of the pH that developed above the ZMA-Ge surface, ZMA-0 Ge was subject to an inkblot test. The sample was prepared identically as for SVET experiments. A droplet of 0.17 M NaCl pH 7 solution was then added to cover the area. After 1-hour universal indicator paper was applied to the droplet. The colour change in universal indicator paper for ZMA-0 Ge is presented in Figure 3.13. The figure illustrates that a pH of 9-10 has developed over the exposed sample area similar to that observed in Figure 3.10 and Figure 3.11.

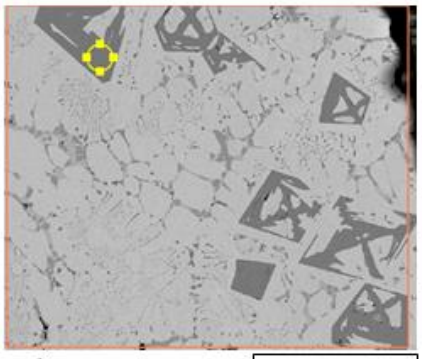

a)

Element	Norm. C (wt. %)
Germanium	52.98
Magnesium	40.92
Zinc	6.09
Aluminium	0

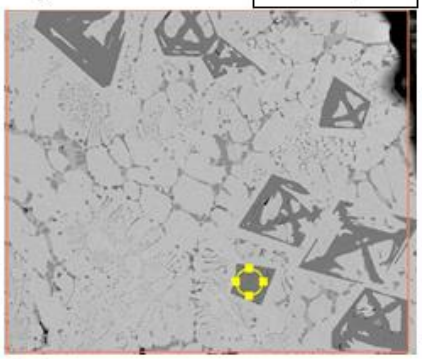

b)

Element	Norm. C (wt. %)
Germanium	52.08
Magnesium	40.36
Zinc	7.53
Aluminium	0.03

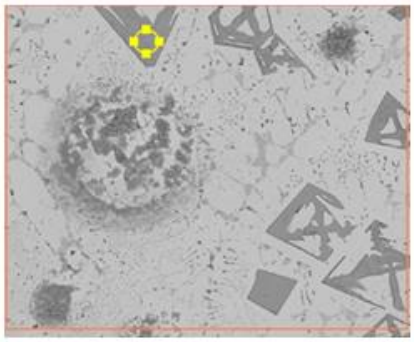

c)

Element	Norm. C (wt. %)
Germanium	61.90
Magnesium	20.91
Zinc	16.88
Aluminium	0.31

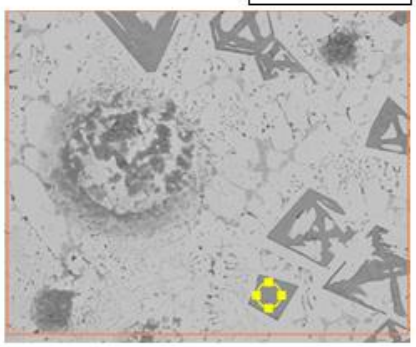

d)

Element	Norm. C (wt. %)
Germanium	65.89
Magnesium	17.63
Zinc	16.40
Aluminium	0.08

30 µm

30 µm

Figure 3.9: SEM image of the ZMA-1.8 Ge surface with EDS analysis of two different individual Mg_2Ge crystals obtained (a & b) prior to and (c & d) after 2 hours of immersion in pH 7 0.17 M NaCl.

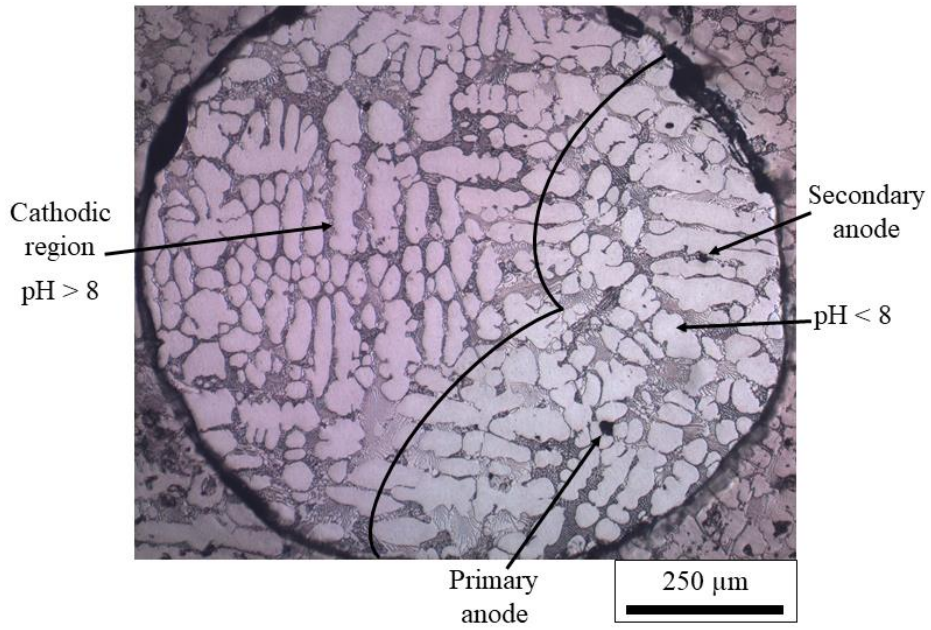

Figure 3.10: Optical microscope image of ZMA-0 Ge surface taken after 4 minutes of immersion in pH 7 0.17M NaCl solution in the presence of phenolphthalein indicator.

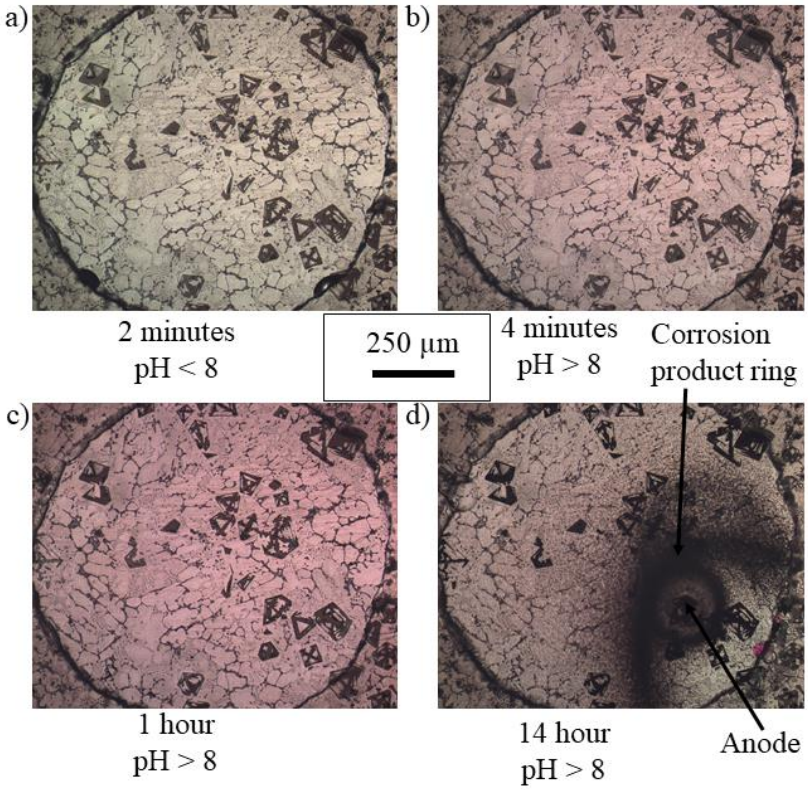

Figure 3.11: Optical microscope image of ZMA-1.8 Ge surface taken after a) 2 minutes, b) 4 minutes, c) 1 hour and d) 14 hours of immersion in pH 7 0.17M NaCl solution in the presence of phenolphthalein indicator.

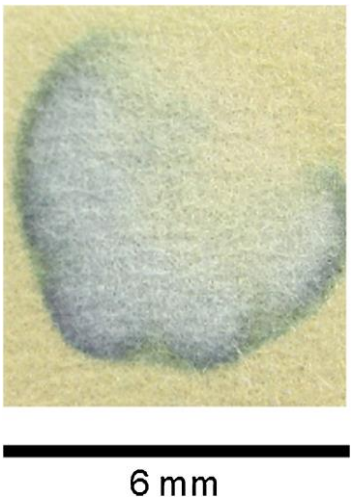

Figure 3.12: A photo of universal indicator paper which had been applied to a droplet of 0.17 mol.dm-3 NaCl pH 7 applied to ZMA-0 Ge for 1 hour.

3.7 Discussion

The precise mechanism by which additions of Ge (> 0.87 wt.%) provide enhanced corrosion protection is yet to be fully determined however it would seem reasonable to suggest that the principal microstructural components responsible for the increased resistance observed, are the Mg_2Ge. Once exposed to the corrosive electrolyte, it is understood that Mg_2Ge undergoes preferential anodic de-alloying by loss of Mg^{2+}, leaving behind a surface enriched in Ge (Figure 3.9) thus acting as a reservoir/source of Mg^{2+} ions. This initial anodic dissolution relates to the initial corrosion potential fall observed for all three Ge containing samples (Figure 3.5). The Mg^{2+} ions released from the Mg_2Ge crystals react with the hydroxyl ions (OH^-) generated at the cathode to form $Mg(OH)_2$. $Mg(OH)_2$ has a solubility product K_{sp} of 1.8 x 10^{-11} $mol^3.dm^{-9}$ [132] and the production of $Mg(OH)_2$ will ensure that local electrolyte pH is maintained at ~10.5, at which pH the zinc surfaces are passive [64], [71]. This phenomenon is reinforced by the pink appearance (pH > 8) of the electrolyte above the ZMA-1.8 Ge sample in the presence of 1 wt. % phenolphthalein (Figure 3.11). In comparison, both Zn^{2+} and Mg^{2+} are formed during the dissolution of the eutectic phase (Primary zinc & $MgZn_2$) which occurs during the corrosion of ZMA-0 Ge [32], [71], [75]. The hydrolysis of Zn^{2+} metal cations will result in local acidification [133] and limit the increase in pH which occurs during Mg dissolution. As a result, a favourable environment for Zn surface passivation across the entire exposed surface of ZMA-0 Ge is not established in contrast to ZMA-1.8 Ge.

ZMA-1.8 Ge takes approximately 6 hours to stabilise after the initial drop in potential and this relates to the time taken to observe anodic activity in TLM (Figure 3.8) and SVET (Figure 3.7) experiments. The chemical conditions created on the surface of the ZMA-1.8 Ge alloy due to initial Mg_2Ge dissolution seems to provide a transient level of protection to the zinc. Subsequently, the protection locally breaks down and the zinc phase begins to corrode, initiating initially at boundaries with the Mg_2Ge crystals. However, the increased bulk electrolyte pH means that the zinc cations (produced at the anodes) are only required to travel a short distance before the solubility limit associated with $Zn(OH)_2$ is reached. This means that once initiated, corrosion on ZMA-1.8 Ge is constrained compared to that on ZMA-0 Ge (Figure 3.7) as shown by the smaller radius of the corrosion product ring. Evidence of zinc dissolution in these regions is demonstrated in Figure 3.11(d) by the visual attack of the zinc phase in the TLM images, and the establishment of a pH <8 around this anodic region indicative of Zn^{2+} hydrolysis.

At this point, a question appears as to why the initial anodic de-alloying of Mg_2Ge is not detected on SVET for ZMA-1.8 Ge (Figure 3.6). As illustrated by the SEM images in Figure 3.2, the average size of a Mg_2Ge crystal is ~ 100 μm which is below the instrumental *whm* of the SVET (~260 μm)[89]. Thus, SVET may not individually resolve each crystal due to its size. Also, the anode to cathode spacing (i.e Mg_2Ge crystals to the primary zinc phase) may be less than the SVET tip scan height of 100 μm above the sample surface. As a result, the lines of current flux between the anode and cathode might not intersect the SVET plane of scan and therefore will not be detected. This may lead to underestimation of ZMA-1.8 Ge metal loss (Table 3.4). However, the R_p values (Table 3.3) of ZMA-1.8 Ge are approximately 10 times lower than ZMA-0 Ge throughout the first 5 hours indicating the corrosion kinetics of ZMA-1.8 Ge are diminished in comparison to ZMA-0 Ge.

The increase in potential (Figure 3.5) and anodic activity (Figure 3.6) observed for ZMA-1.8 Ge samples after ~ 6 hours of immersion implies that Mg_2Ge is only able to provide a transient inhibitive effect. Nevertheless, the introduction of Mg_2Ge into ZMA coatings, (and absence of $MgZn_2$ and Mg_2Zn_{11}) to provide enhanced corrosion protection is of interest, particularly for applications where electrolyte exposure is limited (for example in the case of organically coated systems in which ZMA is typically used), and is worthy of further investigation.

3.8 Conclusions

A systematic study into the effect of Ge additions on the microstructure and corrosion resistance afforded by Zn-Al-Mg alloy coatings has been completed to reveal that;

- the addition of Ge into the ZMA alloy system resulted in the formation of a Mg_2Ge phase within the microstructure. This phase existed in two different forms. At all levels of Ge addition, a Mg_2Ge plate-like structure was observed and at the highest concentration, large Mg_2Ge crystals were also observed. The area fraction of the eutectic phase decreased with increasing Ge content.
- A decrease in open circuit potential was initially observed for all ZMA-Ge samples. The decrease was larger at increased levels of Ge content.
- The SVET derived mass loss decreased with Ge content for values of Ge $\geq$ 0.87 wt. %. A 57.88 % decrease in mass loss was achieved at the highest levels of Ge additions (1.8 wt. %).
- The addition of 1.8 wt. % Ge delayed the initiation of corrosion of zinc phase and once initiated corrosion is somewhat constrained compared to that observed in the absence of Ge additions.
- In the absence of Ge a pH gradient is established with respect to anodic and cathodic sites. In comparison, the pH in the electrolyte above the entire surface of a corroding ZMA-1.8 Ge sample was above 8 until the dissolution of the zinc phase.

It is proposed that the Mg_2Ge crystals, present within ZMA-Ge alloys undergo anodic de-alloying by loss of Mg^{2+}, leaving behind a surface enriched in Ge. The Mg^{2+} ions released during this process react with the OH^- (generated at the cathode) to form $Mg(OH)_2$ which will ensure that local electrolyte pH values at which the zinc surface is passive. The findings of this work highlight the potential use of Ge to form thermally and mechanically stable, intermetallic ‘smart release’ capsules which can be incorporated into metallic coatings.

Chapter 4 Mechanical properties of ZMA-Ge alloys

4.1 Introduction

The hot-dip galvanised (HDG) prefinished steel are used in numerous industries and are shaped into the desired forms by bending, stamping and pressing. Such processing can cause large deformations in the steel substrate and could also induce cracks onto the coating alloy. The efficiency of the protection provided by the coating is affected by the presence of these cracks. The propagation of induced cracks provides pathways for moisture and air to ingress leading to steel causing accelerated coating and galvanic corrosion causing potentially premature steel corrosion. It is commercially desirable to minimise the formation of cracks on the coatings in order to prolong the life of the HDG prefinished steel products. Therefore, the mechanical property, the formability of coating alloys is of paramount importance for metallic coatings.

Investigation on cracking of HDG zinc magnesium aluminium (ZMA) coating showed that the cracks initiate on intermetallic $MgZn_2$ present in the binary eutectic phase [134]. Crack initiation occurs in the $MgZn_2$ phase of the microstructure and the crack propagation leads to the exposure of the underlying steel which is illustrated in Figure 4.1.

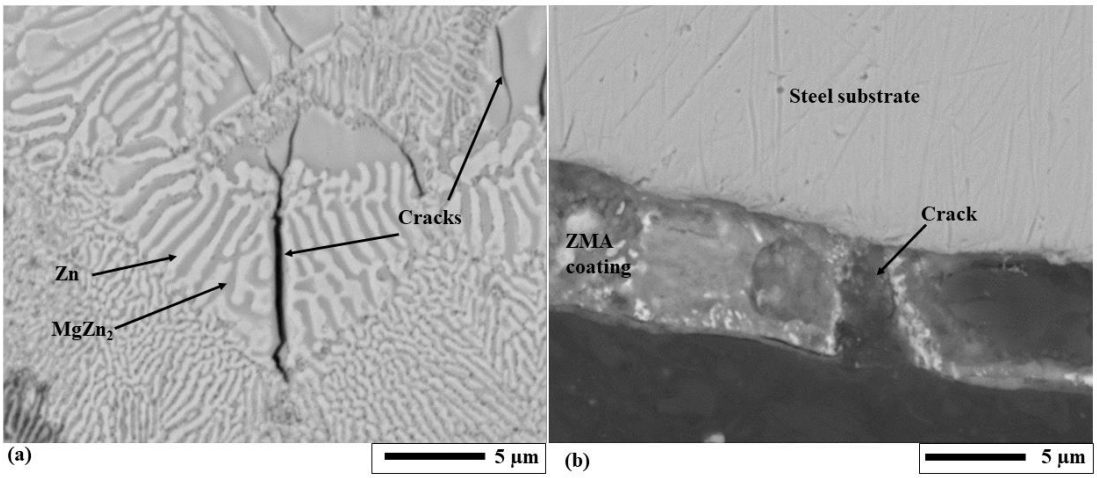

Figure 4.1: (a) Cracks initiation on $MgZn_2$ phase on ZMA coating (b) Crack propagation leading to exposure of underlying steel substrate after bend test.

In Chapter 3, the effects of Ge additions (0 - 1.8 wt.%) in terms of the alloy's microstructure and corrosion resistance was investigated. Here, the impact of Ge

additions (0 - 1.8 wt.%) in terms of mechanical properties is investigated. Furthermore, Galv Zn (99.8 wt. % Zn - 0.2 wt. % Al) and Galfan (95 wt.% Zn - 5 wt.% Al) were both obtained from TATA Steel's Galvanising Line bath and solidified via casting are also investigated. A combination of miniature testing techniques, Vickers Hardness & Nano-indentation techniques are utilized to study the hardness and a Small Punch test is used to study the tensile properties.

4.2 Vickers Hardness Measurements

Vickers Hardness measurements were conducted to investigate the effect on hardness due to varying amounts of Ge additions (0 - 1.8 wt.%) on ZMA. The average Vickers Hardness values (H_V) for ZMA alloy with various Ge additions along Galv Zn and Galfan are presented in Table 4.1. The errors shown are based on the standard deviation of 10 measurements.

Table 4.1: Vickers Hardness values of zinc and its alloys.

Sample	**H_V**
Galv Zn	51.60 ± 1.94
Galfan	72.28 ± 2.04
ZMA - 0 Ge	88.03 ± 4.00
ZMA - 0.19 Ge	91.56 ± 3.87
ZMA - 0.87 Ge	82.14 ± 4.65
ZMA - 1.8 Ge	71.50 ± 5.33

Among the commercially available metallic coatings tested, the result shows hardness in the order Galv Zn < Galfan < ZMA - 0 Ge. The addition of 5 wt.% of Al (Galfan) has increased the H_V of Galv Zn by 40.08 % from 51.60 to 72.28. Similarly, the addition of 1.6 wt.% of Al and 1.6 wt.% of Mg has increased the H_V of Galv Zn by 70.60 % from 51.60 to 88.03.

In the case of ZMA-Ge alloys, the result shows a general decrease in H_V with an increase of Ge addition except for ZMA - 0.19 Ge where a slight increase in H_V is observed. The result shows hardness in the order ZMA - 1.8 Ge < ZMA - 0.87 Ge < ZMA - 0 Ge < ZMA - 0.19 Ge. The addition of 0.19 wt. % of Ge has increased the H_V of ZMA by 4 % from 88.03 to 91.56 whereas the addition of 1.8 wt. % of Ge has reduced the H_V of ZMA by 18.78 % from 88.03 to 71.50. The relationship between

the hardness (H_V) and the area % of the eutectic phase of ZMA alloys is presented in Figure 4.2.

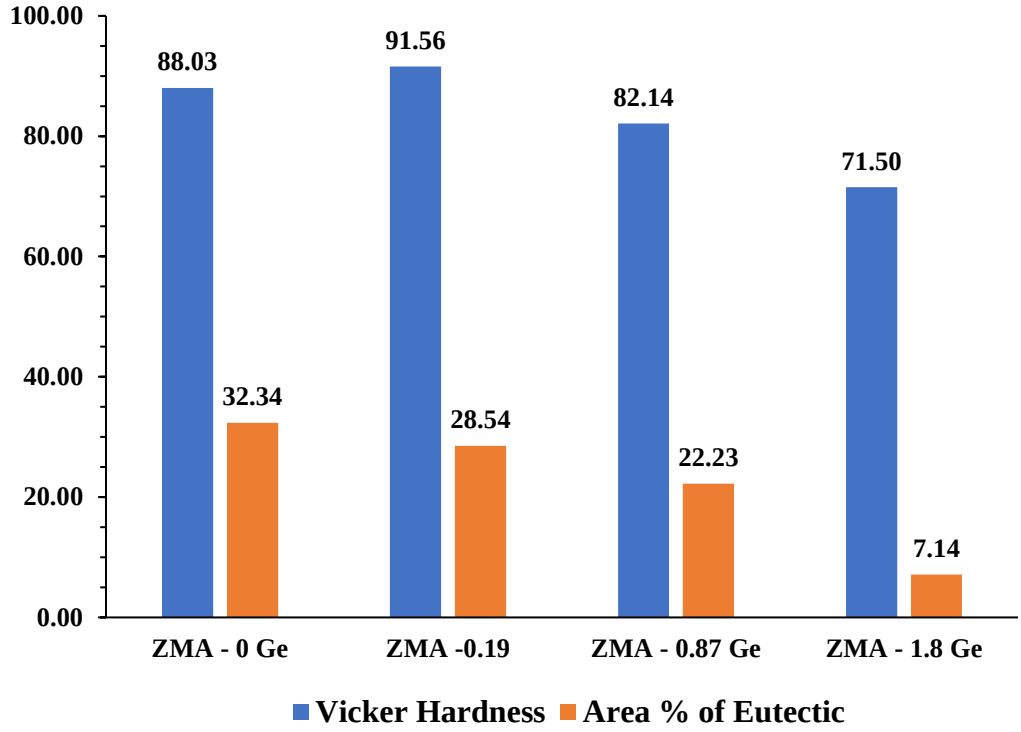

Figure 4.2: Relationship between the hardness and the area % of the eutectic phase of ZMA alloys.

In section 3.2 and Table 3.2, we observed a decrease in the area % of the eutectic phase with an increase in Ge concentration. Correspondingly, the same trend is observed for H_V in Figure 4.2 except for the lowest Ge concentration. Therefore, a direct relationship between the H_V and area % of the eutectic phase is observed.

4.3 Nanoindentation Technique

In section 4.2, the highest Ge concentration displayed a relatively higher reduction in H_V compared to the other Ge concentrations. Therefore, here ZMA - 0 Ge and ZMA - 1.8 Ge are the subject of the Nanoindentation technique investigation. In order to estimate the nanomechanical properties of the different phases of ZMA alloys [primary zinc (Zn phase) of ZMA -0 Ge, eutectic phase of ZMA - 0 Ge and Zn phase of ZMA-1.8 Ge], nanoindentation tests were performed to precisely measure the reduced elastic modulus (E_r) and hardness (H) values. In addition, Galv Zn and Galfan were also investigated.

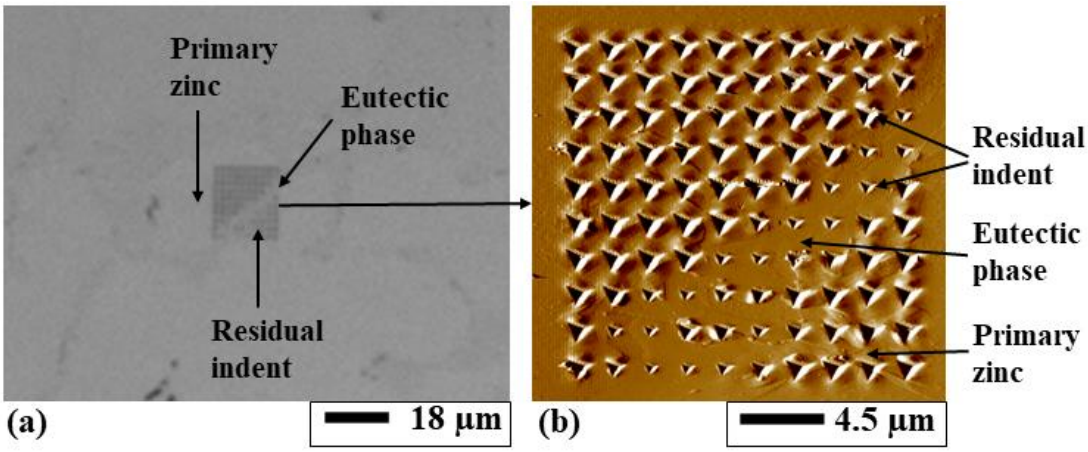

Figure 4.3: (a) Optical microscope image of ZMA – 0 Ge alloy showing primary zinc, eutectic phase and residual indents (b) AFM image of residual indents due to 500 µN maximum load on ZMA alloy.

The optical microscope and atomic force microscope (AFM) image of ZMA - 0 Ge alloy after the nanoindentation experiment is presented in Figure 4.3. Distinct triangular impressions of the nanoindenter after single loading with a maximum load of 500 µN are presented in Figure 4.3. The distance between indents was set at 3 µm, in order to prevent possible intersecting of plastic deformation zone onto nearby indents. The residual indents on the primary zinc phase appear larger in comparison to the eutectic phase. This difference in residual indents suggests there exists a difference in hardness between the primary zinc phase and the eutectic phase of ZMA alloy. Hence, indicating the eutectic phase is much harder compared to the Zn phase.

The load-depth (P-h) curves obtained after nanoindentation tests are divided into three different phases in accordance with the load shift. The first phase is the loading phase prior to the maximum indentation load is reached. During this loading phase, the elastic deformation gradually decreases, whereas the plastic deformation increases. The second phase is the dwelling phase where the maximum load is maintained for 5 seconds. This dwelling is presented as a short flat line at maximum load in Figure 4.4. The final is the unloading phase. The applied load is gradually lowered until it is entirely unloaded. The indentation deformation consists of elastic and plastic deformation during loading whereas pure elastic deformation during unloading [135].

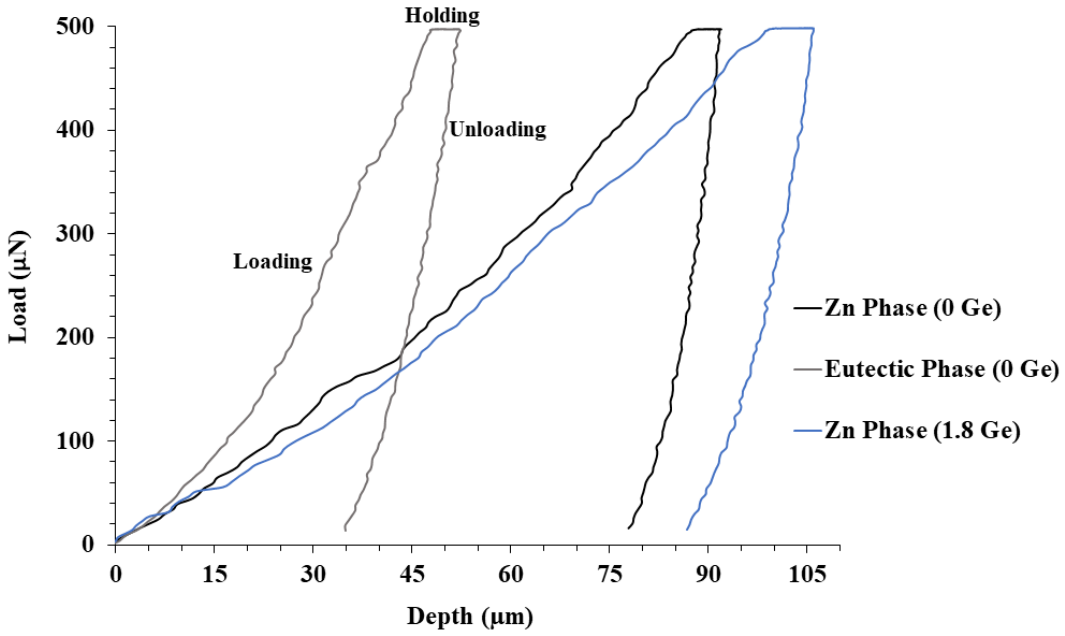

Figure 4.4: Load-depth (P-h) curves obtained from nanoindentation on the primary zinc phase of ZMA-0 Ge and ZMA- 1.8 Ge along with the eutectic phase of ZMA-0Ge.

Figure 4.4 demonstrates the (P-h) curves for the Zn phase of ZMA - 0 Ge (0 Ge) & ZMA - 1.8 Ge (1.8 Ge) and eutectic phase of 0 Ge. In the case of 0 Ge, the eutectic phase P-h curve has shifted to the left direction relative to the Zn phase. Also, for the eutectic phase, an appreciable decrease in the depth of penetration and an increase in the slope of the loading stage is observed. This shift of the P-h curve toward the left direction, decrease in the penetration depth and increase in loading curve slope indicates an increase in hardness for the eutectic phase compared to the Zn phase.

In the case of 1.8 Ge, the addition of 1.8 wt. % of germanium (Ge) has shifted the P-h curve of the Zn phase to the right direction relative to the Zn phase of 0 Ge. It is also observed that the slopes of the loading stage of the Zn phase of 0 Ge and 1.8 Ge are indistinguishable at the beginning but as the load increases (> 50 μN) the slope of the Zn phase of 1.8 Ge decreases subsequently achieving a higher depth of penetration. Therefore, the addition of 1.8 wt. % of Ge indicates the reduction in hardness of the Zn phase.

Figure 4.5 demonstrates the (P-h) curves Zn phase of 0 Ge & 1.8 Ge, eutectic phase of 0 Ge, Galv Zn and Galfan. The obtained P-h curves of Galv Zn and Galfan are similar to that of the Zn phase of 1.8 Ge.

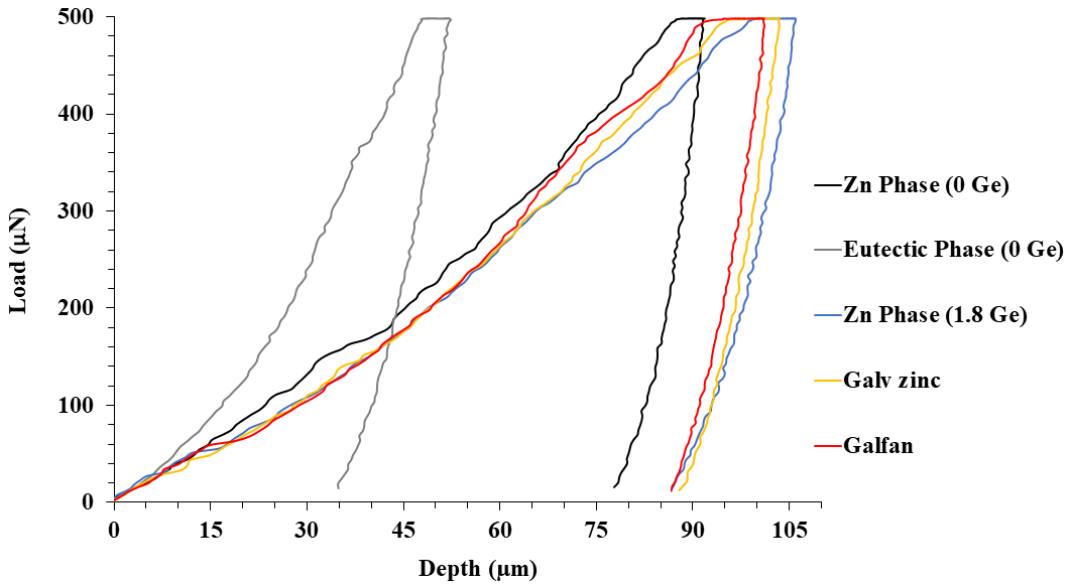

Figure 4.5: Load-depth (P-h) curves obtained from nanoindentation for the primary zinc phase of ZMA - 0 Ge and ZMA - 1.8 Ge, the eutectic phase of ZMA- 0Ge, Galv zinc and Galfan.

Table 4.2, presents the reduced elastic modulus (E_r), hardness (H), maximum depth (Max depth) and contact depth values obtained from the load-depth curves. The errors shown are based on the standard deviation of five indentation measurements. The E_r for Zn phase of 0 Ge, eutectic phase of 0 Ge, Zn phase of 1.8 Ge, Galv Zn and Galfan are 113.02 GPa, 125.92 GPa, 78.07 GPa, 89.92 GPa and 93.22 GPa respectively. Similarly, the H values for Zn phase of 0 Ge, eutectic phase of 0 Ge, Zn phase of 1.8 Ge, Galv Zn and Galfan are 1.96 GPa, 4.55 GPa, 1.65 GPa, 1.34 GPa and 1.93 GPa respectively.

Galv Zn which contains 0.2 wt. % Al has H value of 1.34 GPa. Addition of 5 wt. % of Al (Galfan) has increased the H value by 44.03 % to 1.93 GPa. Similarly, the addition of 1.6 wt. % of Mg and 1.6 wt. % of Al (ZMA- 0 Ge) has also increased the H value of the Zn phase by 46.27 % to 1.96 GPa.

In the case of 0 Ge, the E_r and H of the eutectic phase are 11.41 % and 132.14 % higher compared to the Zn phase whereas, the addition of 1.8 wt % of Ge has had a positive impact in terms of reducing the E_r and H of Zn phase. The 1.8 wt % of Ge additions has diminished the E_r and H of the Zn phase by 30.92 % and 15.81 % compared to the Zn phase of 0 Ge.

Table 4.2: Reduced elastic modulus and hardness values obtained after nanoindentation tests.

	Zn phase (0 Ge)	Eutectic phase (0 Ge)	Zn phase (1.8 Ge)	Galv Zn	Galfan
Reduced Elastic Modulus (E_r)(Gpa)	113.02 ± 2.46	125.91 ± 10.82	78.07 ± 6.37	89.92 ± 4.02	93.22 ± 4.93
Hardness (H) (Gpa)	1.96 ± 0.10	4.55 ± 1.17	1.65 ± 0.15	1.34 ± 0.27	1.93 ± 0.04
Max Depth (µm)	89.82 ± 2.24	61.08 ± 7.11	100.68 ± 4.94	124.32 ± 13.18	101.96 ± 1.18
Contact Depth (µm)	84.01 ± 2.45	53.23 ± 7.47	92.95 ± 4.67	118.30 ± 13.80	94.96 ± 1.14

4.4 Small Punch Test

4.4.1 Pre-corrosion Small Punch Tensile Test

Small Punch Tensile (SPT) test has been employed to evaluate the mechanical performance of alloys with various (0.19 - 1.8 wt.%) additions of germanium, Galv Zn and Galfan. The sample preparation procedure for the SPT is explained in section 2.8.3. SPT results, load-displacement (P-u) curves obtained are presented in Figure 4.6. Significant differences can be observed between the responses of the different materials.

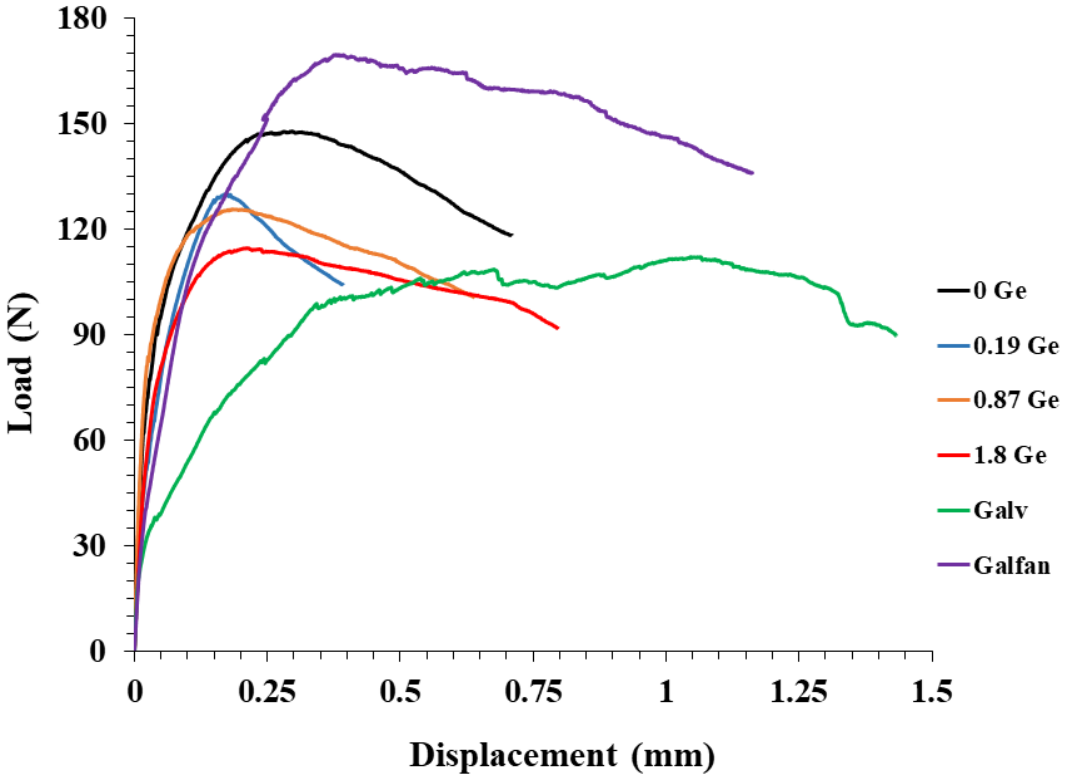

Figure 4.6: Load-displacement curves of the SPT test conducted at room temperature at a displacement rate of 0.5 mm.min^{-1} for ZMA-Ge alloys along with Galv Zn and Galfan.

The maximum load (P_m) and displacement at maximum load (u_m) can easily be obtained from the P- u curve. The elastic-plastic transition point (yield point, P_y) is not clearly defined as yielding occurs successively in different areas of the specimen during the test [126]. Different methods of determining P_y are found in the literature [126], [136]. Here, we use the method proposed by Mao and Takahashi [128] where P_y is defined as the intersection of two tangents outlining the elastic regime (zone I) and the plastic regime (zone II). Figure 4.7 illustrates the method used to define the

P_y along with the other different SPT test characteristic points. Characteristic points Pm, Py, u_m and displacement at P_y (u_o) of all the materials are presented in Table 4.3.

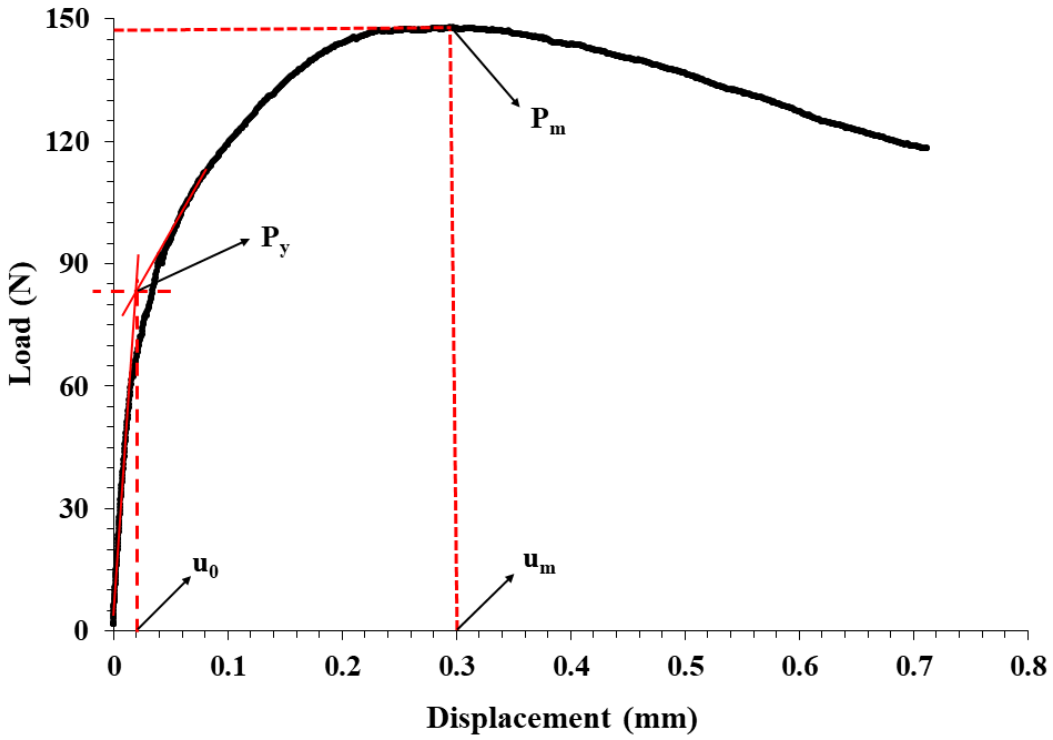

Figure 4.7: Load-displacement curve for 0 Ge with different SPT test characteristic point along with the method used to determine P_y.

Table 4.3: Characteristic points for different test specimens.

Sample	P_m (N)	u_m (mm)	P_y (N)	u_o (mm)	u_m-u_o (mm)
0 Ge	147.82	0.30	83	0.02	0.28
0.19 Ge	130.04	0.17	42	0.01	0.16
0.87 Ge	125.67	0.18	81	0.01	0.17
1.8 Ge	114.84	0.21	66.5	0.02	0.19
Galv Zn	112.20	1.04	97	0.02	1.02
Galfan	169.70	0.38	45	0.04	0.34

Figure 4.6 and Table 4.3 demonstrates that among commercially available metallic coatings investigated, Galv Zn has shown the superior deformation with 1.04 mm displacement and 0 Ge has the weakest response to deformation, with an achieved displacement of 0.30 mm at its P_m. However, Galfan has the highest P_m value with 169.7 N and Galv Zn has the lowest P_m value with 112.2 N.

Among the ZMA-Ge alloys, 0 Ge exhibited the superior deformation with 0.30 mm displacement and 0.19 Ge the least with 0.17 mm displacement. The addition of a small amount of Ge (0.19 wt.%) in ZMA has significantly reduced the displacement from 0.30 mm to 0.17 mm at P_m however further higher addition of Ge had minimal impact on their displacement, with 0.18 mm and 0.21 mm for 0.87 and 1.8 Ge respectively at P_m.

It can be seen that during the early stages of the tests up to the yield stress point (P_y), the plots for all the tests are relatively comparable however it is the plastic deformation region and membrane stretching region of the test that difference could be identified. The P-u curves of 0 Ge and 0.87 Ge display the steepest gradient before the significant shallowing of the gradient. In comparison to 0 Ge, the 1.8 Ge displays a relatively less steep gradient in the plastic deformation and membrane stretching section and the gradient shallowed much earlier. The shallowing of the gradient is attributed to the onset of cracking in the specimen and the higher P_m is an indication of higher resistance to the onset of cracking [137]. Among the ZMA-Ge alloys, the P_m decreases gradually with an increase in Ge concentration. The result shows P_m in the order 0 Ge > 0.19 Ge > 0.87 Ge > 1.8 Ge.

The formability of material is associated with the plastic deformation region on a tensile test curve and it can be represented in terms of displacement as the difference between displacement at u_m and u_0. The u_m - u_0 for all the investigated materials are presented in Table 4.3. Among the three commercial available metallic coatings; Galv Zn, Galfan and ZMA-0 Ge (MagiZinc) Galv Zn has demonstrated the best formability and outperformed the other two. Galfan and ZMA-0 Ge demonstrated similar formability. The displacement of Galv Zn is three times the displacement of Galfan the second-best and ~ four times the ZMA- 0 Ge.

A small addition of Ge (0.19 wt.%) reduced the displacement by almost half from 0.28 mm for 0 Ge to 0.16 mm. The addition of 0.87 wt.% of Ge seems to slightly improve the displacement in comparison to 0.19 Ge from 0.16 mm to 0.17 mm. Further, increase in Ge addition to 1.8 wt. % achieved a displacement of 0.19 mm. The higher Ge addition alloys performed better than the low Ge additions.

4.4.2 Post-corrosion Small Punch Tensile Test

The post corrosion mechanical performance of ZMA - Ge alloys, Galv Zn and Galfan were also investigated. To do so the test ready samples were immersed in 0.17 M NaCl pH 7 solution for 24 hours before performing SPT tests. Post corrosion SPT test results load-displacement (P-u) curves and characteristic points Pm, Py, u_m and u_o of all the materials are presented in Figure 4.8 and Table 4.4 respectively.

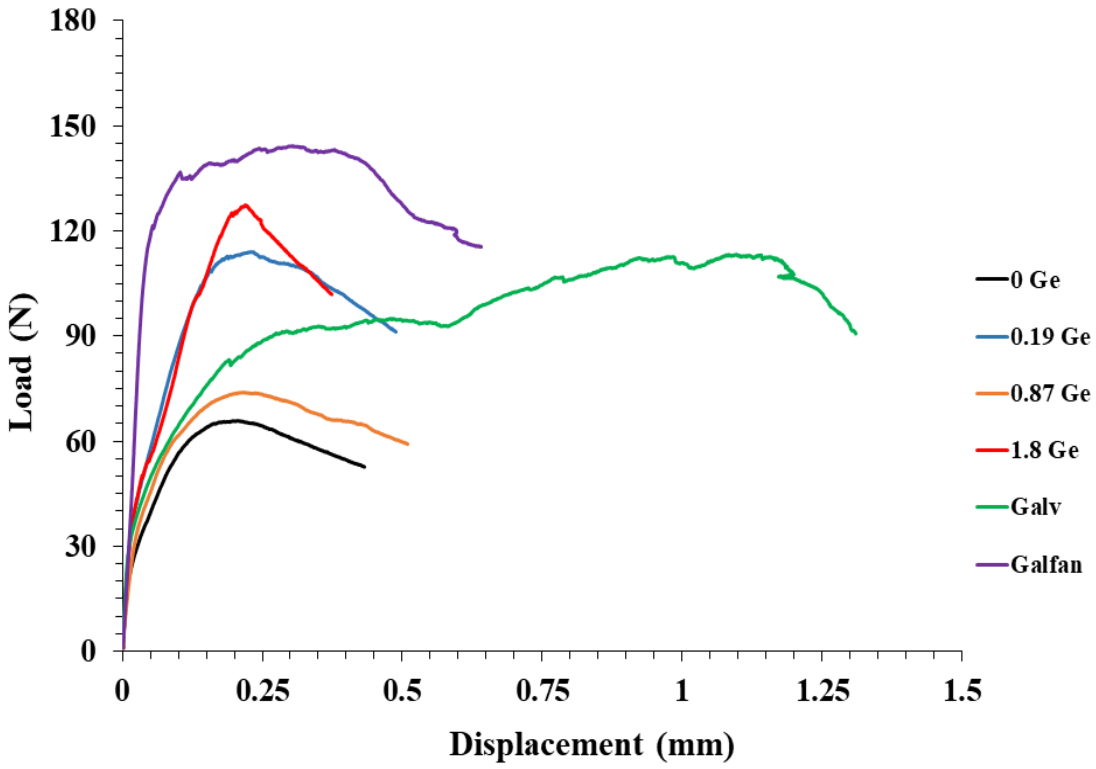

Figure 4.8: Load-displacement curves of SPT tests conducted at room temperature at a displacement rate of 0.5 mm.min^{-1} after immersion in 0.17 M NaCl pH 7 solution for 24 hours for ZMA-Ge alloys along with Galv Zn and Galfan.

Immersion in 0.17 M NaCl pH 7 solution for 24 hours has had a significant reduction in strength of material except for Galv Zn which has maintained its structural integrity (Table 4.3). Similar to the pre-corrosion investigation among the commercially available metallic coatings, Galv Zn has exhibited superior displacement with 1.10 mm at P_m and 0 Ge exhibited the weakest response to displacement with 0.21 mm at P_m. However, Galfan has the highest P_m value with 144.4 N and ZMA - 0 Ge has the lowest P_m value with 65.9 N.

Among the ZMA-Ge alloys, all four alloys exhibited similar displacement at P_m. 0.19 Ge and 0.87 Ge have the weakest response to deformation, with an achieved displacement of 0.21 mm at its P_m. The addition of a varying amount of Ge has had a minimal impact on the alloys response to displacement at P_m. No particular trend is observed between the Ge content and its impact on the P_m of the ZMA – Ge alloys.

Table 4.4: Characteristic points for different test specimens after immersion in 0.17 M NaCl pH 7 solution for 24 hours

Sample	P_m (N)	u_m (mm)	P_y (N)	u_o (mm)	u_m-u_o (mm)
0 Ge	65.9	0.21	24	0.01	0.20
0.19 Ge	113.9	0.23	35.5	0.01	0.22
0.87 Ge	73.8	0.21	37	0.02	0.19
1.8 Ge	127.2	0.22	39	0.03	0.19
Galv Zn	113.4	1.10	48.5	0.02	1.08
Galfan	144.4	0.30	116	0.04	0.26

Similar to the pre-corrosion study Galv Zn has demonstrated superior plastic deformation in comparison to all investigated samples with a displacement of 1.08 mm. Galfan has the second-best plastic deformation with 0.26 mm of displacement followed by the 0.19 Ge with 0.22 mm. The displacement of Galv Zn is four or more times greater compared to Galfan and 0 Ge. Among the ZMA- Ge samples, all four alloys demonstrated similar plastic deformation with 0.19 Ge gaining 0.02 mm more displacement compared to 0.87 Ge and 1.8 Ge.

4.5 Discussion:

The change in hardness of different alloys present in Table 4.1 and 4.2 can be explained by solid solution strengthening and grain- boundary strengthening theory. As shown in Table 4.1, the microhardness (H_V) of the Galv Zn increased with the addition of 1.6 wt. % of Mg and Al (ZMA- 0 Ge) from 51.60 to 88.03. The addition of Mg and Al leads to the formation of eutectic phases; binary (Zn and $MgZn_2$) and ternary (Zn, $MgZn_2$ and Al) around the Zn phase (Figure 3.1). These eutectic phases behave as holding points and obstruct dislocation movement [138]. Therefore, more energy is required for dislocations to move to the adjacent phase and consequently disrupting the dislocation movement in a continuous slip plane.

The addition of 1.6 wt.% Mg & 1.6 wt.% Al (ZMA-0 Ge) has also increased the nano hardness from 1.34 GPa of Galv Zn to 1.96 GPa for the Zn phase of ZMA - 0 Ge. Though limited there is some dissolution of Mg and Al into zinc matrix. The solubility of Mg and Al zinc are presented in Table 4.5 [139], [140]. The Mg and Al atoms present within the crystalline lattices of the Zn phase of ZMA - 0 Ge interrupt the regularity of the crystal lattice. The movement of the dislocations is interrupted or prevented by these irregularities and therefore requires higher stress or thermal energy to overcome irregularities consequently increasing the hardness.

Table 4.5: Solubility of magnesium and aluminium in zinc matrix.

Temperature ^{o}C	**Mg, wt.%**
364	0.1
	Al, at.%
RT	0.07

The microhardness of the ZMA- Ge alloys decreased as the Ge addition increased (Table 4.1). This softening can be explained due to the changes in the microstructure. Due to the high affinity of Ge to Mg, the addition of Ge has led to the formation of the Mg_2Ge phase (Figure 3.2). As the addition of Ge increases the area of eutectic phases which consists of intermetallic $MgZn_2$ decreases (Table 4.1). Hence, contributing to the microhardness softening.

The addition of Ge to ZMA alloy has indicated the improvement of the formability as a decrease in the hardness was observed during the Vicker Hardness test, however, in contrast, SPT tests demonstrated a decrease in the plastic deformation thus the formability. The improvement observed during the Vicker Hardness test could be due to the decrease in area % of the brittle eutectic phase with an increase in Ge concentration and also on average indents hits more of Zn matrix per unit area. However, SPT tests showed a reduction in formability and it could be due to the substitution of intermetallic $MgZn_2$ by another intermetallic Mg_2Ge which could potentially act as crack nucleators during the SPT test. Furthermore, even in ZMA - 1.8 Ge, the eutectic phase is not entirely substituted and some eutectic phase is still present. This presence of the residual eutectic phase could have a significant impact on the alloy plasticity as cracks could initiate and propagate off them.

4.6 Conclusion:

Combination of miniature testing techniques; the Vicker Hardness test, Nano-indentation technique and Small Punch tensile test are used to investigate the mechanical properties of ZMA-Ge alloys, Galv Zn and Galfan. Among the commercially available hot-dip galvanising metallic coatings, ZMA - 0 Ge has the highest Vicker hardness value. The addition of Ge has led to a reduction in the hardness. The hardness of ZMA - Ge alloys reduced with an increase in the Ge addition with ZMA - 1.8 Ge displaying 18.78 % reduction in hardness compared to ZMA - 0 Ge.

In ZMA - 0 Ge, a significant difference was observed between the nano hardness of the Zn phase and eutectic phase, the eutectic phase is 2.3 times harder compared to the Zn phase. The addition of 1.8 wt. % Ge has decreased the hardness of the Zn phase of ZMA - 0 Ge by 31.63 %.

The addition of Ge into ZMA alloys has led to the reduction in plastic deformation and the strength of ZMA-Ge alloys. 1.8 wt. % of Ge addition decreased the plastic deformation and maximum force of ZMA-0 Ge alloy by 32.14 % and 22.31 % respectively.

Chapter 5 Use of Mg_2Si particles as corrosion inhibitors

5.1 Introduction

In Chapter 3, the effect of germanium (Ge) additions in terms of microstructure and corrosion resistance of ZMA alloy was investigated. Mg_2Ge phase formed within the microstructure of ZMA due to Ge addition corroded preferentially to zinc phase consequently enhancing the overall corrosion resistance of ZMA alloy. It was suggested that Mg_2Ge behaves as a magnesium (Mg) reservoir and therefore there is a potential that the Mg_2Ge could be integrated into metallic coatings as inhibitors. Previous investigations have revealed that the addition of silicon (Si) to Zn-6Al-3Mg [141], the addition of magnesium (Mg) to Al-Zn-Si [142] and the addition of zinc (Zn) and Mg together to Al-Si leads to the formation of intermetallic Mg_2Si phase. Corrosion experiments on these materials have proven to provide improved corrosion resistance. This improvement in corrosion resistance was attributed to the selective leaching of Mg from Mg_2Si protecting the surrounding matrix [143].

Therefore here, in this study, Mg_2Si particles are embedded into a zinc-rich powder-based galvanising system (ZINGA Zinc / Zn) as a source of Mg. This approach was adopted rather than the addition of Si to molten ZMA or Mg_2Si to molten Zn/Zn-Al in order to prevent Mg from taking part in the solidification process and avoiding the formation of Zn/Mg intermetallic such as $MgZn_2$ or Mg_2Zn_{11}. The effects of Mg_2Si particles were investigated using a combination of techniques. Scanning Vibrating Electrode Technique (SVET) was utilised to resolve corrosion features and evaluate relative corrosion performance and Time-lapse Microscopy (TLM) was used to understand the aqueous in-situ corrosion mechanism. The investigation was supported by open-circuit potential measurements. Additionally, the corrosion driven cathodic delamination of the zinc-rich powder-based galvanising system and the effect of Mg_2Si on cathodic delamination (CD) is also investigated with the help of Scanning Kelvin Probe (SKP). Investigations on zinc alloys with magnesium additions have demonstrated to profoundly diminish the CD rate [144], [145]. The Mg-rich Zn surfaces stop the CD by lowering the potential of the organic coated metal to a value similar to that of the bare metal in the defect region.

5.2 Sample production:

Low carbon steel substrate 0.8 mm in thickness obtained from TATA Steel UK was cut into 2 cm x 2 cm and 5 cm x 5 cm coupons. The coupons were ground to a European grade P80 finish using abrasive silicon carbide (SiC) paper followed by cleaning with ethanol and deionised water. The prepared coupon surface was sprayed by ZINGA Zinc (Zn) and dried for a half-hour, Mg_2Si particles obtained from Sigma-Aldrich were manually sprayed on a semi-solid ZINGA layer then another layer of ZINGA Zinc was sprayed on top. The coupons were then allowed to dry at room temperature. ZINGA Zinc is a Zn rich powder-based galvanising system that contains 96% Zinc powder in the dry film. The schematic of the sample production process is presented in Figure 5.1.

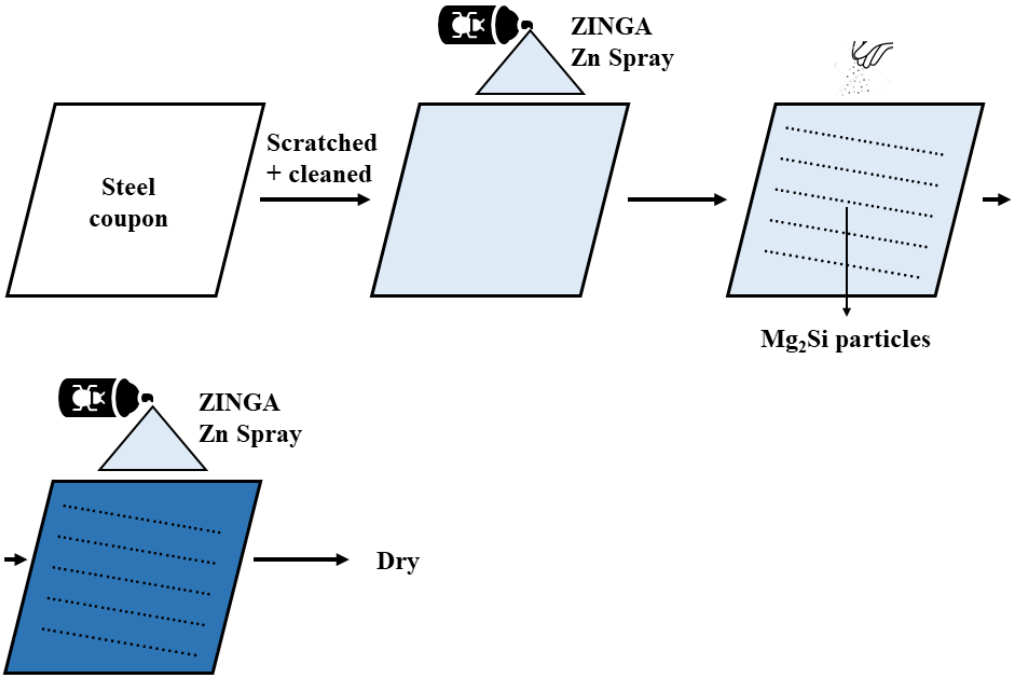

Figure 5.1: Schematic representation of production process of ZINGA Zinc-Mg_2Si samples.

5.3 Study of the microstructure of the zinc-rich powder-based galvanising system

SEM image along with EDS analysis of the ZINGA Zinc (Zn) is displayed in Figure 5.2. The image clearly shows distinct zinc particles held together by a binder. The EDS analysis showed ZINGA Zn contains 99.23 wt.% Zn. According to the

manufacturer [146], ZINGA Zn is made up of zinc powder, aromatic hydrocarbons and binder.

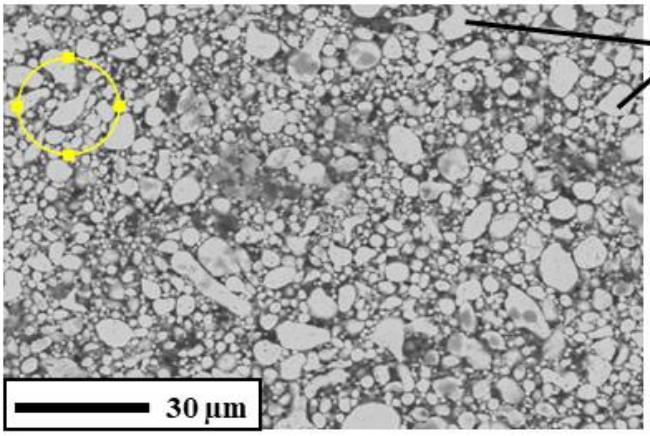

Element	Atom. C (wt. %)
Magnesium	0.00
Silicon	0.77
Zinc	99.23

Figure 5.2: SEM image with EDS analysis of the zinc-rich powder-based galvanising system.

An SEM image of Zn + Mg_2Si is presented in Figure 5.3. The microstructure of Zn + Mg_2Si consists of Mg_2Si particles entrapped in between zinc particles.

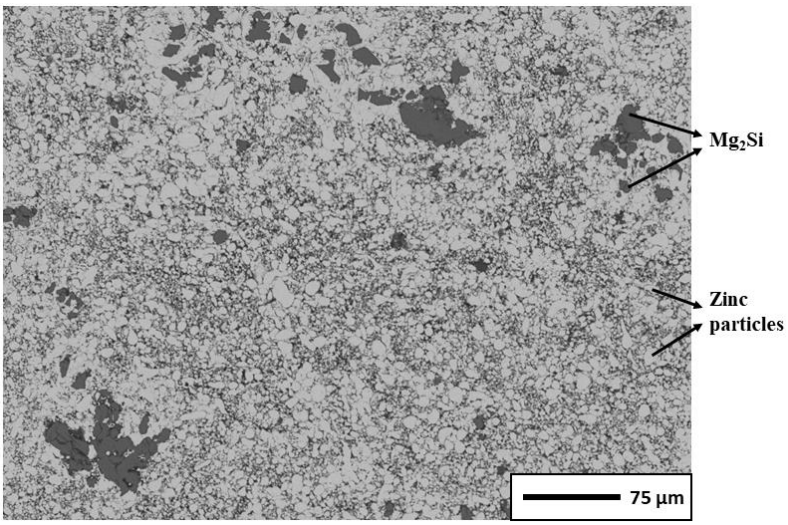

Figure 5.3: SEM image of Mg_2Si particles embedded in the zinc-rich powder-based galvanising system(Zinga Zn).

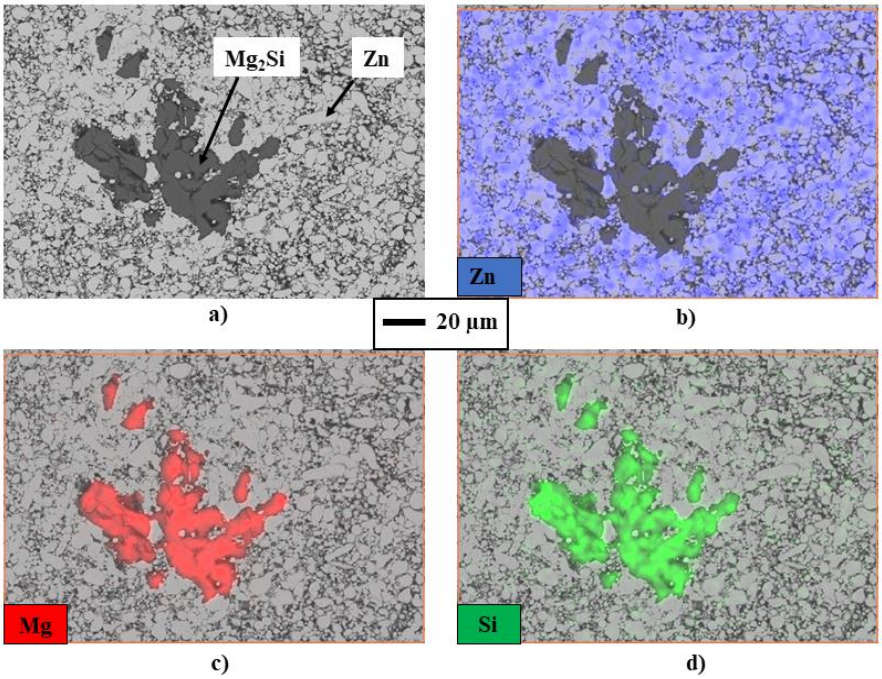

Figure 5.4: SEM images and colour maps for EDS elemental analysis for Zn-Mg_2Si.(a) SEM image of Zn-Mg_2Si surface (b) Distribution of Zn (c) Distribution of Mg (d) Distribution of Si.

The distribution of elements within Zn + Mg_2Si was identified using Energy Dispersive X-Ray Spectroscopy (EDS). Colour maps identifying the elements zinc (Zn), magnesium (Mg) and silicon (Si) were produced using SEM/EDS software and is presented in Figure 5.4 (b-d). The EDS analysis (Figure 5.4) confirms that the discrete particles surrounded and entrapped within the Zn particles matrix as Mg_2Si.

5.4 Investigation of corrosion behaviour using Scanning Vibrating Electrode Technique (SVET)

The SVET was used to investigate the corrosion of Zn and Zn + Mg_2Si samples surface over 24 hours in pH 7 0.17 M NaCl solution, as described fully in section 2.4. The resulting surface normal current density maps have been plotted, also the estimated metal loss over 24 hours was calculated. As Zn is the predominant element in both samples, Zn was selected during the metal loss calculations. During the corrosion of Zn + Mg_2Si, both Zn (Zn^{2+}) and Mg (Mg^{2+}) are likely to participate and it is difficult to predict the contribution of individual species for metal loss. However, due to the identical charge associated with each ion the relative metal loss value would be directly comparable across the specimens irrespective of the element selected. The SVET derived metal loss in this investigation is used to compare the

relative corrosion performance among samples, the metal loss does not represent an exact metal loss for a 24-hour experiment period. Besides metal loss, SVET data could be used to plot normal current density maps which provide a visual representation of the location and intensity of anodic and cathodic activities as recorded by the SVET probe. Red and blue colours are indicative of anodic and cathodic activities respectively. The average surface area percentage of Mg_2Si present in the Zinga Zn surface used during the SVET experiments was 3.35 ± 1.62. The errors shown are based on the standard deviation of measurements of the three samples used during this investigation.

Figure 5.5 shows the normal current densities measured above the surface of the Zn and Zn + Mg_2Si samples freely corroding in pH 7 0.17 mol.dm^{-3} NaCl for 6 hours, 12 hours, 18 hours and 24 hours. In both the samples, the corrosion is localized in nature and multiple point anodes are well established by 6 hours of immersion. The intensity and radius of these focal anodes grow and diminish with time. However, for both samples, the overall anodic and cathodic activities remain constant between 6-24 hours. Peak anodic current densities of approximately 6 A.m^{-2} are recorded.

Figure 5.6 represents the normal current densities measured above the surface of the Zn and Zn + Mg_2Si freely corroding in pH 7 0.17 mol.dm^{-3} NaCl for 1 minute, 1 hour, 2 hours and 3 hours. A significant difference in the SVET measured normal current densities is observed between Zn and Zn + Mg_2Si. Peak anodic current densities of approximately 100 A.m^{-2} and 6 A.m^{-2} are recorded for Zn and Zn + Mg_2Si respectively. In the case of Zn, focal anodic sites are established from the onset and the intensity of anodes diminishes with time, however, in the case of Zn + Mg_2Si the anode are of lower intensity compared to Zn and the anodic and cathodic activities remain constant throughout.

Figure 5.7(a) shows an optical image of the Zn + Mg_2Si surface and Figure 5.7 (b-h) represents the normal current densities measured above the surface of the Zn + Mg_2Si freely corroding in pH 7 0.17 mol.dm^{-3} NaCl for up to 3 hours measured at an interval of 30 minutes. The corrosion is highly localised and intense anodic activities are recorded from the onset of the experiment (Figure 5.7 (b)). The peak anodic current densities of approximately 3 A.m^{-2} are recorded. The anodes observed immediately on immersion coincide exactly with the location of the Mg_2Si

agglomerates. Hence, Mg_2Si particles act as the sites of anodic activities and sacrificially to the remainder of the Zn surface. With time the anodic activities/current emerging from the Mg_2Si agglomerates decreases as a result of progressive dealloying of the Mg_2Si. This selective attack of Mg_2Si and release of Mg^{2+} ions will probably provide some inhibition of corrosion.

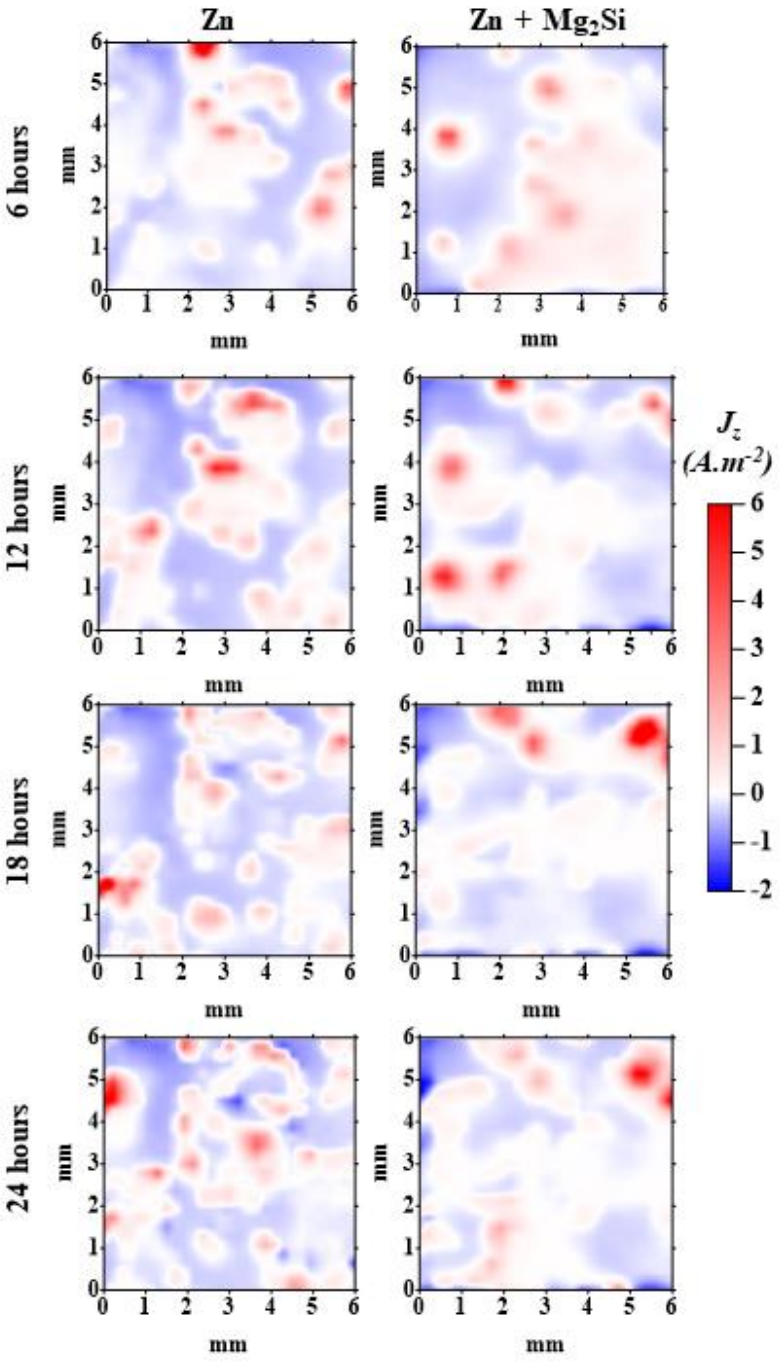

Figure 5.5: SVET false colour maps representing normal current density measured above Zn and Zn + Mg_2Si immersed in pH 7 0.17 M NaCl.

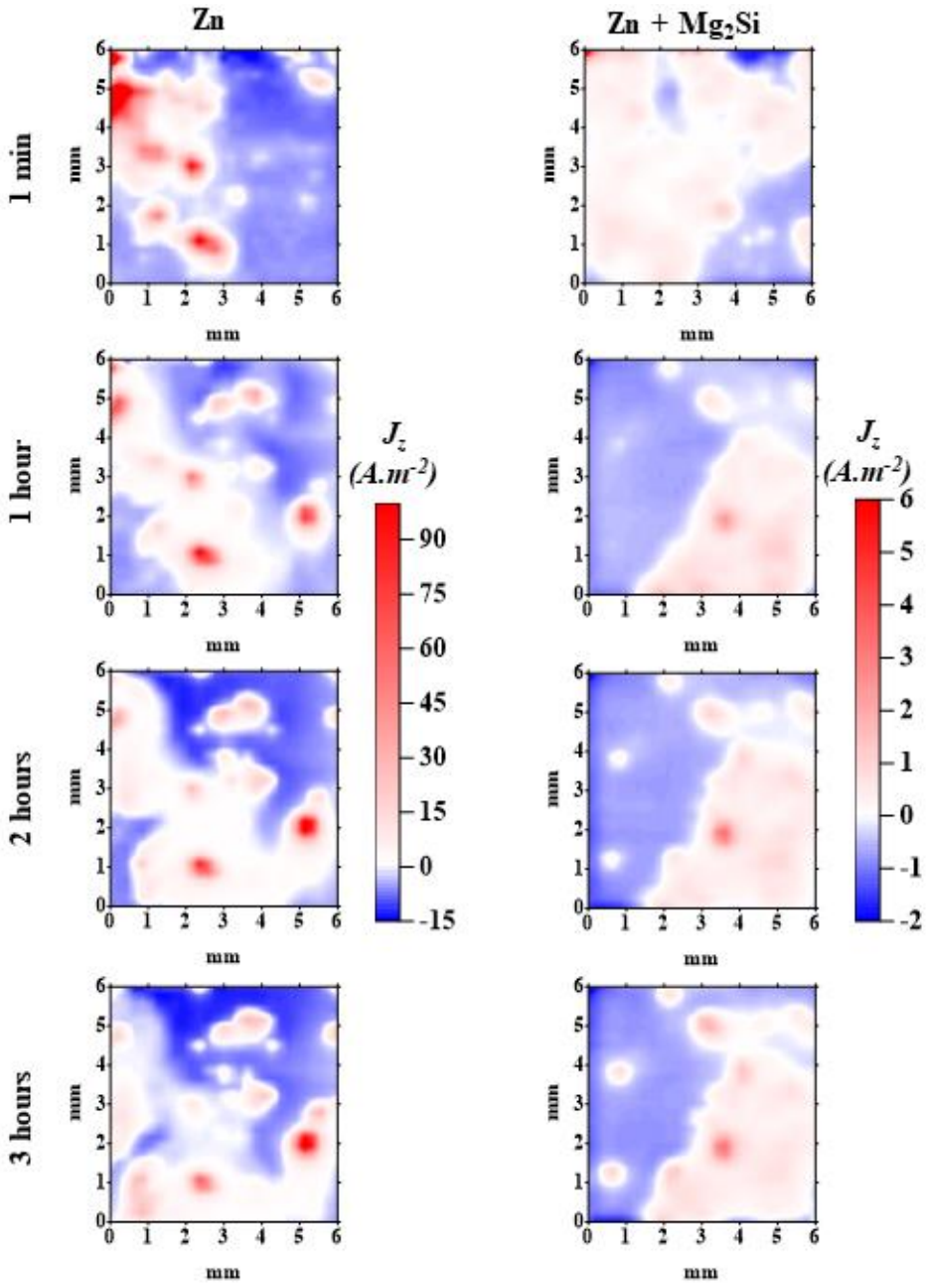

Figure 5.6: SVET false colour maps representing normal current density measured above Zn and Zn + Mg_2Si immersed in pH 7 0.17 M NaCl for up to 3 hours.

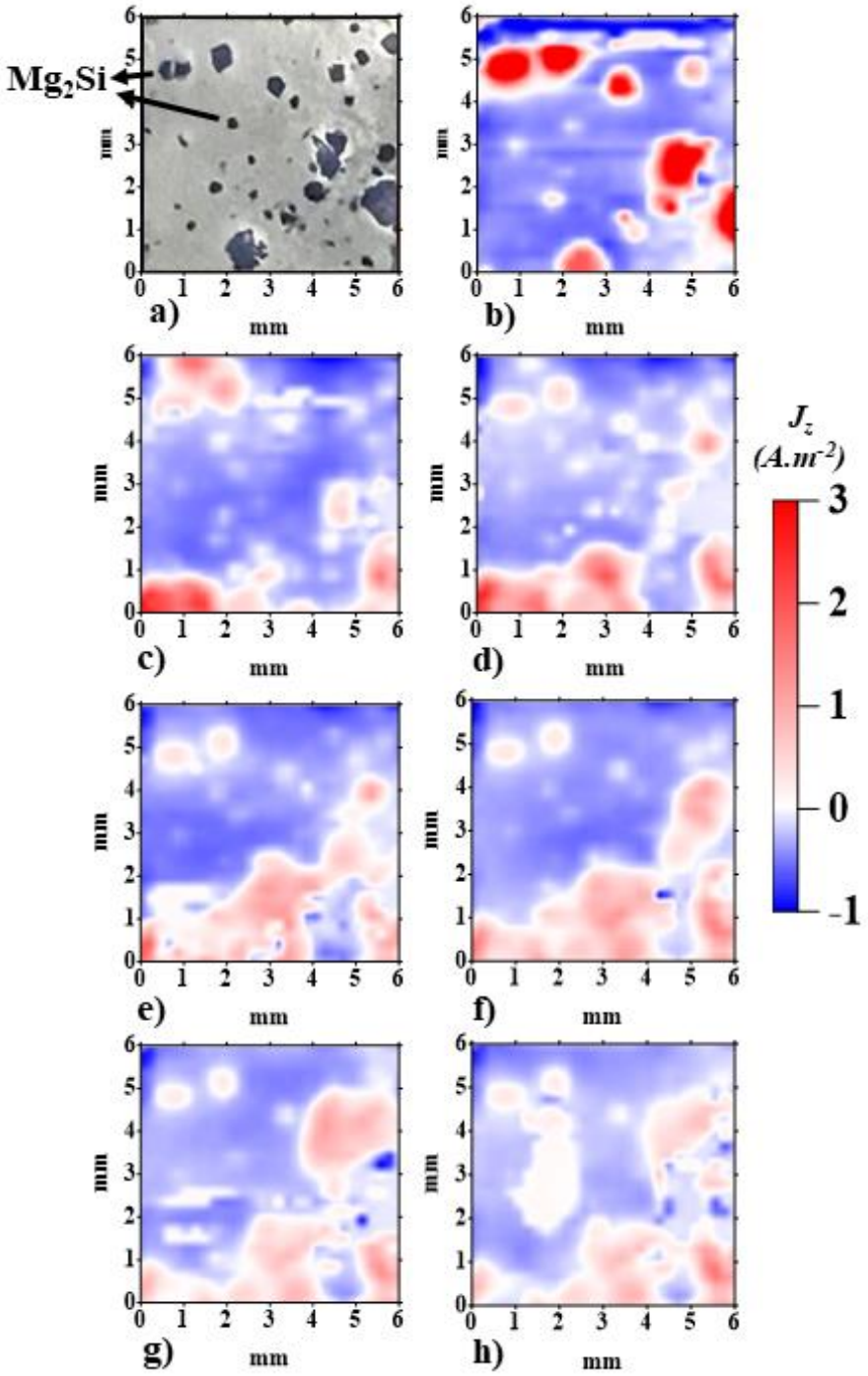

Figure 5.7: SVET false colour maps representing normal current density measured above Zn + Mg_2Si immersed in pH 7 0.17 M NaCl for up to 3 hours;(a) Zn + Mg_2Si sample surface (b) 1min (c) 30 minutes (d) 1hour (e) 1.5 hours (f) 2 hours (g) 2.5 hours (h) 3 hours.

The SVET derived metal loss for both Zn and Zn + Mg_2Si after immersion on pH 7 0.17 M NaCl for 24 hours are shown in Table 5.1. The errors shown are based on the standard deviation of three measurements. The derived metal loss for Zn + Mg_2Si is 6.86 $g.m^{-2}$ compared to 23.60 $g.m^{-2}$ for Zn. The addition of Mg_2Si particles exhibited a decrease in the measured metal loss by 70 % compared to that of Zn. Therefore, suggest a pronounced increase in corrosion performance of Zn + Mg_2Si compared to Zn.

The SVET derived hourly metal loss (average of three measurements) as a function of time for both Zn and Zn + Mg_2Si during immersion on pH 7 0.17 M NaCl for 24 hours are shown in Figure 5.8. For the first three hours, there is a significant difference in the metal loss between the two different samples similar to the SVET measured normal current densities observed in Figure 5.6. Zn exhibits at least three times more metal loss compared to Zn + Mg_2Si. However, from the fourth hour onwards the metal losses for both Zn and Zn + Mg_2Si are similar and to some extent identical up till the 16^{th} hour. For Zn, the initial scan i.e 1 minute (beginning of the experiment),1 Hr, 2 Hr and 3 Hr metal loss is 7.20 $g.m^{-2}$, 5.23 $g.m^{-2}$, 2.52 $g.m^{-2}$ and 2.44 $g.m^{-2}$ respectively. Thereafter the hourly metal loss is ~ 0.30 gm^{-2} throughout the experiment. The increased corrosion activity observed at the initial hours (0-3 hrs) of the experiment for Zn is not observed for Zn + Mg_2Si. The hourly metal loss of Zn + Mg_2Si is constant ~ 0.30 $g.m^{-2}$ throughout the experiment period.

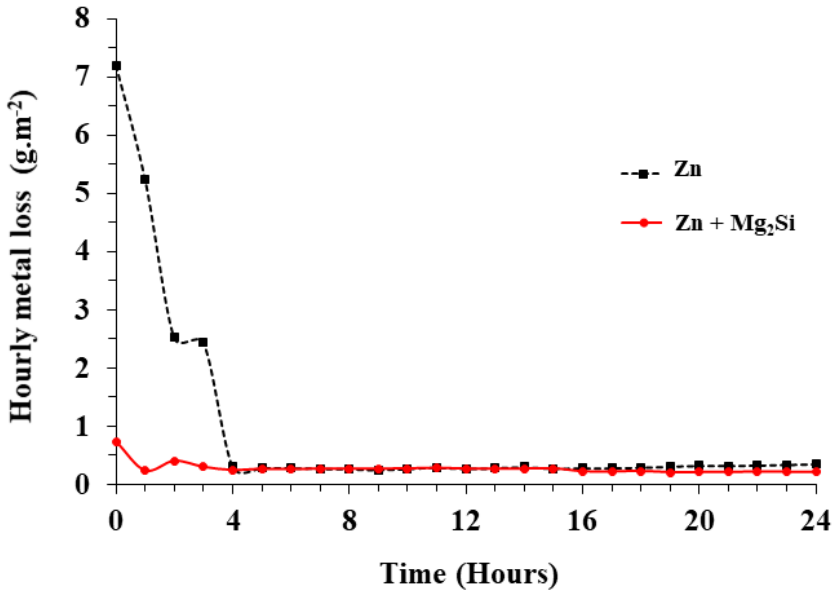

Figure 5.8: SVET derived hourly metal loss as a function of time for Zn and Zn + Mg_2Si after immersion in pH 7 0.17 M NaCl solution for 24 hours.

Table 5.1: SVET derived metal loss for Zn and Zn + Mg_2Si after immersion in pH 7 0.17 M NaCl for 24 hours

Sample	Metal loss ($g.m^{-2}$)
Zn	23.60 ± 4.56
Zn + Mg_2Si	6.86 ± 0.51

5.5 Electrochemical Measurements

Figure 5.9 shows the open circuit potential (OCP) of the Zn and Zn + Mg_2Si immersed in pH 0.17 $mol.dm^{-3}$ NaCl over 24 hour time period. In both cases, the initial potential is approximately -1.01 V vs SCE after which a shift to more negative potential is observed. The shift to negative potential is larger in Zn compared to Zn + Mg_2Si before stabilisation and the Zn + Mg_2Si consistently displays a more noble potential than Zn. The results exhibit both samples obtain some degree of stabilisation with time. However, Zn + Mg_2Si takes longer (~ 8 hours) compared to Zn (~ 4 hours). Zn stabilises at ~ -1.055 V vs SCE compared to ~ -1.05 V vs SCE for Zn + Mg_2Si.

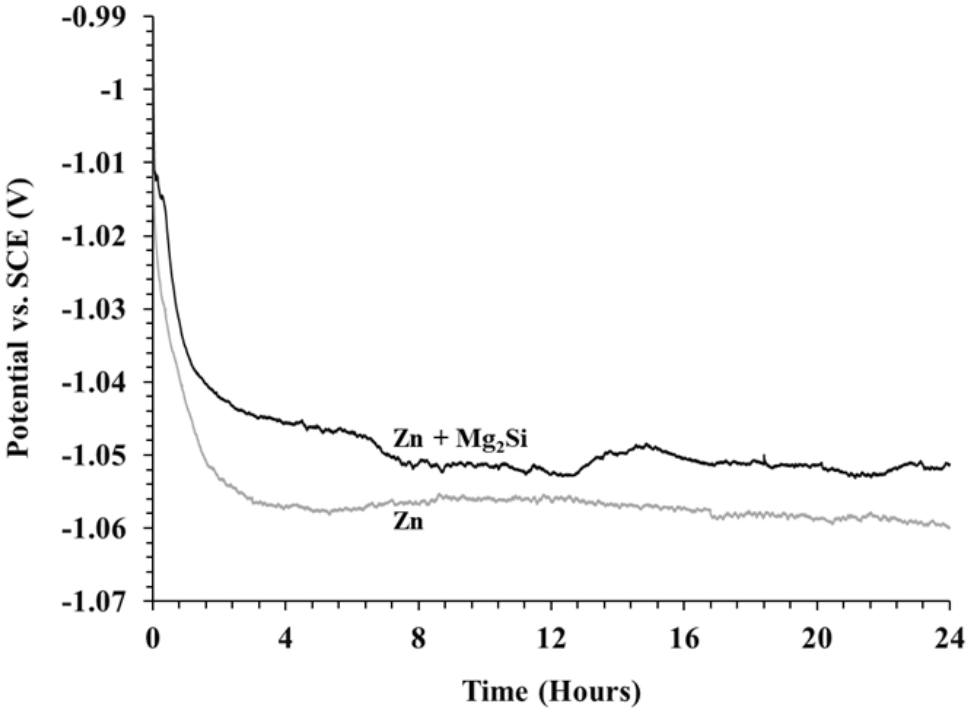

Figure 5.9: The time-dependent OCP for Zn and Zn + Mg_2Si immersed in pH 7 0.17 M NaCl for 24 hours.

5.6 Study of corrosion mechanism using Time-lapse microscopy (TLM)

The enhanced corrosion resistance provided by Zn + Mg_2Si observed during SVET experiments was further examined using TLM. TLM allows for the acquisition of microstructural corrosion mechanism information with respect to time. Figure 5.10 shows optical microscope images of the surfaces of Zn and Zn + Mg_2Si after various times of immersion in pH 7 0.17 M NaCl. The big dark blob present in the middle of the images for the Zn + Mg_2Si (Figure 5.10 (e-f)) is the Mg_2Si particle. The figure features the images captured at 2 minutes, 2 hours, 4 hours and 6 hours. It can be observed that in both cases multiple anodes initiates from the onset (see video V5 for Zn and V6 for Zn + Mg_2Si). As described in section 5.3 both the samples consist of numerous zinc particles held together by the binder. In both cases, in the early stage of the experiments, numerous anodes initiate and develop corrosion products are deposited at the edges of the exposed surfaces. In contrast, corrosion products were precipitated above the corroding area during the latter stage which becomes thicker with time. The 6 hours optical images of Zn and Zn + Mg_2Si presented in Figure 5.10 indicates some improvement in corrosion resistance of Zn + Mg_2Si compared to Zn due to the relatively fewer amount of corrosion products present above the corroding surfaces.

In order to investigate the effect of the addition of Mg_2Si particles into Zn, the corrosion of Mg_2Si particles within the Zn matrix was studied by completing EDS analysis prior to and following the immersion in pH 7 0.17M NaCl solution for 1.5 hours. Figure 5.11(a) presents an SEM image with EDS analysis of Mg_2Si prior to immersion in NaCl. The weight percentage of Mg, calculated using EDS is 61.11 wt. %. Figure 5.11(b) reveals the Mg content of the same Mg_2Si has dropped to 41.05 wt. % after 1.5 hours of immersion. This suggests that Mg^{2+} is preferentially released from these particles during the first hours of corrosion.

The effect of dissolution of Mg was further investigated by dosing the NaCl solution with 1 wt. % phenolphthalein. Phenolphthalein is an indicator that is colourless at pH values below pH 8 whereas turns pink above pH 8. Figure 5.12 and Figure 5.13 shows the TLM images of Zn and Zn + Mg_2Si surfaces respectively immersed in pH 7 0.17 M NaCl solution dosed with 1 wt. % phenolphthalein. Both the figures contains images at time intervals of 30 minutes between images until 4 hours because

on SVET metal loss experiments, it is the first four hours where a significant difference in hourly metal loss between the samples was observed as described in section 5.4.

In contrast to ZMA-0 Ge (Chapter 3, Figure 3.10) where the establishment of pH gradient (pH > 8 surrounding the cathodic sites and pH < 8 surrounding the anodic sites) was observed here for Zn (Figure 5.12 and Video V7), no such establishment of pH gradient is observed. This could be due to the establishment of multiple anodes all over the exposed surface. As the Zn^{2+} metal cations are released into the electrolyte, the hydrolysis of Zn^{2+} results in local acidification [133] and the absence of a large cathodic area where the production of OH^- occurs prohibits the formation of potential gradient as seen on ZMA-0 Ge (Figure 3.10).

In the case of Zn + Mg_2Si (Figure 5.13 and Video V8), the colourless electrolyte on onset turns pink across the entire exposed surface after 30 minutes (Figure 5.13(a)) indicating a pH value greater than 8. This high pH is maintained until 4 hours (Figure 5.13(h)). However, with time the pink colour of the electrolyte fades away. This phenomenon is well captured in Video V8.

The increase in pH is likely due to the preferential release of Mg^{2+} metal cations from Mg_2Si particles due to galvanic effects. Mg^{2+} cations will not readily hydrolyse in contrast to Zn^{2+} metal cations and the subsequent production of OH^- due to cathodic activities leads to an increase in pH in the early hours of the experiment where galvanic protection of Zn is offered. Although there is also the release of Zn^{2+} metal cations the local acidification due to hydrolysis of $Zn^{2+}$is not visible. This might be as the amount of Mg^{2+} metal cations present in the electrolyte is significantly higher in comparison to Zn^{2+} metal cations.

In video V8, it is also observed that the increase and decrease of pH of the electrolyte are periodic (flashing effect). This effect could be due to the shift/change in the location of the active anodic site.

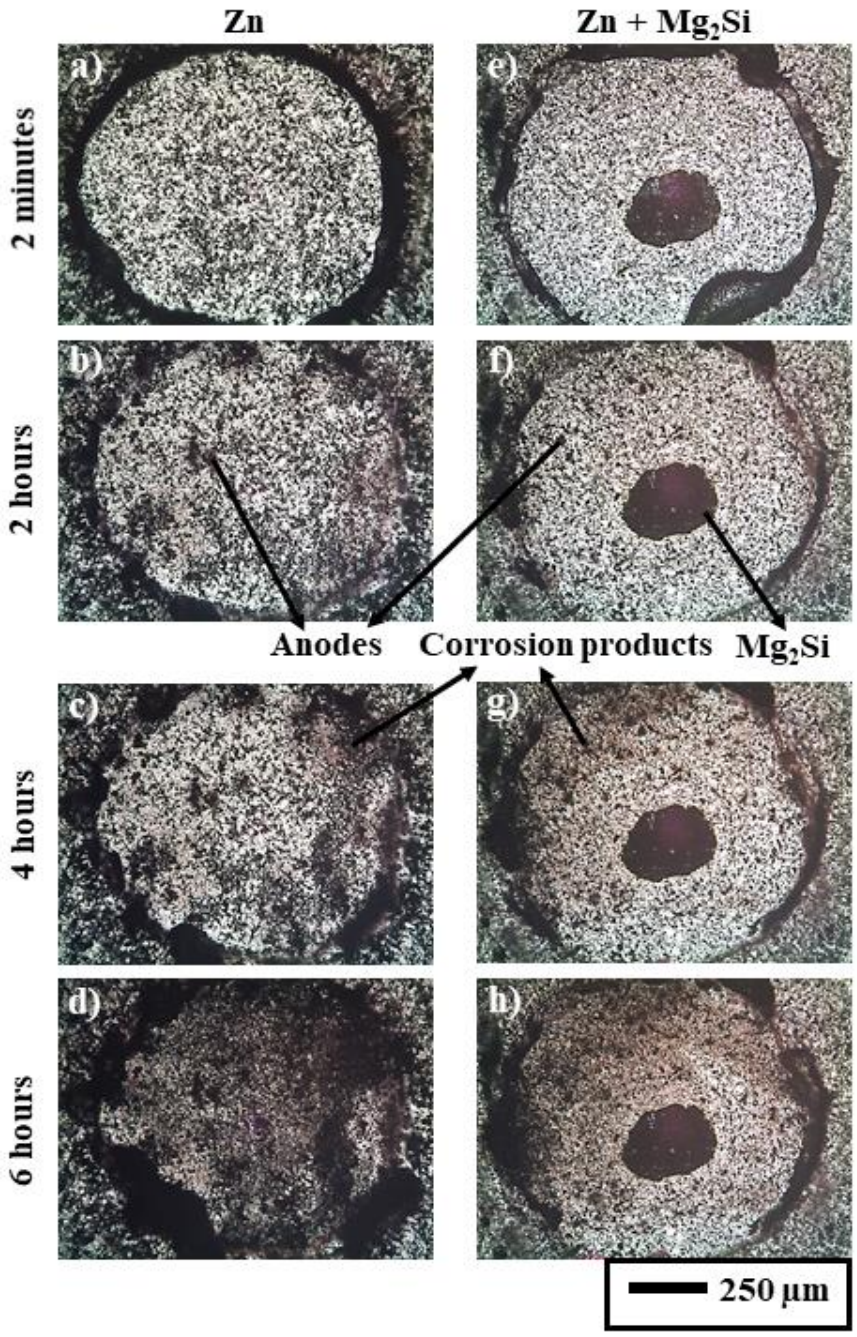

Figure 5.10: Optical microscope images of Zn and Zn + Mg_2Si surface taken in situ under immersion in pH 7 0.17 M NaCl.

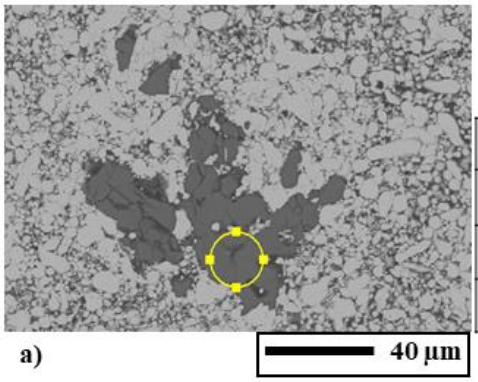

Element	Norm. C (wt.%)
Magnesium	61.11
Silicon	38.55
Zinc	0.34

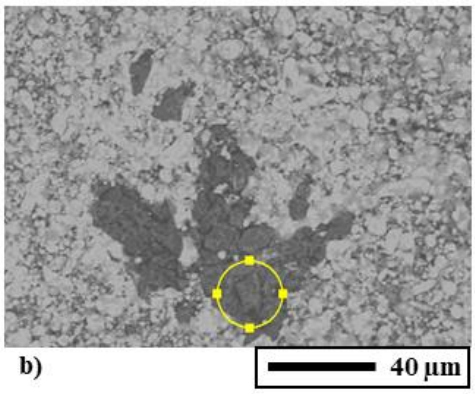

Element	Norm. C (wt.%)
Magnesium	41.05
Silicon	31.60
Zinc	27.34

Figure 5.11: SEM image of Zn + Mg_2Si surface with EDS analysis of an individual Mg_2Si particle obtained (a) prior to and (b) after 1.5 hours of immersion in pH 7 0.17 M NaCl.

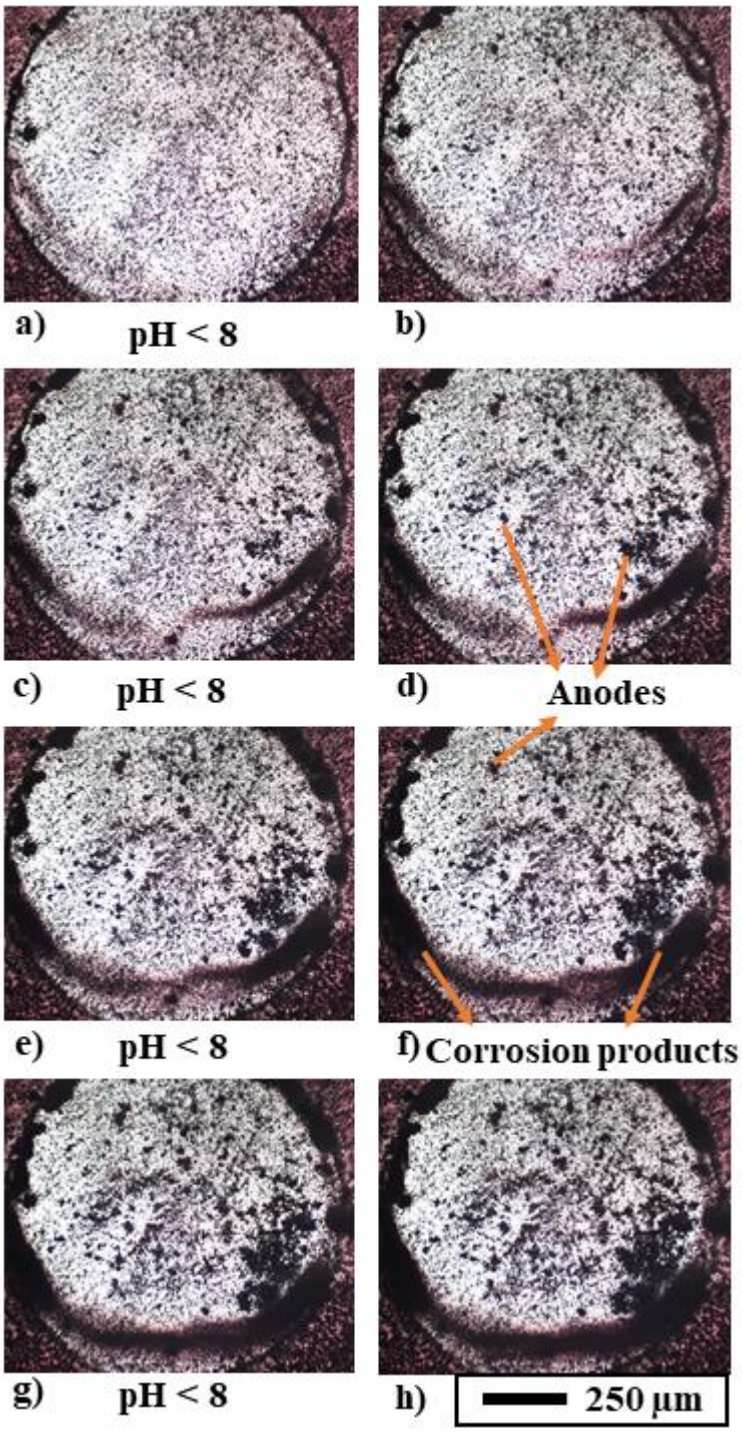

Figure 5.12: Optical microscope image of Zn surface after (a) 30 minutes (b) 1 hour (c) 1.5 hours (d) 2 hours (e) 2.5 hours (f) 3 hours(g) 3.5 hours (h) 4 hours immersion in pH 7 0.17 M NaCl in the presence of phenolphthalein indicator.

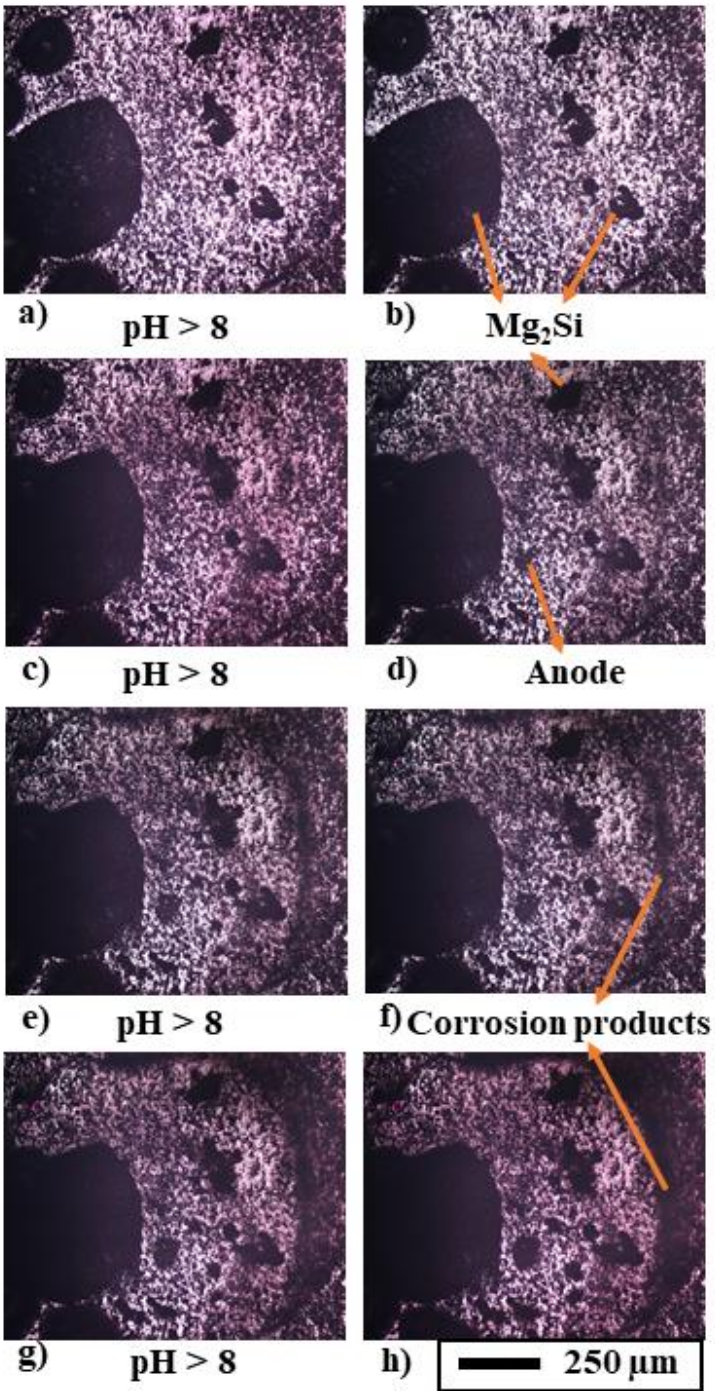

Figure 5.13: Optical microscope image of Zn + Mg_2Si surface after (a) 30 minutes (b) 1 hour (c) 1.5 hours (d) 2 hours (e) 2.5 hours (f) 3 hours(g) 3.5 hours (h) 4 hours immersion in pH 7 0.17 M NaCl in the presence of phenolphthalein indicator.

5.7 Discussion – Aqueous corrosion mechanism

SVET investigations suggested significant improvement in corrosion resistance for Zn + Mg_2Si compared to Zn. It is rational to suggest that the improved resistance offered is due to the presence of Mg_2Si particles. When Zn + Mg_2Si surface is exposed to a corrosive electrolyte, although initiation of anodic features in Zn was observed in TLM (Figure 5.10 and Video V6), Mg_2Si particles offer a degree of galvanic protection to the surrounding Zn and undergo preferential anodic de-alloying (Figure 5.11) by loss of Mg^{2+}, leaving behind a surface enriched in silicon (Si). This phenomenon is also supported by SVET investigation (Figure 5.8) where the Mg_2Si particles act as the site of anodic activities, consequently releasing Mg^{2+} into the electrolyte. Hence, Mg_2Si act as a reservoir of Mg^{2+} ions. These initial releases of Mg^{2+} ions enable the pH to rise above 8 as demonstrated in Figure 5.13 as Mg^{2+} ions will not hydrolyse. This rise in pH will encourage the precipitation of $Mg(OH)_2$ [147] and also stabilise pre-existing Zinc oxide/hydroxides on the samples' surface. The formation of $Mg(OH)_2$ is highly likely because $Mg(OH)_2$ is formed at pH 10 [147]. Hence the combination of galvanic protection offered by Mg_2Si and stabilised oxide/hydroxides reduces the rate of Zn loss during the initial hours until the reservoir of Mg^{2+} is exhausted from the Mg_2Si crystals. At this point, the corrosion rate becomes similar for both systems as demonstrated by the SVET data.

5.8 Inhibition of cathodic delamination by Mg_2Si

Corrosion driven cathodic delamination (CD) is a major failure mechanism in organically coated, lacquered and painted metal substrates where the intact coating is physically detached from the substrate [148]. Defects such as cut edges or scratches exposing the metallic surface act as the initiation site for CD. The cathodic oxygen reduction reaction which occurs at the delamination front is connected to the anodic metal dissolution occurring at the defect via a thin film of electrolyte ingressed beneath the coating completing the CD cell [145]. Studies have indicated that galvanised zinc surfaces finished with a top coat (paint, lacquer) exposed to electrolyte through penetrative defects are susceptible to CD, therefore it is of particular interest [92], [96], [149].

SVET investigation in section 5.4 has suggested a significant improvement in aqueous corrosion for coatings of Zn + Mg_2Si. Here, the effect of Mg_2Si particles on corrosion driven cathodic delamination is investigated. The comparison of Zn and Zn + Mg_2Si is conducted to help elucidate and evaluate the corrosion inhibiting properties of Mg_2Si particles. Using the same methodology found in section 2.6.4, a "Stratmann type" experiment was utilised in conjunction with a Scanning Kelvin probe (SKP) to measure the corrosion-driven unpigmented PVB coating delamination on Zn and Zn + Mg_2Si. Two different Zn + Mg_2Si samples with relatively lower and higher amounts of Mg_2Si were investigated. A relatively lower amount of Mg_2Si particles is denoted as Zn + Mg_2Si(L) and a relatively higher amount of Mg_2Si particles is denoted as Zn + Mg_2Si(H). The samples used for the SKP experiments are presented in Figure 5.14. The surface area fractions of Mg_2Si present on Zn, Zn + Mg_2Si(L) and Zn + Mg_2Si(H) samples present in Figure 5.14 used during SKP experiments are presented in Table 5.2.

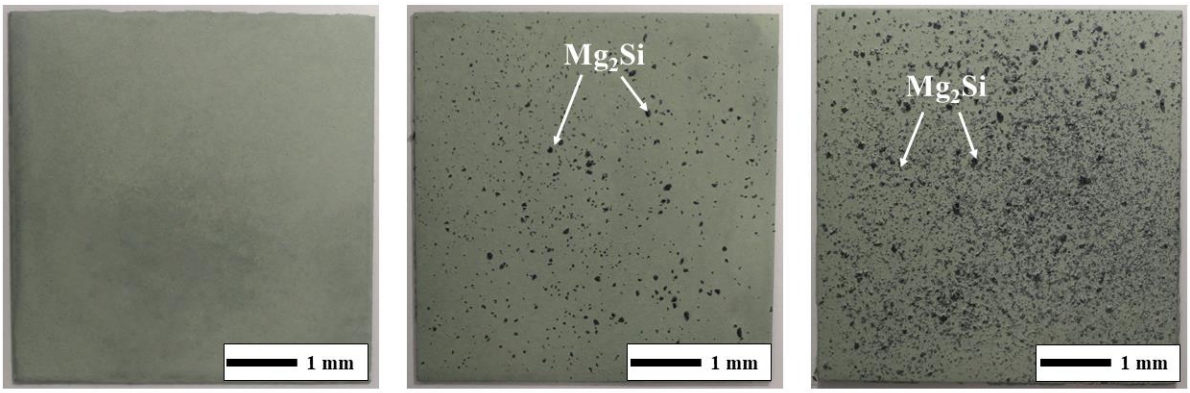

Figure 5.14: Photographs of samples used for SKP experiments a) Zn b) Zn + Mg_2Si(L) c) Zn + Mg_2Si(H).

Table 5.2: Surface area percentage of Mg_2Si

Sample	Surface area percentage of Mg_2Si
Zn	0.00
Zn + Mg_2Si(L)	0.96
Zn + Mg_2Si(H)	14.5

An experiment was carried out using an unpigmented PVB coating applied to the Zn surface to establish the baseline kinetics of organic coating disbondment and also to determine the characteristics of the delamination cell. Figure 5.15 presents the potential measured by the SKP gold reference probe converted to E_{corr} vs SHE plotted against the delamination of coated PVB layer for Zn. For Zn, the intact potential (E_{intact}) which corresponds to a "passive state" was measured as ~ -50 mV vs SHE. When the corrosive electrolyte was introduced into the defect the PVB coating delamination was initiated well before the first-hour scan and was well established by 60 minutes as shown in Figure 5.15. ~ 6 mm of delamination was measured at 1 hour and ~ 12 mm delamination was measured by 2 hours. This rapid rate of delamination could be due to the poor adhesion between the PVB layer and the Zn surface. A sharp potential drop then a gradual drop in potential connects the delamination front adjoining to the intact region to the coating defect. A potential of ~ -750 mV was recorded for the defect.

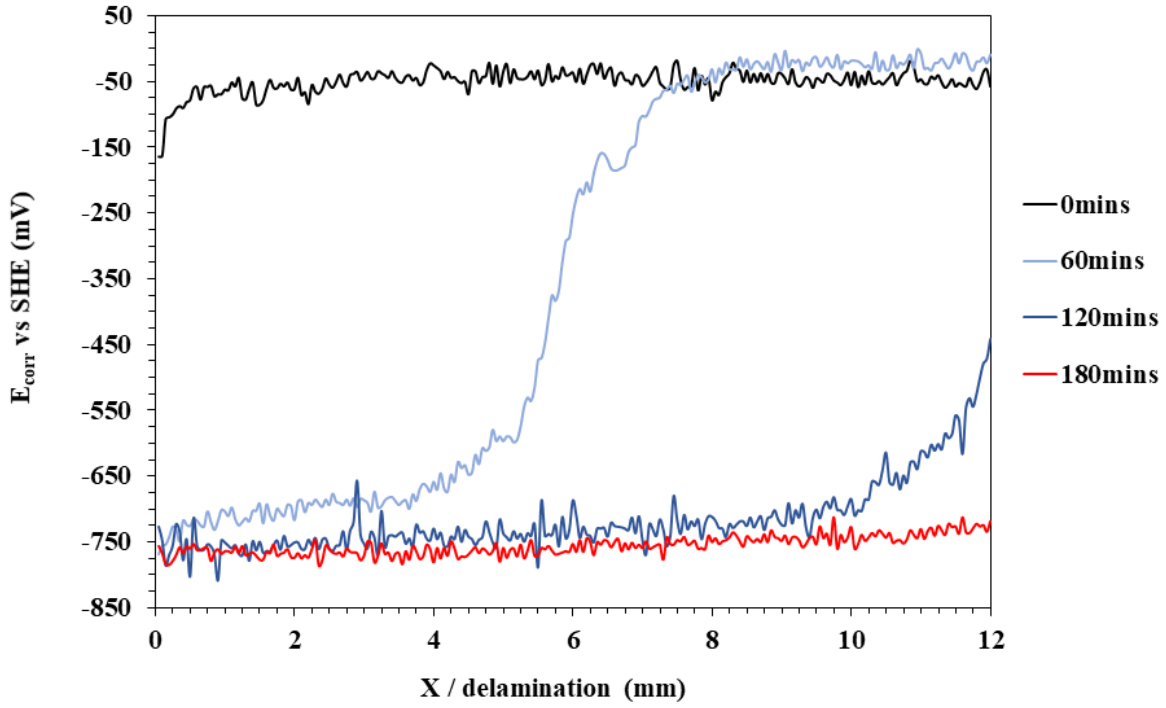

Figure 5.15: SKP scans for Zn coated with PVB shown commercing after 1 hour and shown thereafter at 1-hour intervals. 12 mm of delamination is measured after 2 hours.

It has been postulated elsewhere [95], [96], [144] that during CD on zinc, the anodic dissolution of zinc occurs at the defect region via equation 5.1 and reduction of oxygen occurs via equation 5.2 at the delamination front.

$$Zn \rightarrow Zn^{2+} + 2e^{-} \qquad [5.1]$$

$$O_2 + 2H_2O + 4e^{-} \rightarrow 4OH^{-} \qquad [5.2]$$

The potential at the intact region (E_{intact}) is relatively higher because anodic zinc dissolution is disfavoured in the absence of the electrolyte. On the contrary, in the near defect region potentials (E_{corr}) thidrop to values equivalent to freely corroding zinc. The net anode at the coating defect is connected to the cathodic site at the delamination front via the ionic current flux passing through the thin layer of electrolyte which ingresses beneath the delaminated coating. The sharp potential drop at the delamination front is thought to occur due to ingress of Na^{+} and loss of adhesion of PVB coating caused by the oxygen reduction [144]. The approximately linear potential gradient linking the defect and delamination front occurs due to the finite ionic conductivity of the under film electrolyte layer. The difference in

potential of the intact region and the defect i.e E_{intact} - E_{corr} signifies the magnitude of the polarity of the delamination cell. This polarity of the delamination cell is considered a driving force for CD [144]. The polarity of the delamination cell of Zn in the present case is ~ -700 mV.

Having established the characteristics of delamination on Zn, further experiments were conducted in presence of Mg_2Si. Figure 5.16 and Figure 5.17 presents the E_{corr} vs SHE plotted against the delamination of coated PVB layer for Zn + Mg_2Si(L) and Zn + Mg_2Si(H) respectively. For both Zn + Mg_2Si samples (Figure 5.16 and 5.17), the addition of Mg_2Si produced a decrease in E_{intact} compared to Zn from ~ -50mV to ~ -200mV vs SHE. Likewise, E_{corr} at the defect has also demonstrated a similar effect and indicated that the amount of Mg_2Si affects defect potential. E_{corr} of ~ -800mV and ~ -850 mV was recorded for Zn + Mg_2Si(L) and Zn + Mg_2Si(H) respectively.

Sudden drops in the measured potential to ~ -300 mV at certain sections (Figure 5.17) was observed for E_{intact}, this sudden drop in potential could be due to the presence of Mg_2Si particles. In Figure 5.17, it is also observed that the E_{intact} increases with time. In literature, E_{intact} indicates the open circuit potential of the oxide-covered metal surface and is influenced by the oxide interaction with the oxygen and/or Brosted acid-base interactions occurring between the polymer coating and the oxide [92], [150], [151]. Therefore, the time-dependent evolution of E_{intact} seen in Figure 5.17 could be the time taken for the electrochemical reaction occurring at the Zn + Mg_2Si - PVB coating interface to reach a steady state.

In the case of Zn + Mg_2Si(L), the E_{corr} vs delamination profiles obtained (Figure 5.16) in comparison to Zn (Figure 5.15) demonstrate improvement in the inhibition of corrosion driven cathodic delamination with the addition of Mg_2Si. In comparison to Zn, the delamination has reduced from ~6 mm to ~3 mm at 1 hour. 12 mm delamination is measured at 4 hours compared to 2 hours for Zn. Therefore, the presence of Mg_2Si particles indicates the improvement in the inhibition of corrosion driven cathodic delamination by reducing the rate of delamination by half.

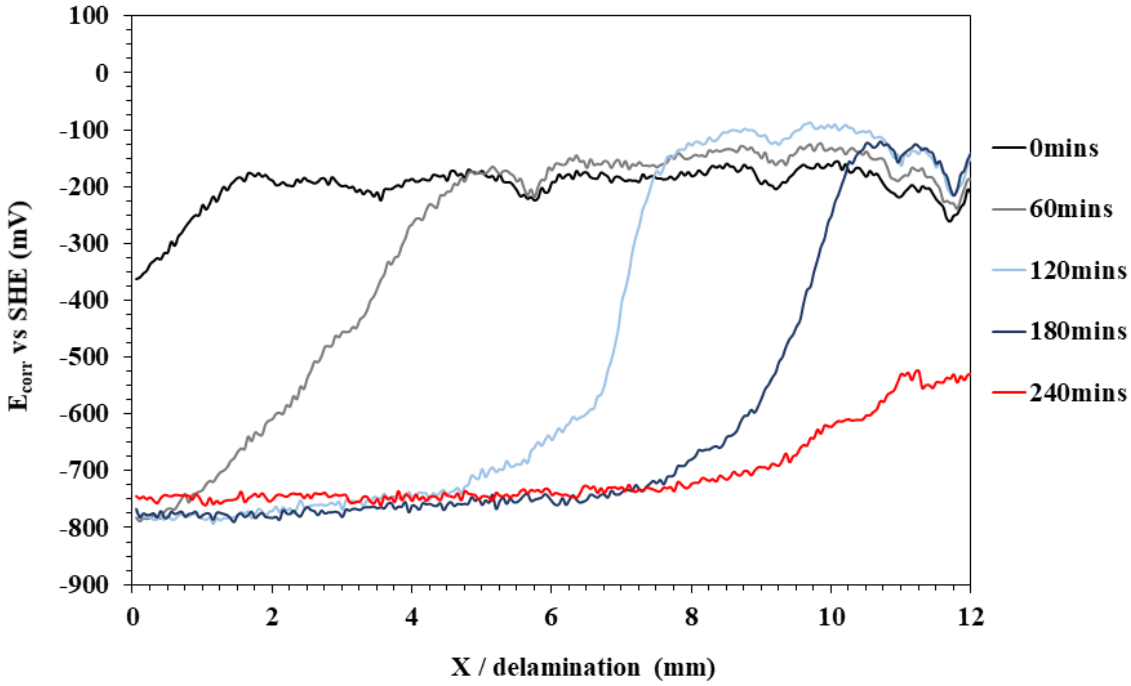

Figure 5.16: SKP scans for Zn + Mg_2Si(H) coated with PVB shown commercing after 1 hour and shown thereafter at 1-hour intervals. ~12 mm of delamination is measured after 4 hours.

In the case of Zn + Mg_2Si(H), the E_{corr} vs delamination profiles obtained (Figure 5.17) were found to become significantly modified in comparison to Zn (Figure 5.15) and Zn + Mg_2Si(L) (Figure 5.16). The initiation of delamination was delayed by ~ 4 hours. The time-dependent E_{corr} vs delamination distance (X) from the defect edge was well established by ~4 hours as shown in Figure 5.17. Delamination of 12 mm was delayed significantly and was measured after 16 hours. The addition of additional Mg_2Si particles indicates the further improvement in the inhibition of corrosion driven cathodic delamination by delaying the delamination initiation as well as reducing the rate of delamination (Figure 5.17). Also, the polarity of the delamination cells of Zn + Mg_2Si(L) and Zn + Mg_2Si(H) has fallen to ~ 600 mV and ~ 650 mV respectively from ~700 mV for Zn.

Delamination as a function of time after initiation using a 0.86 M NaCl electrolyte for Zn, Zn + Mg_2Si(L) and Zn + Mg_2Si(H) is presented in Figure 5.18. The figure represents the rate of delamination of all three samples investigated. It demonstrates the rate of delamination being diminished with the increase in the amount of Mg_2Si. Usually, PVB coated Zn surfaces demonstrate parabolic delamination kinetics [92].

The plot of delamination vs time for Zn + Mg_2Si(H) (Figure 5.18) also suggests that the rate of delamination slows with time hence suggesting normal parabolic kinetics. However, of Zn and Zn + Mg_2Si(L) the rate of delamination is simply too rapid to observe the subtle differences in kinetics.

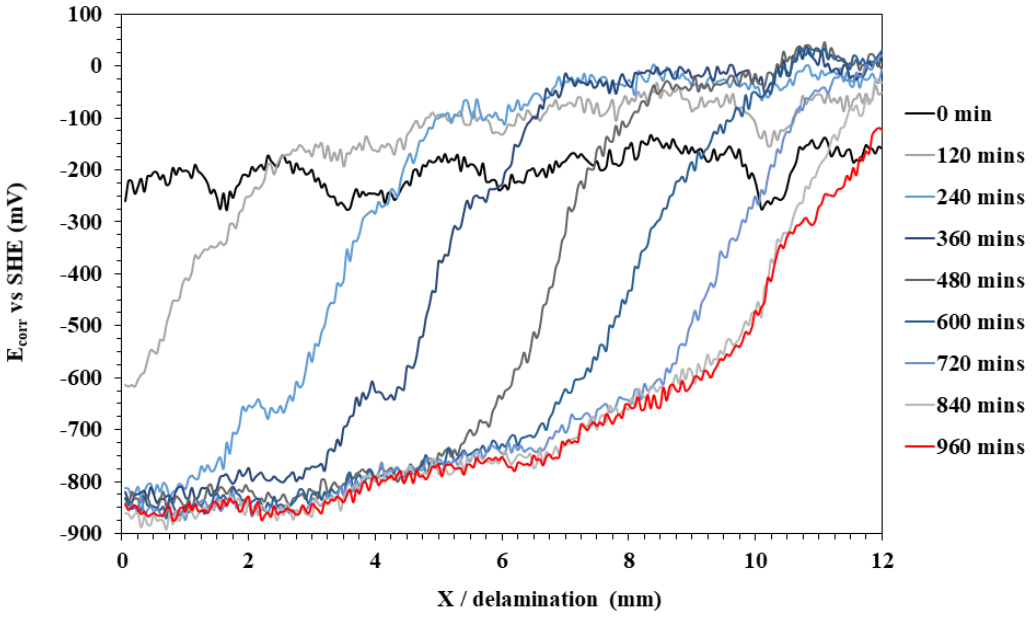

Figure 5.17: SKP scans for Zn + Mg_2Si(H) coated with PVB shown commercing after 2 hours and shown thereafter at 2-hour intervals. ~11 mm of delamination is measured after 14 hours.

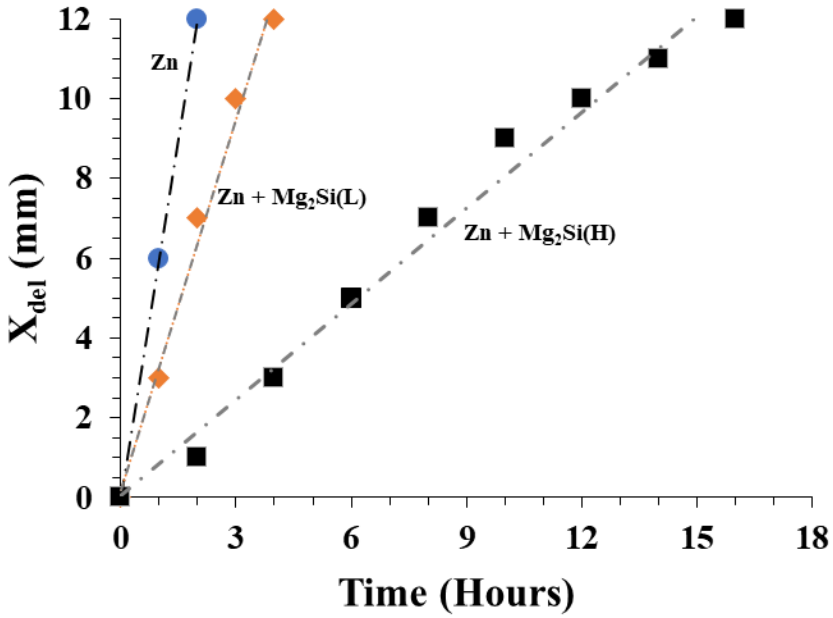

Figure 5.18: Delamination as a function of time for Zn and Zn+Mg_2Si samples after initiation using a 0.86 M NaCl electrolyte.

5.9 Discussion – delamination mechanism

Numerous investigations have suggested that delamination in hot-dip galvanised steel and PVD Zn proceeded via the establishment of a "delamination cell" and is controlled by under-film mass transport/migration of cations (Na^+) from the defect site to the delamination front [53], [144]. The precise mechanism by which the delamination on Zn occurs is difficult to suggest however number of mechanisms are suggested in the literature which could be occurring alone or concurrently [148].

The initial possible mechanism for PVB disbondment on Zn could be the dissolution of the preexisting zinc oxide layer formed at the coating-substrate interface. The cathodic oxygen reduction reaction occurring at the delamination front creates a favourable environment for zinc oxide dissolution as it is strong amphoteric oxide and dissolves at a moderately high pH [148]. The possibility of an alkaline electrolyte physically displacing the coating from the substrate also exists [148]. In addition, the degradation of the coating due to the hydrolysis of the coating itself i.e the break down in covalent chemical bonds within the coating due to high alkaline condition [148] and the presence of short-lived intermediates of O_2 reduction such as $O_2^{-\bullet}$, $HO_2^{\bullet}$, H_2O_2, HO_2^- and $HO^{\bullet}$ [148]. One or a combination of various mechanisms mentioned have resulted in the delamination of ZINGA Zn.

Figure 5.14 demonstrates that the surface of Mg_2Si samples is much rougher compared to the Zn sample due to the presence of Mg_2Si particles. These Mg_2Si particles increase the tortuosity of the substrate-coating interface as a result hinds the flow of Na^+ cations subsequently decreasing the delamination rate and it has been postulated elsewhere [152].

5.10 Conclusion:

A systematic study into the effect of Mg_2Si additions on the corrosion resistance of the zinc-rich powder-based galvanising system (Zn) has been conducted. SVET derived metal loss was reduced by 70 % with the addition of Mg_2Si particles. Mg_2Si particles preferentially anodically dissolved galvanically protecting the Zn surface.

An in-situ time-lapse microscopy technique has been used to investigate the aqueous corrosion mechanism of Zn and Zn + Mg_2Si. The technique, along with SEM-EDS, helped to support the initial dissolution of Mg^{2+} ions from the Mg_2Si particles. For Zn + Mg_2Si, the entire electrolyte above the exposed surface was above pH 8 due to the initial flush of Mg^{2+} and their low tendency for hydrolysis ions during the early hours of exposure. The formation of Magnesium hydroxide and passivation of Zn surfaces due to high pH consequently reduce the rate of aqueous corrosion.

The rate of corrosion driven cathodic delamination reduced with the increase in Mg_2Si particles present on the Zn surface. The Mg_2Si particles improved the corrosion driven cathodic delamination by delaying the delamination initiation time as well as reducing the rate of delamination.

Chapter 6 Study of effects of Calcium and phosphate on the corrosion behaviour of Zinc alloy

6.1 Introduction

Combinations of a metallic and organic coating (duplex coating system) are widely adopted in the engineering industries to protect the underlying steel substrate. The metallic coating which provides sacrificial protection is over-coated with organic layers which act as a barrier between the metallic coating and the environment. The duplex coating system provides better protection compared to metallic or organic coating individually [31]. Zinc and its alloys applied via galvanisation are predominately used as a metallic coating on steel followed by an organic layer. The organic layer consists of pretreatment, primer and topcoat. The corrosion inhibitors are usually embedded in the primer layer in the form of pigments which provide further electrochemical protection to the steel. The inhibitors operate by releasing ionic species consequently altering the local electrolytic conditions. These ionic species can produce insulating films either at anodic or cathodic sites by precipitation or by involvement in the electrochemical process [153].

Traditionally for hot-dip galvanised systems Chromium-based hexavalent (Cr(VI)) CrO_4^{2-} or Cr_2O_7 have proven to be very effective due to the presence of Cr^{6+} ions. Nevertheless, it has been discontinued due to its toxicity and carcinogenicity towards human health and the natural environment [154]–[157]. Therefore, there is a necessity for equally effective as well as safe and eco-friendly inhibitors. As a result, it is an area of research interest. One probable alternative to chromates is phosphates compounds. Typically in the presence of oxygen, phosphates behave as an anodic inhibitor [31], [32], [153], [158], [159] however under the certain condition such as in presence of divalent metal ions, Ca^{2+}, phosphates may also act as cathodic inhibitors by forming a surface film, as a result, impeding oxygen diffusion at the metal surface [160], [161].

Here, in this investigation, we aim to create an environmental friendly duplex coating system with a synergy between the metallic and organic layers. In order to do so Zinc coating (Zn) has been modified with the addition of 1 wt. % Calcium (Ca) to produce Zn-1Ca alloy. Phosphate in the form of Sodium phosphate has been selected as a corrosion inhibitor because of its relevance as phosphates have been

incorporated in industry. The effects of alloying Zn with Ca in terms of microstructural and electrochemical properties along with the effects of phosphate addition to electrochemical properties of Zn and Zn-1Ca were investigated using a combination of techniques. Scanning Vibrating Electrode Technique (SVET) was utilised to resolve corrosion features and evaluate relative corrosion performance and Time-lapse Microscopy (TLM) was used to understand the aqueous in-situ corrosion mechanism. The investigation was supported by open-circuit potential, potentiodynamic and linear polarization resistance measurements.

6.2 Sample production

The production of Zn and Zn-1Ca samples were completed using MTI Corporation manufactured KSL-1100X-SV compact crucible melting furnace. Zn pieces provided by TATA Steel and Calcium pieces bought from Sigma Aldrich were heated to 600^{o}C in a crucible. After stirring the melt it was further heated to 850^{o}C. The melt was then cooled to 600^{o}C within the crucible and then splat cast onto a copper plate. The temperature was measured using the inbuilt temperature controller with +/- 1^{o}C accuracy.

6.3 Microstructural analysis of Zn-1Ca

The target composition of the produced samples under investigation are presented in Table 6.1. The Zn alloy (Zn) is composed of 99.80 wt.% of Zn and 0.20 wt.% of Aluminium (Al). The Zn-1Ca is composed of 98.80 wt.% of Zn, 1 wt.% of Ca and 0.20 wt.% of Aluminium (Al). There is a slight decrease in wt % of Zn for Zn-1Ca alloy from 99.80 to 98.80 wt .% compared to Zn alloy.

Table 6.1: Compositions in wt.% of the Zn and Zn-Ca alloys

Sample	Zn (wt.%)	Ca (wt.%)	Al (wt.%)
Zn	99.80	/	0.20
Zn-1Ca	98.80	1.00	0.20

High-resolution images of Zn and Zn-1Ca alloys captured using a Scanning Electron Microscope (SEM) are presented in Figure 6.1. A microstructural image of Zn-1Ca captured using optical light microscopy is presented in Figure 6.2. Figure 6.1 (b) and Figure 6.2 show the changes within the microstructure due to the addition of 1 wt.%

of Ca. The addition of Ca into the Zn system has led to the formation of a new phase within the microstructure.

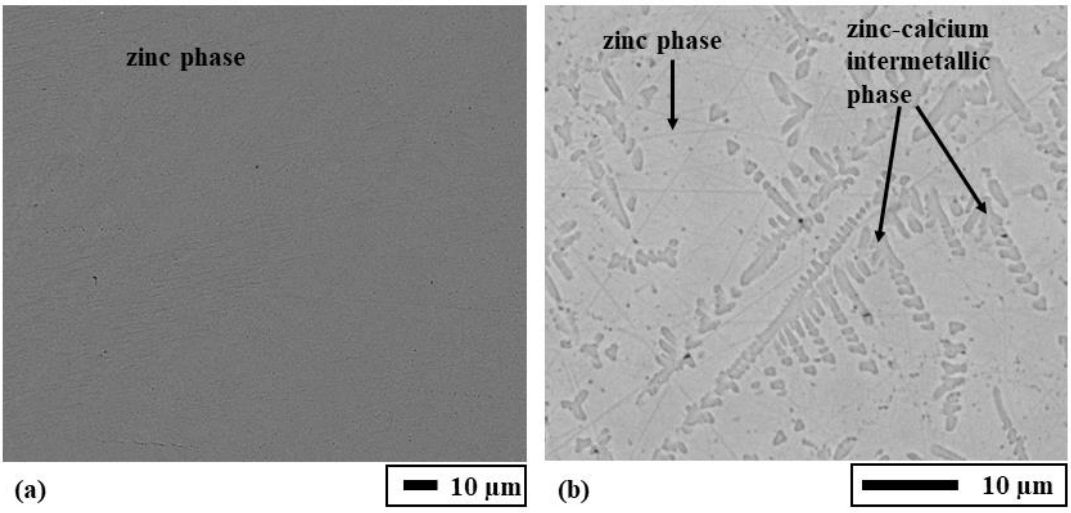

Figure 6.1: SEM images showing (a) Zn (b) Zn-1Ca

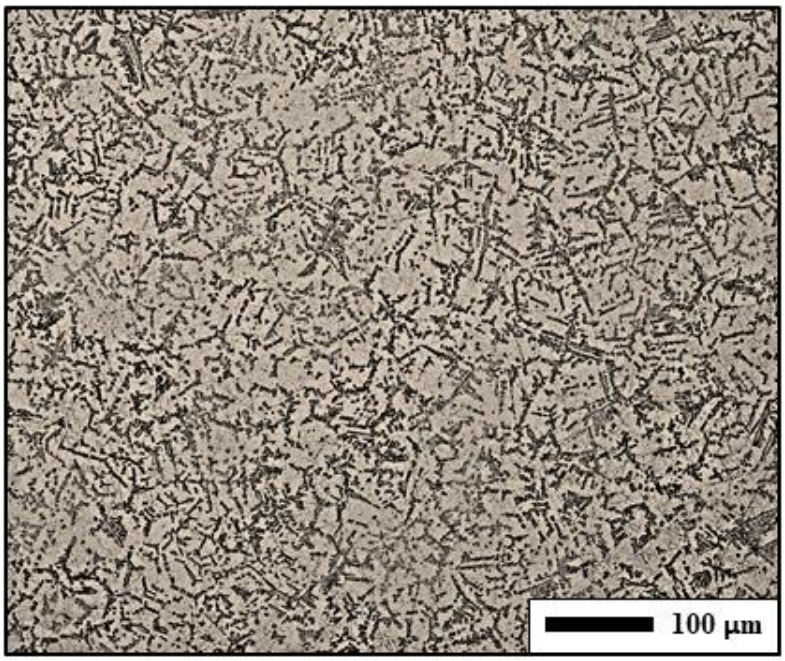

Figure 6.2: Optical light microscope image of the microstructure of the Zn-1Ca alloy

Energy Dispersive X-Ray Spectroscopy (EDS) was utilized to identify the distribution of elements within the Zn-1Ca alloy. Colour maps identifying the elements Zn, and Ca were produced using SEM/EDS software and is presented in Figure 6.3 (b-d). The EDS analysis (Figure 6.3(e)) along with the Ca-Zn phase diagram [162] suggests the new phases formed due to Ca additions are intermetallic

$CaZn_{13}$. The previous investigation on the alloying of Zn with 1 wt.% of Ca has also demonstrated the formation of intermetallic $CaZn_{13}$ [163], [164].

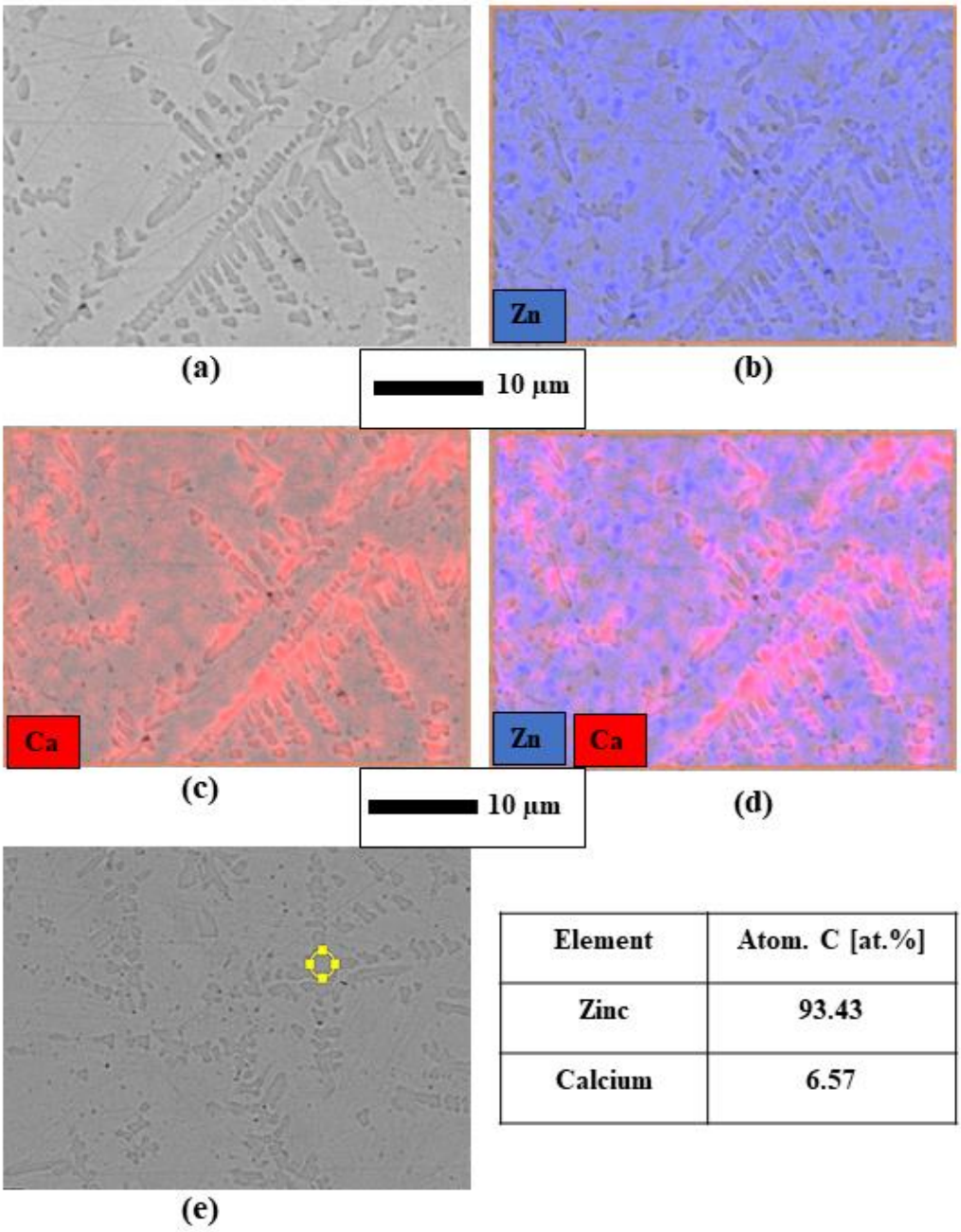

Element	Atom. C [at.%]
Zinc	93.43
Calcium	6.57

Figure 6.3: (a) SEM image of Zn-1Ca, (b-d) Colour maps for EDS elemental analysis for Zn-1Ca, (e) EDS analysis for Zn-1Ca.

6.4 Study of corrosion behaviour of Zn and Zn -1Ca alloys

6.4.1 Investigation of corrosion behaviour using Scanning Vibrating Electrode Technique (SVET)

The SVET was used to investigate the surface corrosion performance of Zn and Zn-1Ca samples over 24 hours in an aerated 0.17 M NaCl pH 7 solution, as described fully in section 2.4. The SVET results include surface normal current density maps, estimated metal loss over 24 hours and average hourly estimated metal loss. Similar to Chapter 3 and Chapter 5 Zn being the predominant element in both the samples, Zn was selected during the metal loss calculations. Although during the corrosion of Zn-1Ca, both Zn (Zn^{2+}) and Ca (Ca^{2+}) are likely to participate it is difficult to predict the contribution of individual species for metal loss. However, due to the identical charge associated with both ions type the relative metal loss value would be directly comparable across the samples irrespective of the element selected. The SVET derived metal loss in this investigation is used to compare the relative corrosion performance among samples however the metal loss does not represent an exact metal loss for the experiment period. Besides metal loss, SVET data could be used to plot normal current density maps which provide a visual representation of the location and intensity of anodic and cathodic activities as recorded by the SVET probe. Red and blue colours are indicative of anodic and cathodic activities respectively.

The corrosion activity occurring on the surface could be represented as normal current density maps. Figure 6.4 shows the normal current densities measured above the surface of the Zn and Zn-1Ca samples freely corroding in pH 7 0.17 $mol.dm^{-3}$ NaCl for 1 hour, 6 hours, 12 hours, 18 hours and 24 hours. In both the samples, corrosion activities were detected immediately (1-hour scans for both Zn and Zn-1Ca) however, a distinguished difference in corrosion mechanism is observed between the Zn and Zn-1Ca samples. In the Zn, multiple islands of anodes are established and are spread throughout the sample surface whereas for Zn-1Ca the exposed surface is approximately diagonally separated into the anodic and cathodic areas.

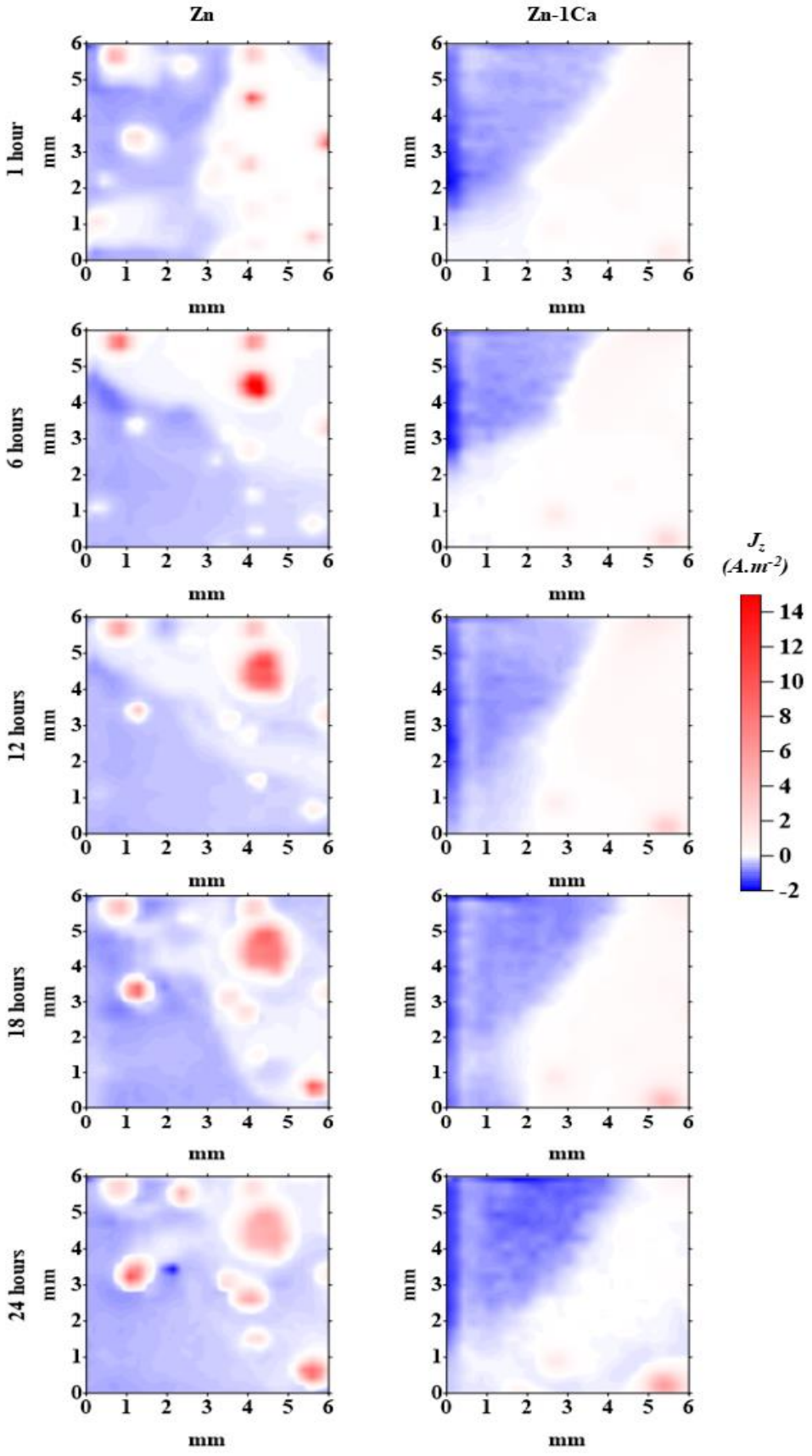

Figure 6.4: SVET false colour maps representing normal current density measured above Zn and Zn-1Ca immersed in pH 7 0.17 M NaCl.

For Zn, the intensity and size of anodes established vary with time. The anodes formed from the onset, grow in intensity and radially in size with time. It is also observed that some of the individual anodes passivate with time and new active anodes are formed. In the case of Zn-1Ca, on the contrary, no individual multiple point anodes are observed. The normal current densities contour maps suggest one half of the surface is acting as an anode and the other half as a cathode. However, with time an individual point anode is formed by 24 hours of exposure (the bottom right corner, Figure 6.4). It is also observed that the intensity of anodic sites for Zn-1Ca is much lower compared to Zn. Therefore, these contour maps in Figure 6.4 indicates that the corrosion activities occurring on the Zn-1Ca surface is lesser in comparison to the Zn surface throughout the experimental time consequently indicating better corrosion resistance.

The SVET derived metal loss for both Zn and Zn-1Ca after immersion on pH 7 0.17 M NaCl for 24 hours are shown in Table 6.2. The errors shown are based on the standard deviation of three measurements. The derived metal loss for Zn-1Ca is 4.32 $g.m^{-2}$ compared to 9.83 $g.m^{-2}$ for Zn. The alloying of Zn with Ca exhibited a decrease in the measured metal loss by 56 % compared to that of Zn without Ca. Therefore, it appears that the addition of Ca has significantly improved the corrosion resistance of Zn-1Ca compared to Zn.

The SVET derived hourly metal loss (average of three measurements) as a function of time for both Zn and Zn-1Ca during immersion on pH 7 0.17 M NaCl for 24 hours are presented in Figure 6.5. For both samples, the metal loss is ~ 0.10 $g.m^{-2}$ for the initial (0 Hr) scan. For Zn, a steep increase in metal loss is observed from 0 Hr to 1 Hr. However, from 1 Hr onwards up to 20 Hr, a gradual linear increase with a less steep gradient in metal loss is observed. Despite the similar hourly metal loss for Zn and Zn-1Ca for the initial scan, in contrast to Zn, Zn-1Ca hourly metal loss is comparatively constant with ~ 0.125 $g.m^{-2}$ throughout. This difference in hourly metal loss gradient suggests Zn-1Ca endorse a greater extend of corrosion resistance compared to Zn throughout the 24 hours.

Table 6.2: SVET derived metal loss for Zn and Zn - 1Ca after immersion in pH 7 0.17 M NaCl for 24 hours.

Sample	Metal loss ($g.m^{-2}$)
Zn	9.83 ± 0.75
Zn - 1Ca	4.32 ± 1.67

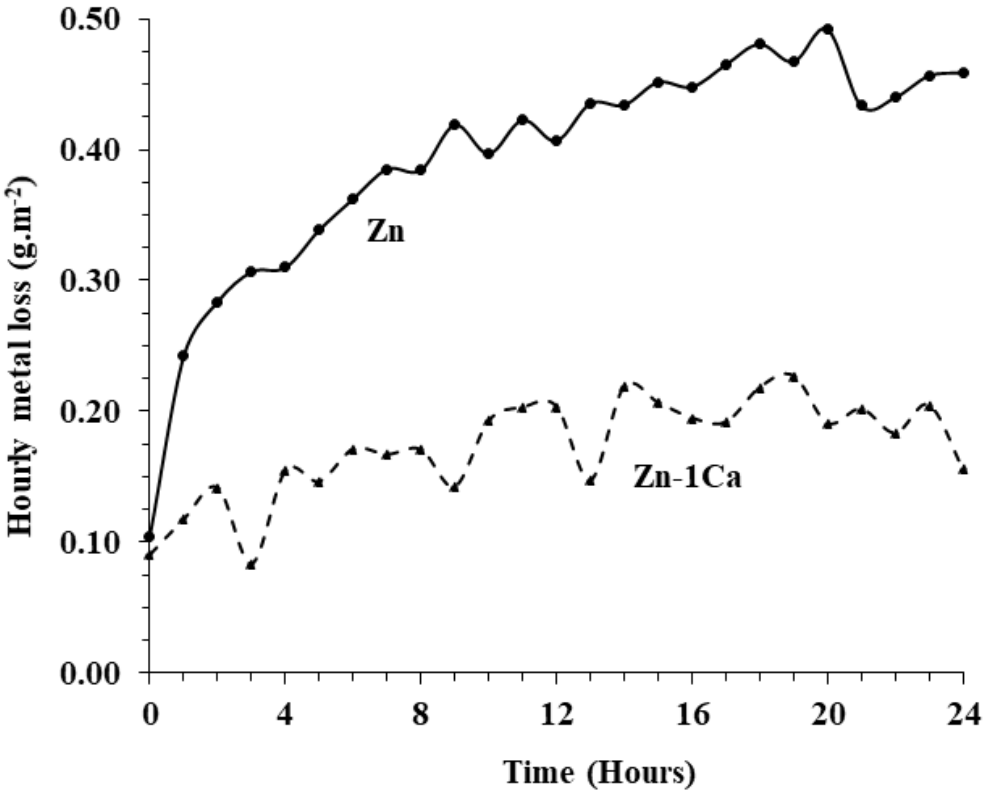

Figure 6.5: SVET derived hourly metal loss as a function of time for Zn and Zn-1Ca after immersion in pH 7 0.17 M NaCl solution for 24 hours.

6.4.2 Investigation of corrosion mechanism using Time-lapse Microscopy (TLM)

The improvement in corrosion resistance and the change in the corrosion mechanism of Zn due to 1 wt.% of Ca addition is further investigated using TLM. The corrosion mechanism occurring at the microstructural level could be obtained using TLM. Figure 6.6 shows optical microscope images of the Zn surface at various times of immersion in 0.17 M NaCl pH 7. Figure 6.6 presents the images captured at 2 minutes, 2 hours, 4 hours, 6 hours, 8 hours and 10 hours. It can be observed that an anode develops from the onset, concurrently darkening of the grain boundaries is also observed (see video V9). The anode grew in size preferentially via the grain boundaries (see video V9). As an anode grew in size, corrosion products are precipitated in a form of a semi-circle/ring at the periphery, a certain distance away from the anode. It has been suggested this ring indicates the boundary between ionic counter currents where the metal ions produced at the anode and hydroxide ions produced at the cathode encounter each other [32]. The corrosion product ring thickened and was observed to be mobile with time. As the anode grew in size, the corrosion product ring dissolved and re-precipitated away from the anode (see video V9 and Figure 6.6(c) and Figure 6.8(f)). This occurrence of re-solubility and precipitation is due to the reduction in local pH at the anodic front. This phenomenon of change in local pH was also observed for ZMA-Ge alloys and has been described in detail in Section 3.6. It is also worth noting that the cathodic site (opposite side to the anodic site) where oxygen reduction occurs is fairly clear and no corrosion product precipitation occurred.

Figure 6.7 shows optical microscope images of Zn-1Ca surface at 2 minutes, 2 hours, 4 hours, 6 hours, 8 hours and 10 hours of immersion in pH 7 0.17 M NaCl. In contrast to Zn (Figure 6.6), multiple anodes are observed for the onset and parallel darkening of the intermetallic metallic phase $CaZn_{13}$ is also observed (see video V10). The 4-minute optical image of Zn-1Ca presented in Figure 6.8 and video V10 indicates that the anodes initiate off the intermetallic $CaZn_{13}$ phase. The anodes grow in size with time preferentially via the intermetallic phase $CaZn_{13}$ leaving behind islands of Zn. This preferential attack phenomenon could be observed in video V10 and Figure 6.8(b). Similar to Zn, precipitation of corrosion products ring is also observed for Zn-1Ca at a certain distance away from the anodes which get thicker and denser with time. However, for Zn-1Ca dissolution and re-precipitation of

corrosion product ring is not observed but instead, corrosion products start to precipitate inward, towards the anode and on the cathodic site too (Figure 6.7).

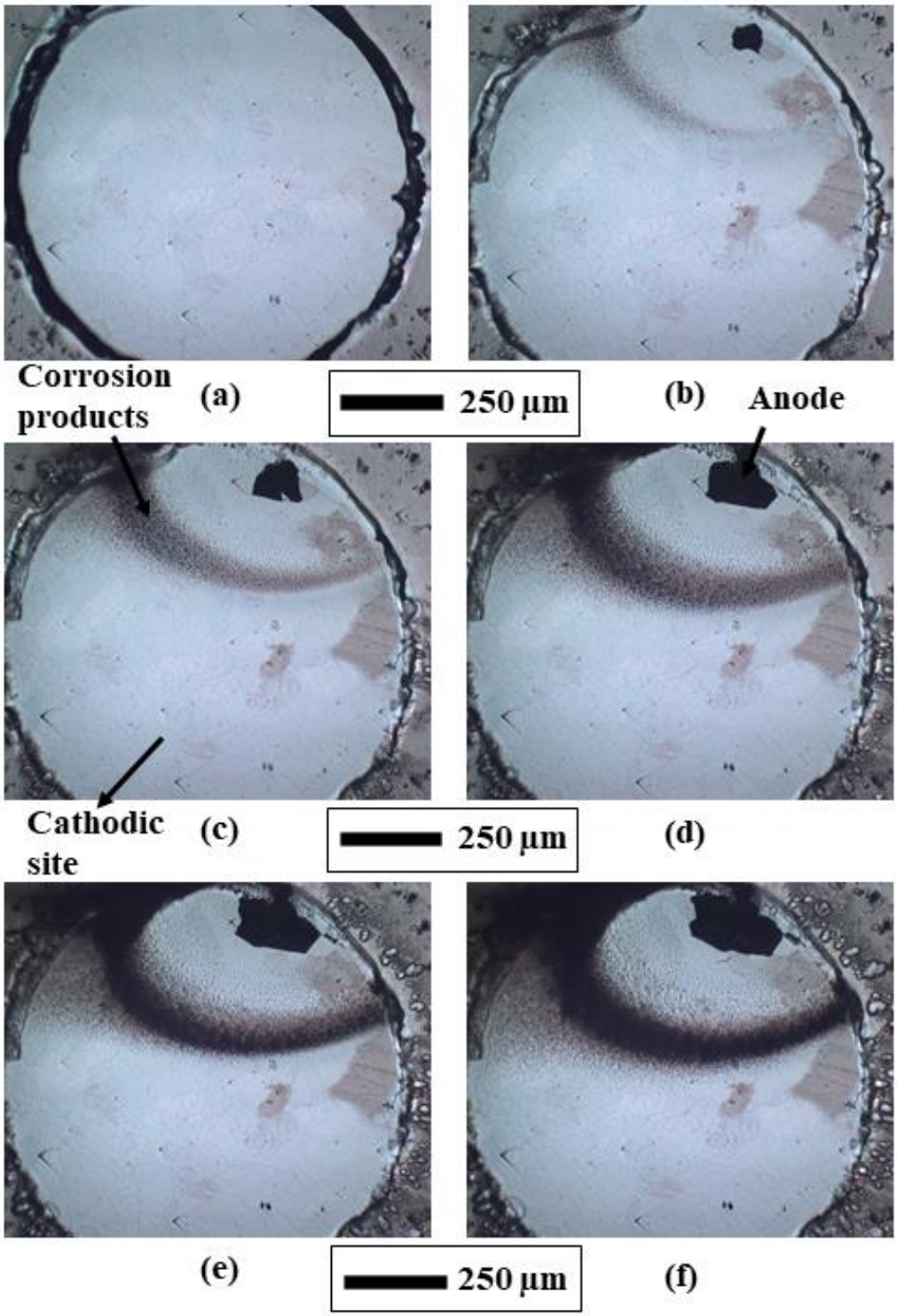

Figure 6.6: Time-lapse Microscope images of Zn taken in-situ under immersion conditions in pH 7 0.17 M NaCl. The images (a-f) shown were taken at 2 minutes, 2 hours, 4 hours, 6 hours, 8 hours and 10 hours respectively

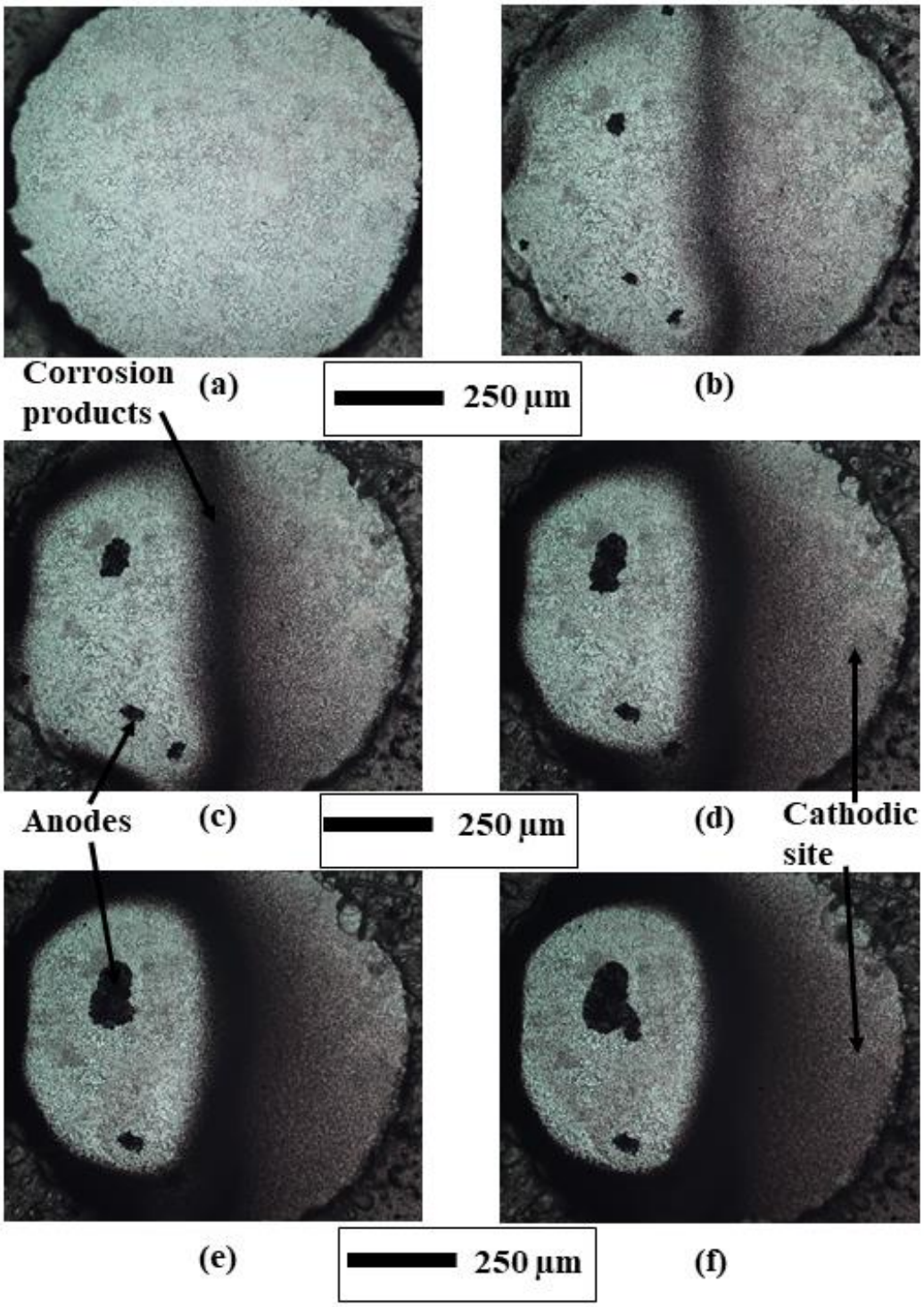

Figure 6.7: Time-lapse Microscope images of Zn-1Ca taken in-situ under immersion conditions in pH 7 0.17 M NaCl. The images (a-f) shown were taken at 2 minutes, 2 hours, 4 hours, 6 hours, 8 hours and 10 hours respectively.

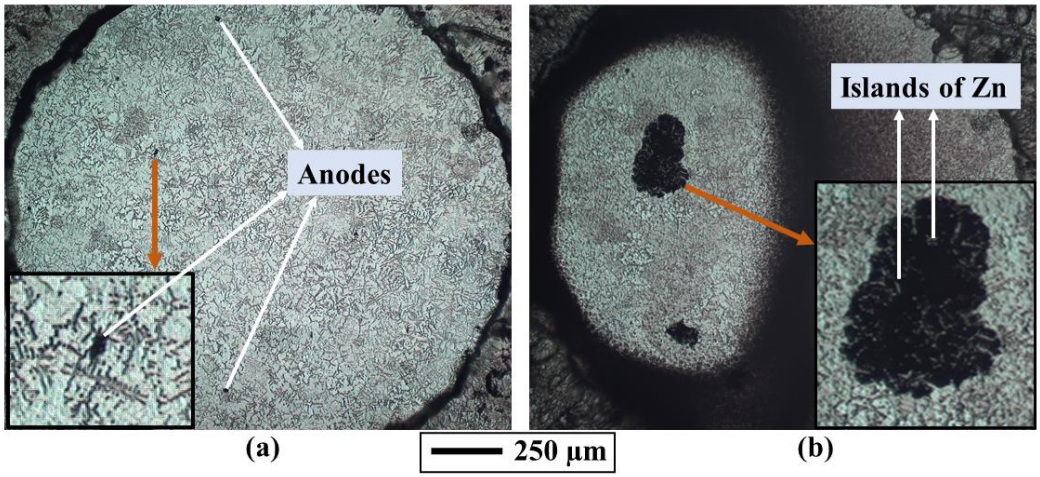

Figure 6.8: Time-lapse Microscope images of Zn-1Ca taken in-situ after (a) 4 minutes and (b) 8 hours under immersion conditions in pH 7 0.17 M NaCl.

6.4.3 Electrochemical Measurements

A series of electrochemical experiments, open circuit potential, potentiodynamic polarization and linear polarisation resistance, were performed to further investigate the influence of the addition of 1 wt.% Ca into Zn. The experiments were initiated at the shortest time possible after the introduction of the electrolyte. Figure 6.9(a) shows the OCP measurements of Zn and Zn-1Ca immersed in pH 7 0.17 M NaCl over 24 hours time period. The initial potential is ~ -1.04 V vs SCE for Zn and ~ -1.02 V vs SCE for Zn-1Ca after which a shift to more negative potential is observed. A shift to more negative potential is observed for both Zn and Zn-1Ca. A shift of potential ~ 0.046 V vs SCE is observed for Zn-1Ca which continued for ~ 2 hours whereas, for Zn, the shift was ~ 0.016 V vs SCE lasting ~ 0.5 hours.

For Zn, after the initial shift from ~ 1.04 V vs SCE to ~ 1.056 V vs SCE, the potential gradually increases to ~ 1.03 V vs SCE. From ~ 1.03 V vs SCE, the potential again shifts to more negative potential consequently obtaining some degree of stabilisation after ~ 6 hours at ~ -1.048 V vs SCE. However, for Zn-1Ca this fluctuation of potential after the initial potential drop is not observed. Zn-1Ca stabilised at ~ 1.064 V vs SCE after 4 hours.

Potentiodynamic polarization measurements performed on Zn and Zn-1Ca samples immersed in 0.17 M NaCl pH 7 is presented in Figure 6.9(b). The polarization curves demonstrate that there are no obvious changes on the anodic branch due to the addition of 1 wt.% of Ca however on the cathodic branch a significant decrease in

current is measured at the early stage of the experiment. At -1.20 V vs SCE, the values of the current (Log I) showed a large drop between the Zn and Zn-1Ca, a reduction by more than half the order of magnitude is observed for Zn-1Ca.

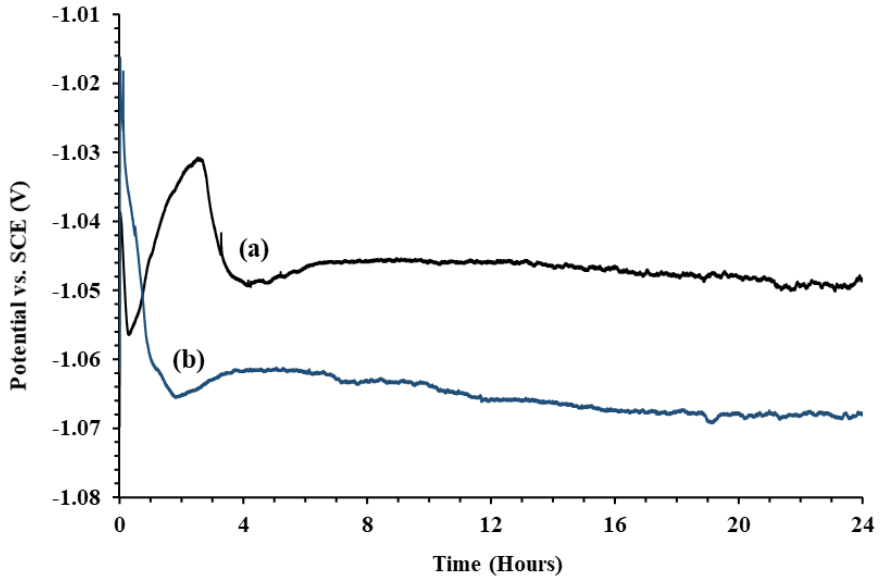

Figure 6.9(a): The time-dependent OCP for (a) Zn and (b) Zn-1Ca immersed in pH 7 0.17 M NaCl for 24 hours.

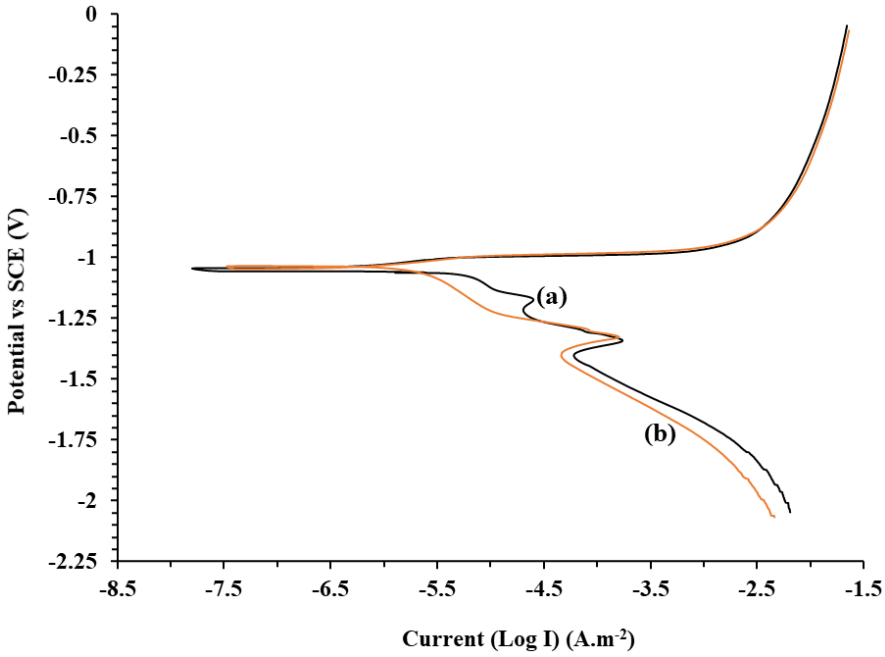

Figure 6.9(b): Polarisation curves for (a) Zn and (b) Zn-1Ca immersed in pH 7 0.17 M NaCl solution.

In order to further understand the relative corrosion rate of Zn and Zn-1Ca, linear polarization resistance (LPR) measurements were performed. During the measurement, the samples were polarised by ± 15 mV from OCP at a scan rate of 0.166 mVs^{-1}. Polarisation resistance (R_p) values are presented in Table 6.3. The R_p value of Zn-1Ca is 2.5 times greater than Zn. Therefore, indicating Zn-1Ca provides better corrosion resistance as $i_{corr} \alpha 1/R_p$.

Table 6.3: Linear polarization resistance measurements obtained for Zn and Zn-1Ca where the samples were polarised by ±15 mV at a scan rate of 0.166 mVs^{-1} in pH 7 0.17 M NaCl.

Sample	Polarisation Resistance, R_p, ($Ohms.cm^{-2}$)
Zn	4438
Zn - 1Ca	12141

6.4.4 Discussion

SVET experiments have suggested that Zn-1Ca provide superior corrosion protection compared to Zn. Here, it is proposed that this enhanced protection afforded by Zn-1Ca is due to the change in microstructure as Ca addition leads to the formation of Zn-Ca intermetallic. Once in contact with the electrolyte, these intermetallic provide galvanic protection to the Zn phases by preferential anodic dissolution and release of Zn^{2+} and Ca^{2+} ions (Figure 6.8(b) and Video V10). The Ca^{2+} ions react with hydroxyl ions (OH^-) generated at the cathode to form sparingly soluble Calcium hydroxide ($Ca(OH)_2$) with a large bandgap of 3.67 eV [165], [166]. The formation of $Ca(OH)_2$ restricts the movement of ions as well as the movement of oxygen diffusion to the cathodic site (precipitation of corrosion product in the cathodic site Figure 6.7 and Figure 6.9). $Ca(OH)_2$ is a strong base [167], [168] dissociates to produce Ca^{2+} and OH^- ions. As the concentration of OH^- ions increase, it enables the pH above the surface to rise. A $Ca(OH)_2$ saturated solution has a pH of 12.5 [169]. This alkalization of local pH creates a suitable environment for stabilisation of the pre-existing Zinc oxide/hydroxides consequently passivating the Zn surface [170].

In Figure 6.2 the intermetallic $CaZn_{13}$ are spread consistently in proximity (separated by < 100 µm) throughout the surface. Here, we observed that the multiple anodes initiate at these intermetallic (Figure 6.8 and Video V10) before growing into the Zn phase however on SVET contour maps (Figure 6.5) no focal anodes are established

until the 18th hour. As illustrated in section 2.4.3 SVET is only able to resolve individual localised features separated by a distance greater than 150 µm as the SVET scan height is 100 µm. Therefore, for Zn-1Ca the spacing between the cathodic and anodic sites may be less than 150 µm and the lines of current flux between anode and cathode may not intersect the SVET scan plane. However, SVET has resolved the net corrosion activities on the Zn-1Ca surface. By itself, there is a potential the SVET derived metal loss in Table 6.2 has been underestimated for Zn-1Ca. However, the linear polarisation resistance measurement suggests that the corrosion kinetics of Zn-1Ca are reduced in comparison to Zn as R_p value of Zn-1Ca is 2.5 times greater than Zn. Therefore suggests the corrosion rate of Zn-1Ca is 2.5 times lower compared to Zn.

6.5 Study of the inhibition effects of Phosphate during corrosion of Zn and Zn-1Ca alloys

Further investigation was conducted to evaluate the performance of phosphate ions on the inhibition of corrosion of Zn and Zn-1Ca. Sodium phosphate monobasic dihydrate ($NaH_2PO_4.2H_2O$) was used as a source of phosphate ions. The 0.17 M NaCl was dosed with 1 x 10^{-3} mol.dm^3 sodium phosphate and was adjusted to pH 7. The inhibitor concentration of 1 x 10^{-3} mol.dm^3 was selected because of its proven inhibition efficiency previously of 92 % on ZMA coatings.

6.5.1 Investigation of inhibition effect of Phosphate using Scanning Vibrating Electrode Technique (SVET)

The SVET was utilized to investigate the effect of sodium phosphate (Na_3PO_4) as an inhibitor on Zn and Zn-1Ca. Figure 6.10 shows the normal current densities measured above the surface of the Zn freely corroding in pH 7 0.17 mol.dm^{-3} NaCl containing 1 x 10^{-3} mol.dm^3 Na_3PO_4 for 1 hour, 6 hours, 12 hours, 18 hours and 24 hours. The addition of Na_3PO_4 has led to the passivation of the exposed surface for a short period as no anodic or cathodic features are present for the 1 hour. However, from 6 hours onwards multiple point anodes are established. The addition of Na_3PO_4 has also significantly reduced the number and intensity of the established anodic features. The SVET contour maps for 12 hours, 18 hours and 24 hours indicates that the established anodes do not grow radially as we observed for Zn without Na_3PO_4 but new anodic features are developed around the already established anodic site.

Figure 6.11 shows the normal current densities measured above the surface of the Zn-1Ca freely corroding in pH 7 0.17 mol.dm^{-3} NaCl containing 1 x 10^{-3} mol.dm^3 Na_3PO_4 for 1 hour, 6 hours, 12 hours, 18 hours and 24 hours. The presence of Ca and Na_3PO_4 has had a significant impact on the measured current densities. The Zn-1Ca surface has led to the extended period of passivation of the exposed surface as no anodic or cathodic features are present for up to 12 hours. The anodic features are established by 18 hours and grow in intensity and size with time. The mechanism observed for Zn-1Ca, i.e ~ half the exposed surface behaving as an anodic site and the other half as cathodic site, is not observed for Na_3PO_4 addition as focal anodes are present on 18 hours and 24 hours scans.

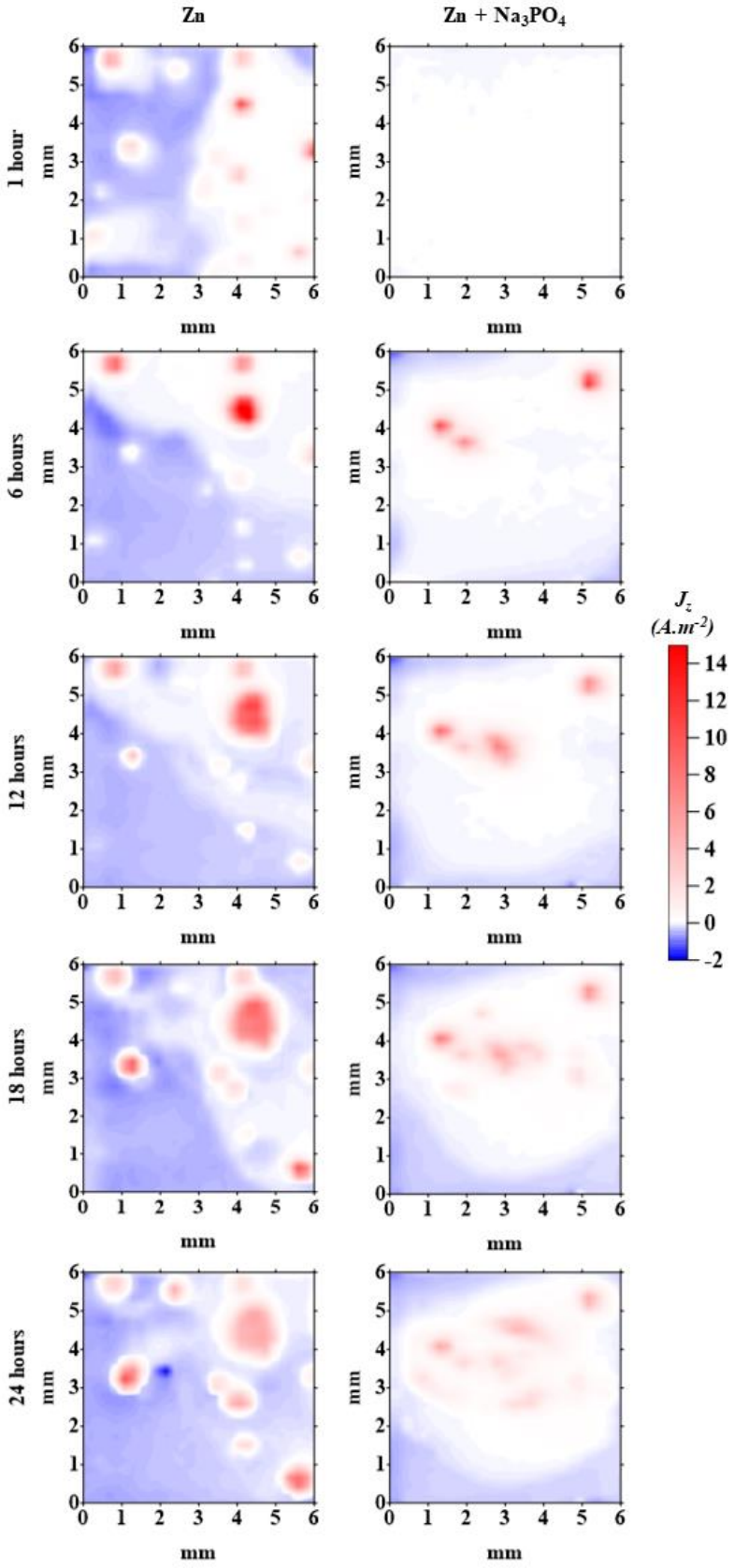

Figure 6.10: SVET false colour maps representing normal current density measured above Zn immersed in pH 7 0.17 M NaCl containing 1 x 10^{-3} mol.dm^{-3} Na_3PO_4.

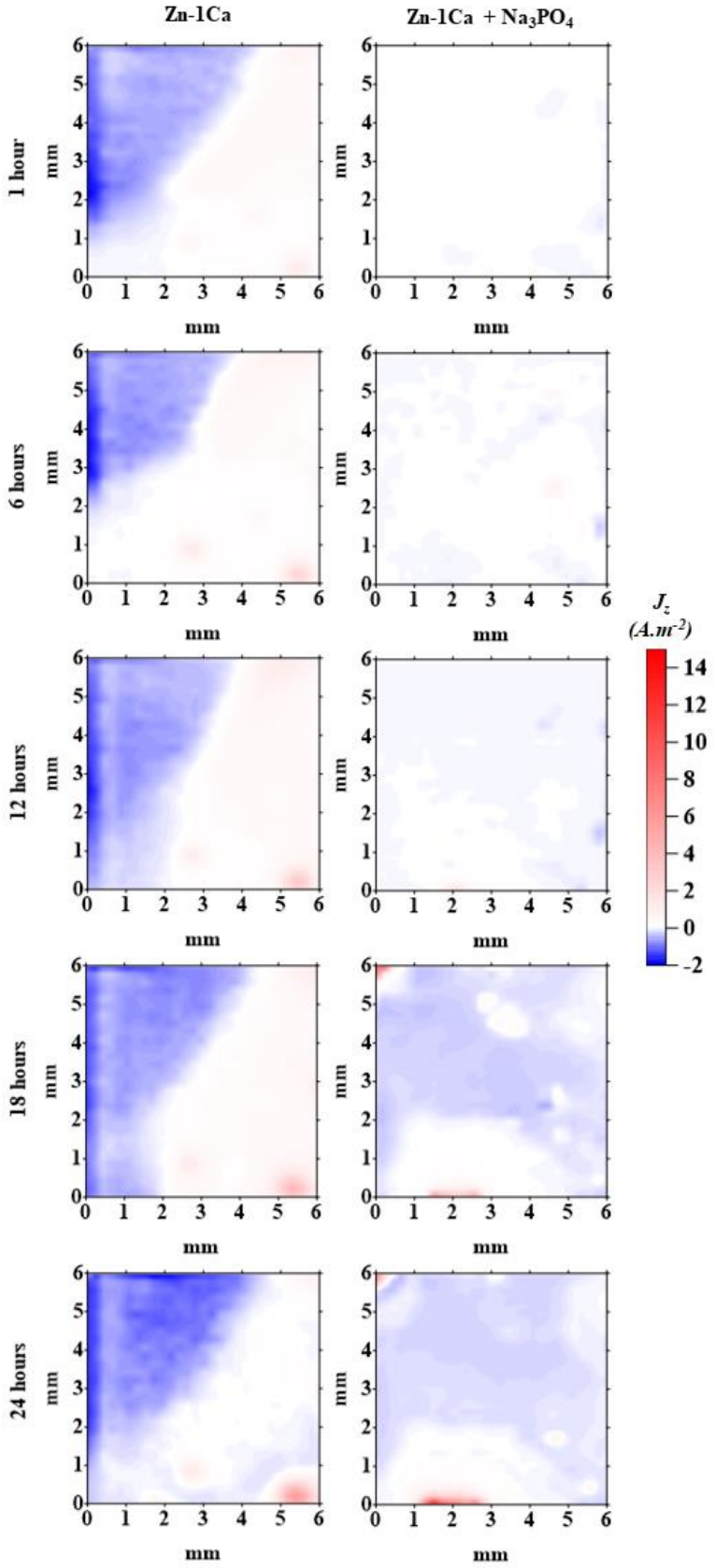

Figure 6.11: SVET false colour maps representing normal current density measured above Zn-1Ca immersed in pH 7 0.17 M NaCl containing 1 x 10^{-3} mol.dm^{-3} Na_3PO_4.

The SVET derived metal loss for both Zn and Zn-1Ca after immersion on pH 7 0.17 M NaCl containing 1 x 10^{-3} mol.dm^3 Na_3PO_4 for 24 hours and 48 hours are shown in Table 6.4. The errors shown are based on the standard deviation of three measurements. The SVET derived metal loss for Zn-1Ca is 1.19 g.m^{-2} compared to 5.12 g.m^{-2} for Zn for 24 hours. The addition of sodium phosphate had a significant impact on SVET derived metal loss. For both Zn and Zn-1Ca, a reduction in metal loss of 48 % and 72 % was observed respectively (Table 6.2 and Table 6.4). Although the metal loss for both Zn and Zn-1Ca has significantly decreased with the addition of sodium phosphate, the effectiveness to inhibit corrosion is much higher in Zn-1Ca compared to Zn. Zn-1Ca alloy in pH 7 0.17 M NaCl containing 1 x 10^{-3} mol.dm^3 sodium phosphate provide 76.75 % reduction in metal loss compared to Zn in pH 7 0.17 M NaCl.

The metal loss of Zn and Zn-1Ca with/without Na_3PO_4 are in the order Zn (9.83 g.m^{-2}) > Zn + Na_3PO_4 (5.12 g.m^{-2}) > Zn-1Ca (4.32 g.m^{-2}) > Zn-1Ca + Na_3PO_4 (1.19 g.m^{-2})(Table 6.2 and 6.4). Therefore, it is reasonable to assume that the significant enhancement of the effectiveness of Na_3PO_4 in Zn-1Ca could be due to the presence of Ca.

For 48 hours with Na_3PO_4 addition, the SVET derived metal loss for Zn-1Ca is reduced by 51 % to 7.01 g.m^{-2} compared to 14.57 g.m^{-2} for Zn. Therefore, Zn-1Ca provides twice the resistance compared to Zn. In a 48 hours SVET experiment, the metal loss from 25th hour to 48th hour with Na_3PO_4 addition and metal loss for 1 to 24 hours without Na_3PO_4 addition for Zn and Zn-1Ca is presented in Table 6.5. The metal loss for Zn and Zn-1Ca with/without Na_3PO_4 addition presented in Table 6.4 suggests that the Na_3PO_4 has minimal inhibition effect after 24 hours as the metal loss are similar.

Table 6.4: SVET derived metal loss for Zn and Zn - 1Ca after immersion in pH 7 0.17 M NaCl containing 1 x 10^{-3} mol.dm^3 sodium phosphate for 24 hours and 48 hours.

Sample	Metal loss for 24 hours (g.m^{-2})	Metal loss for 48 hours (g.m^{-2})
Zn	5.12 ± 1.27	14.57 ± 1.74
Zn-1Ca	1.19 ± 0.42	7.01 ± 2.84

Table 6.5 SVET derived metal loss for Zn and Zn - 1Ca after immersion in pH 7 0.17 M NaCl with and without 1 x 10-3 mol.dm3 sodium phosphate addition.

Sample	Metal loss from 25th hours - 48th hour with phosphate (g.m^{-2})	Metal loss for 24 hours without phosphate (g.m^{-2})
Zn	9.45 ± 1.94	9.83 ± 0.75
Zn-1Ca	5.82 ± 3.21	4.32 ± 1.67

The SVET derived hourly metal loss (average of three measurements) as a function of time for both Zn and Zn-1Ca during immersion on pH 7 0.17 M NaCl containing 1 x 10^{-3} mol.dm^3 Na_3PO_4 for 24 hours and 48 hours are presented in Figure 6.12 and Figure 6.13 respectively. The addition of phosphate has reduced the hourly metal loss from the onset for both Zn and Zn-1Ca. The addition of 1 x 10^{-3} mol.dm^3 Na_3PO_4 has significantly reduced the rate of hourly metal loss for both Zn and Zn-1Ca.

Figure 6.12 also demonstrates that the rate of hourly metal loss for Zn + Na_3PO_4 is lower than the Zn-1Ca for the first 12 hours however its performance degrades with time. Figure 6.13 shows that Na_3PO_4 is much more effective in presence of Ca however with time the effect of Ca and Na_3PO_4 nullifies as hourly metal loss plots for Zn + Na_3PO_4 and Zn-1Ca + Na_3PO_4 start to converge after 42 hours.

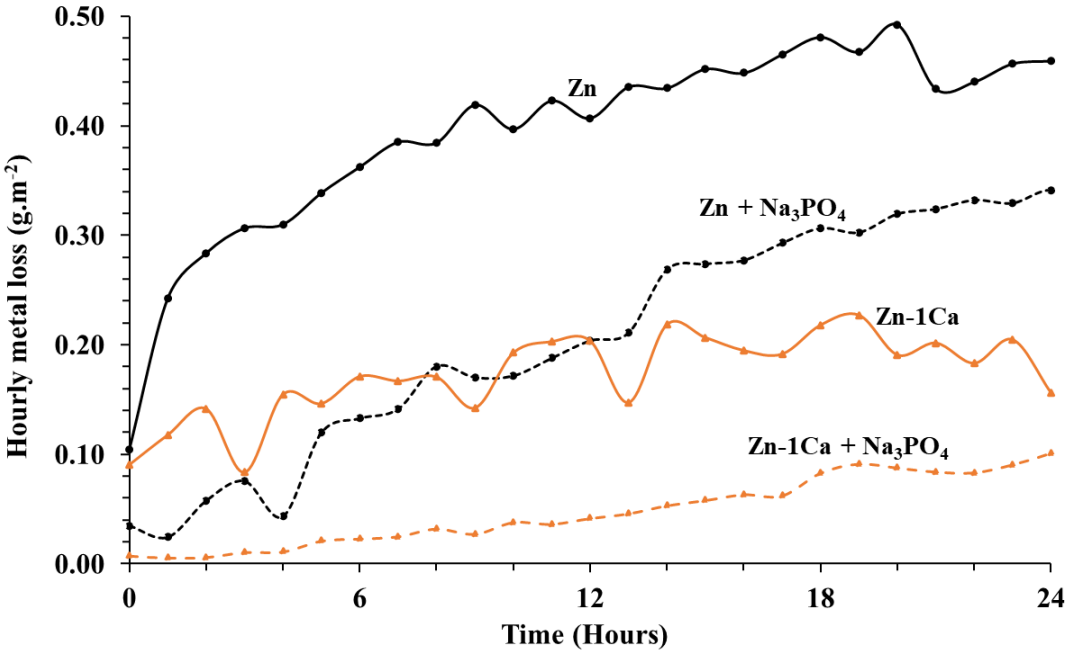

Figure 6.12: SVET derived hourly metal loss as a function of time for Zn and Zn-1Ca after immersion in pH 7 0.17 M NaCl with and without 1 x 10^{-3} mol.dm^3 Na_3PO_4 addition for 24 hours.

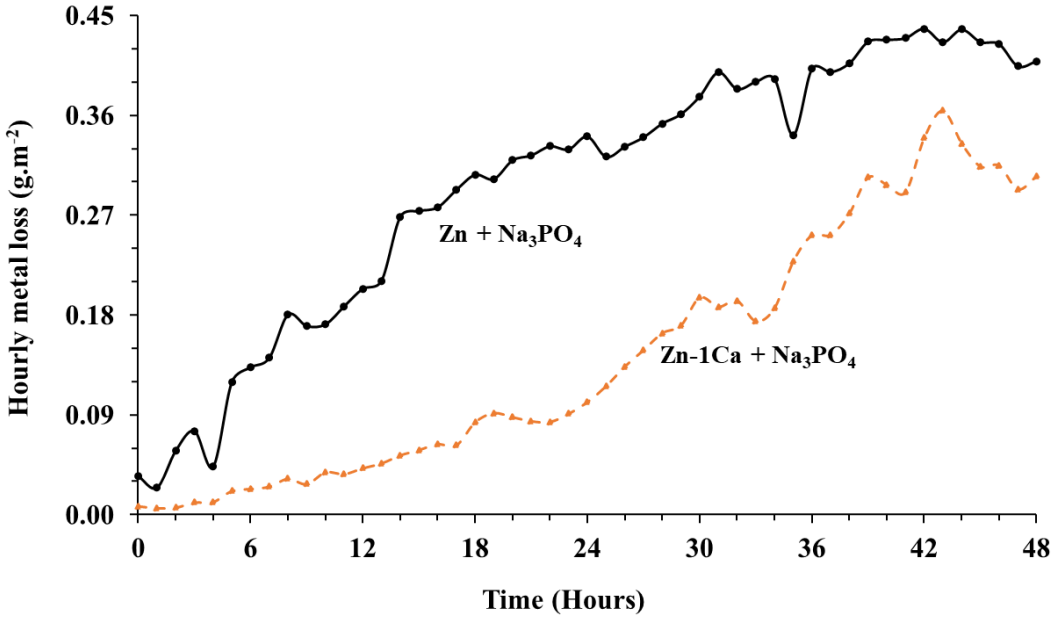

Figure 6.13: SVET derived hourly metal loss as a function of time for Zn and Zn-1Ca after immersion in pH 7 0.17 M NaCl containing 1 x 10^{-3} mol.dm^3 Na_3PO_4 for 48 hours.

6.5.2 Investigation of inhibition effect of Phosphate using Time-lapse Microscopy (TLM)

To assess the behaviour and role of Na_3PO_4 on the enhancement of corrosion resistance observed during SVET experiments further investigation was conducted utilizing TLM. Figure 6.14 shows optical microscope images of the surfaces of Zn after various times of immersion in pH 7 0.17 M NaCl containing 1 x 10^{-3} mol.dm^3 Na_3PO_4. Figure 6.14 features the images captured at 2 minutes, 2 hours, 6 hours, 12 hours, 18 hours and 24 hours. It can be observed that two anodes develop from the onset, concurrently darkening of the grain boundaries similar to Zn without Na_3PO_4 (see video V9). The addition of Na_3PO_4 has drastically altered the corrosion products precipitation phenomenon. For Zn, precipitation of corrosion products occurred at a certain distance away from the anode (Figure 6.6 and video V9) however in the presence of phosphate ions corrosion products are precipitated on top or in the vicinity of the anode. It is also observed that these corrosion products precipitation restricts the growth of the anodes. However, with time the initiated anodes grow and eventually lead to the formation of corrosion product ring as well. Throughout the experiment, the cathodic region remained clean free of corrosion product precipitation (left-hand side of images in Figure 6.14).

Figure 6.15 shows optical microscope images of the surface of Zn-1Ca at 2 minutes, 2 hours, 6 hours, 12 hours, 18 hours and 24 hours of immersion in pH 7 0.17 M NaCl containing 1 x 10^{-3} mol.dm^3 Na_3PO_4. The presence of phosphate ions has drastically altered the corrosion behaviour of the Zn-1Ca (Video V12 and Figure 6.15). Contrary to Zn where the formation of anodes at the Zn phase was observed at the onset, no such activity was observed for Zn-1Ca for an initial short period. However, with time darkening of the intermetallic $CaZn_{13}$ was observed. The darkening of intermetallic starts from the periphery of the exposed area and then grow inwards. As the darkening of the intermetallic continues it leads to a formation of a protective film that covers the whole of the exposed surface with some patches of uncovered area. For the experimental time of 24 hours, the bulk Zn phase is protected from anodic attack as no focal anodes as seen for Zn samples are observed for Zn-1Ca.

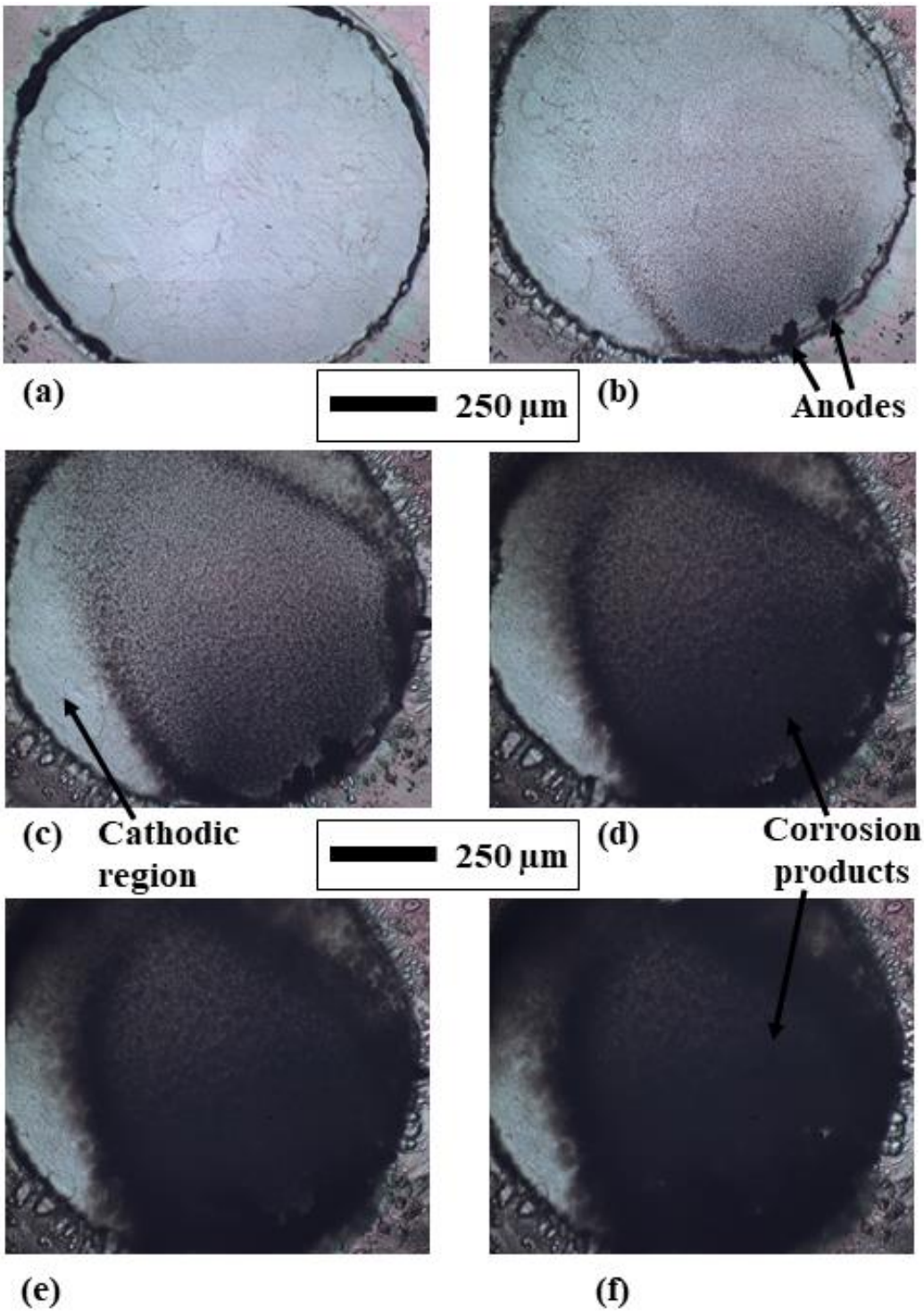

Figure 6.14: Time-lapse Microscope images of Zn taken in-situ under immersion conditions in pH 7 0.17 M NaCl containing 1 x 10^{-3} mol.dm^{-3} Na_3PO_4. The images (a-f) shown were taken at 2 minutes, 2 hours, 6 hours, 12 hours, 18 hours and 24 hours respectively

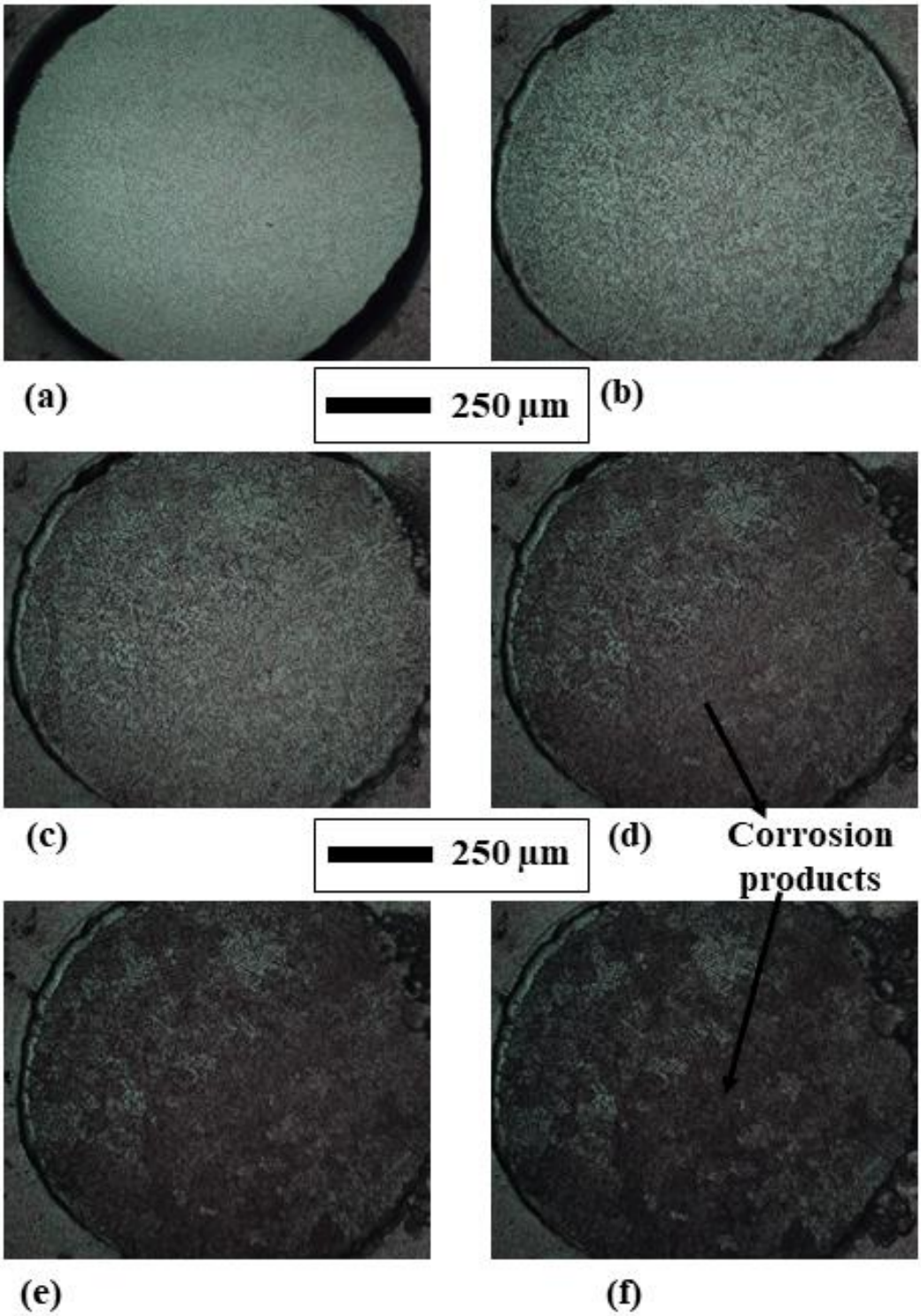

Figure 6.15: Time-lapse Microscope images of Zn-1Ca taken in-situ under immersion conditions in pH 7 0.17 M NaCl containing 1 x 10^{-3} mol.dm^{-3} Na_3PO_4. The images (a-f) shown were taken at 2 minutes, 2 hours, 6 hours, 12 hours, 18 hours and 24 hours respectively.

6.5.3 Electrochemical measurements

Open circuit potential measurements were performed to assess the behaviour of Zn and Zn-1Ca in pH 7 0.17 M NaCl containing 1 x 10^{-3} mol.dm^{-3} Na_3PO_4. The results obtained are presented in Figure 6.16. In the presence of phosphate ions, there is a steep rise towards positive potential from the onset for both Zn and Zn-1Ca. The gradient of the potential increment is higher in Zn-1Ca compared to Zn. Zn-1Ca takes ~1.5 hours to reach its highest potential of ~ -1.01 V vs SCE whereas Zn takes ~3.5 hours to reach its highest potential of ~ -1.02 V vs SCE.

From the highest positive potential for both samples, there is a similar linear shift towards negative potential and both obtain some degree of stabilisation at ~ 1.145 V vs SCE. However, Zn takes ~ 8 hours from the onset of the experiment to obtain this stabilisation compared to Zn-1Ca taking 12 hours. Also, in contrast to Zn, Zn-1Ca obtains some degree of stabilisation at ~ 1.026 V vs SCE for the duration of ~ 4 hours before final stabilisation at ~ 1.045 V vs SCE.

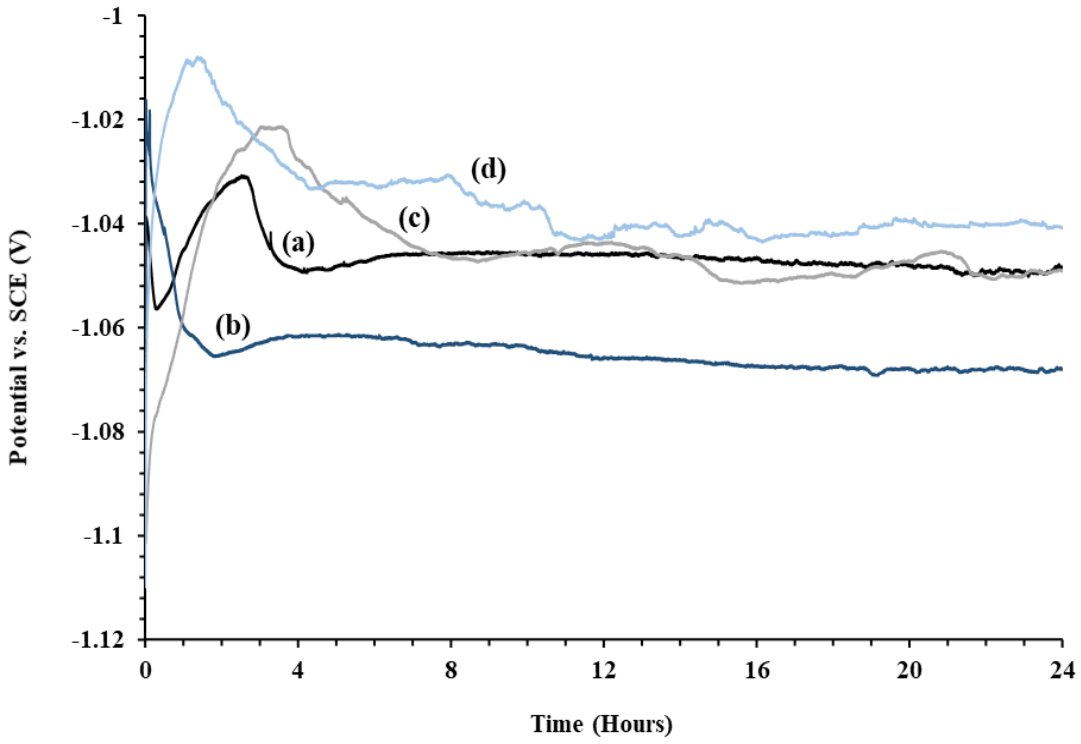

Figure 6.16: The time-dependent OCP for (a) Zn and (b) Zn-1Ca (c) Zn + Na_3PO_4 (d) Zn-1Ca + Na_3PO_4 immersed in pH 7 0.17 M NaCl for 24 hours.

The mechanism of corrosion product deposition observed in section 6.5.2 and Figure 6.14 along with the literature [32], [171] indicates that phosphate acts as an anodic inhibitor. Therefore, anodic polarization experiments were performed to gain more insight into this behaviour and are presented in Figure 6.17. The samples were allowed to corrode freely for 135 minutes to gain stable OCP in the electrolyte before conducting anodic polarization. This procedure was adopted because during the OCP measurement (Figure 6.16) for Zn and Zn-1Ca in the phosphate-containing electrolyte, approximately after 2 hours, Zn and Zn-1Ca obtained the positive most potential and hence suggesting the period of superior phosphate efficiency.

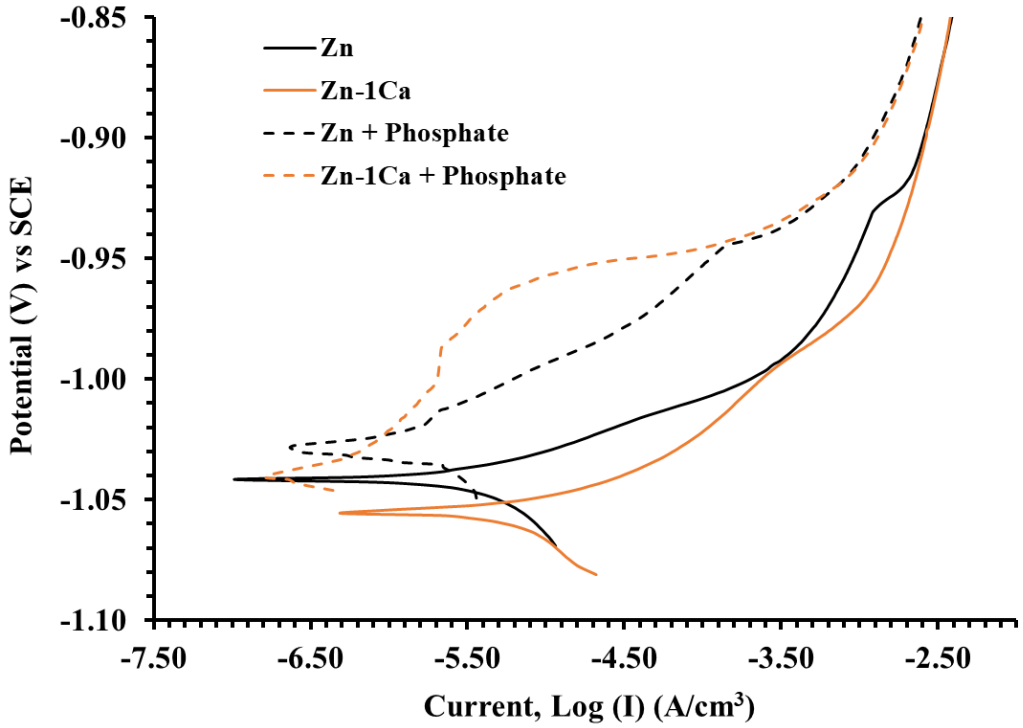

Figure 6.17: Plot of anodic polarisation curves for Zn, Zn-1Ca, Zn + Na_3PO_4 and Zn-1Ca + Na_3PO_4 immersed in pH 7 0.17 M NaCl after OCP stabalisation for 135 minutes.

The addition of 1 wt.% of Ca to Zn has shifted the E_{corr} by 20 mV to a more negative potential. The curves for Zn and Zn-1Ca appear to merge at ~ -1.0 V vs SCE and then again at ~ -0.92 V vs SCE. In presence of 1 x 10^{-3} mol.dm^3 Na_3PO_4 E_{corr} of Zn shifted to more positive potential (anodic) by 10 mV. Similarly for Zn-1Ca in presence of 1 x 10^{-3} mol.dm^3 Na_3PO_4 E_{corr} has shifted to more positive potential by 20 mV compared to Zn-1Ca with no phosphate addition however in comparison to

Zn + Na_3PO_4 E_{corr} shifted towards more negative potential (cathodically). Hence, phosphate ions behave as an anodic inhibitor on Zn as well as Zn-1Ca.

In presence of phosphate ions, Zn and Zn-1Ca inhibited the anodic current significantly. Furthermore, both Zn and Zn-1Ca show some degree of self-passivation behaviour however this behaviour is much more prominent in Zn-1Ca. The passivity for Zn was observed between -1.020 V vs SCE to - 0.9045 V vs SCE whereas for Zn-1Ca the passivity was observed between -1.030 V vs SCE to -0.9045 V vs SCE. The passivity was extended by 10 mV for Zn-1Ca compared to Zn in the phosphate-containing electrolyte.

LPR measurements were also performed as described in section 6.4.3 after OCP stabilisation for 135 minutes. Polarisation resistance (R_p) values are presented in Table 6.6. The R_p value of Zn-1Ca is slightly greater than Zn. Therefore, indicating Zn-1Ca provides better corrosion resistance as $i_{corr} \alpha 1/R_p$.

Table 6.6: Linear polarization resistance measurements obtained for Zn and Zn-1Ca where the samples were polarised by ±15 mV at a scan rate of 0.166 mVs^{-1} in pH 7 0.17 M NaCl after OCP stabilisation for 135 minutes.

Sample	Polarisation Resistance, R_p, ($Ohms.cm^{-2}$)
Zn + Na_3PO_4	13494.00
Zn - 1Ca + Na_3PO_4	15134.00

6.5.4 Discussion

Corrosion (SVET) experiments have indicated that the presence of phosphate ions has significantly enhanced the protection ability of Zn. The enhanced protection ability of Zn is further upgraded in presence of Calcium. TLM revealed a dramatic modification of the corrosion mechanism for both Zn and Zn-1Ca due to the addition of phosphate inhibitors.

For Zn, precipitation of triangular feature tapering away from the anodic site was observed (Figure 6.14) which implies that a local concentration of metal ions (Zn^{2+}) has been established [32]. These metal ions react with the phosphate ions present within the electrolyte to precipitate metal phosphate. As the concentration of metal ions is highest at the vicinity of the anode and decreases with distance away from the anode, hence, adequate metal ions (Zn^{2+}) are available to exceed the solubility limit,

as a result, precipitation of metal phosphate is observed local to the anodic site [32]. The precipitation of these metal phosphate at the vicinity of anodic sites impede the movement of Zn^{2+} ions consequently reducing the corrosion activity and increasing the corrosion resistance. This phenomenon of anodic inhibition on the Zn surface by phosphate ions is supported by the anodic polarization curve as E_{corr} is shifted to more positive potential (Figure 6.17).

In the case of Zn-1Ca, the Zn-Ca intermetallic corroded preferentially protecting the Zn phase (Figure 6.15(b)) releasing metal ions Zn^{2+} and Ca^{2+} into the electrolyte. These released metal ions of Zn and Ca react with phosphate ions present within the electrolyte to precipitate protective film (Figure 6.15) containing metal phosphates of Zn ($Zn_3(PO_4)_2$), Ca ($Ca_3(PO_4)_2$) and/or both (. It has been found that modification of zinc phosphate bath by calcium ions leads to the formation of a more compact structure $Zn_2Ca(PO_4)_2.2H_2O$ with better corrosion prevention ability [172], [173]. The initial release of Ca^{2+} ions through galvanic effects also enables the rise in solution pH as $Ca(OH)_2$ is much more soluble than $Zn(OH)_2$ and further dissociates of $Ca(OH)_2$ produces Ca^{2+} and OH^- ions, therefore, increasing the pH of the solution rapidly and passivate the surrounding Zn surface more quickly than when Zn^{2+} ions are released alone.

As the intermetallic is distributed throughout the exposed surface, a protective film is formed covering the entire exposed surface. This protective film act as a barrier and decreases the oxygen diffusion rate consequently reducing the corrosion rate. This phenomenon of inhibition on the Zn surface by phosphate ions in presence of Ca is supported by the anodic polarization curve as some degree of self passivation is observed (Figure 6.17). The extended passivity of added 10 mV of Zn-1Ca compared to Zn in presence of phosphate ions suggest the enhanced inhibitory effect in presence of Ca. Thus, extended passivity indicates the formation of additional metal phosphates in addition to zinc phosphate.

6.6 Conclusion

Investigation on the addition of 1 wt.% of Calcium on the microstructure and corrosion resistance afforded by Zn alloy has been concluded to show that;

- the alloying of Zn with Ca has resulted in the formation of an intermetallic $CaZn_{13}$
- The SVET derived metal loss decreased significantly with Ca addition. A 56 % decrease in the metal loss was measured for Zn-1Ca.
- TLM revealed that for Zn-1Ca, the corrosion initiates and preferentially grow via intermetallic $CaZn_{13}$
- A decrease in OCP and current during cathodic polarization was observed for Zn-1Ca
- LPR indicated a decrease in the corrosion rate by 2.5 times.

Investigation of the addition of 1×10^{-3} $mol.dm^{-3}$ Na_3PO_4 on the corrosion resistance and mechanism afforded by Zn and Zn-1Ca alloys has been concluded to show that;

- The SVET derived metal loss decreased by 48 % for Zn
- In presence of Calcium (i.e Zn-1Ca), the SVET derived metal loss decreased significantly. A 72 % decrease in metal loss was measured.
- TLM and anodic polarization measurements showed Na_3PO_4 acts as an anodic inhibitor on Zn. TLM revealed the precipitation of corrosion products in the vicinity of anodic sites and the anodic polarization curve displayed the shift of E_{corr} to a more positive potential.
- TLM and anodic polarization measurements showed Na_3PO_4 also acts as an anodic inhibitor in Zn-1Ca. TLM revealed a formation of the protective film covering the entire surface and the anodic polarization curve displayed some degree of extended passivation.

Chapter 7 Conclusion and further work

7.1 Conclusions

From the work presented within this thesis, several conclusions have been drawn and are outlined below.

ZMA alloy systems with varying amounts of Germanium (Ge) additions (0.19 wt.% - 1.8 wt.%) were investigated to establish their influence on microstructure and its impact on corrosion and mechanical properties. The addition of Ge has induced microstructural changes which led to the formation of a new phase, which was identified as magnesium germanide (Mg_2Ge) and existed in two different forms. Mg_2Ge plate-like structures were observed in all Ge additions and large Mg_2Ge crystals were observed only in the highest concentration.

The SVET experiments conducted in 0.17 M NaCl pH 7 showed improvement in corrosion resistance of ZMA with an increase in Ge content ($\geq$ 0.87 wt.%). A reduction of more than 50 % SVET derived metal loss was observed for the highest Ge concentration (ZMA-1.8 Ge). This significant improvement in corrosion resistance in the highest Ge concentration was also supported by the linear polarization measurements as R_p values were one order of magnitude larger compared to ZMA - 0 Ge.

A significant change in the corrosion mechanism of ZMA-1.8 Ge was shown by SVET and TLM. Both techniques showed a significant delay in anode formation for ZMA-1.8 Ge, with further analysis, post-corrosion of Mg_2Ge using SEM-EDS indicated leaching of Mg from Mg_2Ge during this period. In addition, the TLM experiment conducted in presence of phenolphthalein indicator showed an increase in electrolyte pH and absence of pH gradient which was observed for ZMA- 0 Ge. The observed corrosion enhancement was associated with the preferential anodic de-alloying of Mg_2Ge by loss of Mg^{2+}, leaving behind a surface enriched in Ge. The Mg^{2+} ions released reacts with the hydroxyl ions (OH^-) generated at the cathode to form $Mg(OH)_2$ and also as they do not hydrolyse they increase the pH of the electrolyte, creating a favourable environment where Zn surfaces are passive.

The formability of ZMA-Ge alloys was conducted using a Small Punch tensile test in conjunction with Vicker hardness and Nanoindentation techniques. The

nanoindentation technique revealed that for ZMA- 0 Ge, the eutectic phase is 2.3 times harder than the zinc phase. The Vicker hardness data showed hardness value (H_v) reduces with an increase in Ge concentration with ZMA- 1.8 Ge achieving a reduction of 18.78 %. The reduction in hardness with an increase in Ge concentration suggested the improvement in formability of ZMA-Ge alloys however the Small Punch tensile test revealed the opposite. All the ZMA-Ge alloys displayed a significant reduction in displacement at F_m. This reduction in formability is attributed to the presence of Mg_2Ge. Although the Ge addition led to the decrease in the eutectic phase, it is not 100 % eliminated and has been replaced by intermetallic Mg_2Ge which mostly likely behave as a site of crack formation under tensile load.

The potential of incorporating 'smart release' capsules within metallic coatings is further explored by embedding Mg_2Si particles as inhibitors in a zinc-rich powder-based galvanising system (Zn). SVET was utilized to study the inhibitory effects of these Mg_2Si particles in a 0.17 M NaCl pH 7 solution. SVET and post-corrosion of Mg_2Si analysis using SEM-EDS revealed Mg_2Si preferentially anodically dissolve galvanically protecting Zn surface. TLM was utilized to study the corrosion mechanism of Zn and Zn + Mg_2Si. TLM revealed that for Zn + Mg_2Si, due to the discharge of Mg^{2+} ions the pH of the electrolyte rise above 8. This increased pH creates a suitable environment for the precipitation of $Mg(OH)_2$ and passivates the Zn surface. The SKP was used to evaluate the ability of Mg_2Si to inhibit the corrosion driven coating failure mechanism. The presence of Mg_2Si particles have delayed the delamination initiation time and reduced the rate of delamination. The inhibitory efficiency improved with the increase in Mg_2Si particles present on the Zn surface.

The addition of 1 wt.% of Ca to Zn has resulted in the formation of new intermetallic $CaZn_{13}$. SVET experiments and linear polarization measurements revealed the improvement in corrosion resistance of Zn-1Ca. The SVET contour maps revealed the change in the corrosion mechanism of Zn-1Ca. In contrast to the formation of focal anodes observed for Zn, the exposed surface of Zn-1Ca was diagonally separated into anodic and cathodic halves. TLM identified that the anodes initiate off the $CaZn_{13}$ phase and grow preferentially via the $CaZn_{13}$. The improvement in corrosion resistance of Zn-1Ca is attributed to the formation of $Ca(OH)_2$ at the

cathodic site and hindering the oxygen diffusion rate. Also, $Ca(OH)_2$ being a strong base it dissociates to create an alkali environment where the Zn surface passivate.

The efficiency of Na_3PO_4 (1×10^{-3} mol.dm^{-3}) in 0.17 M NaCl pH 7 on Zn and Zn-1Ca was investigated. SVET showed a significant decrease in SVET derived metal loss with the addition of sodium phosphate however the effectiveness to inhibit corrosion is much higher in Zn-1Ca compared to Zn. TLM revealed that the presence of Na_3PO_4 has drastically altered the corrosion mechanism of both Zn and Zn-1Ca. For Zn, precipitation of corrosion products occurred in the vicinity of the anode restricting the growth of the anodes suggesting the formation of zinc metal phosphate. However, for Zn-1Ca, TLM revealed a different mechanism. As corrosion progressed a protective film developed covering the entire exposed surface which acts as a barrier and decreases the oxygen diffusion rate consequently reducing the corrosion rate. It is also suggested that during the corrosion of Zn-1Ca, both Zn^{2+} and Ca^{2+} are discharged therefore in the presence of Na_3PO_4 in addition to the formation of Zn and Ca metal phosphate more compact structural $Zn_2Ca(PO_4)_2.2H_2O$ with better corrosion prevention ability is formed consequently drastically enhancing corrosion resistance.

7.2 Further works

Although quaternary metallic coating systems have been the subject of interest not much research has been undertaken to date. Investigations into the addition of a quaternary element to the ternary ZMA system have demonstrated promising results in terms of corrosion enhancement however in-depth investigations by which it inhibits has not been undertaken therefore is not well understood.

Here, we conducted an in-depth investigation using various techniques to understand the effect of the quaternary element (Germanium) addition to the ZMA system. The study provided us with valuable insight into how quaternary metallic coating system ZMA-Ge inhibits. Conducting physical metal loss experiments on ZMA-Ge would quantify the corrosion improvement as the techniques utilized were semi-quantitative. Furthermore, the investigations were conducted on alloy rather than coating therefore the production and investigation of ZMA-Ge coating are highly suggested.

The use of Mg_2Si particulates as corrosion inhibitors also displayed encouraging results in terms of improving resistance to aqueous and cathodic delamination corrosion, therefore, incorporating Mg_2Si particles on the outer layer of HDG Zn coating would be something to pursue.

In conclusion, there are several areas worthy of further investigation in the near future to better understand the results obtained so far and are listed below.

- Characterisation of corrosion products of ZMA-Ge alloys using SEM, XRD and SIM etc.
- Uniaxial tensile test of ZMA-Ge alloys.
- A hardness measurement of ZMA-Ge alloys using indentation plastometry.
- Hardness test of Mg_2Ge using nanoindentation technique.
- Repeats of cathodic delamination experiments using Mg_2Si as inhibitors and also with a range of varying amounts of Mg_2Si in Zn surface.
- Blot test using universal indicator paper on Zn and Zn-1Ca during corrosion.
- Characterisation of corrosion products of Zn + Phosphate and Zn-1Ca + Phosphate using SEM, XRD and SIMS etc.
- Cathodic polarization of both Zn + Phosphate and Zn-1Ca + Phosphate systems.

- Hardness measurement of Zn-1Ca using Vicker Hardness, Nanoindentation and indentation plastometry.
- Production of Zn-1Ca coatings and conduct electrochemical experiments.
- Investigate the varying amount of Ca addition into Zn alloy and coating system.
- Investigate a range of sodium phosphate concentrations on Zn and Zn-1Ca.

Chapter 8 References

8.1 References:

[1] "Global crude steel output increases by 3.4% in 2019," *Worldsteel Association*. https://www.worldsteel.org/media-centre/press-releases/2020/Global-crude-steel-output-increases-by-3.4--in-2019.html (accessed Mar. 23, 2020).

[2] G. Koch, J. Varney, N. Thopson, O. Moghissi, M. Gould, and J. Payer, "International Measures of Prevention , Application , and Economics of Corrosion Technologies Study," *NACE Int.*, pp. 1–216, 2016, [Online]. Available: http://impact.nace.org/.

[3] B. Chatterjee, "Zinc Alloy Plating – General Considerations," *Jahrb. Oberflachentechnik*, no. January 2005, pp. 7–30, 2018, doi: 10.1201/9781351074025.

[4] W. J. Smith and F. E. Goodwin, "Hot Dip Coatings," *Ref. Modul. Mater. Sci. Mater. Eng.*, no. November 2015, pp. 1–19, 2017, doi: 10.1016/b978-0-12-803581-8.09214-6.

[5] W. Schulz and M. Thiele, *General Hot-Dip Galvanizing*, 1st ed. 2012.

[6] P. Pokorny, J. Kolisko, L. Balik, and P. Novak, "Effect of chemical composition of steel on the structure of hot – Dip galvanized coating," *Metalurgija*, vol. 55, no. 1, pp. 115–118, 2016.

[7] E. Palma, J. M. Puente, and M. Morcillo, "The atmospheric corrosion mechanism of 55%Al-Zn coating on steel," *Corros. Sci.*, vol. 40, pp. 61–68, 1998, doi: 10.1016/S0010-938X(97)00112-1.

[8] D. Persson, D. Thierry, and N. LeBozec, "Corrosion product formation on Zn55Al coated steel upon exposure in a marine atmosphere," *Corros. Sci.*, vol. 53, pp. 720–726, 2011, doi: 10.1016/j.corsci.2010.11.004.

[9] H. Townsend and T. C. Consultants, "Atmospheric Corrosion Behavior of Aluminum- Zinc Alloy-Coated Steel," *ASTM Spec. Tech. Publ.*, pp. 165–184, 1978.

[10] E. Diler, B. Rouvellou, S. Rioual, B. Lescop, G. Nguyen Vien, and D. Thierry, “Characterization of corrosion products of Zn and Zn-Mg-Al coated steel in a marine atmosphere,” *Corros. Sci.*, vol. 87, pp. 111–117, 2014, doi: 10.1016/j.corsci.2014.06.017.

[11] N. LeBozec *et al.*, “Corrosion performance of Zn-Mg-Al coated steel in accelerated corrosion tests used in the automotive industry and field exposures,” *Mater. Corros.*, vol. 64, no. 11, pp. 969–978, Nov. 2013, doi: 10.1002/maco.201206959.

[12] D. Persson, D. Thierry, N. LeBozec, and T. Prosek, “In situ infrared reflection spectroscopy studies of the initial atmospheric corrosion of Zn-Al-Mg coated steel,” *Corros. Sci.*, vol. 72, pp. 54–63, 2013, doi: 10.1016/j.corsci.2013.03.005.

[13] N. Wint *et al.*, “The Effect of Microstructural Refinement on the Localized Corrosion of Model Zn-Al-Mg Alloy Coatings on Steel,” *J. Electrochem. Soc.*, vol. 166, pp. C3147–C3158, 2019, doi: 10.1149/2.0171911jes.

[14] N. LeBozec, D. Thierry, D. Persson, C. K. Riener, and G. Luckeneder, “Influence of microstructure of zinc-aluminium-magnesium alloy coated steel on the corrosion behavior in outdoor marine atmosphere,” *Surf. Coatings Technol.*, vol. 374, pp. 897–909, 2019, doi: 10.1016/j.surfcoat.2019.06.052.

[15] S. Schuerz *et al.*, “Corrosion behaviour of Zn – Al – Mg coated steel sheet in sodium chloride-containing environment,” *Corros. Sci.*, vol. 51, no. 10, pp. 2355–2363, 2009, doi: 10.1016/j.corsci.2009.06.019.

[16] J. Elvins, J. A. Spittle, J. H. Sullivan, and D. A. Worsley, “The effect of magnesium additions on the microstructure and cut edge corrosion resistance of zinc aluminium alloy galvanised steel,” *Corros. Sci.*, vol. 50, no. 6, pp. 1650–1658, 2008, doi: 10.1016/j.corsci.2008.02.005.

[17] T. Prosek, A. Nazarov, F. Goodwin, J. Šerák, and D. Thierry, “Improving corrosion stability of Zn-Al-Mg by alloying for protection of car bodies,” *Surf. Coatings Technol.*, vol. 306, pp. 439–447, 2016, doi: 10.1016/j.surfcoat.2016.03.062.

[18] S. Mehraban, J. Malone, J. Sullivan, D. Penney, and S. Brown, “Increased Corrosion Resistance of Zinc Magnesium Aluminum Galvanised Coating through Germanium Additions,” *ECS Trans.*, vol. 75, no. 30, pp. 1–15, 2017, doi: 10.1149/07530.0001ecst.

[19] F. Scholz, *Electroanalytical methods: Guide to experiments and applications*. Berlin, 2010.

[20] J. H. Frantz and J. C. Scully, *The Fundamentals of Corrosion*. Taylor & Francis Ltd, 1976.

[21] J. Gelvele, *Corrosion: Aqueous Processes and Passive Films*, vol. 23. New York: Academic Press, 1983.

[22] P. A. Schweitzer, P.E., *Fundamentals of Corrosion*. Cambridge: CRC Press, 2009.

[23] Z. Ahmad, *Principles of Corrosion Engineering and Corrosion Control*. Elsevier, 2006.

[24] E. Lahti, J. Leavitt, and J. Zhang, “Material corrosion in a reactor containment sump following a loss-of-coolant accident,” *Prog. Nucl. Energy*, vol. 75, pp. 1–9, 2014, doi: 10.1016/j.pnucene.2014.03.004.

[25] V. S. Saji, “Review of rare-earth-based conversion coatings for magnesium and its alloys,” *J. Mater. Res. Technol.*, vol. 8, no. 5, pp. 5012–5035, Sep. 2019, doi: 10.1016/j.jmrt.2019.08.013.

[26] G. P. Bierwagen, “Reflections on corrosion control by organic coatings,” *Prog. Org. Coatings*, vol. 28, no. 1, pp. 43–48, May 1996, doi: 10.1016/0300-9440(95)00588-9.

[27] O. Gharbi, S. Thomas, C. Smith, and N. Birbilis, “Chromate replacement: what does the future hold?,” *npj Mater. Degrad.*, vol. 2, no. 1, p. 12, Dec. 2018, doi: 10.1038/s41529-018-0034-5.

[28] F. H. Scholes *et al.*, “Chromate leaching from inhibited primers,” *Prog. Org. Coatings*, vol. 56, no. 1, pp. 23–32, May 2006, doi: 10.1016/j.porgcoat.2006.01.015.

[29] J. K. Hawkins, H. S. Isaacs, S. M. Heald, J. Tranquada, G. E. Thompson, and G. C. Wood, “An investigation of chromate inhibitors on aluminium using fluorescence detection of X-ray absorption,” *Corros. Sci.*, vol. 27, no. 4, pp. 391–399, Jan. 1987, doi: 10.1016/0010-938X(87)90081-3.

[30] S. Morsch, S. Emad, L. A. Farren, M. D. Goodall, S. B. Lyon, and S. R. Gibbon, “The Unexpected Role of Carbonate Impurities in Polyphosphate Corrosion Inhibition,” *Sci. Rep.*, vol. 8, no. 1, pp. 2–8, 2018, doi: 10.1038/s41598-018-35512-2.

[31] I. M. Zin, V. I. Pokhmurskii, J. D. Scantlebury, and S. B. Lyon, “Model Electrochemical Cell Study of Cut-Edge Corrosion Inhibition on Coil-Coated Steel Sheet by Chromate-, Phosphate-, and Calcium-Containing Pigments,” *J. Electrochem. Soc.*, vol. 148, no. 8, p. B293, 2001, doi: 10.1149/1.1381072.

[32] J. Sullivan, N. Cooze, C. Gallagher, T. Lewis, T. Prosek, and D. Thierry, “In situ monitoring of corrosion mechanisms and phosphate inhibitor surface deposition during corrosion of zinc–magnesium–aluminium (ZMA) alloys using novel time-lapse microscopy,” *Faraday Discuss.*, vol. 180, pp. 361–379, 2015, doi: 10.1039/C4FD00251B.

[33] I. M. Zin, S. B. Lyon, and V. I. Pokhmurskii, “Corrosion control of galvanized steel using a phosphate/calcium ion inhibitor mixture,” *Corros. Sci.*, vol. 45, no. 4, pp. 777–788, Apr. 2003, doi: 10.1016/S0010-938X(02)00130-0.

[34] S. M. A. Shibli, B. N. Meena, and R. Remya, “A review on recent approaches in the field of hot dip zinc galvanizing process,” *Surf. Coatings Technol.*, vol. 262, pp. 210–215, Jan. 2015, doi: 10.1016/j.surfcoat.2014.12.054.

[35] M. J. Hornsby, “1. Hot-dip Galvanizing,” in *Hot-dip Galvanizing*, vol. 35, no. 4, Rugby, Warwickshire, United Kingdom: Practical Action Publishing, 1995, pp. 1–69.

[36] E. Almeida, M. Morcillo, and B. Rosales, “Atmospheric corrosion of zinc Part 1: Rural and urban atmospheres,” *Br. Corros. J.*, vol. 35, no. 4, pp. 284–288, Apr. 2000, doi: 10.1179/000705900101501353.

[37] S. Maeda, “Surface chemistry of galvanized steel sheets relevant to adhesion

performance," *Prog. Org. Coatings*, vol. 28, no. 4, pp. 227–238, Aug. 1996, doi: 10.1016/0300-9440(95)00610-9.

[38] S. Feliu, M. Morcillo, and S. Feliu, "The prediction of atmospheric corrosion from meteorological and pollution parameters—II. Long-term forecasts," *Corros. Sci.*, vol. 34, no. 3, pp. 415–422, Mar. 1993, doi: 10.1016/0010-938X(93)90113-U.

[39] P. R. Seré, J. D. Culcasi, C. I. Elsner, and A. R. Di Sarli, "Factores que afectan a la estructura de los recubrimientos de cinc obtenidos por inmersión," *Rev. Metal.*, vol. 33, no. 6, pp. 376–381, Dec. 1997, doi: 10.3989/revmetalm.1997.v33.i6.832.

[40] N. C. Hosking, M. A. Ström, P. H. Shipway, and C. D. Rudd, "Corrosion resistance of zinc-magnesium coated steel," *Corros. Sci.*, vol. 49, no. 9, pp. 3669–3695, 2007, doi: 10.1016/j.corsci.2007.03.032.

[41] A. E. Ares and L. M. Gassa, "Corrosion susceptibility of Zn-Al alloys with different grains and dendritic microstructures in Nacl solutions," *Corros. Sci.*, vol. 59, pp. 290–306, 2012, doi: 10.1016/j.corsci.2012.03.015.

[42] D. de la Fuente, J. G. Castaño, and M. Morcillo, "Long-term atmospheric corrosion of zinc," *Corros. Sci.*, vol. 49, no. 3, pp. 1420–1436, Mar. 2007, doi: 10.1016/j.corsci.2006.08.003.

[43] E. Del Angel, R. Vera, and F. Corvo, "Atmospheric corrosion of galvanised steel in different environments in Chile and Mexico," *Int. J. Electrochem. Sci.*, vol. 10, pp. 7985–8004, 2015.

[44] W. Miao, I. S. Cole, A. K. Neufeld, and S. Furman, "Pitting Corrosion of Zn and Zn-Al Coated Steels in pH 2 to 12 NaCl Solutions," *J. Electrochem. Soc.*, vol. 157, p. C7, 2007, doi: 10.1149/1.2372691.

[45] N. Wint, K. Khan, J. H. Sullivan, and H. N. McMurray, "Concentration Effects on the Spatial Interaction of Corrosion Pits Occurring on Zinc in Dilute Aqueous Sodium Chloride," *J. Electrochem. Soc.*, vol. 166, pp. 3028–3038, 2019, doi: 10.1149/2.0051911jes.

[46] D. Nakhaie and E. Asselin, "Dissolution Kinetics of Pure Zinc: The Effect of

Bulk Solution Concentration and Temperature Studied by the Lead-In Pencil Electrode Technique," *J. Electrochem. Soc.*, vol. 164, p. C758, 2017, doi: 10.1149/2.0661713jes.

[47] E. E. Abd El Aal, "Measurements of pitting corrosion currents of zinc in near neutral media," *Corros. Sci.*, vol. 44, no. 9, pp. 2041–2053, Sep. 2002, doi: 10.1016/S0010-938X(02)00026-4.

[48] S. Böhm, J. H. Sullivan, and D. A. Worsley, "A new corrosion test for organically coated galvanised steel products," *Mater. Corros.*, vol. 52, no. 7, pp. 540–545, Jul. 2001, doi: 10.1002/1521-4176(200107)52:7<540::AID-MACO540>3.0.CO;2-S.

[49] J. Sullivan, C. Weirman, J. Kennedy, and D. Penney, "Influence of steel gauge on the microstructure and corrosion performance of zinc alloy coated steels," *Corros. Sci.*, vol. 52, no. 5, pp. 1853–1862, May 2010, doi: 10.1016/j.corsci.2010.02.032.

[50] G. W. Walter, "A comparison of single frequency and wide frequency range impedance tests for painted metals," *Corros. Sci.*, vol. 30, no. 6–7, pp. 617–629, 1990, doi: 10.1016/0010-938X(90)90027-3.

[51] D. A. Worsley, H. N. McMurray, J. H. Sullivan, and I. P. Williams, "Quantitative Assessment of Localized Corrosion Occurring on Galvanized Steel Samples Using the Scanning Vibrating Electrode Technique," *Corrosion*, vol. 60, no. 5, pp. 437–447, May 2004, doi: 10.5006/1.3299239.

[52] N. Wint, P. Ansell, J. Edy, G. Williams, and H. N. McMurray, "A Method for Quantifying the Synergistic Inhibitory Effect of Corrosion Inhibitors When Used in Combination: A 'Chromate Generating Coating,'" *J. Electrochem. Soc.*, vol. 166, p. 580, 2019, doi: 10.1149/2.1021914jes.

[53] W. Fürbeth and M. Stratmann, "Scanning Kelvin Probe investigations on the delamination of polymeric coatings from metallic surfaces," *Prog. Org. Coatings*, vol. 39, no. 1, pp. 23–29, 2000, doi: 10.1016/S0300-9440(00)00095-3.

[54] M. Stratmann, A. Leng, W. Fürbeth, H. Streckel, H. Gehmecker, and K. H.

Große-Brinkhaus, “The scanning Kelvin probe; a new technique for the in situ analysis of the delamination of organic coatings,” *Prog. Org. Coatings*, pp. 261–267, 1996, doi: 10.1016/0300-9440(94)00542-7.

[55] X. Zhang, C. Leygraf, and I. Odnevall Wallinder, “Atmospheric corrosion of Galfan coatings on steel in chloride-rich environments,” *Corros. Sci.*, vol. 73, pp. 62–71, Aug. 2013, doi: 10.1016/j.corsci.2013.03.025.

[56] P. L. Cabot, M. Cortés, F. A. Centellas, J. A. Garrido, and E. Pérez, “Potentiodynamic passivation of zinc in aqueous KOH solutions,” *J. Electroanal. Chem.*, vol. 201, pp. 85–100, 1986, doi: 10.1016/0022-0728(86)90089-6.

[57] M. G. Alvarez and J. R. Galvele, “PITTING OF HIGH PURITY ZINC AND PITTING POTENTIAL SIGNIFICANCE.,” *Corrosion*, vol. 32, pp. 285–294, 1976, doi: 10.5006/0010-9312-32.7.285.

[58] S. Feliu and V. Barranco, “XPS study of the surface chemistry of conventional hot-dip galvanised pure Zn, galvanneal and Zn–Al alloy coatings on steel,” *Acta Mater.*, vol. 51, no. 18, pp. 5413–5424, Oct. 2003, doi: 10.1016/S1359-6454(03)00408-7.

[59] J. Sullivan, D. Penney, J. Elvins, and K. Khan, “The effect of ultrasonic irradiation on the microstructure and corrosion rate of a Zn–4.8wt.% Al galvanising alloy used in high performance construction coatings,” *Surf. Coatings Technol.*, vol. 306, pp. 480–489, Nov. 2016, doi: 10.1016/j.surfcoat.2016.01.050.

[60] F. Weinberg, M. Mager, and L. Frederick, “Segregation in Galfan Hot Dipped Sheet Steel,” *Can. Metall. Q.*, vol. 29, no. 2, pp. 163–166, Apr. 1990, doi: 10.1179/cmq.1990.29.2.163.

[61] J. Elvins, J. a. Spittle, and D. A. Worsley, “Relationship between microstructure and corrosion resistance in Zn–Al alloy coated galvanised steels,” *Corros. Eng. Sci. Technol.*, vol. 38, no. 3, pp. 197–204, Sep. 2003, doi: 10.1179/147842203770226924.

[62] A. R. Marder, “The metallurgy of zinc-coated steel,” *Prog. Mater. Sci.*, vol.

45, no. 3, pp. 191–271, Jun. 2000, doi: 10.1016/S0079-6425(98)00006-1.

[63] J. Elvins, J. A. Spittle, and D. A. Worsley, “Microstructural changes in zinc aluminium alloy galvanising as a function of processing parameters and their influence on corrosion,” *Corros. Sci.*, vol. 47, no. 11, pp. 2740–2759, 2005, doi: 10.1016/j.corsci.2004.11.011.

[64] M. Salgueiro Azevedo, C. Allély, K. Ogle, and P. Volovitch, “Corrosion mechanisms of Zn(Mg,Al) coated steel: 2. The effect of Mg and Al alloying on the formation and properties of corrosion products in different electrolytes,” *Corros. Sci.*, vol. 90, pp. 482–490, Jan. 2015, doi: 10.1016/j.corsci.2014.07.042.

[65] D. J. Penney, J. H. Sullivan, and D. A. Worsley, “Investigation into the effects of metallic coating thickness on the corrosion properties of Zn-Al alloy galvanising coatings,” *Corros. Sci.*, vol. 49, no. 3, pp. 1321–1339, 2007, doi: 10.1016/j.corsci.2006.07.006.

[66] T. Tsujimura, A. Komatsu, and A. Andoh, “International Conference on Zinc and Zinc Alloy Coated Steel,” in *Galvatech “01,”* 2001, pp. 145–152.

[67] S. Schürz *et al.*, “Chemistry of corrosion products on Zn-Al-Mg alloy coated steel,” *Corros. Sci.*, vol. 52, no. 10, pp. 3271–3279, 2010, doi: 10.1016/j.corsci.2010.05.044.

[68] M. B. Dmitriy Petrov, Andy Watson, Joachim Gröbner, Peter Rogl, Jean-Claude Tedenac and V. Turkevich, “Al-Mg-Zn (Aluminium - Magnesium - Zinc),” in *Light Metal sustems. Part 3*, G. Effenberg and S. Ilyenko, Eds. 2006, pp. 191–209.

[69] Mehraban Shahin, “Corrosion mechanism, inhibition and mechanical properties of zinc magnesium aluminium alloy coated galvanised steel,” Swansea University, 2013.

[70] N. Lebozec, D. Thierry, M. Rohwerder, D. Persson, G. Luckeneder, and L. Luxem, “Effect of carbon dioxide on the atmospheric corrosion of Zn – Mg – Al coated steel,” *Corros. Sci.*, vol. 74, pp. 379–386, 2013, doi: 10.1016/j.corsci.2013.05.011.

[71] P. Volovitch, T. N. Vu, C. Allély, A. Abdel Aal, and K. Ogle, “Understanding corrosion via corrosion product characterization: II. Role of alloying elements in improving the corrosion resistance of Zn-Al-Mg coatings on steel,” *Corros. Sci.*, vol. 53, no. 8, pp. 2437–2445, 2011, doi: 10.1016/j.corsci.2011.03.016.

[72] T. Prosek, A. Nazarov, U. Bexell, D. Thierry, and J. Serak, “Corrosion mechanism of model zinc-magnesium alloys in atmospheric conditions,” *Corros. Sci.*, vol. 50, no. 8, pp. 2216–2231, 2008, doi: 10.1016/j.corsci.2008.06.008.

[73] P. Volovitch, C. Allely, and K. Ogle, “Understanding corrosion via corrosion product characterization: I. Case study of the role of Mg alloying in Zn-Mg coating on steel,” *Corros. Sci.*, vol. 51, no. 6, pp. 1251–1262, 2009, doi: 10.1016/j.corsci.2009.03.005.

[74] T. Prosek *et al.*, “Effect of the microstructure of Zn-Al and Zn-Al-Mg model alloys on corrosion stability,” *Corros. Sci.*, vol. 110, pp. 71–81, Sep. 2016, doi: 10.1016/j.corsci.2016.04.022.

[75] T. Prosek, D. Persson, J. Stoulil, and D. Thierry, “Composition of corrosion products formed on Zn–Mg, Zn–Al and Zn–Al–Mg coatings in model atmospheric conditions,” *Corros. Sci.*, vol. 86, pp. 231–238, Sep. 2014, doi: 10.1016/j.corsci.2014.05.016.

[76] E. Diler, S. Rioual, B. Lescop, D. Thierry, and B. Rouvellou, “Chemistry of corrosion products of Zn and MgZn pure phases under atmospheric conditions,” *Corros. Sci.*, vol. 65, pp. 178–186, Dec. 2012, doi: 10.1016/j.corsci.2012.08.014.

[77] B. Li *et al.*, “Investigation of the corrosion behaviors of continuously hot-dip galvanizing Zn–Mg coating,” *Surf. Coatings Technol.*, vol. 206, pp. 3989–3999, May 2012, doi: 10.1016/j.surfcoat.2012.03.079.

[78] J. Sullivan, S. Mehraban, and J. Elvins, “In situ monitoring of the microstructural corrosion mechanisms of zinc–magnesium–aluminium alloys using time lapse microscopy,” *Corros. Sci.*, vol. 53, no. 6, pp. 2208–2215, Jun. 2011, doi: 10.1016/j.corsci.2011.02.043.

[79] R. Bolton *et al.*, “Studying the Influence of Mg Content on the Microstructure and Associated Localized Corrosion Behavior of Zn-Mg PVD Coatings Using SVET-TLI,” *J. Electrochem. Soc.*, vol. 166, pp. C3305–C3315, 2019, doi: 10.1149/2.0391911jes.

[80] M. Zhang, G. Zhou, H. Sun, X. Teng, and Z. Zhao, “Effects of Ti and Zr elements addition on the microstructure and corrosion resistance of Zn-2.5Al-2Mg alloy,” *Mater. Res. Express*, vol. 7, p. 026525, 2020, doi: 10.1088/2053-1591/ab6fab.

[81] T. Lostak *et al.*, “Zr-based conversion layer on Zn-Al-Mg alloy coated steel sheets: Insights into the formation mechanism,” *Electrochim. Acta*, vol. 137, pp. 65–74, 2014, doi: 10.1016/j.electacta.2014.05.163.

[82] S. Verdier, N. van der Laak, F. Dalard, J. Metson, and S. Delalande, “An electrochemical and SEM study of the mechanism of formation, morphology, and composition of titanium or zirconium fluoride-based coatings,” *Surf. Coatings Technol.*, vol. 200, no. 9, pp. 2955–2964, 2006, doi: 10.1016/j.surfcoat.2004.10.139.

[83] J. Hölzl and F. K. Schulte, “Work function of metals,” 1979, pp. 1–150.

[84] V. E. Henrich, P. A. Cox, and U. Diebold, “The Surface Science of Metal Oxides,” *Phys. Today*, vol. 48, no. 2, pp. 58–59, Feb. 1995, doi: 10.1063/1.2807916.

[85] Topic Inc, “Relation between Salt Solution and Sugar Concentration (Brix) and refractive index at 20oC.” https://www.topac.com/Salinity_brix.html (accessed Apr. 13, 2020).

[86] A. C. Bastos, M. C. Quevedo, O. V. Karavai, and M. G. S. Ferreira, “Review—On the Application of the Scanning Vibrating Electrode Technique (SVET) to Corrosion Research,” *J. Electrochem. Soc.*, vol. 164, no. 14, pp. C973–C990, Nov. 2017, doi: 10.1149/2.0431714jes.

[87] A. C. Bastos, M. L. Zheludkevich, and M. G. S. Ferreira, “Concerning the efficiency of corrosion inhibitors as given by SVET,” *Port. Electrochim. Acta*, 2008, doi: 10.4152/pea.200801047.

[88] H. N. McMurray, S. M. Powell, and D. A. Worsley, “Mechanistic changes in cut edge corrosion induced by variation of inhibitor pigmentation in organically coated galvanised steel,” *Br. Corros. J.*, vol. 36, no. 1, pp. 42–48, Jan. 2001, doi: 10.1179/000705901101501479.

[89] S. Böhm, H. . McMurray, S. . Powell, and D. . Worsley, “Photoelectrochemical investigation of corrosion using scanning electrochemical techniques,” *Electrochim. Acta*, vol. 45, no. 14, pp. 2165–2174, Mar. 2000, doi: 10.1016/S0013-4686(99)00442-9.

[90] G. Williams and H. Neil McMurray, “Localized Corrosion of Magnesium in Chloride-Containing Electrolyte Studied by a Scanning Vibrating Electrode Technique,” *J. Electrochem. Soc.*, vol. 155, no. 7, p. C340, 2008, doi: 10.1149/1.2918900.

[91] W. F. Kieffer, “Tables of physical and chemical constants. Eleventh edition (Kaye, G.W.C., and Laby, T.H.),” *J. Chem. Educ.*, p. 219, 1957, doi: 10.1021/ed034pa34.1.

[92] G. Williams and H. N. McMurray, “Chromate Inhibition of Corrosion-Driven Organic Coating Delamination Studied Using a Scanning Kelvin Probe Technique,” *J. Electrochem. Soc.*, vol. 148, no. 10, p. B377, 2001, doi: 10.1149/1.1396336.

[93] M. Stratmann, H. Streckel, and R. Feser, “A new technique able to measure directly the delamination of organic polymer films,” *Corros. Sci.*, vol. 32, no. 4, pp. 467–470, Jan. 1991, doi: 10.1016/0010-938X(91)90126-A.

[94] M. Stratmann, R. Feser, and A. Leng, “Corrosion protection by organic films,” *Electrochim. Acta*, vol. 39, no. 8–9, pp. 1207–1214, Jun. 1994, doi: 10.1016/0013-4686(94)E0038-2.

[95] W. Fürbeth and M. Stratmann, “The delamination of polymeric coatings from electrogalvanised steel – a mechanistic approach.,” *Corros. Sci.*, vol. 43, no. 2, pp. 207–227, Feb. 2001, doi: 10.1016/S0010-938X(00)00047-0.

[96] W. Fürbeth and M. Stratmann, “The delamination of polymeric coatings from electrogalvanized steel – a mechanistic approach.,” *Corros. Sci.*, vol. 43, no. 2,

pp. 229–241, Feb. 2001, doi: 10.1016/S0010-938X(00)00048-2.

[97] G. Guillonneau, G. Kermouche, S. Bec, and J.-L. Loubet, “Determination of mechanical properties by nanoindentation independently of indentation depth measurement,” *J. Mater. Res.*, vol. 27, no. 19, pp. 2551–2560, Oct. 2012, doi: 10.1557/jmr.2012.261.

[98] G. Sundararajan and M. Roy, “Hardness Testing,” *Encycl. Mater. Sci. Technol.*, pp. 3728–3736, Jan. 2001, doi: 10.1016/B0-08-043152-6/00665-3.

[99] K. . Kumar, H. Van Swygenhoven, and S. Suresh, “Mechanical behavior of nanocrystalline metals and alloys,” *Acta Mater.*, vol. 51, no. 19, pp. 5743–5774, Nov. 2003, doi: 10.1016/j.actamat.2003.08.032.

[100] F. Cellini, Y. Gao, and E. Riedo, “Å-Indentation for non-destructive elastic moduli measurements of supported ultra-hard ultra-thin films and nanostructures,” *Sci. Rep.*, vol. 9, no. 1, p. 4075, Dec. 2019, doi: 10.1038/s41598-019-40636-0.

[101] R. Saha and W. D. Nix, “Effects of the substrate on the determination of thin film mechanical properties by nanoindentation,” *Acta Mater.*, vol. 50, no. 1, pp. 23–38, Jan. 2002, doi: 10.1016/S1359-6454(01)00328-7.

[102] H. Rhee, J. P. Lucas, and K. N. Subramanian, “Micromechanical characterization of thermomechanically fatigued lead-free solder joints,” *J. Mater. Sci. Mater. Electron.*, pp. 477–484, 2002.

[103] R. R. Chromik, R. P. Vinci, S. L. Allen, and M. R. Notis, “Nanoindentation measurements on Cu–Sn and Ag–Sn intermetallics formed in Pb-free solder joints,” *J. Mater. Res.*, vol. 18, no. 9, pp. 2251–2261, Sep. 2003, doi: 10.1557/JMR.2003.0314.

[104] D. R. Frear and P. T. Vianco, “Intermetallic growth and mechanical behavior of low and high melting temperature solder alloys,” *Metall. Mater. Trans. A*, vol. 25, no. 7, pp. 1509–1523, Jul. 1994, doi: 10.1007/BF02665483.

[105] J.-Y. Rho, T. Y. Tsui, and G. M. Pharr, “Elastic properties of human cortical and trabecular lamellar bone measured by nanoindentation,” *Biomaterials*, vol. 18, no. 20, pp. 1325–1330, Oct. 1997, doi: 10.1016/S0142-9612(97)00073-2.

[106] W. H. Roos and G. J. L. Wuite, “Nanoindentation Studies Reveal Material Properties of Viruses,” *Adv. Mater.*, vol. 21, no. 10–11, pp. 1187–1192, Mar. 2009, doi: 10.1002/adma.200801709.

[107] W. C. Oliver and G. M. Pharr, “Measurement of hardness and elastic modulus by instrumented indentation: Advances in understanding and refinements to methodology,” *J. Mater. Res.*, vol. 19, no. 1, pp. 3–20, Jan. 2004, doi: 10.1557/jmr.2004.19.1.3.

[108] G. M. Pharr and W. C. Oliver, “Measurement of Thin Film Mechanical Properties Using Nanoindentation,” *MRS Bull.*, vol. 17, no. 7, pp. 28–33, Jul. 1992, doi: 10.1557/S0883769400041634.

[109] D. Q. Chen, G.-Y. Zhou, Z. P. Liu, and S.-T. Tu, “Nanoindentation Experimental Study on Mechanical Properties of As-cast BNi-2 Solder Alloy,” *Procedia Eng.*, vol. 130, pp. 652–661, 2015, doi: 10.1016/j.proeng.2015.12.289.

[110] A. Karimzadeh, S. S. R. Koloor, M. R. Ayatollahi, A. R. Bushroa, and M. Y. Yahya, “Assessment of Nano-Indentation Method in Mechanical Characterization of Heterogeneous Nanocomposite Materials Using Experimental and Computational Approaches,” *Sci. Rep.*, vol. 9, no. 1, p. 15763, Dec. 2019, doi: 10.1038/s41598-019-51904-4.

[111] E. Lucon, “Material damage evaluation and residual life assessment of primary power plant components for long-term operation using specimens of non-standard dimensions,” *Rev. Métallurgie*, vol. 98, no. 12, pp. 1079–1091, Dec. 2001, doi: 10.1051/metal:2001149.

[112] T. E. García, C. Rodríguez, F. J. Belzunce, and C. Suárez, “Estimation of the mechanical properties of metallic materials by means of the small punch test,” *J. Alloys Compd.*, vol. 582, pp. 708–717, Jan. 2014, doi: 10.1016/j.jallcom.2013.08.009.

[113] R. C. Hurst, R. J. Lancaster, S. P. Jeffs, and M. R. Bache, “The contribution of small punch testing towards the development of materials for aero-engine applications,” *Theor. Appl. Fract. Mech.*, vol. 86, pp. 69–77, Dec. 2016, doi: 10.1016/j.tafmec.2016.07.013.

[114] R. J. Lancaster, H. W. Illsley, G. R. Davies, S. P. Jeffs, and G. J. Baxter, "Modelling the small punch tensile behaviour of an aerospace alloy," *Mater. Sci. Technol.*, vol. 33, no. 9, pp. 1065–1073, Jun. 2017, doi: 10.1080/02670836.2016.1230168.

[115] M. Fernández, C. Rodríguez, F. J. Belzunce, and T. E. García, "Use of small punch test to estimate the mechanical properties of sintered products and application to synchronizer hubs," *Met. Powder Rep.*, vol. 72, no. 5, pp. 355–360, Sep. 2017, doi: 10.1016/j.mprp.2016.02.056.

[116] C. L. Walters, M. Bruchhausen, J.-M. Lapetite, and W. Duvalois, "Fracture Testing of Existing Structures Without the Need for Repairs," Jun. 2017, doi: 10.1115/OMAE2017-61420.

[117] J. SINGH, N. K. SHARMA, and S. S. SEHGAL, "SMALL PUNCH TESTING: AN ALTERNATIVE TESTING TECHNIQUE TO EVALUATE TENSILE BEHAVIOR OF CORTICAL BONE," *J. Mech. Med. Biol.*, vol. 17, no. 06, p. 1750102, Sep. 2017, doi: 10.1142/S0219519417501020.

[118] C. Rodríguez, I. I. Cuesta, M. L. Maspoch, and F. J. Belzunce, "Application of the miniature small punch test for the mechanical characterization of polymer materials," *Theor. Appl. Fract. Mech.*, vol. 86, pp. 78–83, Dec. 2016, doi: 10.1016/j.tafmec.2016.10.001.

[119] C. Rodríguez, J. García Cabezas, E. Cárdenas, F. J. Belzunce, and C. Betegón, "Mechanical properties characterization of heat-affected zone using the small punch test," *Weld. J. (Miami, Fla)*, vol. 88, no. 9, pp. 188s-192s, 2009, [Online]. Available: http://www.scopus.com/inward/record.url?eid=2-s2.0-70349446383&partnerID=40&md5=61c83bc5932eddaaa242faa6b225a2d4.

[120] E. Fleury and J. S. Ha, "Small punch tests to estimate the mechanical properties of steels for steam power plant: I. Mechanical strength," *Int. J. Press. Vessel. Pip.*, vol. 75, no. 9, pp. 699–706, Aug. 1998, doi: 10.1016/S0308-0161(98)00074-X.

[121] T. Misawa, S. Nagata, N. Aoki, J. Ishizaka, and Y. Hamaguchi, "Fracture toughness evaluation of fusion reactor structural steels at low temperatures by small punch tests," *J. Nucl. Mater.*, vol. 169, pp. 225–232, Dec. 1989, doi:

10.1016/0022-3115(89)90538-2.

[122] C. Wen, T. Xu, and K. Guan, “Correlation Factor Study of Small Punch Creep Test and Its Life Prediction,” *Materials (Basel).*, vol. 9, no. 10, p. 796, Sep. 2016, doi: 10.3390/ma9100796.

[123] L. Zhao, H. Jing, L. Xu, Y. Han, J. Xiu, and Y. Qiao, “Evaluating of creep property of distinct zones in P92 steel welded joint by small punch creep test,” *Mater. Des.*, vol. 47, pp. 677–686, May 2013, doi: 10.1016/j.matdes.2012.12.032.

[124] R. Kopriva, M. Brumovsky, and P. Petelova, “Current status of the small punch test standardization within the ASTM,” *Ubiquity Proc.*, vol. 1, no. S1, p. 34, Sep. 2018, doi: 10.5334/uproc.34.

[125] K. Matocha, “Small-Punch Testing for Tensile and Fracture Behavior: Experiences and Way Forward,” in *Small Specimen Test Techniques: 6th Volume*, 100 Barr Harbor Drive, PO Box C700, West Conshohocken, PA 19428-2959: ASTM International, 2015, pp. 1–15.

[126] M. Bruchhausen *et al.*, “Recent developments in small punch testing: Tensile properties and DBTT,” *Theor. Appl. Fract. Mech.*, vol. 86, pp. 2–10, Dec. 2016, doi: 10.1016/j.tafmec.2016.09.012.

[127] S. Davies, S. Jeffs, R. Lancaster, and G. Baxter, “High Temperature Deformation Mechanisms in a DLD Nickel Superalloy,” *Materials (Basel).*, vol. 10, no. 5, p. 457, Apr. 2017, doi: 10.3390/ma10050457.

[128] X. Mao and H. Takahashi, “Development of a further-miniaturized specimen of 3 mm diameter for tem disk (ø 3 mm) small punch tests,” *J. Nucl. Mater.*, vol. 150, no. 1, pp. 42–52, Sep. 1987, doi: 10.1016/0022-3115(87)90092-4.

[129] J. C. Chica, P. M. Bravo Díez, and M. Preciado Calzada, “Improved correlation for elastic modulus prediction of metallic materials in the Small Punch Test,” *Int. J. Mech. Sci.*, vol. 134, pp. 112–122, Dec. 2017, doi: 10.1016/j.ijmecsci.2017.10.006.

[130] J. Malone, “Novel advancements to galvanised steel coating using quaternary additions and ultrasound,” Swansea University, 2016.

[131] R. L. Liu, Z. R. Zeng, J. R. Scully, G. Williams, and N. Birbilis, "Simultaneously improving the corrosion resistance and strength of magnesium via low levels of Zn and Ge additions," *Corros. Sci.*, vol. 140, pp. 18–29, Aug. 2018, doi: 10.1016/j.corsci.2018.06.027.

[132] J. V. D., "Stability constants of metal-ion complexes (Sillen, Lars Gunnar; Martell, Arthur E.)," *J. Chem. Educ.*, vol. 42, no. 9, p. 521, Sep. 1965, doi: 10.1021/ed042p521.1.

[133] K. H. Gayer, "The Hydrolysis of Cations Baes, Charles F., Jr.; Mesmer, Robert E.)," *J. Chem. Educ.*, vol. 54, no. 10, p. A429, Oct. 1977, doi: 10.1021/ed054pA429.1.

[134] Shahin Mehraban, "Corrosion mechanism, inhibition and mechanical properties of zinc magnesium aluminium alloy coated galvanised steel," Swansea University, 2013.

[135] X. Cao, X. Zhou, Z. Li, Z. Luo, and J. Duan, "Interface Microstructure and Nanoindentation Characterization of Laser Offset Welded 5052 Aluminum to Press-Hardened Steel Using a Brass Interlayer," *Metals (Basel).*, vol. 9, no. 11, p. 1143, Oct. 2019, doi: 10.3390/met9111143.

[136] M. F. Moreno, G. Bertolino, and A. Yawny, "The significance of specimen displacement definition on the mechanical properties derived from Small Punch Test," *Mater. Des.*, vol. 95, pp. 623–631, Apr. 2016, doi: 10.1016/j.matdes.2016.01.148.

[137] H. Illsley, R. Lancaster, R. Hurst, S. Jeffs, and G. Baxter, "Mechanical Property Characterisation of Electron Beam Melted (EBM) Ti-6Al-4V via Small Punch Tensile Testing," *Key Eng. Mater.*, vol. 734, pp. 51–60, 2017, doi: 10.4028/www.scientific.net/KEM.734.51.

[138] C. Yao, H. Lv, T. Zhu, W. Zheng, X. Yuan, and W. Gao, "Effect of Mg content on microstructure and corrosion behavior of hot dipped Zn–Al–Mg coatings," *J. Alloys Compd.*, vol. 670, pp. 239–248, Jun. 2016, doi: 10.1016/j.jallcom.2016.02.026.

[139] E. Mostaed, M. Sikora-Jasinska, and M. Vedani, "Zinc-Based Degradable

Implants," in *Encyclopedia of Biomedical Engineering*, vol. 1–3, Elsevier, 2019, pp. 478–487.

[140] J. Drápala, G. Kostiuková, and M. Losertová, "Contribution to the aluminum–tin–zinc ternary system," *IOP Conf. Ser. Mater. Sci. Eng.*, vol. 266, no. 1, p. 012002, Nov. 2017, doi: 10.1088/1757-899X/266/1/012002.

[141] S. Li *et al.*, "The effects of RE and Si on the microstructure and corrosion resistance of Zn–6Al–3Mg hot dip coating," *Appl. Surf. Sci.*, vol. 357, pp. 2004–2012, Dec. 2015, doi: 10.1016/j.apsusc.2015.09.172.

[142] W. Liu *et al.*, "Influence of alloyed magnesium on the microstructure and long-term corrosion behavior of hot-dip Al–Zn–Si coating in NaCl solution," *Corros. Sci.*, vol. 104, pp. 217–226, Mar. 2016, doi: 10.1016/j.corsci.2015.12.014.

[143] C. Nicard, C. Allély, and P. Volovitch, "Effect of Zn and Mg alloying on microstructure and anticorrosion mechanisms of Al-Si based coatings for high strength steel," *Corros. Sci.*, vol. 146, pp. 192–201, Jan. 2019, doi: 10.1016/j.corsci.2018.10.037.

[144] J. L. L. Davies, C. F. F. Glover, J. Van de Langkruis, E. Zoestbergen, and G. Williams, "The effect of Mg concentration on the resistance of PVD Zn-Mg coatings to corrosion driven organic coating delamination," *Corros. Sci.*, vol. 100, pp. 607–618, Nov. 2015, doi: 10.1016/j.corsci.2015.08.036.

[145] N. Wint, Z. S. Barrett, H. N. McMurray, and G. Williams, "Combinatorial Studies into the Effect of Thermally Inter-Diffused Magnesium on the Kinetics of Organic Coating Cathodic Delamination from Zinc Galvanized Steel," *J. Electrochem. Soc.*, vol. 167, no. 2, p. 021502, Jan. 2020, doi: 10.1149/1945-7111/ab6289.

[146] "www.zinga-uk.com." http://www.zinga-uk.com/product-range/zingaspray/technical-data-sheets (accessed May 22, 2020).

[147] J. Han and K. Ogle, "Editors' Choice—Dealloying of MgZn 2 Intermetallic in Slightly Alkaline Chloride Electrolyte and Its Significance in Corrosion Resistance," *J. Electrochem. Soc.*, vol. 164, no. 14, pp. C952–C961, Nov.

2017, doi: 10.1149/2.0341714jes.

[148] H. N. McMurray and G. Williams, “Under film/coating corrosion,” in *Shreir’s Corrosion*, 2010, pp. 988–1004.

[149] W. Fürbeth and M. Stratmann, “The delamination of polymeric coatings from electrogalvanised steel – a mechanistic approach.,” *Corros. Sci.*, vol. 43, no. 2, pp. 207–227, Feb. 2001, doi: 10.1016/S0010-938X(00)00047-0.

[150] A. Leng, H. Streckel, and M. Stratmann, “The delamination of polymeric coatings from steel. Part 1: Calibration of the Kelvinprobe and basic delamination mechanism,” *Corros. Sci.*, vol. 41, no. 3, pp. 547–578, Mar. 1998, doi: 10.1016/S0010-938X(98)00166-8.

[151] R. J. Holness, G. Williams, D. A. Worsley, and H. N. McMurray, “Polyaniline Inhibition of Corrosion-Driven Organic Coating Cathodic Delamination on Iron,” *J. Electrochem. Soc.*, vol. 152, no. 2, p. B73, 2005, doi: 10.1149/1.1850857.

[152] J. F. Watts and J. E. Castle, “The application of X-ray photoelectron spectroscopy to the study of polymer-to-metal adhesion,” *J. Mater. Sci.*, vol. 19, no. 7, pp. 2259–2272, Jul. 1984, doi: 10.1007/BF01058103.

[153] I. M. Zin, S. B. Lyon, V. I. Pokhmurskii, and M. C. Simmonds, “Inhibition of steel and galvanised steel corrosion by zinc and calcium ions in the presence of phosphate,” *Corros. Eng. Sci. Technol.*, vol. 39, no. 2, pp. 167–173, Jun. 2004, doi: 10.1179/147842204225016967.

[154] S. A. Katz, “The analytical biochemistry of chromium.,” *Environ. Health Perspect.*, vol. 92, pp. 13–16, May 1991, doi: 10.1289/ehp.919213.

[155] Z. Fang, M. Zhao, H. Zhen, L. Chen, P. Shi, and Z. Huang, “Genotoxicity of Tri- and Hexavalent Chromium Compounds In Vivo and Their Modes of Action on DNA Damage In Vitro,” *PLoS One*, vol. 9, no. 8, p. e103194, Aug. 2014, doi: 10.1371/journal.pone.0103194.

[156] R. M. Park, J. F. Bena, L. T. Stayner, R. J. Smith, H. J. Gibb, and P. S. J. Lees, “Hexavalent Chromium and Lung Cancer in the Chromate Industry: A Quantitative Risk Assessment,” *Risk Anal.*, vol. 24, no. 5, pp. 1099–1108, Oct.

2004, doi: 10.1111/j.0272-4332.2004.00512.x.

[157] H. J. Gibb, P. S. J. Lees, P. F. Pinsky, and B. C. Rooney, “Lung cancer among workers in chromium chemical production,” *Am. J. Ind. Med.*, vol. 38, no. 2, pp. 115–126, Aug. 2000, doi: 10.1002/1097-0274(200008)38:2<115::AID-AJIM1>3.0.CO;2-Y.

[158] S. M. Powell, H. N. McMurray, and D. A. Worsley, “Use of the Scanning Reference Electrode Technique for the Evaluation of Environmentally Friendly, Nonchromate Corrosion Inhibitors,” *CORROSION*, vol. 55, no. 11, pp. 1040–1051, Nov. 1999, doi: 10.5006/1.3283941.

[159] K. Aramaki, “The inhibition effects of chromate-free, anion inhibitors on corrosion of zinc in aerated 0.5 M NaCl,” *Corros. Sci.*, vol. 43, no. 3, pp. 591–604, Mar. 2001, doi: 10.1016/S0010-938X(00)00085-8.

[160] H. H. Uhlig, D. N. Triadis, and M. Stern, “Effect of Oxygen, Chlorides, and Calcium Ion on Corrosion Inhibition of Iron by Polyphosphates,” *J. Electrochem. Soc.*, vol. 102, no. 2, p. 59, 1955, doi: 10.1149/1.2429995.

[161] Z. Szklarska-Smialowska and J. Mańkowski, “Cathodic inhibition of the corrosion of mild steel in phosphate, tungstate, arsenate and silicate solutions containing Ca 2+ ions,” *Br. Corros. J.*, vol. 4, no. 5, pp. 271–275, Sep. 1969, doi: 10.1179/bcj.1969.4.5.271.

[162] H. Okamoto, “Ca-Zn (Calcium-Zinc),” *J. Phase Equilibria Diffus.*, vol. 34, no. 2, pp. 171–171, Apr. 2013, doi: 10.1007/s11669-012-0180-3.

[163] H. F. Li *et al.*, “Development of biodegradable Zn-1X binary alloys with nutrient alloying elements Mg, Ca and Sr,” *Sci. Rep.*, vol. 5, no. 1, p. 10719, Sep. 2015, doi: 10.1038/srep10719.

[164] H. Li, H. Yang, Y. Zheng, F. Zhou, K. Qiu, and X. Wang, “Design and characterizations of novel biodegradable ternary Zn-based alloys with IIA nutrient alloying elements Mg, Ca and Sr,” *Mater. Des.*, vol. 83, pp. 95–102, Oct. 2015, doi: 10.1016/j.matdes.2015.05.089.

[165] Y. Aierken *et al.*, “Portlandite crystal: Bulk, bilayer, and monolayer structures,” *Phys. Rev. B*, vol. 91, no. 24, p. 245413, Jun. 2015, doi:

10.1103/PhysRevB.91.245413.

[166] C. Xia, W. Xiong, J. Du, T. Wang, Z. Wei, and J. Li, “Robust electronic and mechanical properties to layer number in 2D wide-gap X(OH) 2 (X = Mg, Ca),” *J. Phys. D. Appl. Phys.*, vol. 51, no. 1, p. 015107, Jan. 2018, doi: 10.1088/1361-6463/aa996e.

[167] A. Farhad and Z. Mohammadi, “Calcium hydroxide: a review,” *Int. Dent. J.*, vol. 55, no. 5, pp. 293–301, Oct. 2005, doi: 10.1111/j.1875-595X.2005.tb00326.x.

[168] L. R. G. Fava and W. P. Saunders, “Calcium hydroxide pastes: classification and clinical indications,” *Int. Endod. J.*, vol. 32, no. 4, pp. 257–282, Jul. 1999, doi: 10.1046/j.1365-2591.1999.00232.x.

[169] R. G. Bates, V. E. Bower, and E. R. Smith, “Calcium hydroxide as a highly alkaline pH standard,” *J. Res. Natl. Bur. Stand. (1934).*, vol. 56, no. 6, p. 305, Jun. 1956, doi: 10.6028/jres.056.040.

[170] S. Thomas, I. S. Cole, M. Sridhar, and N. Birbilis, “Revisiting zinc passivation in alkaline solutions,” *Electrochim. Acta*, vol. 97, pp. 192–201, May 2013, doi: 10.1016/j.electacta.2013.03.008.

[171] T. Lewis, “Investigation into the Corrosion Behaviour and Effect of Inhibitor Additions on Commercial Zn-Mg-Al Alloys,” Swansea University, 2018.

[172] A. A. al-Swaidani, “Modified Zinc Phosphate Coatings: A Promising Approach to Enhance the Anti-Corrosion Properties of Reinforcing Steel,” *MOJ Civ. Eng.*, vol. 3, no. 5, Dec. 2017, doi: 10.15406/mojce.2017.03.00083.

[173] R. Zeng, Z. Lan, L. Kong, Y. Huang, and H. Cui, “Characterization of calcium-modified zinc phosphate conversion coatings and their influences on corrosion resistance of AZ31 alloy,” *Surf. Coatings Technol.*, vol. 205, no. 11, pp. 3347–3355, Feb. 2011, doi: 10.1016/j.surfcoat.2010.11.027.